

Dissertation  
submitted to the  
Combined Faculties of the Natural Sciences and Mathematics  
of the Ruperto-Carola-University of Heidelberg, Germany,  
for the degree of  
Doctor of Natural Sciences

Put forward by  
MIRIAM JULIA KEPPLER  
born in Munich, Germany

Oral examination: November 11, 2020



GIANT PLANET FORMATION IN DISKS:  
AN OBSERVATIONAL PERSPECTIVE

REFEREES:

PROF. DR. THOMAS HENNING

PROF. DR. CORNELIS DULLEMOND



## Abstract

This Thesis is dedicated to the characterization of protoplanetary disks – the cradles of planets – and to the search for forming planets embedded in these disks. To this goal, the presented work analyses high-angular resolution observations in the near-infrared and sub-millimeter wavelength regime using the Spectro-Polarimetric High-contrast Exoplanet REsearch instrument (SPHERE) and the Atacama Large Millimeter Array (ALMA).

SPHERE observations of the circumstellar disk around PDS 70 reveal the presence of a planetary-mass companion in the gap of the disk. This discovery is the first unambiguous detection of a planet still caught at formation within its natal disk and thus represents a unique laboratory to observationally study processes of planet-disk interactions.

We perform a thorough analysis of the system using follow-up observations with ALMA, which reveals the disk to be highly structured in both dust and gas. Most prominently, gas and dust are strongly depleted around the location of PDS 70 b, in agreement with the predictions from theoretical models of planet-disk interactions. Further, analysis of the gas kinematics shows perturbations in the disk which can account for the large cavity in the dust disk.

Finally, we present an analysis of SPHERE scattered light observations of the circumbinary disk around GG Tau A. An outer dust ring and the immediate circumbinary environment shows various substructures. These are found to be the result of binary-disk interactions by comparison to hydrodynamical simulations. We conclude that the observed cavity size can be explained by the interactions with the central binary on an orbit which is coplanar with the outer disk.

This system illustrates that in certain configurations, multiple systems are able to sustain massive, gas-rich disks over several million years, providing potentially favourable conditions for planet formation.

## Zusammenfassung

Diese Dissertation ist der Charakterisierung von protoplanetaren Scheiben, den Geburtsstätten von Planeten, sowie der Suche nach Planeten während ihrer Entstehung in diesen Scheiben gewidmet. Mit diesem Ziel analysieren wir in dieser Arbeit hochauflösende Beobachtungen im Nahinfrarot und Submillimeter Bereich, und nutzen dazu das Spectro-Polarimetric High-contrast Exoplanet REsearch (SPHERE) Instrument und das Atacama Large Millimeter Array (ALMA) Interferometer.

Beobachtungen der protoplanetaren Scheibe um PDS 70 enthüllen die Detektion eines Planeten, PDS 70 b, welcher sich in einer breiten Lücke der Scheibe befindet. Diese Entdeckung entspricht der ersten eindeutigen Detektion eines Planeten im Stadium der Entstehung. PDS 70 ist daher ein einzigartiges Testbett um Prozesse der Wechselwirkungen zwischen Planet und Scheibe mit Beobachtungen zu überprüfen.

Nachfolgebeobachtungen mit ALMA ermöglichen uns eine detaillierte Analyse des Systems. Sowohl Staub als auch Gas in der Scheibe zeigen zahlreiche Strukturen auf, wovon die auffälligste eine tiefe Lücke um PDS 70 b ist, welche in Übereinstimmung mit den Vorhersagen theoretischer Modelle ist. Des Weiteren detektieren wir Störungen im Geschwindigkeitsfeld der Scheibe, welche die Weite der Lücke in der Staubverteilung erklären können.

Des Weiteren präsentieren wir eine Analyse von SPHERE Streulichtdaten der zirkumbinären Scheibe um GG Tau A. Wir zeigen auf dass ein äußere Staubring sowie die unmittelbare Umgebung des Doppelsterns von zahlreichen Strukturen durchzogen sind, welche durch die Wechselwirkung des Doppelsterns mit der Scheibe qualitativ erklärt werden können. Im Besonderen ergibt unsere Analyse dass die beobachtete Lücke in der Scheibe durch die Wechselwirkungen mit dem Doppelstern, dessen Umlaufbahn sich in der Scheibenebene befindet, verursacht werden kann.

Dieses System ist ein Beispiel dafür dass unter bestimmten Bedingungen Doppelsterne eine massereiche Scheibe über mehrere Millionen Jahre beibehalten können, und damit möglicherweise über günstige Bedingungen für Planetenentstehung verfügen können.

*Für meine Eltern.*



# Contents

---

<b>1</b>	<b>Introduction</b>	<b>1</b>
1.1	Protoplanetary disks . . . . .	3
1.1.1	The basic inventory of protoplanetary disks . . . . .	4
1.1.2	Radial structure and extent . . . . .	4
1.1.3	Vertical structure . . . . .	5
1.1.4	Radial drift and dust settling . . . . .	6
1.1.5	Disk lifetime and evolution . . . . .	7
1.2	Giant planet formation in a nutshell . . . . .	8
1.2.1	Core accretion . . . . .	8
1.2.2	Disk instability . . . . .	11
1.3	Linking disk theory and observations: radiative transfer models . . . . .	13
1.3.1	Dust opacities . . . . .	13
1.3.2	Radiative transfer equation . . . . .	14
1.3.3	Radiative transfer code: RADMC-3D . . . . .	16
1.4	Observational diagnostics of giant planet formation . . . . .	17
1.4.1	Near-infrared Angular Differential Imaging . . . . .	18
1.4.2	Near-infrared Polarimetric Imaging . . . . .	20
1.4.3	Sub-millimeter Interferometry . . . . .	22
1.5	Observing planet formation: state of the field . . . . .	28
1.6	Motivation and outline of the Thesis . . . . .	31
<b>2</b>	<b>Discovery of a planetary-mass companion within the gap of the transition disk around PDS 70</b>	<b>33</b>
2.1	Motivation . . . . .	33
2.2	The target: PDS 70 . . . . .	34
2.3	Observations and data reduction . . . . .	37
2.3.1	IRDIS polarimetric observations (J-band) . . . . .	37
2.3.2	ZIMPOL polarimetric observations (VBB band) . . . . .	40

2.3.3	IRDIFS angular and spectral differential imaging observations (Y-H-band) . . . . .	40
2.3.4	IRDIFS_EXT angular and spectral differential imaging observations (Y-K-band) . . . . .	41
2.3.5	NaCo angular differential imaging observations (L'-band) . . . . .	42
2.3.6	Archival NICI angular differential imaging observations (L'-band) . . . . .	42
2.4	Disk analysis . . . . .	42
2.4.1	The outer disk in polarized scattered light . . . . .	42
2.4.2	Detection of the inner disk in polarized light . . . . .	46
2.4.3	The disk in IRDIS angular differential imaging . . . . .	47
2.5	Radiative transfer modeling . . . . .	48
2.5.1	Model setup . . . . .	48
2.5.2	Modelling the inner disk . . . . .	50
2.5.3	Discussion of brightness asymmetries in the disk . . . . .	51
2.6	Detection of a planetary mass companion . . . . .	54
2.6.1	Astrometry . . . . .	55
2.6.2	Photometry . . . . .	57
2.6.3	The nature of the point-like source . . . . .	58
2.6.4	Companion properties . . . . .	60
2.7	Summary and conclusions . . . . .	66
2.8	Follow-up studies . . . . .	67
2.8.1	Confirmation and first orbital and atmospheric characterization of PDS 70 b . . . . .	67
2.8.2	A young multiplanetary system at the stage of formation . . . . .	67
<b>3</b>	<b>A highly structured disk around the planet host PDS 70 revealed by high-angular resolution observations with ALMA</b>	<b>71</b>
3.1	Motivation . . . . .	71
3.2	Observations and data reduction . . . . .	72
3.3	Results . . . . .	73
3.3.1	855 $\mu\text{m}$ dust continuum . . . . .	73
3.3.2	$^{12}\text{CO } J = 3 - 2$ . . . . .	81
3.4	Discussion . . . . .	90
3.4.1	Hydrodynamic and radiative transfer models . . . . .	90
3.4.2	Upper limit on CPD dust mass . . . . .	96
3.5	Summary and conclusions . . . . .	97

3.6	Follow-up studies . . . . .	98
3.6.1	Discovery of continuum emission associated with the PDS 70 proto-planets . . . . .	98
3.6.2	Planet-disk interactions in the presence of two planets . . . . .	99
<b>4</b>	<b>An in-depth view of PDS 70 with ALMA at high spectral resolution</b>	<b>101</b>
4.1	Motivation . . . . .	101
4.2	Observations and data reduction . . . . .	102
4.2.1	Continuum self-calibration and imaging . . . . .	103
4.2.2	CO imaging . . . . .	104
4.2.3	Combination with previous data . . . . .	104
4.3	Results . . . . .	106
4.3.1	Continuum . . . . .	106
4.3.2	Analysis of $^{12}\text{CO}$ and $^{13}\text{CO}$ . . . . .	111
4.4	Discussion . . . . .	126
4.4.1	Continuum signal of PDS 70 b . . . . .	126
4.4.2	Potential $^{12}\text{CO}$ kink feature close to PDS 70 c? . . . . .	127
4.4.3	Emission surfaces . . . . .	129
4.5	Summary and conclusions . . . . .	130
<b>5</b>	<b>SPHERE observations of binary-disk interactions in GG Tau A</b>	<b>133</b>
5.1	Motivation . . . . .	133
5.2	Context . . . . .	134
5.3	Stellar properties . . . . .	136
5.4	Observations and data reduction . . . . .	138
5.5	Results . . . . .	140
5.5.1	Inner region . . . . .	140
5.5.2	Outer disk geometry . . . . .	143
5.5.3	Streamers . . . . .	145
5.5.4	Shadows . . . . .	147
5.5.5	Spirals . . . . .	149
5.6	Modeling . . . . .	150
5.6.1	Hydrodynamical model setup . . . . .	150
5.6.2	Postprocessing of hydrodynamical simulations . . . . .	151
5.6.3	Modeling results and comparison to observations . . . . .	152
5.7	Discussion . . . . .	156
5.7.1	Accretion streams within the circumbinary gap . . . . .	156
5.7.2	Spiral structures as imprints of binary-disk interaction . . . . .	156

5.7.3	Gap size as a result of binary-disk interactions . . . . .	157
5.7.4	Implications for planet formation . . . . .	159
5.8	Summary and conclusions . . . . .	159
<b>6</b>	<b>Summary and Outlook</b>	<b>161</b>
6.1	Summary . . . . .	161
6.2	Outlook . . . . .	164
<b>A</b>	<b>Supplementary material</b>	<b>169</b>
A.1	Supplementary material for Chapter 2 . . . . .	169
A.2	Supplementary material for Chapter 4 . . . . .	172
A.2.1	Zoom-in of channels maps for 'LB2' data . . . . .	172
A.2.2	Peak brightness, zeroth moment, and channel maps for combined data . . . . .	173
A.2.3	Opposed spectra for inner disk region . . . . .	176
A.3	Supplementary material for Chapter 5 . . . . .	176
A.3.1	Polarized intensity pattern in the presence of two illumination sources	176
A.3.2	Early meta-stable simulation phase . . . . .	177
<b>B</b>	<b>Appendix</b>	<b>181</b>
B.1	Acronyms . . . . .	181
B.2	List of Figures . . . . .	183
B.3	List of Tables . . . . .	186
<b>C</b>	<b>List of refereed publications</b>	<b>187</b>
<b>D</b>	<b>Bibliography</b>	<b>195</b>
<b>E</b>	<b>Acknowledgements</b>	<b>217</b>

# 1

## Introduction

---

Planets are a by-product of star formation. It is generally agreed that planets form out of protoplanetary disks – the cradles of planets – that surround new-born stars during their first few million years of lifetime. Understanding the processes of planet formation is an active field of research, and many questions are still open.

Also our Sun was once surrounded by a protoplanetary disk, the remnants of which are preserved in solid bodies that still populate, for example, the asteroid belt between Mars and Jupiter. These bodies thus provide one of the rare windows allowing to peek into the history of our Solar System. Isotopic measurements have revealed that meteorites initially originate from two distinct reservoirs in the Solar protoplanetary disk (Warren, 2011; Budde et al., 2016). These reservoirs appear to have remained spatially separated during the first few million years after the formation of the Solar System. It is suspected that this separation was caused by the formation of Jupiter, which opened a gap in the disk and thus prevented the exchange of material between these two reservoirs (Kruijer et al., 2017). Thus, the emergence of the gas giants has likely impacted the structure and dynamics of the early Solar System. But their formation may have been relevant even for Earth.

Water is essential for life on Earth, yet its existence is not self-evident. The planetary building blocks that formed in the terrestrial planet region of our Solar System were likely dry (van Dishoeck et al. 2014; but note recent findings by Piani et al. 2020), still our planet is today surrounded by a layer of oceans, and more water is residing in the Earth's mantle (Hirschmann, 2006; Peslier et al., 2017). Several scenarios to explain the origin of water on Earth are currently discussed in the literature. There are two main groups of models; those that assume Earth's water was acquired locally from the protoplanetary disk, and those that propose that water was delivered from the outer, ice-rich regions of the Solar System (e.g., King et al., 2010; Ikoma & Genda, 2006; Raymond & Izidoro, 2017). In one of the currently most plausible scenarios (Meech & Raymond, 2019), at least parts of Earth's water was delivered by small bodies originating from more distant regions, whose orbits were perturbed by the formation and migration of the giant planets, causing them to be

scattered into the terrestrial planet forming region. This scenario is appealing as it can account for the chemical composition of Earth's water, and is at the same time consistent with current models of the formation and migration history of giant planets within the Solar System (Meech & Raymond, 2019).

While we cannot travel back into the past to directly solve the puzzle of how the Solar System formed, we can try to learn from other, *extrasolar* planetary systems. Also here, the picture emerges that the formation of giant planets, and their interaction with the surrounding material in the primordial disk, may in many cases have played an important role for the final system properties.

In 2019, the number of confirmed exoplanets broke through the 4000 mark<sup>1</sup>, revealing an extraordinary diversity of planetary system architectures (Winn & Fabrycky, 2015). In our Solar System, rocky planets are found in the inner regions, closer to the Sun, and gas giants are located in the outer regions. More than 20 years of questing extrasolar planets have taught us that exoplanetary systems are much more diverse. Among the largest surprises so far was the existence of Hot Jupiters, giant planets that orbit their host stars at distances closer than Mercury surrounds our Sun (Mayor & Queloz, 1995). It has been suggested that those probably formed further out, and subsequently migrated inward as a result of tidal interactions with the disk or of the perturbation by another giant planet within the system (see review by Dawson & Johnson, 2018). Another interesting result that has been established from exoplanetary demographics is the observation that more than half of Sun-like stars appear to be hosts to one or more super-Earth planets, that is planets with a mass in the range of  $\sim 1-10 M_{\oplus}$  with orbital periods of days to months (e.g., Mayor et al., 2011). This contrasts our Solar System, which lacks any planet of this type. One possible explanation for the puzzling absence of Super-Earths around our Sun refers to the formation of Jupiter, which may have prevented the cores of future super-Earth planets, that formed in the outer regions of the system, to migrate inward into the terrestrial planet formation region (Izidoro et al., 2015). In this picture, the building blocks of Uranus and Neptune (and perhaps Saturn) would have developed into Super-Earths if it was not for Jupiter to hold them back.

While those are only exemplary aspects for which the final answer still need to be found, it is clear that a profound understanding of how giant planets form and interact with their surroundings is crucial in order explain the final properties and architectures of planetary systems. Exploring which of the properties of these systems are imprinted by the initial conditions of the disks and which develop through a variety of dynamical interactions is key for understanding the entire planet population, including our own Solar System. One important step on this road is to study giant extrasolar planets and their birth environments – at a stage during which these objects are still being formed.

---

<sup>1</sup>At the date this text was written (August 29, 2020), 4330 exoplanets were confirmed ([exoplanet.eu](http://exoplanet.eu)).

The topic of this Thesis is to observationally characterize these birthplaces of planets, so-called planet-forming or protoplanetary disks, and to search those for direct and indirect tracers of ongoing planet formation. The next two Sections will elaborate the theoretical foundations by introducing the fundamental properties of protoplanetary disks (Sect. 1.1) and by providing an overview of the current understanding of the giant planet formation process (Sect. 1.2). Section 1.3 introduces radiative transfer models, tools to link the theory of protoplanetary disks with observations, followed by Sect. 1.4 which presents the observational diagnostics used in this Thesis. Section 1.5 summarizes the current state of the field regarding the observations of young planetary systems, and Sect. 1.6 outlines the structure of this Thesis.

## 1.1 Protoplanetary disks

Stars are born in molecular clouds, large and massive reservoirs of cold and dense molecular gas in the Milky Way (McKee & Ostriker, 2007; Dobbs et al., 2014). Star formation is triggered when a dense core within the cloud starts to collapse under its own gravity, either spontaneously or initiated by external perturbations (de Boer & Seggewiss, 2008). As a consequence of angular momentum conservation, material in the primordial, rotating cloud cannot spherically fall onto the star but forms a circumstellar disk. In this disk, dissipative forces lead to the outward transport of angular momentum, allowing material to move inward and being accreted onto the star. At a first stage, being heavily obscured by a dusty envelope, these disks are the main funnels through which mass is rapidly transferred onto the central star. After a fraction of a Myr (Evans et al., 2009; Offner & McKee, 2011), the primordial envelope is mostly accreted or otherwise dispersed, the protostar has gained most of its final mass and accretion from the disk continues at a reduced rate. The now so-called pre-main sequence (PMS) star and the residual gas and dust disk become exposed and accessible to observations in the visible and near-infrared (NIR).

PMS stars are usually categorized in two main groups, according to their masses. T Tauri stars are low-mass ( $\lesssim 2 M_{\odot}$ ) PMS stars, corresponding to spectral types between F and M (Appenzeller & Mundt, 1989). Their higher-mass counterparts, Herbig Ae/Be stars, exhibit masses between  $\sim 2$  and  $8 M_{\odot}$ <sup>2</sup>, corresponding to spectral types A or B (Herbig, 1960; Waters & Waelkens, 1998).

At this stage of evolution, the disk is called a *protoplanetary disk*: this is the place and the time when planet formation will occur. While the gaseous disk only survives for  $\sim 10$  Myr

---

<sup>2</sup>Stars more massive than about  $8 M_{\odot}$  are not observed during their PMS phase because it is so short that they have already evolved onto the main sequence before their envelope has been dispersed.

(see Sect. 1.1.5), the PMS star continues to slowly contract on the order several ten million years, depending on its mass. The contraction of the star increases its temperature until it reaches about  $10^7$  K. At this point, hydrogen fusion is ignited and the star starts its long-term evolution on the main sequence.

As protoplanetary disks are the cradles of planets, this Thesis focuses on the first few million years of stellar lifetime, which is where protoplanetary disks are present. The following Sections provide a summary of their properties, as well as some key processes taking place in protoplanetary disks which will be relevant for this Thesis. Detailed reviews on protoplanetary disks can be found in e.g., Williams & Cieza (2011); Armitage (2011); Andrews (2020).

### 1.1.1 The basic inventory of protoplanetary disks

The initial composition of protoplanetary disks is inherited from the interstellar medium (ISM), which consists to 99% of gas and to 1% of dust (Bohlin et al., 1978). The bulk gas in protoplanetary disks is contained in relatively cool ( $T \lesssim 100$  K) molecular hydrogen,  $H_2$ . Dust in protoplanetary disks is initially mainly composed of a mixture of silicates and carbonaceous materials of sub-micrometer size, as observed in the ISM (Draine, 2003a). In cold regions, those grains may become coated by icy mantles through the freeze-out of molecules from the gas phase onto the grain surfaces. Furthermore, dust can grow to larger sizes by mutual collisions of grains and subsequent coagulation (e.g., Blum, 2018) - the very first step toward the formation of planets.

Being one of the fundamental parameters for the potential of planet formation, the total mass of protoplanetary disks remains controversial. Because  $H_2$  emits only weakly at low temperatures, it is very challenging to be observationally traced in planet-forming disks. Disk masses are therefore indirectly inferred from (sub-)millimeter observations of either the dust or of the molecular gas such as CO (and more recently, HD; Bergin et al., 2013; McClure et al., 2016). However, both tracers are afflicted with some uncertainty, since numerous assumptions, e.g., regarding the dust-to-gas mass ratio, dust opacities, or the CO/ $H_2$  abundance have to be made, some of which are currently challenged (e.g., Williams & Best, 2014; Bergin & Williams, 2018).

### 1.1.2 Radial structure and extent

Protoplanetary disks are no static structures. Mass is continuously transported through the disk and being accreted onto the star. In the framework of viscous accretion (see Sect. 1.1.5), the gas surface density of the disk as a function of radius  $r$  can be expressed as a power law with an exponentially tapered edge (Lynden-Bell & Pringle, 1974; Hartmann

et al., 1998):

$$\Sigma(r) = \Sigma_c \left( \frac{r}{R_c} \right)^{-\gamma} \exp \left[ - \left( \frac{r}{R_c} \right)^{2-\gamma} \right], \quad (1.1)$$

where  $R_c$  is a characteristic radius,  $\Sigma_c$  is the normalization, and  $\gamma$  describes the radial dependence of disk viscosity,  $\nu \propto r^\gamma$ .

The radial extent of protoplanetary disks, i.e., the distance between the inner and outer edge of the disk, can span several orders of magnitudes. The innermost stellar environment is subject to strong irradiation and thus high temperatures, leading to the evaporation of dust and to the ionization of gas. In the paradigm of magnetic accretion (e.g., [Bouvier et al., 2007](#)), strong magnetic fields mediate accretion from the inner disk onto the star along funnel flows, leading to a truncation of the gaseous protoplanetary disk at a few stellar radii (i.e., corresponding to a few times 0.01 au). The inner edge of the dusty component of the disk lies somewhat further out (i.e., at distances on the order of 0.1 au), where the temperature has dropped below the silicate sublimation temperature of  $\sim 1500$  K (see review by [Dullemond & Monnier, 2010](#)).

Typical outer radii of protoplanetary disks are found at tens to a few hundred au (e.g., [Isella et al., 2009](#); [Tazzari et al., 2017](#); [Tripathi et al., 2017](#)). It has been observed that the outer radii of the gaseous components universally exceed that of the dust component (e.g., [Ansdell et al., 2018](#)). The smaller dust disk sizes relative to the gas disks can be explained by the combination of several factors, such as different optical depths of the tracers probing the gas and dust component, a fast radial drift of particles which tends to deplete the outer disk regions from dust (see Sect. 1.1.4), and a less efficient growth of micrometer-sized to millimeter-sized particles, which are traced by the continuum observations, in the outer disk regions compared to the inner regions (e.g., [Isella et al., 2007](#); [Birnstiel & Andrews, 2014](#); [Facchini et al., 2017](#)).

### 1.1.3 Vertical structure

Disks are assumed to be in vertical hydrostatic equilibrium, where the vertical component of the stellar gravity is balanced by the gas thermal pressure. The density at midplane radius  $r$  and height  $z$  above the midplane can then be written as

$$\rho(r, z) = \frac{\Sigma(r)}{\sqrt{2\pi}H(r)} \exp \left( - \frac{z^2}{2H(r)^2} \right), \quad (1.2)$$

## 1 Introduction

where  $H(r)$  denotes the pressure scale height of the disk, defined as the ratio of sound speed  $c_s(r)$  and Keplerian angular frequency  $\Omega_K(r)$ :

$$H(r) = \frac{c_s(r)}{\Omega_K(r)}. \quad (1.3)$$

The pressure scale height increases with distance to the star as a power law of the form

$$H(r) \propto r^\beta. \quad (1.4)$$

If  $\beta = 1$ , thus  $H(r) \propto r$ , the disk has a conical shape (i.e., a constant opening angle), while if  $\beta > 1$ , the disk has a flared geometry (i.e., increasing opening angle with radius). As shown by [Chiang & Goldreich \(1997\)](#), for an irradiated disk a value of  $\beta \approx 1.3$  is expected. A flaring geometry of disks has been shown to well explain the spectral energy distributions (SED) of T Tauri stars ([Kenyon & Hartmann, 1987](#)).

### 1.1.4 Radial drift and dust settling

The interplay of dust and gas strongly affects the dynamics of the dust which has important consequences on its spatial distribution.

Without the presence of gas, circumstellar dust would naturally orbit at Keplerian speed. For a dust particle at radius  $r$  and height  $z$  over the disk midplane, the rotational velocity  $v_{rot}$  can then be written as (see [Rosenfeld et al., 2013](#)):

$$\frac{v_{rot,dust}^2}{r} = \frac{r}{(r^2 + z^2)^{1/2}} \left( \frac{GM_\star}{r^2 + z^2} \right), \quad (1.5)$$

with  $G$  the Gravitational constant and  $M_\star$  the mass of the central star.

The rotational velocity of the gas, however, behaves slightly differently. Being in radial hydrostatic equilibrium, the gas has to balance an additional force generated by the radial pressure gradient,  $\partial P_{gas}/\partial r$ . The rotational velocity then becomes :

$$\frac{v_{rot,gas}^2}{r} = \frac{r}{(r^2 + z^2)^{1/2}} \left( \frac{GM_\star}{r^2 + z^2} \right) + \frac{1}{\rho_{gas}} \frac{\partial P_{gas}}{\partial r}, \quad (1.6)$$

where  $\rho_{gas}$  is the density of the gas. In a smooth, unperturbed disk,  $P(r)$  is monotonically decreasing, which implies  $\partial P/\partial r < 0$  throughout the disk. Therefore, the gas rotates at sub-Keplerian velocities.

The resulting relative motion of dust and gas causes the dust to experience a drag force exerted by the gas. The strength of this interaction depends on the particle size, as well as on the surface density of the gas (e.g., [Birnstiel et al., 2010](#); [Testi et al., 2014](#)). Small,

micrometer-sized particles, having a large surface-to-mass ratio, become quickly coupled with the gas motion and are thus carried along with the fluid at sub-Keplerian speed. If particles grow larger in size, thus reducing their surface-to-mass ratio, they experience a continuous headwind exerted by the gas. As a consequence, they decouple from the gas, lose angular momentum, and spiral inwards, a phenomenon known as *radial drift* (Weidenschilling, 1977).

A similar effect resulting from the interactions of dust and gas affects the vertical motion of dust grains (Dullemond & Dominik, 2004). If no gas was present, dust particles at a certain height would naturally orbit the star on an inclined orbit, leading to a vertical component in the movement of the dust particle. Because small particles are swept along with the gas motion, they experience only a very slow vertical movement toward the midplane. This vertical movement is further counteracted by turbulent mixing, which tends to lift the dust again up into higher altitudes. In contrast to that large particles are less well coupled to the gas, leading to a much faster settling toward the midplane. This process of *vertical settling* results in a vertical gradient of dust grain size distribution, with the largest grains being settled down closely toward the midplane, and the small grains having a much broader vertical distribution, populating as well disk layers at higher altitudes (Villenave et al., 2020).

### 1.1.5 Disk lifetime and evolution

With time, a decreasing fraction of stars is observed to be surrounded by protoplanetary disks (e.g., Haisch et al., 2001; Ribas et al., 2014), implying a typical disk lifetime of  $\lesssim 10$  Myr. Thus, material in disks is evolving with time, being either accreted onto the star, transformed into larger bodies, such as planets, or otherwise removed from the system. Several processes have been proposed to drive the evolution of protoplanetary disks.

The dominant evolution process, at least at early stages, is viscous accretion. For a disk in Keplerian rotation, the specific angular momentum increases with radius, therefore, the accretion of material onto the star requires the redistribution of angular momentum within the disk in order to conserve it. This barrier can be overcome by attributing a viscosity to the gas, which allows the outward transport of angular momentum, and thus the inward movement of material. Because pure molecular viscosity is inefficient at transporting angular momentum (Pringle, 1981), it is assumed that the viscosity in disks is of turbulent nature, generated by several possible mechanisms, such as the magnetorotational instability (Balbus & Hawley, 1991), or different types of hydrodynamical instabilities (see e.g., Lyra & Umurhan, 2019, and references therein). Regardless of its origin, the strength of viscosity can be parametrized by the  $\alpha$  parameter (Shakura & Sunyaev, 1973; Pringle, 1981). The exact value of  $\alpha$  is not known, but recent observations of individual disks sug-

gest rather low values of  $\lesssim 10^{-3}$  (Teague et al., 2016, 2018c; Flaherty et al., 2015, 2017, 2020). As an alternative hypothesis, accretion may be regulated by disk winds, removing material from the surface layers of the disk and thus take angular momentum away (see Turner et al., 2014, for a review).

Once the stellar accretion rate decreases as time goes by, disk material may be eroded by photoevaporation (see reviews by Gorti et al., 2016; Ercolano & Pascucci, 2017). High-energetic photons from the star heat the atmosphere of the disk, and launch a thermal wind beyond a critical radius. If the mass-loss rate of the wind exceeds that of the accretion rate, the inner disk is no longer re-supplied with material from the outer disk and drains on a short timescale. As a consequence, an inner hole of a few au in radius is formed, directly exposed to the radiation from the central star, leading to a rapid photoevaporation of the gas from the inside out.

Finally, material in the disk may not only be accreted or removed, but also transformed into larger bodies, and eventually form planets. The processes of giant planet formation are summarized in the next Section.

## 1.2 Giant planet formation in a nutshell

In order to form giant planets, dust needs to grow by more than 13 order of magnitudes in size. Two main group of models have been put forward to explain how giant planets form. The standard model of *core accretion* (Bodenheimer & Pollack, 1986; Pollack et al., 1996) builds planets from the bottom up through coagulation and growth of dust and planetesimals to a planetary core, which subsequently accretes a gaseous envelope. In contrast to that, the *disk instability* scenario (Boss, 1997) is a top-down model, where giant planets form directly from the gravitational fragmentation of the disk. This section summarizes the main steps involved in the two models.

### 1.2.1 Core accretion

#### Core formation

In the classical picture of core accretion, planet formation starts with the building-up of a core out of solid material (Pollack et al., 1996). In a first step, mutual collisions of initially  $\sim$ micrometer-sized dust at gentle relative velocities lead to the coagulation of aggregates (e.g., Blum, 2018), allowing dust to grow to  $\sim$  cm-sized pebbles. As explained in Sect. 1.1.4, when growing to larger sizes, the motion of pebbles will decouple from the gas, and as a consequence, these particles will experience radial drift toward the star. This leads on the one hand to a rapid depletion of pebbles within the disk, and on the other hand to

increasing relative velocities, impeding further particle growth. In order to allow dust to grow beyond the sizes of pebbles, it has been proposed that these concentrated dust streams can gravitationally collapse to form  $\sim$ km-sized planetesimals (Youdin & Goodman, 2005), which then provide the first building blocks of planets. These bodies can further grow by the accretion of other planetesimals, and in particular by large amounts of pebbles which come into their gravitational reach while drifting inward (e.g., Ormel & Klahr, 2010; Lambrechts & Johansen, 2012). These processes will eventually lead to the formation of a planetary embryo, which will develop into a terrestrial planet, or become the core of a giant planet.

### Envelope accretion

When the growing core of a giant planet approaches a fraction of Earth's mass ( $M_{\oplus}$ ), its escape velocity may eventually exceed that of the local thermal speed of the gas, triggering the accretion of a gaseous envelope from the surrounding protoplanetary disk (see review by Helled et al., 2014, and references therein). At a first stage, the growth rate of the envelope is determined by its cooling rate, resulting in a slow and steady concurrent accretion of gas and solids. Once the envelope mass approaches that of the core (which happens at a core mass on the order of  $10 M_{\oplus}$ ), however, the envelope is no longer able to maintain hydrostatic equilibrium, and the planet undergoes a phase of accelerated ('run-away') gas accretion. In this phase, its growth is determined by the supply of gas from the disk, driven by the accelerated contraction of the outer envelope and the increasingly rapid expansion of the planet's sphere of influence (Pollack et al., 1996). It is thought that this short phase of gas runaway accretion is when the planet accretes the bulk of its mass (e.g., Machida et al., 2010).

### Circumplanetary disk

Because material that enters into the gravitational reach of the planet carries angular momentum, accretion onto the surface of the planet is thought to happen through a circumplanetary disk (CPD; e.g., Kley, 1999; Lubow et al., 1999; Tanigawa et al., 2012). Recent simulations have suggested that the accretion process occurs mostly in vertical direction (Tanigawa et al., 2012; Szulágyi et al., 2014). Gas in the upper layers of the circumstellar disk flows into the gap carved by the planet (see following Section), where the gravity of the planet causes it to fall down at almost free-fall velocity from high altitudes toward the polar region of the protoplanet and the CPD. The gas shocks at the surface of the CPD and experiences a significant reduction of the specific entropy while passing through the shock front (Szulágyi & Mordasini, 2017). Part of that gas is then accreted onto the planet through the CPD, while a certain fraction is pushed away in an outward flow near the

disk midplane. These processes thus lead to a circulation pattern across the Hill sphere (Morbidei et al., 2014).

Simulations show that the CPD radially extends out to a fraction of the Hill radius (Quillen & Trilling, 1998; D’Angelo et al., 2003; Ayliffe & Bate, 2009; Szulágyi et al., 2014).

### Gap opening and particle trapping

The gravitational interaction of a giant planet with the disk leads to an exchange of angular momentum with the disk, resulting in the opening of a gap. This Section summarizes the basic idea of gap opening, but the reader may be referred to the review by Kley & Nelson (2012) for more details.

The presence of a planet excites spiral density waves in the disk which carry angular momentum flux away from the planet. With growing mass, the perturbations become stronger, and eventually lead to shock waves. The angular momentum is then deposited in the disk at the location where the waves are dissipated. As a result, disk material inside the planet’s orbit loses angular momentum, while material outside gains angular momentum, and the gas thus starts to recede from the planet, forming a gap (e.g., Goldreich & Tremaine, 1980; Lin & Papaloizou, 1986a). The depth and width of the gap carved by the planet depend on the mass of the planet, but also on disk properties such as viscosity and scale height (e.g., Kanagawa et al., 2015a; Dong & Fung, 2017), because the tidal torques driving the opening of the gap need to overcome the counteracting effect of viscous diffusion.

The perturbation of the gas surface density also modifies the radial pressure gradient, and thus the azimuthal velocity of the gas in the disk (Bryden et al., 2000; Kanagawa et al., 2015b). While the overall negative pressure gradient in a smooth disk causes the gas to rotate at sub-Keplerian speed (see Eq. 1.6), the presence of a gap causes a region of positive pressure gradient at its outer edge. This leads to a halt of particles that are radially drifting inward from the outer disk regions at the location of maximum pressure (i.e., where  $\partial P/\partial r = 0$ ), and causes an accumulation of dust in a ring beyond the outer edge of the gap (e.g., Bryden et al., 2000; Pinilla et al., 2012c).

Although the planet is opening a gap within the disk, mass flow to the planet can continue through the gap (e.g., Lubow & D’Angelo, 2006; Morbidelli et al., 2014). Accretion may be ongoing until the planet has opened such a deep gap in the disk that it starves from gas re-supply (e.g., Tanigawa & Tanaka, 2016; Ginzburg & Chiang, 2019).

### Orbital migration

The tidal interaction of the protoplanet with the disk affects the planet’s orbit (see review by Kley & Nelson, 2012). Typically, the torque exerted by the outer spiral density wave

on the planet exceeds that of the inner one, causing the planet to lose angular momentum and migrate inwards, a phenomenon referred to as Type I migration. This regime applies for planets that do not significantly modify the density structure of the disk. The picture is different if the planet is sufficiently massive to open a gap. Due to the low density in the vicinity of the planet, the impact of the disk torques on the planets is significantly reduced. As a consequence, the planet is locked to the viscous evolution of the disk, leading to a slow inward migration on viscous timescales, called Type II migration. It should be noted, however, that recent work on Type II migration has revealed a more complex picture, in particular as gas can still cross the gap even in the presence of a deep gap. These simulations have shown that migration rates can significantly deviate from viscous timescales, dictated by both planet and disk parameters (Duffell et al., 2014; Dürmann & Kley, 2015; Kanagawa et al., 2018). In the case of two planets, opening a common gap, migration can under certain conditions also happen in outward direction (Masset & Snellgrove, 2001).

### Post-formation contraction and cooling

After accretion has terminated, further evolution happens at constant mass. Energy is released by slow contraction in hydrostatic equilibrium, and, if the mass of the planet is more than about  $13 M_{\text{Jup}}$ , additionally by deuterium burning. This energy is removed by radiative cooling, which leads to the gradual decline of planetary luminosity with time. The predicted cooling tracks mainly depend on the planetary mass and the initial (post-formation) entropy (e.g., Marleau & Cumming, 2014). The latter is determined by the properties of the accretion shock at the surface of the planet and the CPD (e.g., Mordasini, 2013): depending on how efficiently the liberated gravitational potential energy is radiated away at the shock, the planet will show evidence of a low ('cold start') or high ('hot start') post-formation entropy (e.g., Marley et al., 2007; Mordasini et al., 2017). Figure 1.1 shows the post-formation evolution of planetary luminosity, radius, and effective temperature as a function of time for different planetary masses obtained from the Bern Exoplanet (BEX) evolution models (Mordasini et al., 2017), considering different efficiencies of accretional heating.

### 1.2.2 Disk instability

An alternative pathway to form giant planets is disk instability. This process can be initiated when a disk happens to be sufficiently dense and cool to experience significant self-gravity (Kuiper, 1951; Cameron, 1978; Boss, 1997). Disk regions may then become unstable if self-gravity starts to overcome the counter-acting forces of internal gas pressure and shear forces from differential rotation. As a consequence, parts of the disk fragment into dense, gaseous clumps which may further develop into a giant planet (e.g., Boley

## 1 Introduction

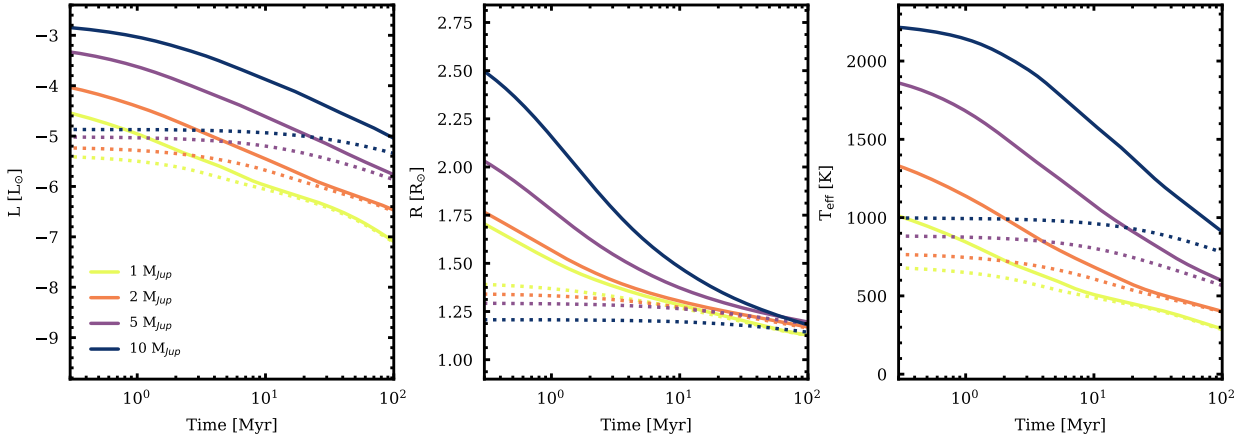


**Figure 1.1:** Evolution of luminosity, radius and effective temperature of planets with masses of 1, 2, 5, and 10  $M_{\text{Jup}}$ , using the evolutionary models by [Mordasini et al. \(2017\)](#), for a population of high (solid) and intermediate (dashed) initial post-formation entropy.

[et al., 2010](#)). The estimated mass of such clumps is on the order of a few Jupiter masses (see review by [Kley, 2019](#)). While this scenario has shown to successfully form clumps in the Jupiter-mass regime at distances beyond  $\sim 50$  au, some challenges associated with the subsequent evolution are still debated. Simulations show that after their formation, the clumps tend to further grow by rapid accretion of gas, and often reach masses within the brown dwarf regime. Moreover, they are subject to rapid inward migration, and can possibly get tidally disrupted in the inner region of the disk ([Zhu et al., 2012](#); [Tsukamoto et al., 2013](#)).

The formation scenario of giant planets via disk instability is of particular interest to explain the presence of giant planets far away from the star, such as the four directly imaged  $\sim 5\text{-}10 M_{\text{Jup}}$  planets orbiting the star HR 8799 at separations of 17 to 70 au ([Marois et al., 2008, 2010](#)). At these far-out distances of several tens of au, core accretion has been thought to be not efficient enough to form giant planets before the gas disk dissipates ([Dodson-Robinson et al., 2009](#)), although the picture is more optimistic in the framework of pebble accretion ([Johansen & Lambrechts, 2017](#)). In contrast to that, the formation process via disk instability can take place on very short timescales, on the order of  $10^3$  years ([Boss, 1997](#)). However, the final pathway of the formation of giant planets on wide orbits is still under debate.

## 1.3 Linking disk theory and observations: radiative transfer models

As will be discussed in Sect. 1.4, protoplanetary disks can be probed by spatially resolved observations at different wavelengths, tracing different physical regions (e.g., disk mid-plane, elevated surface layers) and components (e.g., small or large dust grains, molecular gas). While light propagates through the disk, the interaction with the medium can alter its properties. Dust grains can absorb, scatter, polarize or re-emit radiation, processes which strongly depend on grain properties. In order to correctly interpret the data and put constraints on the physical disk structure from multi-wavelength observations, it is thus crucial to understand how radiation interacts with the dusty medium of the protoplanetary disk before being registered on the detector. A helpful tool in this context are radiative transfer codes which allow to model the spatially resolved intensity and polarization maps, as well as the spectral energy distribution of the disk, given an underlying disk density distribution.

### 1.3.1 Dust opacities

How efficiently dust can absorb and scatter light at a given frequency  $\nu$  is characterised by its extinction opacity  $\kappa_{\nu}^{ext}$ , which corresponds to a cross section per unit mass.  $\kappa_{\nu}^{ext}$  is the sum of the individual contributions from scattering and absorption, respectively,  $\kappa_{\nu}^{ext} = \kappa_{\nu}^{abs} + \kappa_{\nu}^{sca}$ .  $\kappa_{\nu}^{abs}$  and  $\kappa_{\nu}^{sca}$  depend on the dust size, composition, and shape, and of course on the wavelength. Optical properties of dust can be calculated from laboratory measurements of the complex index of refraction<sup>3</sup>. This is often done using Mie theory, which provides a general solution for the scattering process of an electromagnetic wave by a homogeneous sphere (Mie, 1908). As a note, while this is a commonly used approach to compute the optical constants, in reality, the shapes of dust grains will differ from homogeneous spheres. Alternative approaches have been developed to account for more realistic properties of dust grains (e.g., Min et al., 2005).

One important parameter for determining the optical properties is the grain size  $a$  in relation to the wavelength  $\lambda$ . There are two limiting cases: the case of very small grains,  $a \ll \lambda$ , called Rayleigh scattering. In this regime, the scattering cross section is highly dependent on wavelength  $\propto \lambda^{-4}$ . On the other side, the case  $a \gg \lambda$  approaches the limit of geometric optics. The opacities can also be computed, instead for a single size, for a grain size *distribution*, where the opacities for a certain range of grain sizes are averaged.

---

<sup>3</sup>Such measurements can be obtained, e.g., from the Jena database:  
<https://www.astro.uni-jena.de/Laboratory/Database/databases.html>

## 1 Introduction

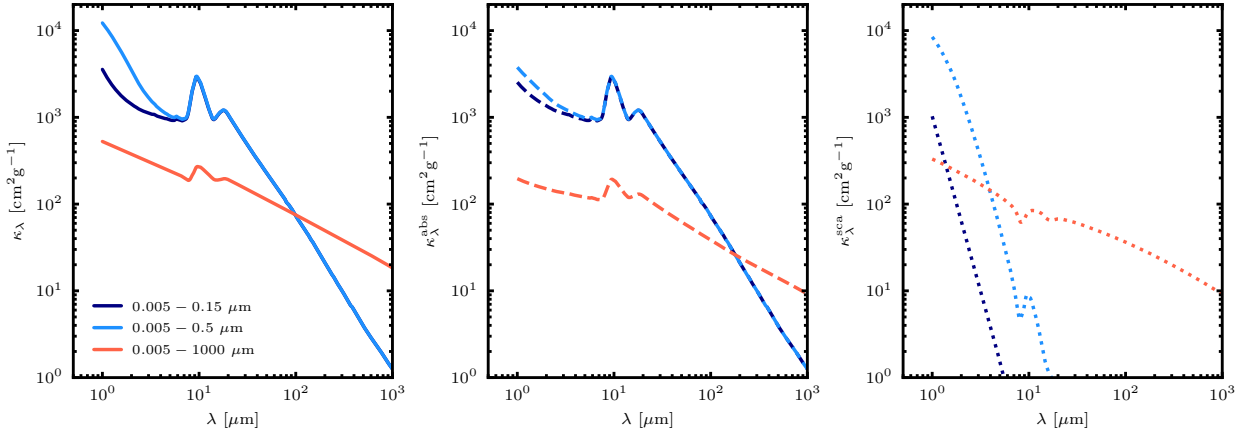


**Figure 1.2:** Dust opacities ( $\kappa_{\lambda}^{ext}$ ,  $\kappa_{\lambda}^{abs}$ ,  $\kappa_{\lambda}^{sca}$ , from left to right) for a mixture of 70% silicates (Draine, 2003b) and 30% carbon (Zubko et al., 1996) grains, as described in Sect. 2.5.1. The opacities are plotted for three different grain size distributions (0.005-0.15  $\mu\text{m}$ , 0.005-0.5  $\mu\text{m}$ , 0.005-1000  $\mu\text{m}$ ), assuming a power law index of -3.5.

For illustration, Fig. 1.2 shows  $\kappa_{\nu}^{ext}$ ,  $\kappa_{\nu}^{abs}$  and  $\kappa_{\nu}^{sca}$  as a function of wavelength for a mixture of silicate and carbon grains, obtained with Mie theory using the BHMIE code (Bohren & Huffman, 1983), and assuming three grain size distributions with identical minimum, but different maximum grain sizes.

### 1.3.2 Radiative transfer equation

Let us first consider the simplest case, and ignore scattering. The radiation field at frequency  $\nu$ , at a location  $\mathbf{x}$  and propagating in direction  $\mathbf{n}$  is described by the specific intensity  $I_{\nu}(\mathbf{x}, \mathbf{n})$ . Energy may be added to the radiation field (e.g., by stellar irradiation, or thermal emission by the dust itself), or taken up by dust grains through absorption and transformed in internal energy. The differential change of  $I_{\nu}$  along a path  $s$  can be described by the radiative transfer (RT) equation (see review by Steinacker et al., 2013):

$$\frac{dI_{\nu}}{ds}(\mathbf{x}, \mathbf{n}) = -\kappa_{\nu}^{abs}(\mathbf{x})\rho(\mathbf{x})I_{\nu}(\mathbf{x}, \mathbf{n}) + j_{\nu}(\mathbf{x}, \mathbf{n}), \quad (1.7)$$

where  $j_{\nu}$  describes the emissivity and  $\rho$  the density of the medium. The resulting intensity is obtained by integrating Equ. 1.7 over the path  $s$ .

The opaqueness of a medium experienced by a light beam propagating along path  $s$  is

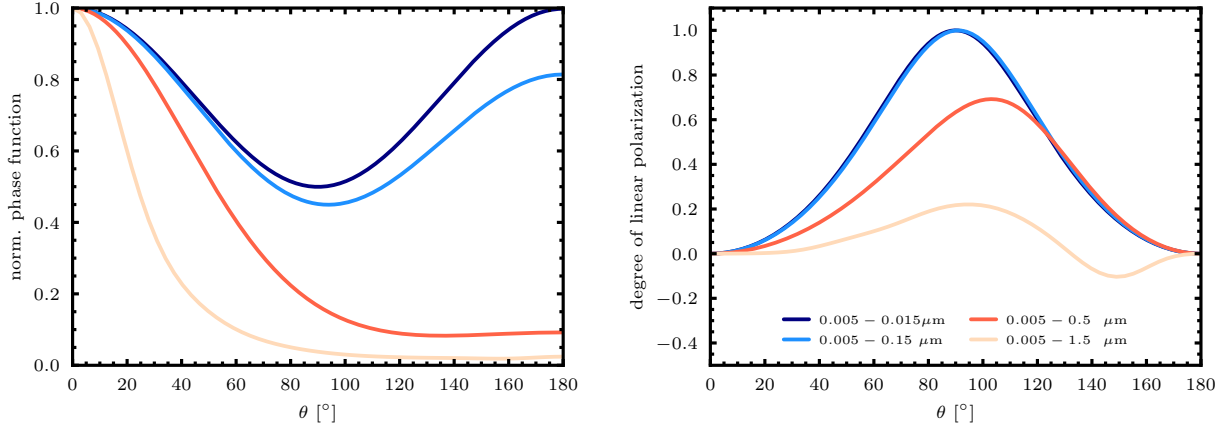


**Figure 1.3:** Normalized phase functions (left) and polarization degrees (right panel) for a mixture of 70% silicates (Draine, 2003b) and 30% carbon (Zubko et al., 1996) grains evaluated at  $1.67 \mu\text{m}$  using Mie theory, as described in Sect. 2.5.1. The plots show four different grain size distributions ( $0.005\text{-}0.015 \mu\text{m}$ ,  $0.005\text{-}0.15 \mu\text{m}$ ,  $0.005\text{-}0.5 \mu\text{m}$ ,  $0.005\text{-}1.5 \mu\text{m}$ ), assuming a power law index of  $-3.5$ .

expressed in terms of the optical depth  $\tau_\nu$ :

$$\tau_\nu(s) = \int_0^s \rho(\mathbf{x}) \kappa_\nu(\mathbf{x}) ds'. \quad (1.8)$$

## Scattering

As shown in Fig. 1.2, scattering can have an important contribution to the opacity. The scattering process represents a second source and sink term in Equ. 1.7. The probability of a photon initially propagating in direction  $\mathbf{n}'$  being scattered into a new direction  $\mathbf{n}$  can be described by the scattering phase function  $\Phi_\nu(\mathbf{n}, \mathbf{n}', \mathbf{x})$ , which is normalized such that:

$$\int_{4\pi} \Phi_\nu(\mathbf{n}, \mathbf{n}', \mathbf{x}) d\Omega' = 1 \quad (1.9)$$

Taking scattering into account, the RT equation then becomes:

$$\frac{dI_\nu(\mathbf{x}, \mathbf{n})}{ds} = -\kappa_\nu^{ext}(\mathbf{x})\rho(\mathbf{x})I_\nu(\mathbf{x}, \mathbf{n}) + \kappa_\nu^{sca}(\mathbf{x})\rho(\mathbf{x}) \int_{4\pi} \Phi_\nu(\mathbf{n}, \mathbf{n}', \mathbf{x}) I_\nu(\mathbf{x}, \mathbf{n}') d\Omega' + j_\nu(\mathbf{x}, \mathbf{n}) \quad (1.10)$$

Figure 1.3 (left panel) plots the normalized scattering phase functions for four different grain size distributions evaluated at a wavelength of  $1.67 \mu\text{m}$  using Mie theory. Very small

grains (in the Rayleigh scattering regime) scatter rather isotropically, while larger grains are efficient forward scatterers.

## Polarization

Finally, while stellar light is mostly unpolarized, scattering by dust grains naturally polarizes radiation.

The polarization state of an electromagnetic wave can be described with the Stokes vector  $\mathbf{S} := (I, Q, U, V)$  (Stokes, 1851). While  $I$  denotes the total intensity of the beam of light, as described above,  $Q$  and  $U$  represent the two linearly polarized intensities measured along two axes rotated by  $45^\circ$  from each other, and  $V$  describes circularly polarized intensity. A scattering event of an incident light wave  $\mathbf{S}(\mathbf{n}')$  being scattered into a new direction  $\mathbf{S}(\mathbf{n})$  can be described by the  $4 \times 4$  Mueller matrix  $\mathbf{M}(\mathbf{n}, \mathbf{n}')$ . The RT equation then transforms into a vector equation:

$$\frac{d\mathbf{S}_\nu(\mathbf{x}, \mathbf{n})}{ds} = -\kappa_\nu^{ext}(\mathbf{x})\rho(\mathbf{x})\mathbf{S}_\nu(\mathbf{x}, \mathbf{n}) + \kappa_\nu^{sca}(\mathbf{x})\rho(\mathbf{x}) \int_{4\pi} \mathbf{M}_\nu(\mathbf{n}, \mathbf{n}', \mathbf{x})\mathbf{S}_\nu(\mathbf{x}, \mathbf{n}')d\Omega' + j_\nu(\mathbf{x}, \mathbf{n}). \quad (1.11)$$

Figure 1.3 (right) plots the polarization degree for four different grain size distributions evaluated at a wavelength of  $1.67 \mu\text{m}$ . It can be seen that larger grains are less efficiently polarized. Scattering phase function and polarization degree will be further discussed in context of observations of the disk around PDS 70 in Chapter 2.

### 1.3.3 Radiative transfer code: RADMC-3D

Due to the complexity of the RT equations, finding an analytical solution is often very challenging. Codes which allow to numerically solve the RT equations for each point of an underlying disk model geometry are therefore an indispensable tool. Several of such codes have been developed in the past (e.g., Wolf et al., 1999; Pinte et al., 2006; Min et al., 2009).

In this Thesis, the 3D RT code RADMC-3D was used (Dullemond et al., 2012). This code allows to calculate synthetic images, spectra and spectral energy distributions for a given model disk, taking into account a full treatment of absorption, emission, scattering and polarization. RADMC-3D uses the Monte Carlo method, which allows to solve the RT equations by stochastic means (see Steinacker et al., 2013). In the Monte Carlo approach, a large number of test particles ('photon packages') is successively released from a luminosity sources (i.e., the central star) and propagates through the model geometry. Each

photon package is being traced along its journey through the disk, while interactions with the dusty medium are determined in a probabilistic way. The final radiation field is then recovered by a statistical analysis of the individual photon paths.

To set up a model run in RADMC-3D, the dust opacities, disk density distribution, and the properties of the central star need to be specified. For a full treatment of scattering, an opacity table for dust of any desired composition including the scattering matrix needs to be provided by the user. In this Thesis (Chapters 2 and 5), these tables were obtained assuming Mie theory using the BHMIE code (Bohren & Huffman, 1983), and assuming a grain size distribution whose number density  $n$  as a function of grain size  $a$  follows  $n(a) \propto a^{-3.5}$  (Mathis et al., 1977). As next, the dust density needs to be defined on a given grid. This can be done by implementing an analytical prescription for the density distribution (e.g., following Eqs. 1.1 and 1.2). This approach has been followed for modeling the NIR images of PDS 70 in Chapter 2. Alternatively, it is possible to use the density output from a hydrodynamical simulation, which allows to model the evolution of the gas density distribution under the gravitational interaction with a stellar or planetary companion. This approach was used for simulating the GG Tau A system in Chapter 5.

After having defined the input parameters, the computation of model images with RADMC-3D consists of two steps. First, the dust temperature distribution is determined with a thermal Monte Carlo simulation. In a second step, an image of the disk at a desired wavelength, inclination and position angle is computed using the ray-tracing capabilities of RADMC-3D. Finally, by integrating over images computed along a wavelength grid, the spectral energy distribution of the disk can be established.

## 1.4 Observational diagnostics of giant planet formation

The motivation of this Thesis is to observationally trace planet formation and characterize the environment in which it takes place, the protoplanetary disks. The presence of a planet may be *directly* evidenced, e.g., by the detection of its thermal emission. Another approach is to *indirectly* infer the presence of an embedded planet, e.g., through its impact on the protoplanetary disk, using dust or molecular gas as tracers. All these processes take place under different physical conditions, thus, it is useful to probe different parts of the electromagnetic spectrum. For an illustration, Fig. 1.4 shows model SEDs of a K7-type star, a circumstellar disk, as well as of a planet with effective temperature of 1500 K. It can be seen that the optical and near-infrared part of the spectrum is dominated by the star, while the mid-infrared and sub-millimeter wavelengths are dominated by the dust continuum from the circumstellar disk. The SED of the planet atmospheric model peaks in

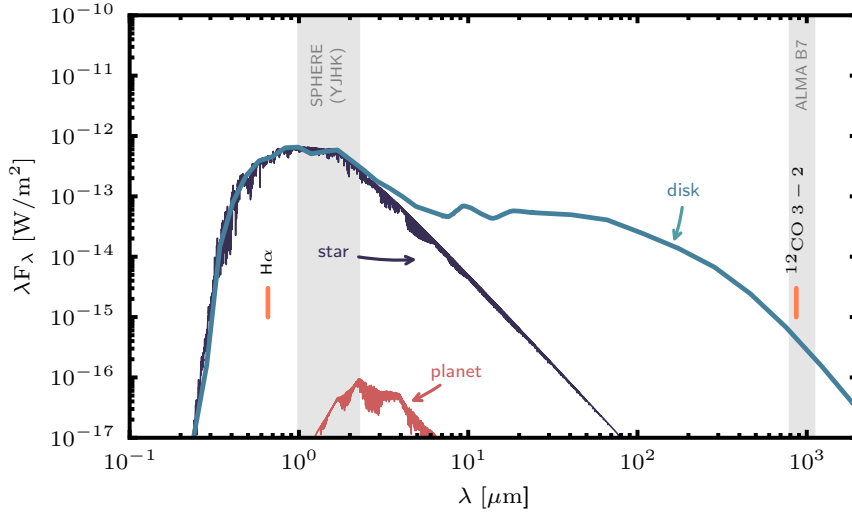


**Figure 1.4:** Model spectrum of a PMS K7-type star (dark blue; using a PHOENIX spectrum as described in [van Boekel et al., 2012](#)), overlaid by a model SED of a protoplanetary disk with a large gap (light blue; using the RT model of PDS 70 described in Chapter 2), as well as a model atmospheric spectrum for a planet with a temperature of 1500 K and a radius of  $1.5 R_{\text{Jup}}$  (red; using the AMES-DUSTY models by [Chabrier et al., 2000](#); [Allard et al., 2001](#)). All three of them are assumed to be observed at the same distance. The grey regions mark the wavelength ranges covered by the SPHERE instrument and by ALMA when used in Band 7. The orange lines mark the location of the H $\alpha$  line and the  $^{12}\text{CO}$  J=3-2 transitions.

the NIR.

The different observational tracers and associated techniques will be discussed in the following Sections by focusing on two wavelength regimes, namely the NIR and the sub-millimeter part of the light spectrum.

### 1.4.1 Near-infrared Angular Differential Imaging

As explained in Sect. 1.2.1, young giant planets are still hot from the formation process, with typical temperatures of several hundred to a few thousand K. This means that their SED will peak at wavelengths of a few microns, making the NIR regime suitable for a direct detection of the planet’s photospheric emission (see Fig. 1.4). Nevertheless, giant planets are extremely faint compared to their host star, with typical contrast ratios on the order of  $\sim 10^{-4} - 10^{-5}$ . Thus, the inherent problem of directly image planets in the NIR is to overcome a high contrast at small separation.

Thanks to the new generation of large, 8-m class ground-based telescopes coupled to extreme adaptive optics, such as the SPHERE (Spectro-Polarimetric High-contrast Exoplanet REsearch; [Beuzit et al., 2019](#)) or GPI (Gemini Planet Imager; [Macintosh et al., 2014](#)) instruments, the angular resolution is close to the theoretical diffraction limit of the telescope ( $\sim 0.04''$  in H-band or  $1.6 \mu\text{m}$ , corresponding to  $\sim 7 \text{ au}$  at 140 pc, a typical distance

of young star forming regions). To reach high contrast, sophisticated coronagraphs allow to reject a large fraction of the stellar light, making it possible to scrutinize objects  $\sim 10^4$  times fainter than the host star at about  $0.1''$  ( $\sim 14$  au at 140 pc). Still, the main limitation under very good observing conditions (i.e., good seeing and short coherence time) are quasi-static speckles. These structures are due to starlight diffracted by residual aberrations in the instrument. Those speckles are long-lived, but still vary in time, e.g., due to changes in temperature and pressure, ranging from minutes to hours (Fitzgerald & Graham, 2006; Hinkley et al., 2007; Goebel et al., 2018). Their removal requires the application of advanced observing strategies and post-processing techniques.

The most commonly used observing strategy for Direct Imaging (DI) of faint companions is angular differential imaging (ADI; Marois et al., 2006). The concept of this method is to obtain a sequence of images while the telescope is operated in pupil tracking mode. In this mode, the instrument and telescope optics remain aligned, while the field of view is rotating during the observation sequence (typically 1-2 hours). As a consequence, the position of the starlight residuals (such as speckles) is kept stable in the field of view throughout the sequence. After basic data reduction of the image cube (e.g., flat fielding, sky and dark calibrations, bad pixel correction, centering) is performed, the next step is to subtract from each individual image a model coronagraphic point-spread function (PSF). This model coronagraphic PSF is built using all other images of the observing sequence (typically a few hundred, depending on the brightness of the target), such to include as much of the starlight residuals, but as few as of the planetary or disk signal possible, which rotates at a deterministic velocity (following the evolution of the parallactic angles). A subsequent derotation and median combination of the individual images is then performed to recover the final image, where most of the residual starlight is removed, while the faint planetary signal is enhanced.

A number of different post-processing algorithms to build the model coronagraphic PSF has been developed. While in the initial version, the temporal median of the image cube is used (classical Angular Differential Imaging, cADI; Marois et al., 2006), the LOCI algorithm generates a linear combination of images that locally minimizes the noise (Lafrenière et al., 2007), whereas a Principal Component Analysis (PCA) approach, which models the PSF through a decomposition into eigen images, is used in the implementations of PynPoint (Amara & Quanz, 2012) and KLIP (Soummer et al., 2012). Finally, the ANgular DiffeRential OptiMal Exoplanet Detection Algorithm (ANDROMEDA; Cantalloube et al., 2015) uses a maximum likelihood estimation in order to automatically detect and characterize planetary signals. We make use of the ANDROMEDA, PCA, LOCI and cADI algorithms for the detection of PDS 70 b in Chapter 2.

Once the detection of a point source is achieved, it is possible to retrieve its astrometry and photometry, e.g., through the injection of negative fake planets (Lagrange et al.,

2009). If multi-epoch observations are available, the temporal evolution of the source's astrometry relative to the star (knowing the stellar proper motion) can be used to exclude its nature as a background star. If the companion candidate exhibits proper motion itself, orbital fitting of the astrometric datapoints can be performed to put constraints on the orbital parameters (e.g., Maire et al., 2019). The extracted photometry can be used to determine the location of the source on a color-magnitude diagram (CMD). Because planets and sub-stellar companions are expected to populate a distinct region in these diagrams, this analysis can yield further constraints on the nature of the source (e.g., Bonnefoy et al., 2018). Additionally, comparing the photometry to synthetic colors of atmospheric and evolutionary models (e.g., Allard, 2014; Baraffe et al., 2003, 2015) allows to constrain the mass of the companion. If the high-contrast instrument provides an integral field spectrograph, the extracted spectrum can be compared against empirical spectra of planets or brown dwarfs compiled from the literature or can be used to fit an atmospheric model in order to obtain more constraints on the properties of the companion, such as its effective temperature, surface gravity, or metallicity (e.g., Chauvin et al., 2017a; Samland et al., 2017).

While the ADI method is very powerful to detect point-like sources, extended signals, e.g., from disk structures, are strongly distorted. ADI processing acts as a spatial frequency filter, affecting structures of low spatial frequencies such as disks. In particular if the field rotation is low, it can create distortions or even artifacts unrelated to the physical structures, that can mimic point sources, which may be misinterpreted as planets (Milli et al., 2012). Section 1.5 discusses these possible issues in light of recent observations. This makes the robust detection of young, still forming planets with DI extremely challenging, since at those early stages disk material is usually still present.

### 1.4.2 Near-infrared Polarimetric Imaging

As illustrated on Fig. 1.2, small, micrometer-sized dust particles are efficient scatterers in the NIR, making these grains a suitable tracer for the disk structure. In this context, polarimetric imaging has turned out a very powerful technique to image disks in the NIR regime (Kuhn et al., 2001). As for the detection of planets, the inherent problem at these wavelengths to overcome is a very large dynamic range, as the stellar residual light is much brighter than the disk. Since light scattered off dust is linearly polarized, the basic idea of polarimetric imaging is to remove the contribution from the intrinsically unpolarized light of the star, which comes back to recovering the Stokes  $Q$  and  $U$  parameters of the incident light beam.

The technical principle of a polarimeter is that the incident light beam, after entering the telescope, passes a rotating half-wave retarder plate (HWP). Such a device has the effect

that it rotates the direction of linear polarization by a specific angle according to its orientation. Then, the light is split into two beams, each of which passes a linear polarizer with respectively orthogonal transmission. The two beams are then recorded on two different parts of the detector, where their intensities can be measured. Performing these measurements at four different orientations of the HWP (i.e., at an orientation of  $0^\circ$ ,  $22.5^\circ$ ,  $45^\circ$  and  $67.5^\circ$ ) allows to recover the Stokes parameters  $I$ ,  $Q$ , and  $U$ <sup>4</sup> (see Patat & Romaniello, 2006), a strategy known as dual-beam polarimetric imaging (DPI). Such a measurement set of four different HWP angles is called a polarimetric cycle.

Polarimeters are no ideal instruments, and the large number of reflections within the telescope and instrument can add artificial instrumental polarization. This can be accounted for by specifically modeling the light path through the telescope and instrument. For the case of SPHERE/IRDIS, this has been implemented in the IRDAP reduction pipeline (van Holstein et al., 2020), which we will use for the polarimetric observations of PDS 70 and GG Tau A presented in Chapters 2 and 5.

The  $Q$  and  $U$  images can be used to determine the linearly polarized intensity ( $PI$ ) as well as the angle of linear polarization  $\theta$  for each pixel:

$$PI = \sqrt{Q^2 + U^2}, \quad \theta = \frac{1}{2} \arctan\left(\frac{U}{Q}\right). \quad (1.12)$$

In practice,  $Q$  and  $U$  are usually transformed into polar coordinates  $Q_\phi$  and  $U_\phi$ , according to Schmid et al. (2006):

$$Q_\phi := Q \cos(2\phi) + U \sin(2\phi) \quad U_\phi := -Q \sin(2\phi) + U \cos(2\phi), \quad (1.13)$$

where  $\phi$  is the angle with respect to the North, measured in anti-clockwise direction.

Any signal which is linearly polarized in azimuthal (radial) direction will then be contained as positive (negative) signal in  $Q_\phi$ , while signal polarized in the direction  $\pm 45^\circ$  with respect to the radial direction will be included in  $U_\phi$ . Thus, to first order, most of the light scattered from disks is expected to be imaged as positive signal in  $Q_\phi$ , while  $U_\phi$  should contain mostly noise. It has been shown, however, that in some cases scattered light from disks may deviate from azimuthal polarization, depending on optical depth, disk inclination and grain properties, such that  $U_\phi$  may also include some physical signal (Canovas et al., 2015). For illustration, Figure 1.5 shows examples  $Q$ ,  $U$ ,  $Q_\phi$ ,  $U_\phi$  and  $PI$  images of the same disk (using the coronagraphic dataset of PDS 70 presented in Chapter 2). As expected,  $Q$  and  $U$  images show evidence of a butterfly pattern, while  $Q_\phi$  contains mostly positive signal, and  $U_\phi$  shows only weak signal.  $PI$  is only positive, by definition.

NIR polarimetric observations are most sensitive to scattering from small, micrometer-

---

<sup>4</sup>Circular polarization is not discussed here.

## 1 Introduction

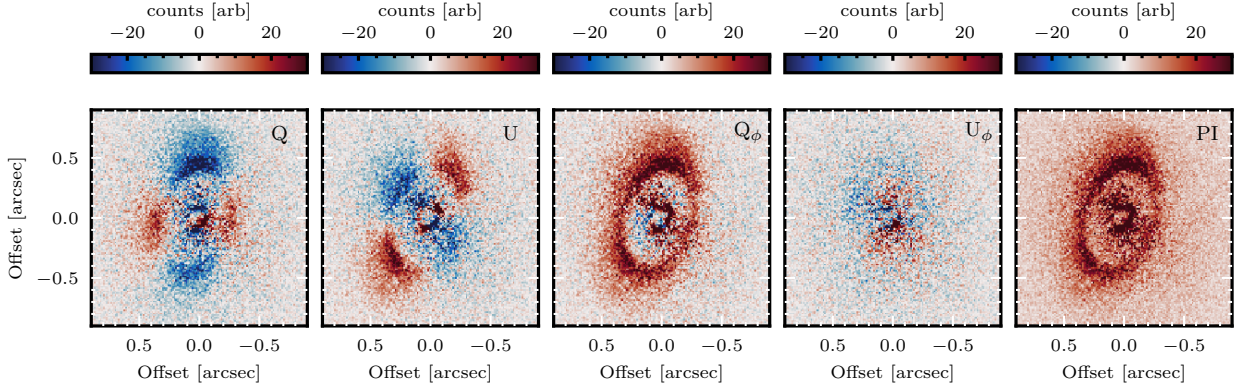


**Figure 1.5:** Exemplary  $Q, U, Q_\phi, U_\phi$  and  $PI$  images of the disk around PDS 70 as observed with the SPHERE instrument (see Chapter 2 for details).

sized dust grains. As explained in Sect. 1.1.4, those are typically well mixed with the gas and therefore lifted high up in the surface layers of the disk. These observations thus trace the upper layers where these dust grains become optically thick, typically found at  $\sim 2$ -4 times the pressure scale height of the disk. Coupled with radiative transfer models, these observations allow to study different properties of protoplanetary disks, such as the scattering behaviour of dust (Sect. 2.5.3), or substructures imprinted by the interaction with a companion (of planetary or stellar nature) within the disk (Sections 2.4, 5.5).

### 1.4.3 Sub-millimeter Interferometry

Observations in the sub-millimeter regime are mostly sensitive to thermal emission from large, pebble-sized dust grains in the cool disk midplane through continuum (i.e., broadband) imaging, and to the gaseous disk component through spectrally resolved imaging of molecular lines. This wavelength regime is therefore particularly suited to probe indirect imprints from embedded planets by analyzing the disk structure. In the following, I briefly introduce the basic principles of sub-millimeter interferometric imaging, and discuss then the applications of continuum and molecular line observations.

#### Basic principles

It is clear that in order to scrutinize disk structures and to study signatures from embedded planets, a very high angular resolution is required. Because of the substantially longer wavelengths in the sub-millimeter regime, the angular resolution of a single antenna is fairly limited, and dishes with unrealistic sizes would be needed to achieve angular resolutions similar to the NIR. For example, in order to reach at a wavelength of  $850 \mu\text{m}$  an angular resolution of  $0.04''$ , comparable to that of SPHERE in the H-band, a dish with

a diameter of about 4.4 km would be needed<sup>5</sup>. This problem can be solved by sampling the sky brightness distribution with a set of several antennas at distinct locations. When combining their individual signals, a large aperture can be synthesised. This principle is called interferometry. The angular resolution is then determined by the longest baseline, i.e., the largest distance between a pair of antennas. This Section describes the basic principles of interferometry; for a detailed review for radio interferometry the reader is referred to [Thompson et al. \(2017\)](#).

Let us first consider the most simple case of an interferometer, consisting of only two antennas, called  $i$  and  $j$  and located at positions  $\mathbf{r}_i$  and  $\mathbf{r}_j$ , observing the same sky brightness distribution  $I_\nu(\mathbf{s})$  in direction  $\mathbf{s}$ . The wavefront coming from that source will have to travel slightly different path lengths before arriving at the two antennas. This path length difference  $\tau_{ij}$  (also called geometric delay) depends on the baseline  $\mathbf{B}_{ij} = (\mathbf{r}_i - \mathbf{r}_j)$  and the direction of the source  $\mathbf{s}$  ([Thompson et al., 2017](#)):

$$\tau_{ij} = \frac{\mathbf{B}_{ij} \cdot \mathbf{s}}{c}, \quad (1.14)$$

where  $c$  is the speed of light. This effect can be used to recover the location of the source by correlating the signals of the two antennas. The response of an antenna pair is a complex quantity called visibility  $V_\nu$ , defined as:

$$V_\nu^{ij} = \int I_\nu(\mathbf{s}) \exp(-2\pi i \nu \mathbf{B}_{ij} \cdot \mathbf{s} / c) d\Omega. \quad (1.15)$$

Because an antenna pair mainly recovers the brightness distribution in direction parallel to its baseline with a resolution determined by the baseline length, interferometric observations benefit from a large number of antennas. Including more baselines of different lengths and in different directions will not only help to better sample the two-dimensional brightness distribution on the sky at different angular scales, but also increase the sensitivity because of a larger collecting area.

Often, the baseline  $\mathbf{B}$  is decomposed into components  $(u, v)$  in units of the observing wavelength, along the east-west and north-south directions, respectively. Similarly, a coordinate system  $(l, m)$  can be used to represent the angular distances on the sky measured in east-west and north-south directions. Using these coordinates, visibility and sky bright-

---

<sup>5</sup>The angular resolution  $\theta$  of a telescope is given by  $\theta \sim \lambda/D$ , where  $\lambda$  is the observing wavelength and  $D$  the diameter of the collecting area.

ness distribution are connected via Fourier transform:

$$\begin{aligned} V_\nu(u, v) &= \int \int I_\nu(l, m) \exp^{-2\pi i(ul+vm)} dl dm \\ I_\nu(l, m) &= \int \int V_\nu(u, v) \exp^{2\pi i(ul+vm)} du dv. \end{aligned} \tag{1.16}$$

It is clear that an image can be reconstructed more accurately the better the visibility in the  $uv$ -plane is sampled, which can be obtained, e.g., by increasing the number of antennas. This Thesis makes use of observations taken with the Attacama Large Millimeter Array (ALMA). At  $850 \mu\text{m}$ , ALMA offers configurations that allow to sample baselines of up to  $8.5 \text{ km}$ <sup>6</sup> resulting in an angular resolution of  $\sim 30 \text{ mas}$  at most.

### Data calibration

The combination of the signals from up to 66 antennas with ALMA relies on an accurate calibration of the data. To this goal, ALMA performs observations of different calibration sources (e.g., for bandpass, phase, amplitude calibration). These allow to compute correction factors to the visibilities in order to account e.g., for variations in the antenna response as a function of time and frequency, as well as to calibrate the absolute flux scale. Often, relatively bright point-like radio sources such as distant quasars with well-known properties, located within a few degrees of the science target, serve as calibrator sources (see Fomalont et al., 2014).

In particular for extended configurations where the distances between antennas are very large, phase calibration is a crucial step. However, despite frequent switching between the phase calibrator and the science target, phase calibration may in general not be perfect (because the external phase calibrator is observed with a slight offset in distance and time), which could lead to residual phase errors. If the source is of sufficiently high signal-to-noise ratio (S/N), *self calibration* can be applied to improve the accuracy of the image. In this approach, a model image of the source itself is used as reference to compute the phase correction tables for each antenna. Because the model image has to be of sufficiently high S/N, the visibilities can be averaged in time, polarization, and/or spectral window prior to compute the calibration solutions. After applying this solution to the visibilities, the data can be re-imaged and inspected (see next Section for details about the imaging process). This procedure is repeated by iteratively changing the averaging parameters (usually, the averaging time interval is little by little decreased), until no significant improvement is achieved any more. While this procedure is well implemented within CASA, it is up to the user to fine-tune the optimal choice of parameters e.g., regarding the averaging and

---

<sup>6</sup>see <https://almascience.eso.org/documents-and-tools/cycle8/alma-proposers-guide>

cleaning process, which may be different from case to case. The process of self-calibration, if successful, can lead to significant decrease of the noise in the final image (see discussion in Sect. 3.6.1).

### Imaging process

Reconstructing an image from the measured visibilities (a process called ‘imaging’), requires the computation of their Fourier transform (called ‘dirty image’) and a subsequent deconvolution with the Fourier transform of the antenna configuration (called ‘dirty beam’; analogue to the PSF of optical telescopes).

A very commonly used algorithm for imaging is the `clean` algorithm (Högbom, 1974). This imaging recipe is based on the assumption that the sky brightness distribution can be represented by a collection of point sources. In the `clean` procedure, the brightest pixels in the dirty image are identified, and added to a ‘clean component’ list. The sources on this list are then convolved with the dirty beam and subtracted from the dirty image, resulting in a residual image which is again searched for the brightest pixels. This process is repeated iteratively, until a certain threshold in the residual map is met. The final image is then obtained by reconvolving the identified clean component list with the clean beam, i.e., a Gaussian representing the size of the dirty beam, and adding it to the residual map (see, e.g., Thompson et al., 2017).

The sensitivity and angular resolution of the final image can be influenced by according a relative weight to the individual visibilities. There are two extreme weighting schemes, *natural* and *uniform*. Natural weighting gives more weight to shorter baselines. Because the  $uv$ -plane is typically more densely sampled at short baselines, natural weighting results in an optimum point source sensitivity, at the cost of angular resolution. In contrast to that, uniform weighting gives more weight to longer baselines, leading to an image which is characterised by the highest angular resolution possible, but which suffers from a poor point source sensitivity. Finally, *briggs* weighting allows to choose a weighting scheme in a smooth transition between these two extreme cases. It provides a parameter, called *robust* or simply  $r$  parameter, which allows to tune the relative weighting of short and long baseline visibilities, optimizing either the angular resolution or point-source sensitivity.

### Dust continuum imaging

Continuum observations are obtained by integrating over a large bandwidth, and can thus achieve a high S/N even in relatively short integration times. At sub-millimeter wavelengths, continuum observations trace the thermal emission from pebble-sized dust grains which populate the midplanes of disks. Because these grains are decoupled from the gas motion, their spatial distribution is sensitive to variations in the radial pressure gradient

within the disk. As explained in Sect. 1.2.1, local pressure bumps, as they are thought to be generated by planets, can efficiently trap large dust grains, leading to the presence of annular substructures observable in the sub-millimeter continuum. The observations of such substructures may therefore be interpreted as an indirect tracer for the presence of an embedded planet. The width and depth of the associated gaps measured from continuum observations, often combined with NIR measurements, can be compared to hydrodynamical simulations in order to set constraints on the mass of the putative gap-carving planet (e.g., de Juan Ovelar et al., 2013; Kanagawa et al., 2015a; Rosotti et al., 2016; Zhang et al., 2018). However, although the generation of gaps is a very certain outcome of giant planet-disk interactions, also other mechanisms have been proposed to account for such substructures, such as ice lines (Zhang et al., 2015; Okuzumi et al., 2016), dead zones (Pinilla et al., 2016), magneto-hydrodynamical instabilities (e.g., Flock et al., 2015; Ruge et al., 2016; Riols & Lesur, 2019), or magnetic disk winds (Suriano et al., 2018).

With the advent of ALMA and its powerful capabilities in terms of angular resolution and sensitivity, it has also been suggested to search directly for the thermal emission from dust in the CPD itself through sub-millimeter continuum observations (e.g., Szulágyi et al., 2018; Zhu et al., 2018). Section 3.3.1 is dedicated to the search for sub-millimeter continuum emission from a CPD around PDS 70 b.

### Molecular line imaging

For molecular line observations, the emission is not integrated over the entire bandwidth. Instead of a two-dimensional image, the product of spectrally resolved observations is a three-dimensional cube with the third axis representing the frequency.

For an inspection of the data, these cubes can be collapsed to different *moment maps* containing different information about the spectral line emission. For the work presented in this Thesis, the so-called zeroth and first moment maps are of interest.

The zeroth moment is computed by integrating the intensity along the spectral axis in each pixel,

$$\mu_0 = \int I_\nu d\nu \tag{1.17}$$

Zeroth moment maps are therefore representative for the total flux receiving from a given pixel, and are often used to probe the basic structure of a disk.

The first moment corresponds to the intensity-weighted average velocity

$$\mu_1 = \frac{\int \nu I_\nu d\nu}{\int I_\nu d\nu} = \frac{1}{\mu_0} \int \nu I_\nu d\nu \tag{1.18}$$

and can be used to recover the velocity field of the disk.

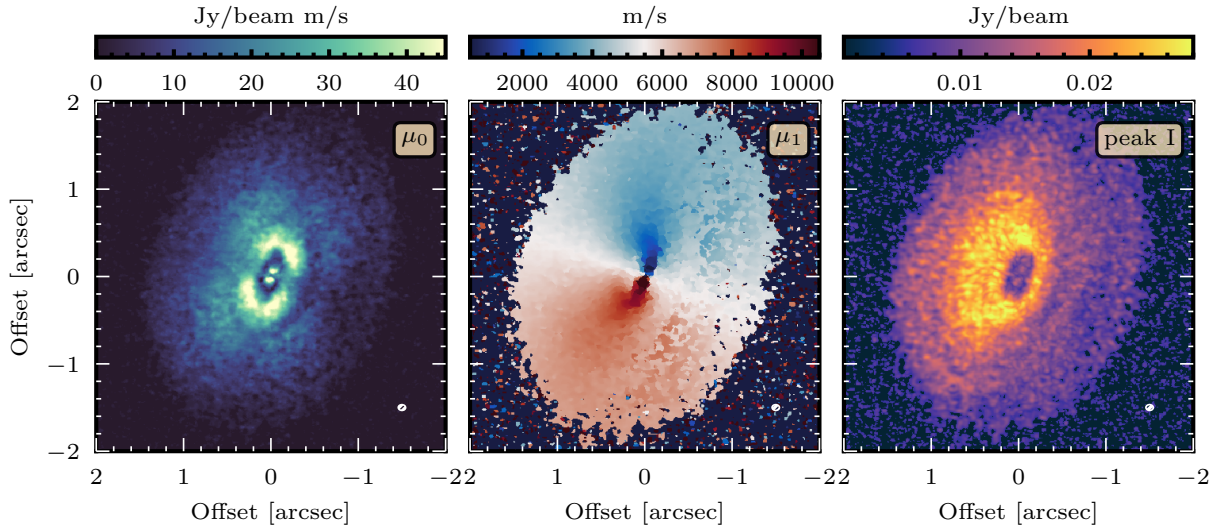


**Figure 1.6:** Example maps of integrated intensity (zerorth moment), velocity (first moment) and peak intensity maps for PDS 70. The maps were generated using the data presented in Chapter 4.

Finally, maps of the peak intensity of the spectrum at a given pixel are often used as a diagnostic tool of disk observations. Using the Planck formula,  $I_\nu$  can be converted into a brightness temperature  $T_b$ , which corresponds to the equivalent temperature of a black-body producing the same intensity. At sub-millimeter wavelengths, the Planck function can usually be approximated in the Rayleigh-Jeans limit, such that:

$$I_\nu \approx 2\nu^2 k_B T_b / c^2, \quad (1.19)$$

where  $k_B$  is the Boltzmann constant. If the emitting gas is in local thermodynamic equilibrium and the considered emission line is optically thick,  $T_b$  approximates the temperature of the gas in the emitting layer.

Figure 1.6 shows an example zeroth moment, first moment and peak intensity maps for PDS 70.

The prime interest of molecular line observations in this work is to search for possible imprints of planet-disk interactions in the gas component of the disk. While gap structures generated by planet-disk interactions are thought to also reveal in radial intensity profiles of the molecular gas, the spatial variation of the line intensity may not uniquely trace the gas surface density distribution, due to complicating effects related to the thermal and chemical structure of the disk, as well as optical depth effects (Facchini et al., 2018).

In this context, the analysis of the disk kinematics is a very powerful approach to en-

compass these complications. According to Eq. 1.6, steep gradients of gas density and pressure at the edges of gaps will cause gas to rotate at different velocities with respect to the smooth background disk, resulting in a hastening of the gas at the outer edge of the gap, and a slowing down at the inner edge of the gap (Bryden et al., 2000; Kanagawa et al., 2015b; Perez et al., 2015; Teague et al., 2018a). Measuring the rotation velocity and its variation with radius will thus allow to trace variations in the gas pressure gradient, and infer on the potential presence of planet-induced gaps.

Because the  $^{12}\text{CO}$  emission comes from an elevated layer above the midplane, we need to deproject the data in order to precisely analyze the velocity structure. Recent progress has been made to recovering the emission height of molecular line emission, either by fitting a Keplerian model to a velocity map (Teague, 2019), or by a geometric analysis of the isovelocity contours (i.e., regions where the projected velocity of the gas corresponds to the velocity of the given channel) detected in the individual channel maps (Pinte et al., 2018a). With the knowledge of the emission height, it is then possible to correctly deproject the data and to reconstruct the gas rotation velocity as a function of radius by azimuthally stacking the spectra at a given radius (Teague et al., 2018a,b). This method is applied to study the disk kinematics of PDS 70 in Sect. 3.3.2.

While the perturbation of the disk kinematics by the planet will affect all azimuths, it will be strongest close to the location of the planet, where the spiral wakes are launched. Such localised perturbations could be spotted on the individual channel maps, where the emission arises from regions concentrated around the isovelocity contours. Localised perturbations of the disk kinematics will lead to a local discontinuity ('kink') of the otherwise smooth contours, visible in a limited range of frequencies (Pérez et al., 2015; Pinte et al., 2018b, 2019). Those may also show up as localised residuals ('Doppler flips') when subtracting smooth model from the first moment map (Pérez et al., 2018).

Finally, it is thought that the rotation of the CPD itself may be detected through molecular line observations. Perez et al. (2015) predicted that the rotation of a CPD may be sufficiently large to be discernible from the background disk rotation, implying a broadening of the line at the location of the planet.

## 1.5 Observing planet formation: state of the field

The previous Sections have introduced the current theoretical understanding of giant planet formation (Sect. 1.2), and presented observing techniques used to search for direct and indirect tracers of forming planets (Sect. 1.4). This Section gives a summary of the current state of the field concerning the observational evidence of planet formation.

While more than 4000 planets have been discovered, most of the detected exoplanets are

found around mature stars, and are therefore already at a later stage of their evolution. Very young stars are usually avoided by radial velocity and transit surveys, the most successful planet hunting techniques, hampered by the stellar noise which is typical at these young ages. In contrast to that, the DI technique benefits from young ages, since young planets are still hot and are therefore detectable through their thermal emission. Still, direct detections of planets around these young, disk-bearing stars has remained a challenging task, and only a few, yet unconfirmed candidates of forming protoplanets have been reported in the literature. A reason for possible confusion is that in the presence of disks, the ADI process can cause distortions or even create artifacts that could mimic point-like features (see Sect. 1.4.1).

Among the most compelling targets to search for forming planets are transition disks (TDs). These disks were initially identified by a significantly reduced NIR excess compared to the median SED of young stars with disks (Strom et al., 1989), which indicates the depletion of dust in the inner region of the disk (e.g., see review by Espaillat et al., 2014). Indeed, recent high-resolution imaging observations of disks at infrared as well as (sub-)millimeter wavelengths have revealed large gaps (e.g. Thalmann et al., 2010; Andrews et al., 2011), azimuthal asymmetries (e.g. van der Marel et al., 2013), spirals (e.g. Benisty et al., 2015; Tang et al., 2017), and multiple rings (e.g. ALMA Partnership et al., 2015; Ginski et al., 2016; van Boekel et al., 2017; Avenhaus et al., 2018), as well as shadowed regions and brightness dips, some of which show evidence of temporal variation (e.g. Stolker et al., 2017; Pinilla et al., 2018b). In particular, the stunning images revealed by recent ALMA surveys at high angular resolution, such as the DSHARP (Disk Substructures at High Angular Resolution Project; Andrews et al., 2018) and the Taurus survey (Long et al., 2018a) have evidenced a prevalence of substructures in young protoplanetary disks, in particular gaps and rings. Often, these features have been attributed to being carved by young, embedded planets (e.g., Dipierro et al., 2015; Fedele et al., 2018; Zhang et al., 2018).

The quest for planets within these disks have revealed candidates in only four systems so far, namely HD 169142, HD 100546, LkCa 15, and MWC 758, most of which are currently still under debate. One of the point sources detected around HD 169142 (Biller et al., 2014; Reggiani et al., 2014) was shown to be related to an inhomogeneous ring structure (Pohl et al., 2017b) in the inner region of the disk by Ligi et al. (2018). These authors also found that another compact structure in that system detected at about 100 mas projected separation could possibly be related to a further ring structure at the given separation, while another protoplanet candidate in this system identified by Gratton et al. (2019) is still pending confirmation. Two companion candidates were also found around HD 100546 (Quanz et al., 2013, 2015; Brittain et al., 2014; Currie et al., 2015), but are challenged in the light of recent GPI and SPHERE observations, because they do not appear point-like at

all wavelengths (Rameau et al., 2017; Follette et al., 2017; Currie et al., 2017; Sissa et al., 2018). For the case of LkCa15, Kraus & Ireland (2012) and Sallum et al. (2015) reported three companion candidates in this system. Thalmann et al. (2016) found that the planets were co-located with the bright, near side of the inner component of the LkCa 15 disk. They concluded that this disk structure might be responsible for at least some of the signal attributed to the protoplanets detected by Sallum et al. (2015), a result which was later confirmed through additional observations and modelling efforts by Currie et al. (2019). While one of the three candidates, LkCa 15b, was considered as yet the most convincing case for a protoplanet in this system due to the detection of  $H_\alpha$  emission (Sallum et al., 2015), a possible tracer of ongoing accretion onto the protoplanet, recently, Mendigutía et al. (2018) showed that the signal at the  $H_\alpha$  line was inconsistent with that of a point source but could be rather explained by an extended source of emission. Finally, the presence of a point source interior to the spiral arms within the MWC 758 disk was reported by Reggiani et al. (2018). While follow-up observations lead by Wagner et al. (2019) could not recover this source (although their image quality should have been sufficient for a re-detection, given its brightness reported by Reggiani et al., 2018), their observations revealed another companion candidate near the end of one of the spiral arms.

Figure 1.7 shows the polarimetric SPHERE images of the HD 169142, LkCa 15 and MWC 758 disks, with the positions of the companion candidates indicated by grey crosses. This illustrates that several of the detected sources are located close to disk structures recovered in the scattered light images, suggesting a possible relation to ADI artifacts. All these debates highlight that a careful analysis of companion candidates detected with DI and located in protoplanetary disks with respect to a possible link to disk features is required, and that a robust detection requires confirmation through multi-wavelength and/or multi-epoch observations.

During the time this Thesis was carried out, significant progress has been made on revealing kinematical imprints of protoplanets. So has the rotation curve of the disk around HD 163296 inferred from ALMA observations of the CO isotopologue emission shown evidence of perturbations in the radial pressure gradient co-located with gaps in the continuum, best explained by the effect of two Jupiter-mass planets embedded at radial distances of 83 and 138 au (Teague et al., 2018a). In that same system, Pinte et al. (2018b) identified another far-out giant planet candidate at about 260 au through the detection of a spatially localized deviation from Keplerian rotation ('kink') in the CO channel maps. Following those detections, more planets candidates have been suggested from their kinematic signatures, in the disks around HD 97048 (Pinte et al., 2019), and around HD 100546 (Casassus & Pérez, 2019; Pérez et al., 2020), as well as in some of the disks observed within the DSHARP program (Pinte et al., 2020).

As a summary, the frequent detection of disk substructures, be it in dust or gas, suggests

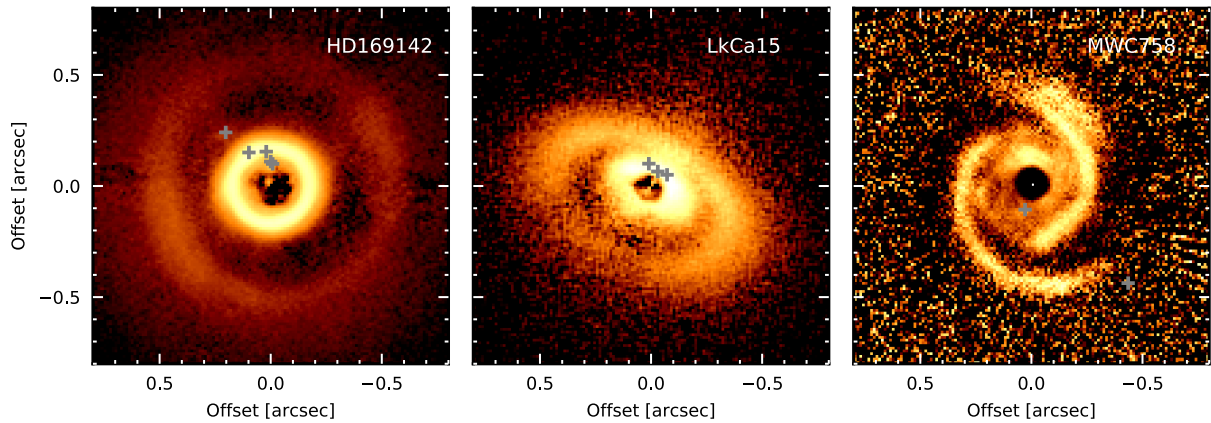


**Figure 1.7:** Polarimetric ( $Q_\phi$ ) images of three transition disks for which protoplanet candidates have been reported in the literature. The observations were carried out with the SPHERE instrument, and the data have been published by Pohl et al. (2017b); Thalmann et al. (2016); Benisty et al. (2015). The gray crossed mark the approximate locations of the protoplanet candidates discussed in Sect. 1.5. Note that the size of the crosses is not representative for the error bars.

a population of young, forming planets interacting with their parental disks. Prior to the work presented in this Thesis, however, no unambiguous direct detection of a planet forming in a disk has been put forth in the literature. It is clear that the robust *direct* detection of a planet within a disk is key in order to probe the *indirect* imprints of its presence on the protoplanetary disk.

## 1.6 Motivation and outline of the Thesis

The field of planet formation has seen a quantum leap during the last years. Yet numerous open questions remain. One reason for these uncertainties is that there is still very few constraints for planet formation from observations. Young planets still embedded in their parental disks provide a unique window to observe planet formation while it is happening. However, observing these systems is challenging, and so far, no robust and convincing detection has been put forward.

The goal of this Thesis is to search for direct and indirect traces of giant planet formation, and to characterize the properties and structures of protoplanetary disks, the cradles of planets. To this goal, different observing techniques in two wavelength regimes, the NIR using the SPHERE instrument, and the sub-millimeter using the ALMA interferometer, are employed in this work.

In Chapter 2, we present NIR images in polarized scattered light and total intensity of PDS 70, a young,  $\sim 5$  Myr star surrounded by a disk with a prominent gap, which has previously been suspected to be a possible scene of ongoing planet formation. These data are used to perform a detailed study of the disk structure as seen in scattered light. Analysis of the intensity images reveal the robust detection of a point source within the gap of a disk, confirmed at several different epochs and filter bands. The analysis of photometry and astrometry allow us to conclude on the presence of a young, planetary-mass companion, possibly surrounded by warm material. This discovery corresponds to the first unambiguous detection of a forming planet embedded in its disk, called PDS 70 b hereafter, opening the door to a so far observationally unexplored parameter space of young forming planets.

With PDS 70 being a unique testbed to observationally probe planet-disk interactions, we present in Chapter 3 new ALMA data at high angular resolution, and in Chapter 4 at high spectral resolution to search for direct and indirect imprints of PDS 70 b in the dust continuum and CO emission of the protoplanetary disk. These observations reveal that PDS 70 b is located within a deep gap carved in both, dust and gas, as predicted from theoretical models.

A large portion of stars is found to be part of binary or higher-order multiple systems (Duchêne & Kraus, 2013), and an increasing number of planets is found in multiple systems (Orosz et al., 2019; Bonavita & Desidera, 2020). Still, very little is known about the conditions of planet formation in these systems. In Chapter 5, we characterize the morphology of the circumbinary disk around GG Tau A disk using polarimetric observations obtained with SPHERE. We find the disk to be highly structured, and relate these substructures to the interactions with the central binary through the comparison to hydrodynamical simulations.

Chapter 6 provides a summary of this Thesis with a prospect to future works.

# 2

## Discovery of a planetary-mass companion within the gap of the transition disk around PDS 70

---

The content of this Chapter is based on [Keppler et al. \(2018\)](#), published in *Astronomy & Astrophysics (A&A)*, 617, 44.

**Details of authorship:** I am the first author of this paper and led this team effort involving 124 co-authors under the supervision of Prof. Thomas Henning, and in close collaboration with Roy van Boekel and Myriam Benisty. The text was written by me, with contributions from Rob van Holstein and André Müller for Sect. 2.3. I performed the analysis and radiative transfer modeling of the polarimetric and total intensity data of the disk, and carried out the astrometric and photometric analysis and discussion of PDS 70 b. The polarimetric data were reduced by Rob van Holstein, Henning Avenhaus and Christian Ginski. The reduction of the ADI data, as well as the photometric and astrometric extraction of the point source was performed using SPHERE consortium tools and private pipelines by André Müller, Faustine Cantalloube, and Anne-Lise Maire. The gradient reduction of the ADI data described in Sect. 2.3.3 was contributed by Anthony Boccaletti. Finally, Fig. 2.14 was provided by Mickael Bonnefoy, and Fig. 2.13 was generated using SPHERE consortium tools. All co-authors provided comments to the paper manuscript.

### 2.1 Motivation

As pointed out in Chapter 1, more than two decades of exoplanet quests have revealed a tremendous diversity of planetary systems, but still little is known about their initial conditions and their properties at very early evolutionary stages. It is therefore an essential goal to search for young, forming planets and characterize the properties of their natal protoplanetary disks at the time where planet formation processes are still ongoing.

With this goal, this Chapter presents NIR observations of the transition disk around PDS 70. This system is one of the most promising transition disks to host forming planets,

due to the presence of a wide gap in its disk which has long been suspected to be sculpted by forming planets.

The observations comprise an extensive dataset using SPHERE, complemented with archival data obtained with other instruments. The data were taken with both angular differential imaging and polarimetric observations at multiple wavelengths and epochs, from the optical to the NIR, covering a time period of more than four years. On the basis of these data, the robust detection of a point source within the gap of the disk is reported, which is interpreted as a planetary-mass companion. Further, the analysis of the well-known outer disk with respect to its morphological appearance is presented, and its structure is investigated with a radiative transfer model.

Section 2.2 introduces the target, PDS 70, while the observational setup and reduction strategy of the different datasets are described in Sect. 2.3. The analysis of the disk is presented in Sect. 2.4, and Sect. 2.5 describes the modelling efforts. Section 2.6 is dedicated to the analysis of the point source, and the results are summarised in Sect. 2.7. Finally, Section 2.8 highlights recent literature results following the publication of the work presented in this Chapter which will be relevant for the subsequent Chapters.

## 2.2 The target: PDS 70

PDS 70 is a K7-type member of the Upper Centaurus-Lupus subgroup (UCL), part of the Scorpius-Centaurus association (Riaud et al., 2006; Pecaú & Mamajek, 2016), located at a distance of  $113.43 \pm 0.52$  pc (Gaia Collaboration et al., 2016, 2018). The young age of PDS 70 is evidenced by strong lithium absorption and the presence of a protoplanetary disk ( $\lesssim 10$  Myr) (Gregorio-Hetem & Hetem, 2002; Metchev et al., 2004).

For a more detailed analysis of the stellar properties, it is possible to compare the location of PDS 70 on a Hertzsprung-Russell diagram with pre-main sequence evolutionary tracks and isochrones. Using low-resolution optical spectra, Pecaú & Mamajek (2016) derived a stellar temperature of 3972 K, corresponding to a K7 spectral type. Assuming a distance of 98.9 pc, these authors derived a luminosity of  $0.27 L_{\odot}$ , which, scaled to a distance of 113.4 pc, translates to a luminosity of  $0.35 L_{\odot}$ . Figure 2.1 compares the position of PDS 70 with the pre-main sequence evolutionary tracks and isochrones from Tognelli et al. (2011), assuming a metallicity  $Z = 0.02$ , an initial helium abundance of 0.27, a mixing length of 1.68 and a deuterium abundance of  $2 \times 10^{-5}$ . This comparison implies a stellar mass of 0.7-0.85  $M_{\odot}$ , and an age of  $6 \pm 2$  Myr. These values compare well to the results by Müller et al. (2018), who fitted the stellar evolutionary models from the MIST project (Dotter, 2016; Choi et al., 2016; Paxton et al., 2011, 2013, 2015) using a Markov Chain Monte Carlo approach to determine the stellar parameters. The authors found a stellar age of

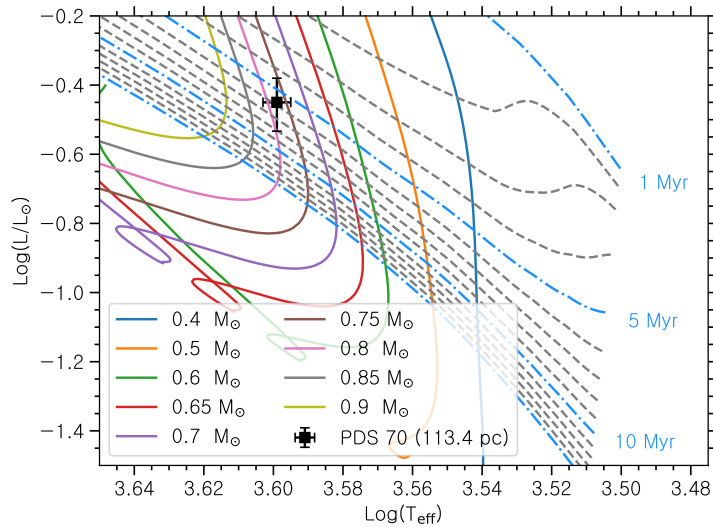


**Figure 2.1:** The location of PDS 70 on a Hertzsprung-Russell diagram in comparison with the pre-main sequence evolutionary tracks and isochrones from [Tognelli et al. \(2011\)](#).

$5.4 \pm 1.0$  Myr and a mass of  $0.76 \pm 0.02 M_{\odot}$ , which is consistent with the above given values. These values are taken as a reference throughout this Chapter. It is worth noting that these mass estimates are in good agreement with the dynamical mass of PDS 70 ( $0.6$ - $0.8 M_{\odot}$ ; [Hashimoto et al., 2015](#); [Long et al., 2018b](#)). The stellar properties are summarised in [Table 5.1](#).

The first evidence of the presence of a disk was provided by the measurement of infrared (IR) excess in the SED ([Gregorio-Hetem & Hetem, 2002](#); [Metchev et al., 2004](#)). Modelling of the SED predicted that PDS 70 hosts a disk whose inner region is substantially cleared of dust, but with a small optically thick inner disk emitting in the NIR ([Hashimoto et al., 2012](#); [Dong et al., 2012](#)). The first spatially resolved image of the disk was obtained by [Riaud et al. \(2006\)](#) together with the detection of a companion candidate at  $2.2''$  to the North of the host star using the NaCo instrument in the Ks filter. The companion candidate was later identified as a background source ([Hashimoto et al., 2012](#)). The gap was resolved in NIR scattered light observations using Subaru/HiCIAO ([Hashimoto et al., 2012](#)) as well as in the dust continuum observed with the Submillimeter Array (SMA) at  $1.3$  mm ([Hashimoto et al., 2015](#)) and most recently with the Atacama Large Millimeter/-submillimeter Array (ALMA) at  $870 \mu\text{m}$  ([Long et al., 2018b](#)). The latter dataset showed evidence of the presence of an inner disk component extending out to a radius of several au that appears to be depleted of large grains. These recent ALMA observations also show that the surface brightness at sub-millimeter wavelengths, tracing large dust grains, peaks at a radial distance further out ( $\sim 0.7''$ , see [Fig. 5 of Long et al., 2018b](#)) than the

location of the cavity wall<sup>7</sup> ( $\sim 0.39''$ ; see Hashimoto et al., 2012, and Fig. 2.3 of this chapter) measured in scattered light imaging, tracing small micron-sized dust grains in the disk surface layer. This segregation in the spatial distribution of dust grains with various sizes is thought to be generated by a variation of the radial pressure gradient in the disk, and has already been observed in several systems (e.g. Pinilla et al., 2015b; Hendler et al., 2018). As mentioned in Chapter 1, several mechanisms have been proposed to be able to create such pressure bumps, such as magnetohydrodynamic effects or planets carving the gap (e.g. Pinilla et al., 2015a, 2016). The combination of the presence of an inner disk with the spatial segregation of dust grains makes PDS 70 a prime candidate for hosting planets that are carving the gap (Hashimoto et al., 2015).

**Table 2.1:** Photometry and stellar parameters of the PDS 70 system used in this study.

Parameter	Value
$V$	$12.233 \pm 0.123 \text{ mag}^{(a)}$
$J$	$9.553 \pm 0.024 \text{ mag}^{(b)}$
$H$	$8.823 \pm 0.04 \text{ mag}^{(b)}$
$K$	$8.542 \pm 0.023 \text{ mag}^{(b)}$
$L'$	$7.913 \pm 0.03 \text{ mag}^{(c)}$
Distance	$113.43 \pm 0.52 \text{ pc}^{(d)}$
$\mu_\alpha \times \cos(\delta)$	$-29.66 \pm 0.07 \text{ mas/yr}^{(d)}$
$\mu_\delta$	$-23.82 \pm 0.06 \text{ mas/yr}^{(d)}$
Spectral type	K7 <sup>(e)</sup>
$T_{\text{eff}}$	$3972 \pm 36 \text{ K}^{(e)}$
Radius	$1.26 \pm 0.15 R_\odot^{(f)}$
Luminosity	$0.35 \pm 0.09 L_\odot^{(f)}$
Mass	$0.76 \pm 0.02 M_\odot^{(g)}$
Age	$5.4 \pm 1.0 \text{ Myr}^{(g)}$
Visual extinction $A_V$	$0.05^{+0.05}_{-0.03} \text{ mag}^{(g)}$

**Notes.** References: <sup>(a)</sup> Henden et al. (2015); <sup>(b)</sup> Cutri et al. (2003); <sup>(c)</sup>  $L'$ -band magnitude obtained by logarithmic interpolation between the WISE W1 and W2-band magnitudes from Cutri & et al. (2014); <sup>(d)</sup> Gaia Collaboration et al. (2016, 2018); <sup>(e)</sup> Pecaut & Mamajek (2016); <sup>(f)</sup> derived from Pecaut & Mamajek (2016), scaled to a distance of 113.43 pc <sup>(g)</sup>Müller et al. (2018).

<sup>7</sup>Following de Juan Ovelar et al. (2013), the NIR cavity wall is defined as the radial position where the flux equals half the value between the minimum flux at the bottom of the gap and the flux maximum at the wall.

## 2.3 Observations and data reduction

Installed on the VLT, the SPHERE instrument is an extreme adaptive optics system (Fusco et al., 2016) feeding three subsystems: the Zurich IMaging POLarimeter (ZIMPOL; Schmid et al., 2018), operating in the visible, the Integral Field Spectrograph (IFS; Claudi et al., 2008a), and the InfraRed Dual-band Imager and Spectrograph (IRDIS; Dohlen et al., 2008), the latter two working in the NIR. The observations presented in this Chapter make use of all three subsystems. The following Section gives an overview of the observing and data-reduction strategy of the individual datasets. Table 2.2 summarizes the observation setups and conditions.

### 2.3.1 IRDIS polarimetric observations (J-band)

During the nights of March 25, 2016, and July 31, 2017, two datasets of PDS70 were obtained with the IRDIS instrument in PDI mode using the J-band ( $\lambda_J=1.25 \mu\text{m}$ ). The observations were carried out within Open Time (ESO programm identification codes 096.C-0333, 099.C-0891; PI: M. Benisty). As explained in Sect. 1.4, in this mode, the beam is split into two beams with orthogonal polarization states, where the direction of polarization to be measured can be tuned by the rotation of the HWP. In the setup of the here presented observations, one polarimetric cycle consisted of rotating the HWP to four different angles in steps of  $22.5^\circ$ .

During the first epoch (March 25, 2016) an apodized Lyot coronagraphic mask was employed (N\_ALC\_YJ\_S, diameter  $\sim 145$  mas; Martinez et al., 2009; Carbillet et al., 2011). The observations obtained eight polarimetric cycles with two long exposures (64 seconds) per HWP position. Near the end of the sequence, the seeing degraded, and the telescope guiding was lost such that the last polarimetric cycle had to be discarded. Before and after each sequence, several short, non-saturated images of the star outside the coronagraphic mask were obtained. In addition, in order to enable an accurate determination of the stellar position behind the coronagraph, the observing sequence contained calibration images in which four satellite spots in a square pattern centered on the star were generated by introducing a sinusoidal modulation onto the deformable mirror.

The second epoch (July 31, 2017) was obtained without a coronagraph in order to provide access to the innermost disk regions. Very short exposures (2 seconds) were chosen to prevent the star from saturating the detector. The observations consisted of seven polarimetric cycles, with 20 exposures taken per HWP position. The images were aligned by fitting two-dimensional (2D) Gaussians to the target star in each frame.

The first step of data reduction consisted of dark subtraction, flatfielding, interpolation

Table 2.2: Observing log of data used within this study.

Date	ProgID	Instrument	Mode <sup>(a)</sup>	Filter	R <sup>(b)</sup>	Coronagraph	$\Delta\theta$ <sup>(c)</sup>	DIT <sup>(d)</sup> [s]	$\Delta t$ <sup>(e)</sup> [min]	$\epsilon$ ["] <sup>(f)</sup>
2012-03-31	GS-2012A-C-3	NICI <sup>(g)</sup>	ADI	L'	–	–	99.4°	0.76	118	–
2015-05-03	095.C-0298(A)	IRDIS	ADI	H2H3	–	ALC_YJH_S	52.0°	64.0	70	0.7
2015-05-03	095.C-0298(A)	IFS	ADI	YJ	54	ALC_YJH_S	52.0°	64.0	70	0.7
2015-05-31	095.C-0298(B)	IRDIS	ADI	H2H3	–	ALC_YJH_S	40.8°	64.0	70	1.1
2015-05-31	095.C-0298(B)	IFS	ADI	YJ	54	ALC_YJH_S	40.8°	64.0	70	1.1
2015-07-09	095.C-0404(A)	ZIMPOL	PDI	VBB	–	–	–	40.0	114	1.1
2016-03-25	096.C-0333(A)	IRDIS	PDI	J	–	ALC_YJ_S	–	64.0	94	1.9
2016-05-14	097.C-1001(A)	IRDIS	ADI	K1K2	30	–	16.9°	0.837	22	1.0
2016-05-14	097.C-1001(A)	IFS	ADI	YJH	–	–	16.9°	4.0	23	1.0
2016-06-01	097.C-0206(A)	NaCo	ADI	L'	–	–	83.7°	0.2	155	0.5
2017-07-31	099.C-0891(A)	IRDIS	PDI	J	–	–	–	2.0	36	0.7

**Notes.** <sup>(a)</sup>Observing mode: Angular Differential Imaging (ADI) or Polarimetric Differential Imaging (PDI); <sup>(b)</sup>Spectral resolution; <sup>(c)</sup>total field rotation, after frame selection; <sup>(d)</sup>detector integration time; <sup>(e)</sup>total time on target (including overheads); <sup>(f)</sup>mean MASS/DIMM seeing; <sup>(g)</sup>archival data, published in Hashimoto et al. (2012).

of bad pixels, and recentring of the frames. The rotation of the HWP to four different angles allowed us to determine a set of four linear polarization components  $Q^+, Q^-, U^+, U^-$ , which were obtained by making the difference between the images from the two detector halves, respectively. From these components we recovered then the clean Stokes  $Q$  and  $U$  frames using the double-difference method (Canovas et al., 2011), and the normalised double-difference method (van Holstein et al., 2020) for the non-coronagraphic and coronagraphic dataset, respectively.

One of the most important steps in the reduction of polarimetric data is the subtraction of instrumental polarization (IP). Standard techniques to correct for the IP, as described by Canovas et al. (2011), estimate the IP directly from the data itself. Here, the main assumption is that the central unresolved source, consisting of the stellar photosphere plus thermal emission and/or scattered light from the inner disk, if the latter is present, is unpolarized. This implies that they cannot differentiate between intrinsic polarization of the central source and the IP. In this case, correcting for the IP would mean subtracting any (physical) polarization of the central unresolved source. In contrast to that, to correct our measurements for the IP and cross-talk effects, we applied the detailed Mueller matrix model (van Holstein et al., 2017; de Boer et al., 2020; van Holstein et al., 2020). This method models the complete optical path that the beam traverses on its way from entering the telescope to the detector, and has already been applied in the analysis of several circumstellar disks observed with SPHERE (Pohl et al., 2017a; Canovas et al., 2018). The incident Stokes  $Q$  and  $U$  images are recovered by solving a set of equations describing every measurement of  $Q$  and  $U$  for each pixel individually. These Stokes  $Q$  and  $U$  images correspond to the images as they enter the telescope (star and disk convolved with telescope PSF and noise). With this method, we can therefore make a model prediction of the IP, and correct for the IP alone without subtracting the polarized signal from the central source. After the correction for the IP, any remaining polarized signal at the location of the central source, induced by, for example, unresolved material close to the star, such as an inner disk, would then become visible in the form of a central butterfly pattern in the  $Q_\phi$  image and can affect the signal of the outer disk. This leftover signal can then be chosen to be subtracted following the method by Canovas et al. (2011). On the other hand, it can also be kept, if one desires to study the unresolved inner disk (see van Holstein et al., 2020). We prepared two reductions, one for which we subtracted the central source polarization (allowing us to study the morphology of the outer disk; see Sect. 2.4.1), and one where we did not subtract it (for analysing the inner disk; see Sect. 2.4.2). We corrected our data for true north and accounted for the instrument anamorphism (Maire et al., 2016b). We measured a PSF full width at half maximum (FWHM) of  $\sim 52$  and  $\sim 49$  milli-arcseconds (mas) on the unsaturated flux frames of the coronagraphic observations, and of the total intensity frame for the non-coronagraphic data, respectively.

We then transformed our Stokes images into polar coordinates ( $Q_\phi, U_\phi$ ), according to the definition in Eqn. 1.13. As explained in Sect. 1.4, in this formulation, a positive signal in the  $Q_\phi$ -image corresponds to a signal that is linearly polarized in azimuthal direction, whereas radially polarized light causes a negative signal in  $Q_\phi$ . Any signal polarized in the direction  $\pm 45^\circ$  with respect to the radial direction is contained in  $U_\phi$ . Therefore, in the case of low or mildly inclined disks, almost all scattered light is expected to be contained as positive signal in  $Q_\phi$ . However, due to the non-negligible inclination of the disk around PDS 70 ( $49.7^\circ$ , Hashimoto et al., 2012), and because the disk is optically thick such that multiple scattering processes cannot be neglected, we expect some physical signal in  $U_\phi$  (Canovas et al., 2015).  $U_\phi$  can therefore only be considered as an upper limit to the noise level.

### 2.3.2 ZIMPOL polarimetric observations (VBB band)

PDS 70 was observed during the night of July 9, 2015, with the SPHERE/ZIMPOL instrument (Thalmann et al., 2008; Schmid et al., 2018). These non-coronagraphic observations were performed in the SlowPolarimetry readout mode (P2), using the Very Broad Band (VBB, 590-881 nm) filter, which covers the wavelength range from the R- to the I-band. Especially in the second half of the sequence, the conditions were poor (seeing above  $1''$ ), resulting in a PSF FWHM of  $\sim 159$  mas. Since the detailed Mueller matrix model for the correction of the instrumental polarization by van Holstein et al. (2020) only applies to the IRDIS data, our correction for instrumental polarization effects was performed by equalising the ordinary and extraordinary beams for each frame, as described by Avenhaus et al. (2014b). We interpolated two pixel columns in the image that were affected by readout problems.

### 2.3.3 IRDIFS angular and spectral differential imaging observations (Y-H-band)

During the guaranteed time observations (GTO) of the SPHERE consortium, PDS 70 was observed twice within the SHINE (SpHere INfrared survey for Exoplanets; Chauvin et al., 2017b) program on the nights of May 3, 2015, and May 31, 2015. The data were taken in the IRDIFS observing mode, with IRDIS working in the dual-band imaging mode (Vigan et al., 2010) making use of the H2H3 narrow-band filter pair ( $\lambda_{H2} = 1.593 \mu\text{m}$ ,  $\lambda_{H3} = 1.667 \mu\text{m}$ ), and with IFS operating simultaneously in the wavelength range of the Y and J broadband filter (0.95 - 1.33  $\mu\text{m}$ ) with a spectral resolution of  $R \sim 50$  (Claudi et al., 2008b). We made use of the N\_ALC\_YJH\_S coronagraphic mask (apodized Lyot, diameter 185 mas). The observations were performed in pupil-tracking mode to allow for angular differential imaging

(ADI; Marois et al., 2006). Before and after the sequences, we obtained calibration frames for measuring the location of the star behind the coronagraph and unsaturated images of the star without coronagraph for photometric calibration. Each sequence consisted of 64 exposures, from which we removed 10 and 14 bad quality frames for the May 3 and May 31 epochs, respectively.

After basic reduction steps applied to the IRDIS data (flat fielding, bad-pixel correction, sky subtraction, frame registration, frame selection to remove poor-quality frames based on the frame-to-frame photometric variability of the background object north from the star, correction of the instrument distortion, and correction of the flux calibration for the neutral density filter transmission) we used several different strategies to model and subtract the stellar speckle pattern. First of all, we applied the cADI method (classical Angular Differential Imaging; Marois et al., 2006). We then ran a sPCA (smart Principal Component Analysis) algorithm, adapted from Absil et al. (2013), which itself is based on the KLIP algorithm of Soummer et al. (2012). Further, we used the ANDROMEDA package (Cantalloube et al., 2015) which applies a statistical approach to search for point sources. Further, we applied the PCA and TLOCI (Template Locally Optimized Combination of Images; Marois et al., 2014) approach using the SpeCal implementation (Galicher et al., 2018). The main difference between our two PCA reductions is that the SpeCal PCA implementation does not select the frames for building the PCA library, and is therefore considered to be more aggressive than the former one. Finally, to obtain a non-ADI view of the disk morphology, we simply derotated and stacked the frames and applied a Laplacian filter, here referred as ‘gradient reduction’, in order to enhance low spatial frequencies (i.e. fine disk structures) in the image. However, since this reduction is not flux conservative, we used it only for a qualitative analysis of the outer disk structures.

Concerning the IFS data, the basic data reduction was performed using the Data Reduction and Handling software (Pavlov et al., 2008) and custom IDL routines adapted from Vigan et al. (2015) and Mesa et al. (2015). We post-processed the data using the cADI, ANDROMEDA and PCA-SpeCal algorithms. The IRDIS and IFS data were astrometrically calibrated following the methods in Maire et al. (2016b).

### 2.3.4 IRDIFS\_EXT angular and spectral differential imaging observations (Y-K-band)

The star was also observed with SPHERE in IRDIFS\_EXT mode during the night of May 14, 2016. In this mode, the IRDIS K1K2 narrow-band filter pair is used ( $\lambda_{K1} = 2.11 \mu\text{m}$ ,  $\lambda_{K2} = 2.25 \mu\text{m}$ ), whereas IFS is operating in the wavelength range of the YJH broad-band filter (0.97-1.64  $\mu\text{m}$ ) at a spectral resolution of  $R \sim 30$ . No coronagraph was used during the observations, and short detector integration times (DIT; 0.837 seconds for IRDIS, 4 seconds

for IFS) were chosen to prevent any saturation of the detector. As the observing conditions were relatively stable during the sequence, no frame selection was performed. The data-reduction strategy was identical to the one in Sect. 2.3.3, and we post-processed the data with sPCA, PCA-SpeCal, TLOCI and ANDROMEDA.

### 2.3.5 NaCo angular differential imaging observations (L'-band)

We also made use of observations of PDS 70 carried out with the VLT/NaCo instrument within the ISPY (Imaging Survey for Planets around Young stars; [Launhardt et al., 2020](#)) GTO program on the night of June 1, 2016. The sequence was obtained in pupil-stabilised mode making use of the L'-band filter (3.8  $\mu\text{m}$ ) and the 27.1 mas/pixel plate scale. No coronagraph was employed. A DIT of 0.2 seconds was used to prevent any saturation during the sequence. The seeing was rather stable during the observations (average seeing 0.5''), and seven frames were rejected. The data reduction and post-processing strategy was identical to the one in Sect. 2.3.3.

### 2.3.6 Archival NICI angular differential imaging observations (L'-band)

Finally, we used archival Gemini/NICI non-coronagraphic data taken on March 31, 2012 using the L' filter. The data together with the observing conditions and strategy were published in [Hashimoto et al. \(2012\)](#). As for the NaCo observations, no coronagraph was applied. Thirty-seven out of 144 frames were sorted out. We re-reduced and post-processed the data with the same approach as presented in Sect. 2.3.3.

## 2.4 Disk analysis

### 2.4.1 The outer disk in polarized scattered light

In total, we have three observations of the disk taken in PDI mode: two observations in IRDIS J-band (coronagraphic and non-coronagraphic), as well as one observation with the ZIMPOL VBB filter. Figure 2.2 shows the respective  $Q_\phi$  and  $U_\phi$  images. As expected from previous observations, we detect the disk in all three datasets as an elliptical ring. Because the setup of the non-coronagraphic IRDIS data was not optimal to detect the outer disk (very short exposure times, hence lower S/N), we focus here on the IRDIS coronagraphic dataset, and use the reduction where we subtracted the central source polarization (see Sect. 2.3.1). The  $Q_\phi$  images show evidence of residual signal that is contained within a region smaller than  $\sim 12$  pixels (17 au). In both the IRDIS and ZIMPOL data there is some

signal in  $U_\phi$ , but this signal is mostly detected at radii inward of the outer disk and does therefore not impact our analysis of the outer disk.

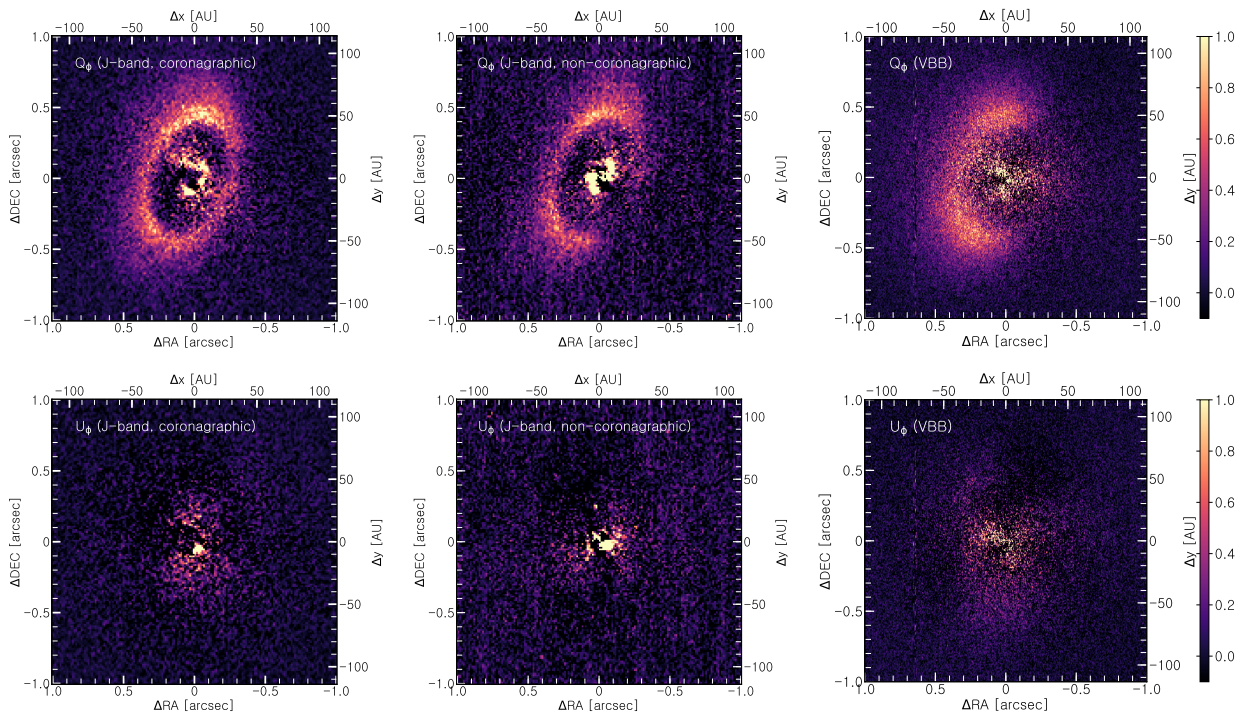


**Figure 2.2:** SPHERE PDI observations. The first row shows the  $Q_\phi$  images, the second row the  $U_\phi$  images. The left and middle columns correspond to the IRDIS J-band observations, taken with coronagraph (March 25, 2016), and without coronagraph (July 31, 2017), after correcting for the instrumental polarization and subtraction of the central source polarization. The right column presents the ZIMPOL observations (July 9, 2015). The colour scale was chosen arbitrarily but is the same for each pair of  $Q_\phi$  and  $U_\phi$ . We note that negative values are saturated to enable a better visual contrast. North is up and east is to the left.

In Fig. 2.3 we present the azimuthally averaged radial brightness profile after deprojecting the disk (using a position angle of  $158.6^\circ$  and an inclination of  $49.7^\circ$ , as determined by Hashimoto et al., 2012). To avoid effects from small-scale noise we smoothed our images with a small Gaussian kernel with a FWHM of 50% of the measured image resolution. The uncertainties were computed from the standard deviation of  $U_\phi$  in the corresponding radial bins, divided by the square-root of the number of resolution elements fitting in that bin. The reader is reminded that especially towards the region close to the star,  $U_\phi$  might contain physical signals, and therefore the error bars only indicate an upper limit for the noise. The mean radius of the disk brightness peak is determined to be  $\sim 54$  au. The outer disk ring appears wider in the VBB profile than in the J-band profile. We note however that the PSF FWHM was about three times larger during the VBB observations than dur-

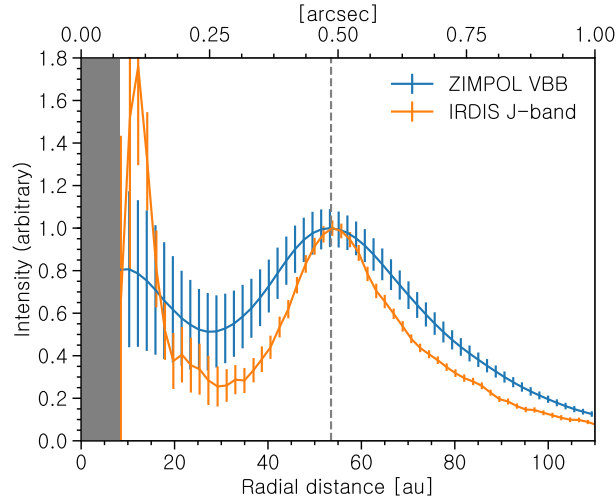


**Figure 2.3:** Radial profile of the VBB (blue) and J-band (orange) deprojected, azimuthally averaged  $Q_\phi$  images. The profiles were normalized according to the brightness peak of the outer disk, whose location ( $\sim 54$  au) is indicated by the grey dashed line. The grey shadow indicates the radius of the coronagraph in the J-band observations ( $\sim 8$  au).

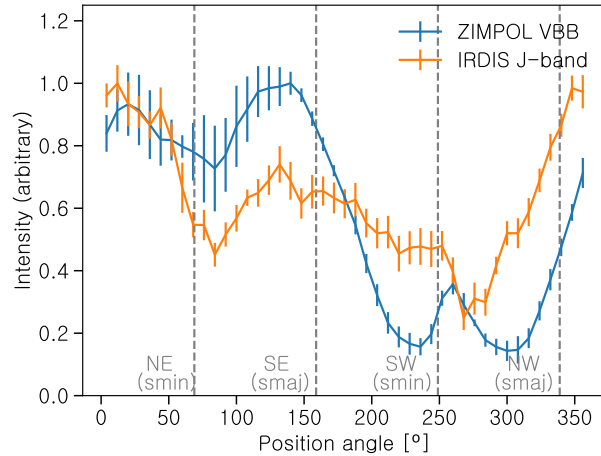


**Figure 2.4:** Azimuthal profile of the  $Q_\phi$  images averaged over an annulus of 35-70 au. The grey lines mark position angles of the SE and NW semi-major axes ('smaj'), as well as NE and SW disk minor axis ('smin'), respectively.

ing the J-band observations. Inside  $\sim 25$  au, the profile rises towards the centre which is associated to emission from the inner disk (see Sect. 2.4.2). The slope is much stronger in the J-band than in the VBB-band. This can be explained by the fact that the regions close to the star in PDI observations are affected by PSF damping effects which are more strongly pronounced at shorter wavelengths where the Strehl ratio<sup>8</sup> is significantly lower (Avenhaus et al., 2014a, 2018). In Fig. 2.4, we plot the azimuthal profile of the deprojected  $Q_\phi$  images. The profile was derived by averaging over azimuthal bins with a size of  $8^\circ$

<sup>8</sup>The Strehl ratio is a quantity to express the quality of the wavefront correction by adaptive optics.

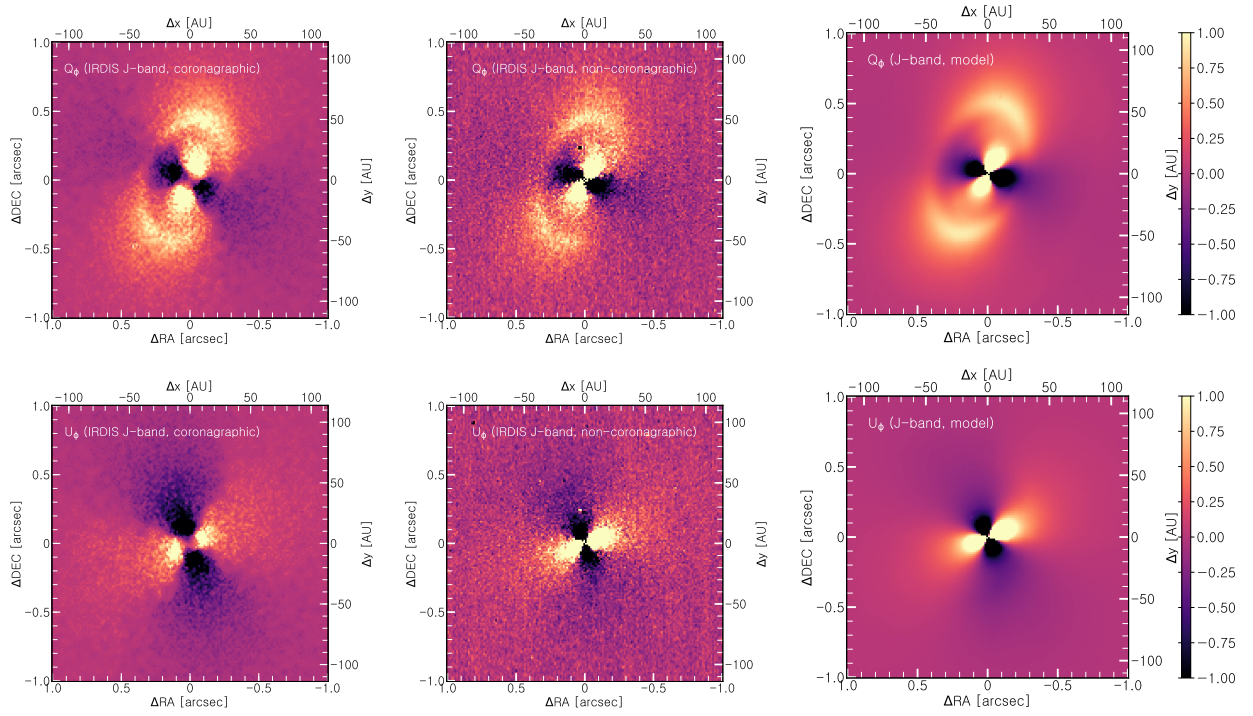


**Figure 2.5:** IRDIS coronagraphic (left column) and non-coronagraphic (middle column) PDI images, corrected for the instrumental polarization but without subtracting the central source polarization. The right column shows the model image as a comparison, including an inner disk with an outer radius of 2 au. The first row corresponds to the  $Q_\phi$  images, the second row to the  $U_\phi$  images. North is up and east is to the left.

between 35 and 70 au in radial direction. We note an azimuthal brightness modulation for both datasets. In each of them, the east side, corresponding to position angles (PA)  $\lesssim 160^\circ$ , appears on average brighter than the west side. By averaging the brightness in azimuthal bins of size  $\pm 20^\circ$  around the PA of the semi-major axes, we derive a brightness contrast of  $\sim 1.8$  on the brightness maxima along the semimajor axis in the south-east (SE) and north-west (NW) in the VBB and  $\sim 0.8$  in the J-band images. We also found a disk brightness ratio of  $\sim 3.1$  and  $\sim 1.4$  along the minor axes, in the NE and SW for the VBB and J-band, respectively. Therefore, the brightness ratio shows the same trend along the minor axis in the VBB and J-band, with the NE side being brighter than the SW side in both the VBB and the J-band. However, along the major axis, the trend is opposite between the two bands, with the SE side being brighter than the NW side in the VBB band, but fainter than the NW side in the J-band. By fitting an ellipse to the disk, Hashimoto et al. (2012) showed that the center of such an ellipse is offset towards the east side with respect to the star. This is due to the flaring geometry of the disk and implies that the east side of the disk corresponds to the far side.

## 2 Discovery of a planetary-mass companion within the gap of the transition disk around PDS 70

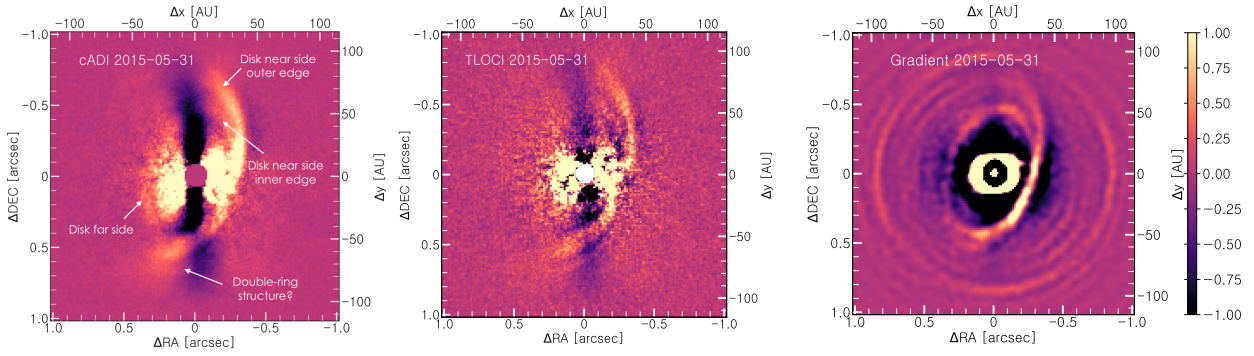


**Figure 2.6:** SHINE IRDIS observations of May 31, 2015, showing the cADI (left), TLOCI (middle), and gradient reduction (right). North is up and east is to the left.

### 2.4.2 Detection of the inner disk in polarized light

The presence of an optically thick inner disk in the innermost few astronomical units was predicted from SED fitting of the NIR excess (Hashimoto et al., 2012; Dong et al., 2012). The ALMA observations by Long et al. (2018b) (beam size of  $0.19'' \times 0.15''$ ) detected thermal emission from an inner disk component, which appears to be depleted of large grains. However, this inner disk component has not been directly detected in scattered light until now.

For the analysis of the inner region, we mainly rely on the IRDIS polarimetric non-coronagraphic dataset, as it allows us to probe regions closer to the star than does the coronagraphic dataset. As seen in Sect. 2.4.1, the outer disk is well recovered in the IRDIS PDI images by subtracting the remaining central source polarization. To study the inner disk region, we therefore choose to focus on the dataset corrected for the IP, but without subtracting the central source polarization. The corresponding  $Q_\phi$  and  $U_\phi$  images (coronagraphic and non-coronagraphic) are presented in Fig. 2.5 (left and middle column).

We detect a strong butterfly pattern in both  $Q_\phi$  and  $U_\phi$ . This pattern affects the outer disk. We determine a central source polarization degree of  $0.75 \pm 0.2\%$ , and an angle of linear polarization of  $66 \pm 11^\circ$ . Hence, the polarization direction in the inner region is approximately perpendicular to the disk semi-major axis. This butterfly pattern can be explained by the fact that we detect signal from the inner disk which is unresolved. If the inner disk is oriented in the same direction as the outer disk (PA of  $\sim 158.6^\circ$ , Hashimoto et al., 2012), the majority of this signal will be polarized in perpendicular direction to the semi-major axis, because the polarization degree is highest along the semi-major axis (scattering angle of  $\sim 90^\circ$ ). This signal gets smeared out when convolved with the instrument PSF, causing a large butterfly pattern in the resulting  $Q_\phi$  and  $U_\phi$  images. The fact that the unresolved signal is polarized perpendicular to the disk semi-major axis implies that the inner and outer disks are approximately aligned. We note that although we cannot determine the

inclination of the inner disk, we can infer that it must be larger than zero, because had the inner disk been seen face-on, its signal would have cancelled out due to axial symmetry. Further, the absence of shadows on the outer disk indicates that the inclination of the inner disk should be similar to that of the outer disk.

We note that even after subtracting the central source polarization from the non-coronagraphic (as well as the coronagraphic) data, a signal in  $Q_\phi$  is detected inside about 17 au. The subtraction of the central source polarization removes almost all signal from an *unresolved* source, and the leftover signal could originate from a partially resolved inner disk (larger than the resolution element). We therefore suspect that the disk is slightly larger than the resolution element, but not extending farther than 17 au, because otherwise we would have detected larger residuals after subtracting the central source polarization. We note that the polarization of the central source is unlikely to be caused by interstellar dust due to the low extinction measured towards PDS 70 ( $A_V=0.05^{+0.05}_{-0.03}$  mag, Müller et al., 2018). We further study the inner disk characteristics by comparison with our radiative transfer models (Sect. 2.5).

### 2.4.3 The disk in IRDIS angular differential imaging

We considered the SHINE IRDIS ADI observations for the characterization of the disk. In comparison to the observations presented in the previous section, they trace the total intensity and were taken at a longer wavelength (H-band). However, whereas the ADI technique is optimised for detecting point sources (see Sect. 2.6), when applied to extended sources as disks, the images suffer from self-subtraction effects. Figure 2.6 shows the resulting cADI image, TLOCI, and gradient images, and the sPCA, PCA-SpeCal images are shown in Fig. 2.7. In all reductions and epochs, the disk’s west side is clearly detected. As previously mentioned, this side corresponds to the near side of the disk. The disk’s extension along the semi-major axis is larger in the ADI images than in polarized light. When overlaying the two images, it appears that the signal we see in ADI in fact corresponds to the *outer* region of the disk as seen in polarized light (see Fig. 2.7). Furthermore, in some reductions, the inner edge of the disk’s far side appears to be detected. This is especially true in the gradient image, but also in the cADI reduction.

The gradient image exhibits many circular artifacts while the disk signal deviates from this circular symmetry, and the inner edge of the outer disk is well detected at all position angles. The cADI, TLOCI and both PCA reductions show a feature near the outer edge of the south-west side of the disk that looks like a double-ring structure beyond the main dust ring. This feature is detected at position angles in the range  $\sim 170\text{-}300^\circ$ . It follows the same shape as the main disk, but with an offset of roughly 125 mas. Although it is detected in four different reductions (sPCA, PCA-SpeCal, TLOCI, cADI), it is not clear if

## 2 Discovery of a planetary-mass companion within the gap of the transition disk around PDS 70

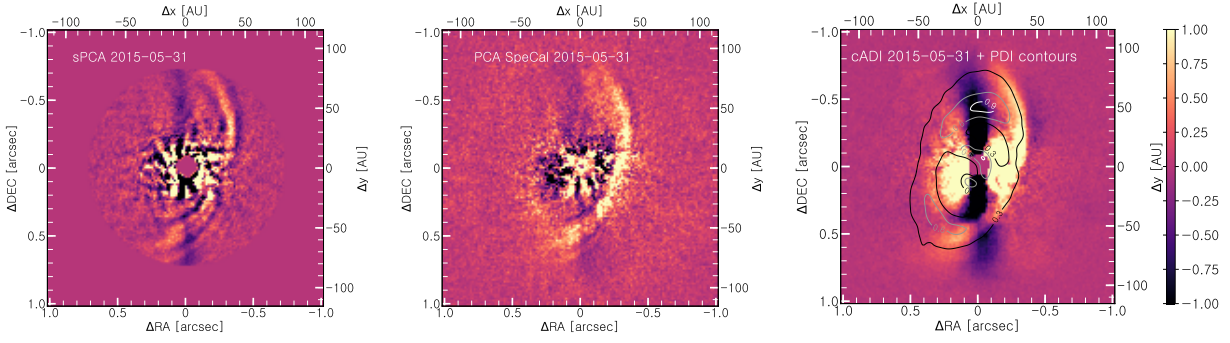


**Figure 2.7:** SHINE IRDIS observations of May 31, 2015: sPCA reduction (left), PCA-SpeCal reduction (middle), and cADI with an contour overlay of the PDI coronagraphic J-band image (right). The contours are drawn with respect to the peak value of the PDI image. For visibility purposes, the images are shown on individual colourscales. North is up and east is to the left.

this feature is real because these observations might suffer from the generation of artificial (sub-)structures due to the self-subtraction. It is also a concern that the structure, if it were real, is not detected in the gradient reduction, or in the PDI images. However, this double ring could be too faint to be detected in the PDI (since disks are in general much fainter in polarized light than in total intensity) and in the gradient image (which is affected by the circular artifacts).

## 2.5 Radiative transfer modeling

### 2.5.1 Model setup

To compare our multiwavelength observations with a physical model, we built a radiative transfer (RT) model, where the basic parametric approach by [Dong et al. \(2012\)](#) is taken as a starting point. We used the RT Monte-Carlo code RADMC-3D ([Dullemond et al., 2012](#)), introduced in Sect. 1.3.3. Our aim is to find a plausible model which reproduces our observations and the SED. We note that we are not looking for a globally best fitting model. RADMC-3D computes the thermal structure of the disk and produces images in scattered polarized light and total intensity by ray-tracing at any desired wavelength. Our grid has an inner radius of 0.04 au and an outer radius of 120 au. The surface density is proportional to  $r^{-1}$  and is truncated by a tapered edge with a characteristic radius  $R_c$ . We radially parametrize the dust surface density according to Eqn. 1.1, setting  $\gamma = 1$ , such that

$$\Sigma_{disk}(r) = \Sigma_0 \frac{R_c}{r} \exp\left(\frac{-r}{R_c}\right), \quad (2.1)$$

where  $\Sigma_0$  scales the amount of dust contained within the disk.

Following Eqn. 1.2, we assume a Gaussian distribution profile in the vertical direction and parametrize the density distribution in terms of the scale height  $h$  as:

$$\rho(r, z) = \frac{\Sigma(r)}{\sqrt{2\pi}h} \exp(-z^2/2h^2). \quad (2.2)$$

The disk is assumed to be flared with a constant power law index  $\beta$ , such that the radial dependence of the scale height can be written as

$$h(r) = h_{100} \times \left( \frac{r}{100 \text{ au}} \right)^\beta, \quad (2.3)$$

where  $h_{100}$  is the scale height at 100 au. To mimic the gap in the disk, we heavily deplete (by a factor of  $10^{-15}$ ) the surface density between the outer radius of the inner disk and the inner radius of the outer disk. To ensure a smooth transition from the gap to the outer disk, we considered an outer disk radius of 60 au, inwards of which we multiplied the surface density with a Gaussian profile parametrized by a standard deviation of 8 au. The surface density of the inner disk is multiplied with a depletion factor  $\delta_{\text{disk}}$  with respect to that of the outer disk. The general shape of the surface density is plotted in Fig. 2.8 (left panel). We consider two grain-size distributions (small and large grains), whose number density follows a power law as a function of the grain size  $a$  with  $n(a) \propto a^{-3.5}$ . The population of small grains ranges from 0.001 to 0.15  $\mu\text{m}$ , and the large grains from 0.15 to 1000  $\mu\text{m}$  in size. To mimic dust settling in a simplified way, we assign a lower scale height (2 au at a radial distance of 100 au) to the disk of big grains, for both the inner and outer disk

**Table 2.3:** Parameters for our RT model.

Parameter	inner disk	outer disk
$R_{in}$ [au]	0.04	60
$R_{out}$ [au]	[2,4,8,12,16,20]	120
$R_c$ [au]	40	40
$h_{100,small}$ [au]	13	13
$h_{100,big}$ [au]	2	2
$\beta$	1.25	1.25
$\delta_{\text{disk}}$	[0.05,0.1,0.25,1.0]	1
disk inclination $i$ [°]	49.7	49.7
disk pos. angle $PA$ [°]	158.6	158.6

**Notes.** Parameters for our model.  $R_{in}$  and  $R_{out}$  denote the inner and outer radius of the inner disk, whereas  $R_c$  is the characteristic radius (truncation radius of exponential cutoff).  $\delta_{\text{disk}}$  corresponds to the depletion factor applied to the surface density of the inner and outer disk.  $h_{100}$  quantifies the scale height of small and big grains at 100 au, and  $\beta$  the flaring index, respectively.

## 2 Discovery of a planetary-mass companion within the gap of the transition disk around PDS 70

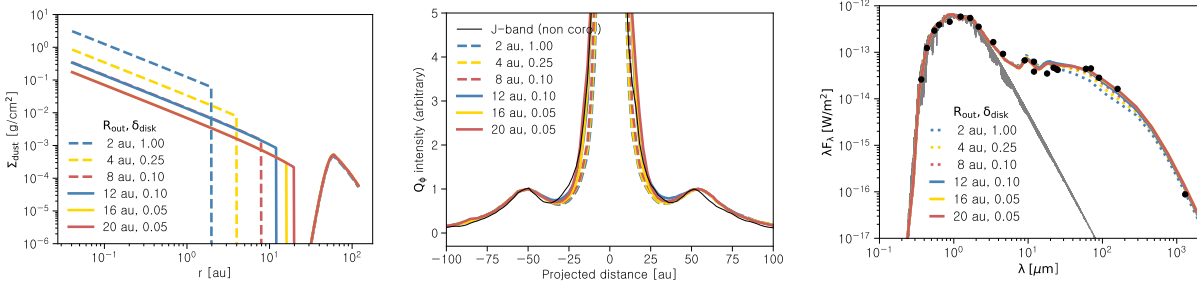


**Figure 2.8:** *Left:* Surface density of our model for the small grains using different outer radii and depletion factors for the inner disk. *Middle:* Cuts along the semi-major axis of model  $Q_\phi$  images for different extents and depletion factors of the inner disk, in comparison with the observations (black line). *Right:* Comparison of photometric measurements of PDS 70 (black points), and the synthetic spectra (coloured lines). The photometry was taken from Gregorio-Hetem et al. (1992), Cutri et al. (2003), and Hashimoto et al. (2012). Due to the low optical extinction toward PDS 70 (Pecaut & Mamajek, 2016), no dereddening was applied to the optical and 2MASS photometric data. The grey line corresponds to the stellar model spectrum (K7 type) that we used for our RT calculations.

parts. The relative mass fraction of small to large grains is 1/31. We determine the optical properties for spherical, compact dust grains according to the Mie theory using the BH-MIE code (Bohren & Huffman, 1983). A total dust mass of  $3.0 \times 10^{-5} M_\odot$  was used. The dust mixture is composed of 70% astronomical silicates (Draine, 2003b), and 30% amorphous carbon grains (Zubko et al., 1996). The opacity mixture was generated according to the Bruggeman mixing rule. The scattering mode in RADMC-3D was set to anisotropic scattering with full treatment of polarization. We computed the Stokes  $Q$  and  $U$  frames, as well as images in total intensity at the wavelengths of interest ( $0.7 \mu\text{m}$  and  $1.25 \mu\text{m}$ ), and convolved our images with the total intensity frames obtained during the corresponding observations. We then computed the  $Q_\phi$  and  $U_\phi$  frames according to Eq. 1.13 as well as a synthetic SED. Table 2.3 summarises the parameters used for our model.

### 2.5.2 Modelling the inner disk

We test different models containing an inner disk and compare the butterfly pattern in the model with the observations. For this purpose, we consider models with different inner disk configurations in terms of two free parameters: outer radius  $R_{\text{out}}$  of the inner disk, and depletion factor  $\delta_{\text{disk}}$  of the surface density of the inner disk. We compare cuts through the convolved  $Q_\phi$  model images along the semi-major axis with the non-coronagraphic observations (without subtracting the central source polarization; see Fig. 2.8 middle panel). The depletion factor was varied between 0.05 and 1.0, and the inner disk outer radius between 2 au (corresponding to the completely unresolved case) and 20 au, by keeping the total dust mass constant. For each radius value, we identified the

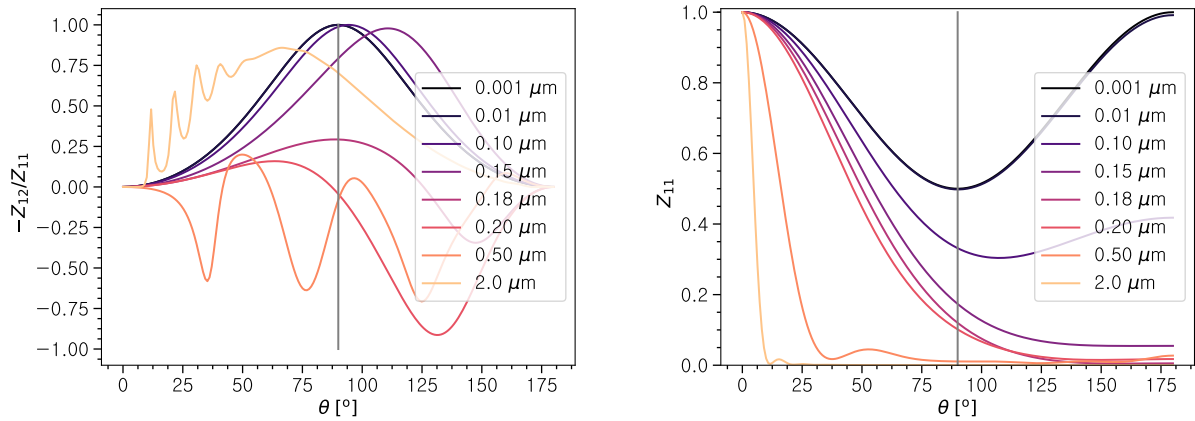


**Figure 2.9:** Linear polarization degrees for silicates of different (semi-mono dispersive) grain sizes (left), and their phase function (right, normalised to  $Z_{11}(0)$ ). The curves were computed for an observing wavelength of  $0.7 \mu\text{m}$ .

best matching depletion factor. Our modelling appears to be degenerate since we could obtain, for both small and large radii values, model images reproducing reasonably well the observations. The range of solutions includes configurations with a small inner disk with a high surface density, as well as those with a larger inner disk with lower surface density. In any case, the inferred surface density outside 20 au in all configurations is very low, indicating that only a small amount of material is left at the location of the companion ( $\sim 22$  au, see Sect. 2.6).

### 2.5.3 Discussion of brightness asymmetries in the disk

In Sect. 2.4.1, we discussed the outer disk asymmetries and found that the east side is brightest in polarized light but is marginally detected in total intensity. Furthermore, along the north-south axis, the brightness maxima differ between the optical and NIR images taken a year apart.

The observed asymmetries between the east and west side might be connected to the scattering properties of the dust. The polarized intensity is the product of the degree of polarization and total intensity. The phase function of both depends on particle size and observing wavelength. In Fig. 2.9, (left) we plot the linear polarization degree expressed by the Mueller matrix elements ( $-Z_{12}/Z_{11}$ ) as a function of scattering angle. For this test, we computed the scattering matrix using Mie theory for different grain sizes. To smooth out the resonances in the phase function appearing when considering perfect spheres of a single size, instead of using a mono-dispersive grain size distribution, we generated for each grain size a narrow Gaussian distribution centred around the considered grain size

## 2 Discovery of a planetary-mass companion within the gap of the transition disk around PDS 70

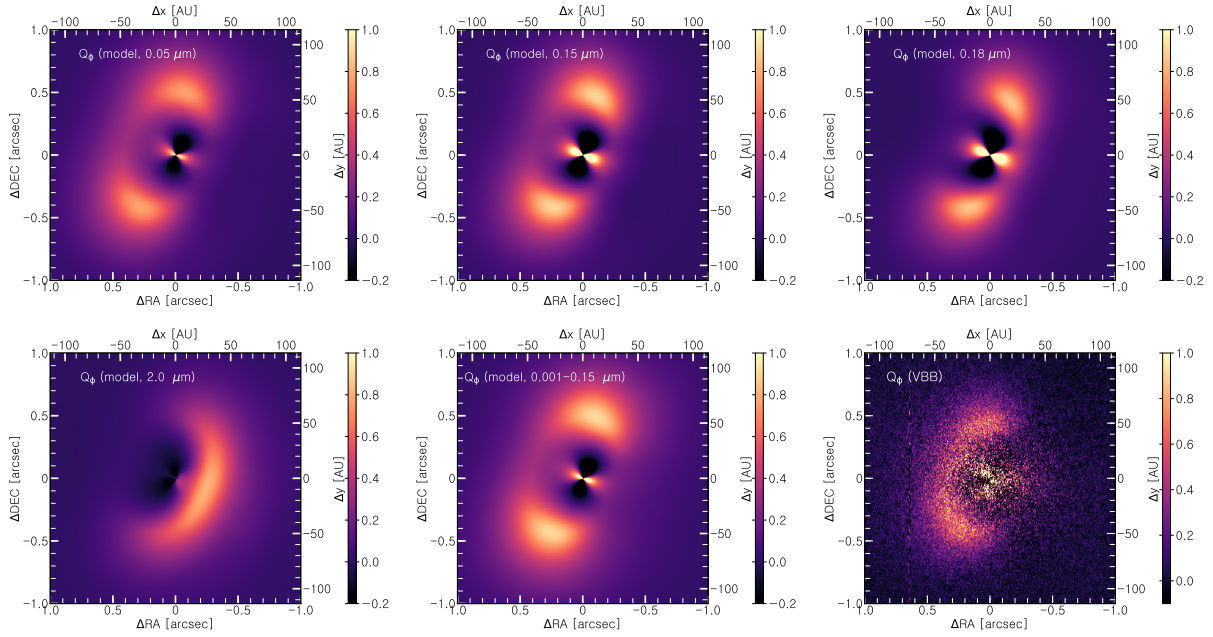


**Figure 2.10:** Convolved ray-traced  $Q_\phi$ -images evaluated at  $0.7 \mu\text{m}$  using different grain size distributions. Successively, the central source polarization emerging from the unresolved inner disk (radius 2 au) was subtracted using a  $U_\phi$ -minimisation. The lower-right panel shows the VBB observation for comparison. North is up and east is to the left.

and with a FWHM of 10% of the grain size. The scattering matrix was evaluated at  $0.7 \mu\text{m}$  which corresponds approximately to the central wavelength of the VBB filter. The plot shows that for very small grains ( $0.001\text{-}0.01 \mu\text{m}$ ), the polarization degree is symmetric around  $90^\circ$ . For larger grains, the polarization degree has several minima, until at grain sizes much larger than the observing wavelength ( $\gtrsim 2 \mu\text{m}$ ), the maximum of the polarization degree is shifted towards angles smaller than  $90^\circ$ . The right panel of Fig. 2.9 shows the scattering phase function, expressed by the Mueller matrix element  $Z_{11}$ . It can be seen that particles smaller than  $\lesssim 0.1 \mu\text{m}$  scatter symmetrically around  $90^\circ$ . Above that value, the phase function becomes asymmetric and forward scattering is increasingly pronounced. The observed polarized intensity is now an interplay between the polarization degree and total intensity, and the disk's geometry. Due to the disk's flared geometry, the scattering angles at the far side are closer to values of  $90^\circ$  than at the near side (the scattering angles are symmetric around  $\theta = 90^\circ - \psi - i$  and  $\theta = 90^\circ - \psi + i$  on the near and far sides, respectively, when  $i$  denotes the inclination and  $\psi$  the opening angle of the disk, see [Min et al., 2012](#)). For smaller grains that are in the Rayleigh scattering regime and therefore not strongly forward scattering, this could therefore make the far side appear brighter than the near side (e.g. [Murakawa, 2010](#); [Min et al., 2012](#)). On the other hand, the larger the grains that are considered, the more forward scattering they are, and the more the polarized intensity is dominated by the phase function of the total intensity. The near side then

becomes the brighter side, the same in total intensity as in polarized intensity.

To test this hypothesis, we computed ray-traced  $Q_\phi$  images at  $0.7 \mu\text{m}$  using different grain sizes. We subtracted the central source polarization after convolving the Stokes  $Q$  and  $U$  images from the  $Q_\phi$  frame using a  $U_\phi$  minimisation. In this procedure, scaled versions of the total intensity  $I$  frame are subtracted from the Stokes  $Q$  and  $U$  model images, such that the absolute value of  $U$  in a defined region is minimised. Figure 2.10 compares the resulting images. As expected, the disk model with larger grains ( $\geq 0.18 \mu\text{m}$ ) shows strong forward scattering even in polarized light, whereas for the disk containing small grains, the far side appears brighter. As a mono-dispersive grain size distribution would be unrealistic, we also tested a grain size distribution of small grains ( $0.001\text{-}0.15 \mu\text{m}$ ), and still find that the far side appears brighter than the near side (Fig. 2.10, lower middle panel). We conclude that if the brightness asymmetry between the east and west sides is real, and not dominated by effects from poor seeing conditions and reduction artifacts, we need predominantly small sub-micron-sized grains ( $\lesssim 0.15 \mu\text{m}$ ) to reproduce the observations in a qualitative way. Although we are able to reproduce the qualitative behaviour of the brightness asymmetries, we are not able to reproduce contrast ratios as large as in the observations between the two sides. Furthermore, our brightness contrast is very similar in the VBB-band and J-band (contrary to the observations).

In total intensity, on the other hand, the near side is always expected to be brighter than the far side, as even in the Rayleigh scattering regime (where the scattering phase function is symmetric around a minimum at  $90^\circ$  and where grains are not forward scattering), the scattering angles at the near side are farther from  $90^\circ$  than at the far side, corresponding to a higher scattering efficiency.

We note that our model is based on Mie scattering. It is certainly worth testing the impact of particles that are not spherical and homogeneous, or that are of a somewhat different chemical composition; for example including water ice mantles that are neglected in our modelling approach. However, this is beyond the scope of this study.

Summarising, by retaining only small ( $\lesssim 0.15 \mu\text{m}$ ) grains in the disk surface layer, we are able to reproduce the brightness contrasts between the east and west sides in a qualitative (although not quantitative) way. The existence of the north/south brightness asymmetry and its different behaviour in the VBB- and J-band on the other hand cannot be explained solely with grain scattering properties, as the scattering angles are expected to be symmetric with respect to the semi-minor axis. One could speculate that the grain properties are different in the north and south region, but more complex modelling would be needed to explain this behaviour.

It should be mentioned that the strong butterfly patterns detected in  $Q_\phi$  and  $U_\phi$  after correcting for instrumental polarization effects affect the outer disk. In the  $Q_\phi$  image, this adds positive signal along the disk semi-major axis, and subtracts signal along the

semi-minor axis. The subtraction of this central component is likely imperfect and some residuals may be present in the images of the outer disk in Fig. 5.1. In addition, all our polarimetric observations suffered from rather poor seeing conditions, which might further influence the apparent brightness distribution in the disk. Therefore, we cannot rule out that artifacts from the data reduction and/or weather conditions affect the azimuthal brightness distribution of the polarimetric datasets.

## 2.6 Detection of a planetary mass companion

In the two SHINE IRDIS epochs, we identified a point source at a separation of about 195 mas and a position angle of about  $155^\circ$  from PDS 70. Upon analysis of the IRDIS K12 Open Time data, as well as of the NaCo data, the point source was detected around the same location as in the IRDIS data. In addition, we reanalysed archival data taken with Gemini/NICI in  $L'$  band on March 31, 2012, published by Hashimoto et al. (2012). The authors reported a non-detection of companion candidates (apart from the previously mentioned background source to the north), but their analysis considered only regions outside of  $\sim 200$  mas. Upon our re-reduction of this dataset, we detected the point source around the expected location. The final detection images obtained with sPCA are shown in Fig. 2.11. As a comparison, the corresponding images retrieved using ANDROMEDA, PCA-SpeCal, and TLOCI are presented in Fig. A.1. We detected the point source in all our available ADI epochs, spanning a total time range of four years.

We also noted another structure present in some of the PCA and TLOCI processed images, located at a similar separation and a PA of about  $280^\circ$ . To check the point-like nature of this structure, we processed the data with the ANDROMEDA algorithm, which is op-

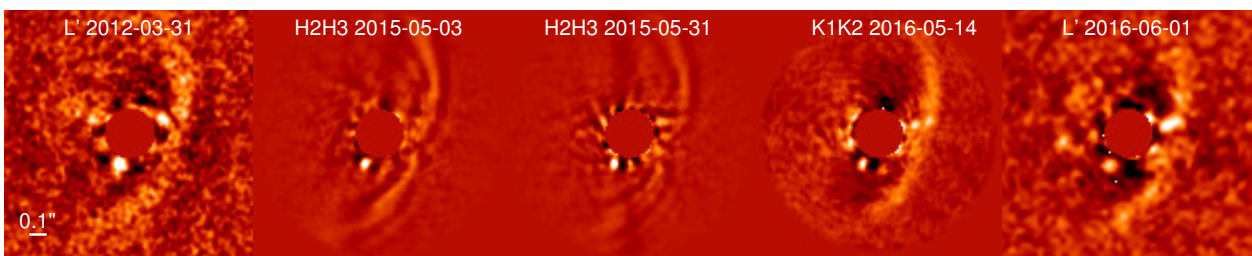


**Figure 2.11:** Images of the point source detection as retrieved with the sPCA reduction (from left to right): NICI  $L'$ -band (2012-03-31), IRDIS H2H3-band (2015-05-03), IRDIS H2H3-band (2015-05-31), IRDIS K1K2-band (2016-05-14), NaCo  $L'$ -band (2016-06-01). North is up and east is to the left. The images were smoothed with a Gaussian kernel of size  $0.5 \times \text{FWHM}$ .

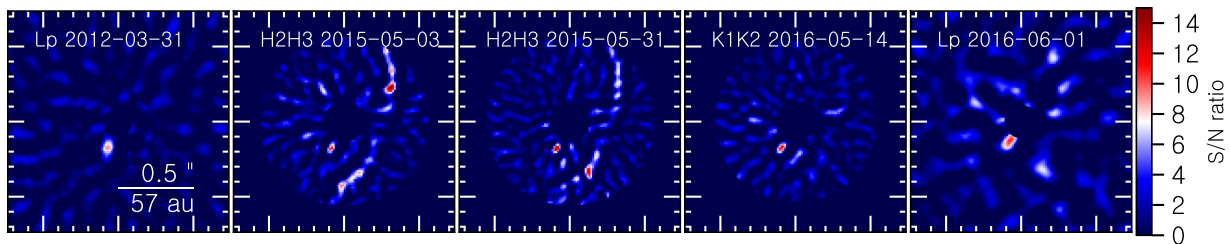


**Figure 2.12:** ANDROMEDA S/N maps of the five ADI epochs.

timised for the retrieval of point sources (Cantalloube et al., 2015). Figure 2.12 shows the corresponding S/N maps, which are a result of forward modelling under the assumption of the presence of a point-like source. It can be seen that this structure is not consistently recovered by ANDROMEDA in the different epochs at significant S/N. Especially towards longer wavelengths, no other source apart from the above-described source at about  $155^\circ$  is detected with any significance. This implies that the structure found at about  $280^\circ$  is not point-like and, if physical, we can associate this structure with a disk feature. The latter interpretation is supported by the projected proximity to the outer disk ring.

### 2.6.1 Astrometry

For the characterization of the point source we extracted the astrometry and the photometry for all epochs. We detected it with all algorithms (sPCA, ANDROMEDA, PCA-SpeCal and TLOCI), and in the following focus on the analysis of the sPCA reduction. In this sPCA reduction, we divided the image in concentric annuli with a width of  $1 \times \text{FWHM}$ . For each annulus we adjusted the number of modes in such a way that the protection angle was maximised. A maximum number of 20 modes was applied and we set the maximum protection angle to  $0.75 \times \text{FWHM}$ . We extracted the astrometry and photometry by injection of a PSF taken from the unsaturated frames out of the coronagraph with negative flux, as proposed by Lagrange et al. (2010). Our approach to find the location and flux of the point source consisted of varying the parameters of this negative signal using a predefined grid to minimise the residuals in the resulting sPCA-processed data set. We therefore computed for each parameter set of position and flux the  $\chi^2$  value within a segment having a radial and azimuthal extension of  $2 \times \text{FWHM}$  and  $4 \times \text{FWHM}$  around the point source, respectively. To derive uncertainties in the astrometric and photometric values, posterior probability distributions for each parameter were computed following the method described by Olofsson et al. (2016). The astrometric uncertainties related to the calibration error take into account the centring accuracy of the stellar position (frame registering was done using the satellite spots for the IRDIS data and fitting a 2D Gaussian to the star in the case of the non-coronagraphic NaCo and NICI data), the detector anamor-

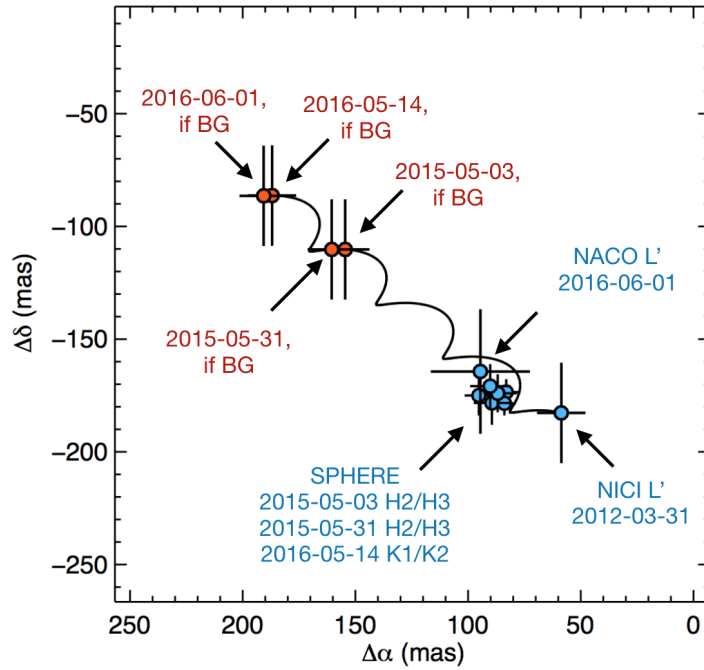


**Figure 2.13:** Relative astrometry of the companion. The blue points show the measurements, and the red ones, labelled ‘BG’, the relative position that should have been measured in case the CC detected in the first epoch (NICI) was a stationary background star.

phism ( $0.6 \pm 0.02\%$  in the case of IRDIS, Maire et al., 2016b), the True North orientation of the images and the uncertainties related to the rotator offset and the pixel scale. The corresponding values are reported in Tab. 2.6.1. We derived the final astrometric uncertainties at each epoch by quadratically summing the errors from these individual contributions. Our astrometric measurements obtained at the different epochs are presented in Table 2.5. As a cross-check, the results of the ANDROMEDA, PCA-SpeCal, and TLOCI reductions are listed in Table A.1.

To test whether the point source is part of a physical system with PDS 70, we compared its measured position relative to the star at the different epochs. Due to the proper motion ( $\mu_\alpha \cos \delta = -29.7$  mas/yr,  $\mu_\delta = -23.8$  mas/yr, Gaia Collaboration et al., 2016, 2018), a stationary background star would have moved by  $\sim 160$  mas within the given timespan. As the relative motion ( $\sim 40$  mas during the  $\sim 4$  years observational time span) differs significantly from the prediction for a stationary background object, the astrometric results strongly imply that the point source is comoving with PDS 70. The measurements, together with the expected trajectory for a background star relative to PDS 70, are displayed in Fig. 2.13. Further, the probability of detecting at least one background contaminant of similar brightness or brighter within the mean separation of the companion is less than  $0.033\%$  according to the Besançon galactic population model (Robin et al., 2003).

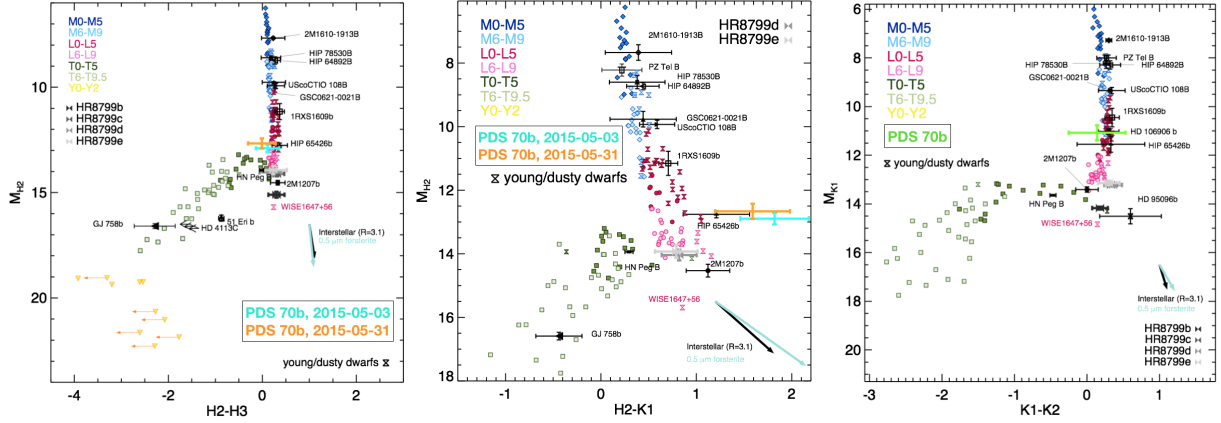


**Figure 2.14:** Colour-magnitude diagrams considering the SPHERE H2-H3 (*left*), H2-K1 (*centre*), and K1-K2 (*right*) colours, comparing PDS 70b with the photometry of M, L, and T field dwarfs, young companions and red dwarfs. The diagrams are overlaid with reddening vectors from interstellar extinction and  $0.5 \mu\text{m}$  fosterite grains. See Chauvin et al. (2018) and Bonnefoy et al. (2018) for details about the CMDs.

The relative position as measured in the NICI data taken in 2012 does not coincide with the positions derived from the SPHERE and NaCo observations performed in 2015 and 2016 within the  $1\text{-}\sigma$  uncertainties. This difference in measured position between the epochs is possibly due to orbital motion. The point source is detected at a mean projected separation of  $\sim 195$  mas, corresponding to  $\sim 22$  au. The orbital period of such a bound object, assuming a stellar mass of  $0.76 M_{\odot}$ , would be  $\sim 119$  years. For a face-on circular orbit, this implies a displacement of  $\sim 3^{\circ}$  per year, resulting in a total change of position angle of  $12.5^{\circ}$  within the time covered by our observations, which is in good agreement with the observations. Further, the observed change in position angle is in clockwise direction, which corresponds to the sense of rotation of the disk (Hashimoto et al., 2015). Therefore, this displacement is consistent with an object on a circular face-on orbit rotating in the same sense as the disk. However, regarding the relatively large uncertainties on the astrometry and the short time span covered by our data, detailed orbital fitting exploring the possibility of an inclined and/or eccentric orbit will be performed in a follow-up study on this source (Müller et al., 2018). Although the possibility of the point source being a background star with almost the same proper motion as PDS 70 is very small, only the detection of orbital motion over a significant part of the orbit will allow to fully exclude the background star scenario.

## 2.6.2 Photometry

Our current information on the physical properties of the companion candidate relies on the H, K, and  $L'$  photometry as derived from our SPHERE/IRDIS, NaCo, and NICI images.

It is marginally detected in the IFS data, when the channels corresponding to J-band and H-band are collapsed. Due to the large uncertainties, this data is not considered here. The low S/N detection of the companion candidate in the IFS data can be explained by its faintness and red colours, the larger IFS thermal background (IFS is not cooled contrary to IRDIS), and the smaller IFS pixel scale (7.46 mas/pixel vs  $\sim 12.25$  mas/pixel). HD 95086 b offers a similar case of a faint companion with red colours for which a detection with IRDIS is achieved in the K-band in individual observation sequences whereas the detection with IFS in the J- and H-bands required the combination of several epochs (Chauvin et al., 2018).

The companion has very red colours, with a magnitude difference of  $H2-K1=1.82\pm 0.36$  mag and  $1.59\pm 0.39$  mag, considering the first and second SHINE H-band epochs, respectively. Accordingly, we measured a magnitude difference of  $H2-L' = 3.67\pm 0.46$  mag and  $3.44\pm 0.48$  mag (considering the NICI L'-band photometry). The properties of the companion are further discussed in Sect. 2.6.4.

### 2.6.3 The nature of the point-like source

Due to the detection of the point source at multiple epochs and using several different instruments, filter bands, and image post-processing algorithms at about the same location, we can exclude that the source is due to an instrumental or atmospheric artifact (speckle). Furthermore, the discrepancy of the relative position of the point source with respect to the predicted trajectory of a stationary background star strongly implies a gravitationally bound object. Several of the proposed companion candidates within protoplanetary disks are currently under debate, because they are not detected consistently at all available wavelengths. A reason for possible confusion is that the ADI process acts as a spatial frequency filter and enhances sharp and asymmetric disk features; as shown by Milli et al. (2012), applied on extended disk structures, it can cause distortions or even create artifacts that are not related to physical structures. Disk structures such as rings, spiral arms, or clumps, when processed with ADI, could therefore lead to a misinterpretation of point-like sources. As discussed in Sect. 1.5, only a handful of protoplanet candidates have been reported in the literature, and most of them are still under debate. All these debates illustrate that a careful analysis of companion candidates located in protoplanetary disks with respect to a possible link to disk features is required. We therefore address the hypothesis that some asymmetric dust structure at or close to the given location of the point source is responsible for our detection. As stated above, we are not able to resolve the detailed structure of the inner disk with our PDI observations, but suspect the inner disk to be smaller than 17 au in radius. To test the impact of the inner disk signal on the structures seen in ADI, we follow the approach by Ligi et al. (2018), and simulate a cADI observation using the IRDIS PDI J-band  $Q_\phi$ -images, after subtracting the central source polarization.

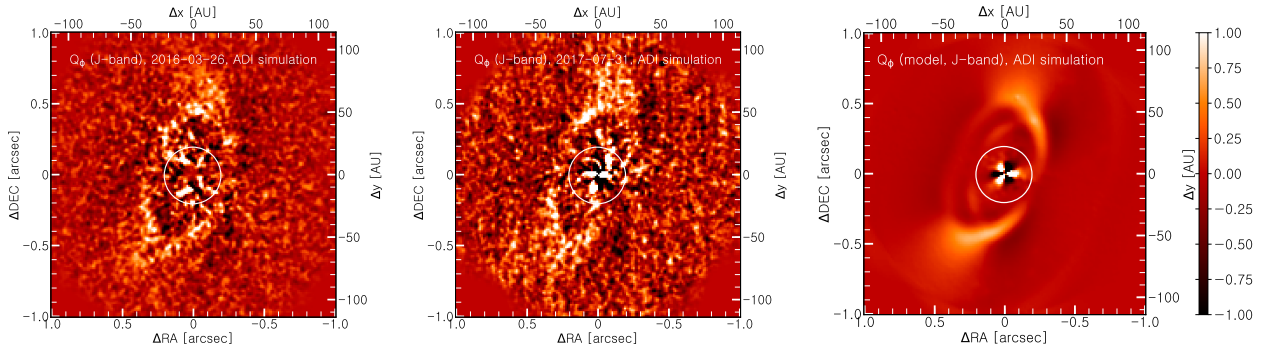


**Figure 2.15:** cADI simulation for the  $Q_\phi$  images of the coronagraphic (left) and non-coronagraphic (middle) J-band observations, after subtracting the central source polarization. The right panel shows the same simulation for our model image. This image was generated by convolving the Stokes  $Q$  and  $U$  images with a real IRDIS J-band PSF, computing the  $Q_\phi$  and  $U_\phi$  images, subtracting the central source polarization by applying a  $U_\phi$  minimisation, and finally applying the cADI algorithm. The model included the presence of an inner disk with an outer radius of 2 au. The white circle marks a radial distance of 200 mas, approximately the separation of the companion. The colour stretch was adapted individually for visibility purposes. North is up and east is to the left.

For this purpose, we created a datacube whose 50 frames correspond to identical copies of the PDI  $Q_\phi$  image, rotated by the respective parallactic angles encountered during the ADI epoch of May 31, 2015. We then subtracted the median of this datacube from each single frame, before de-rotating them and computing their median.

In addition, we applied the same procedure to the  $Q_\phi$  model image, computed at  $1.25 \mu\text{m}$ . We convolved our image with the total intensity frame acquired during the non-coronagraphic J-band observations and subtracted the central source polarization using a  $U_\phi$ -minimisation before applying the cADI algorithm. The inner disk in the model configuration used for this test extends out to 2 au. The result is shown in Fig. 2.15. There is no prominent structure appearing at the distance of interest ( $\sim 200$  mas). While this test does not allow us to completely rule out a disk structure as the cause of this feature, there is at least no obvious polarized inner disk structure that would create this kind of artifact. One further argument against the hypothesis of the companion being a disk feature is the fact that we do not detect strong polarized signal at the location of the companion in the PDI data, which would be consistent with the signal detected in ADI being of thermal origin. We therefore conclude that, given the present data, a physically bound companion is the most plausible explanation for the detected point source, and refer to it as PDS 70b hereafter.

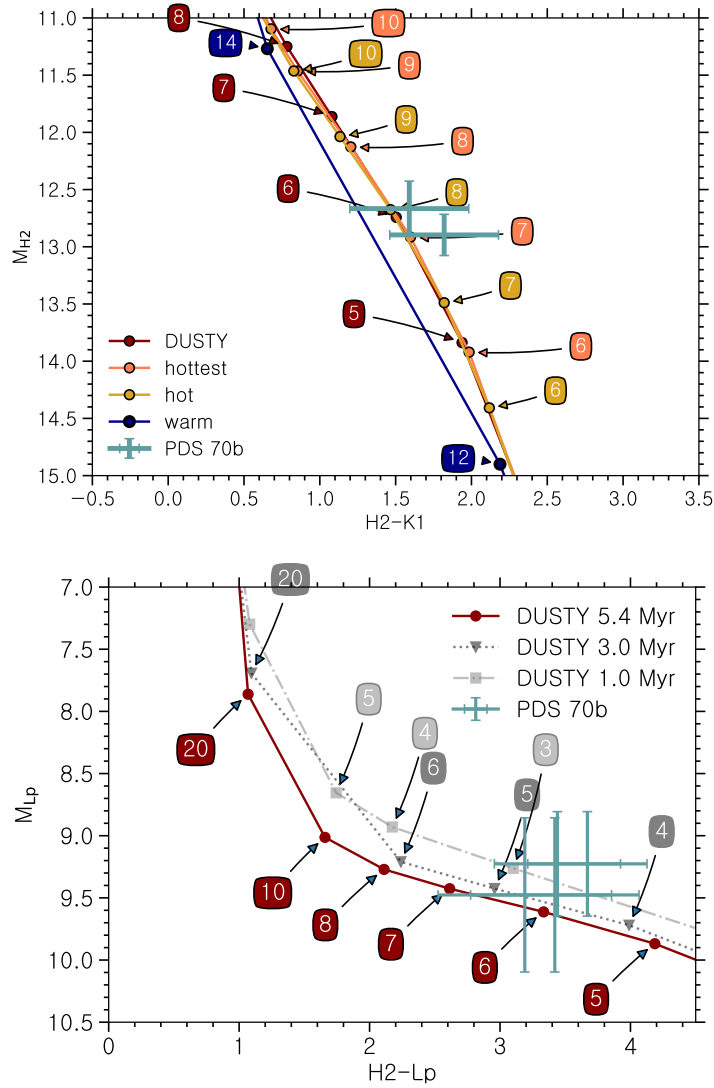


**Figure 2.16:** Photometry of PDS 70b in comparison with evolutionary models, evaluated at an age of 5.4 Myr. The green crosses mark the measurements corresponding to the different H2 and L' epochs. The upper panel shows the 'hottest', 'hot', and 'warm' models from Mordasini et al. (2017), as well as the DUSTY model in a H2 vs. H2-K1 diagram. The lower panel compares the L' vs. H2-L' colour of the DUSTY model with the measured photometry. The corresponding masses in units of  $M_{Jup}$  are indicated on the coloured labels.

### 2.6.4 Companion properties

Figure 2.14 shows the location of PDS 70b in SPHERE H-band and K-band-based colour-magnitude diagrams (CMD). The diagrams are complemented with the synthetic photometry of M, L, and T dwarfs, as well as with the measurements of young companions and red dwarfs of the Sco-Cen association and other regions. We refer the reader to Chauvin et al. (2018) and Bonnefoy et al. (2018) for details regarding these diagrams. The diagrams

show that the absolute H2 magnitude of the companion is consistent with those of L-type dwarfs. PDS 70b is located between the  $\sim 5$ -11 Myr-old,  $\sim 8$ -14  $M_{\text{Jup}}$  planet 1RXS1609b (Lafrenière et al., 2008, 2010; Lachapelle et al., 2015) and the 30 Myr-old  $\sim 7 M_{\text{Jup}}$  planets HR 8799 c,d,e (see Bonnefoy et al., 2016). The location of PDS 70b in the H2-H3 CMD is remarkably close to the recently discovered dusty giant planet HIP 65426b (Chauvin et al., 2017a). Indeed, HIP 65426b’s mass (6-12  $M_{\text{Jup}}$ ) derived from evolutionary models is similar to the one of PDS 70 b (see below), although significantly older ( $14 \pm 4$  Myr, Chauvin et al., 2017a). In addition, the K1-K2 diagram reveals a similar photometry to the  $11 \pm 2 M_{\text{Jup}}$  massive and  $13 \pm 2$  Myr old companion HD 106906b (Bailey et al., 2014).

The colours of PDS 70b are very red. Its H2-K1 colour is redder than most L dwarfs in the field, and is consistent with the very red companions to CD-35 2722 (Wahhaj et al., 2011) and 2M1207 (Chauvin et al., 2004), as well as with HIP 65426 (Chauvin et al., 2017a) within the uncertainties. If due to a photosphere, the red colour is only compatible with an L-type object or with a reddened background object, but this latter possibility is very unlikely due to the proper motion test. The absolute L’-band magnitude is brighter than most of the detected companions and consistent with those of late M- to early L-type objects, but again significantly redder than these sources. The H2-L’ colour is as red as the  $> 50$  Myr-old, very dusty companion to HD 206893 ( $H2-L’ = 3.36 \pm 0.18$  mag), which is one of the reddest brown dwarf companions known (Milli et al., 2017; Delorme et al., 2017). Therefore, the location of PDS 70b on the colour-magnitude diagrams is quite unusual. However, it should be kept in mind that only very few of these objects are of similarly young age as PDS 70, and none of the above objects are detected within the transition disk of its host. PDS 70b might therefore be the only of these objects that is directly observed during its formation process.

In order to estimate the mass of the companion, we compared the photometry of PDS 70b to the Bern Exoplanet (BEX) evolution models. These tracks are obtained from the synthetic planetary populations of Mordasini et al. (2017), which predict the post-formation planetary luminosity as a function of time, considering different efficiencies of the accretional heating during the formation process and including the effect of deuterium burning. The planets formed in the planetary population synthesis are classified in four different populations (‘hottest’, ‘hot’, ‘warm’ ‘coldest’), according to their luminosity as a function of mass at the moment when the disk disappears (see Mordasini et al. 2017 for details). The planets according to the ‘hottest’ and ‘coldest’ populations have the highest and lowest luminosities, and correspond to the traditional hot- and cold start models (e.g. Marley et al., 2007; Chabrier et al., 2000; Baraffe et al., 2003). They describe the two extreme cases where the entire gas accretion shock luminosity is either deposited in the planet’s interior, or radiated away during the formation process. These two populations are superseded by the more realistic cases of the ‘hot’ and ‘warm’ populations, which are representative for

cases with intermediate initial entropies between the extreme ‘hot’ and ‘cold’ start models. For our comparison we made use of the ‘hottest’, ‘hot’, and ‘warm’ populations, but discarded the ‘coldest’ population. For this scenario, a planet mass larger than  $10 M_{\text{Jup}}$  would be required to reproduce the observed magnitudes of PDS 70b. However, to be classified into the ‘coldest’ population requires small core masses which do not develop into planets with such high masses in the planetary population synthesis models (see [Mordasini et al., 2017](#), Fig. 13). In addition, observations suggest that the pure cold start formation is in reality not the preferred formation mechanism and the truth most probably lies somewhere between the two extrema of purely hot and cold start ([Bonnetfoy et al., 2014](#); [Samland et al., 2017](#)). From the theoretical side, recent detailed simulations of the accretion shock suggest that hot starts are preferred (e.g. [Marleau et al., 2017, 2019](#)). To follow the post-formation cooling, the outcome of the population synthesis was combined with the boundary conditions for the atmospheric structure from the COND models ([Baraffe et al., 2003](#)). The synthetic SPHERE magnitudes were then computed using the DUSTY atmospheric model ([Chabrier et al., 2000](#)). These results were linearly interpolated in time to the stellar age (5.4 Myr). Figure 2.16 compares the photometry of PDS 70b with the synthetic colours of the ‘hottest’, ‘hot’, and ‘warm’ tracks from [Mordasini et al. \(2017\)](#), as well as with the original DUSTY model of [Chabrier et al. \(2000\)](#). We find a mass between 5 and  $9 M_{\text{Jup}}$  for the hot start models (‘hottest’, ‘hot’, ‘DUSTY’), and a mass between 12 and  $14 M_{\text{Jup}}$  for the coldest (‘warm’) population considered, implying that in the case of lowest entropy, deuterium burning might play a role. It is important to note that the evolutionary tracks do not take into account the time needed for the planet to form. Since this may take up to several million years, the stellar age is only an upper limit on the age of the planet, and consequently, the estimated masses should be considered as conservative upper limits.

For completeness, Fig. 2.16 (lower panel) shows the H2-L’ colour of PDS 70b in comparison with the DUSTY tracks, which implies a similar mass estimate ( $5\text{-}8 M_{\text{Jup}}$ )<sup>9</sup>. We also plotted the evolutionary tracks corresponding to a planetary age of 1 and 3 Myr to illustrate the mass range in which the planet would be found in the case that it has formed considerably more recently than the star (down to  $2\text{-}4 M_{\text{Jup}}$  for a planetary age of 1 Myr). We also compared the H-band photometry to the warm-start models from [Spiegel & Burrows \(2012\)](#), as well as the hot-start COND models from [Baraffe et al. \(2003\)](#), resulting in a similar finding ( $5\text{-}10 M_{\text{Jup}}$  for the former, and  $4\text{-}5 M_{\text{Jup}}$  for the latter). However, the colours from the COND model do not match those observed for PDS 70b since they are significantly redder than predicted by the COND models, which suggests the presence of a dusty or cloudy atmosphere. We emphasise that none of these models considers the

---

<sup>9</sup>We note that the BEX tracks are currently not available for the NaCo magnitudes, and are therefore not considered for the comparison in the L’-H2L’ diagram.

presence of circumplanetary material, which could affect the observed SED and the corresponding mass estimate. The presence of a circumplanetary disk could also cause an IR excess in the object's SED pushing the photometry towards redder colours. Future ALMA observations will allow us to search for the presence of such material around PDS 70b.

Finally, we used the Exoplanet Radiative-convective Equilibrium Model (Exo-REM) to analyse the SED of PDS 70b (Baudino et al., 2015, 2017). We performed a grid search to determine the parameters that best minimise the  $\chi^2$  taking into account all photometric points from the H2 to the L-band (Baudino et al., 2015). All the determined radii were larger than or equal to  $2 R_{\text{Jup}}$ , which is a large value compared to the evolutionary models. Therefore, instead of simply minimising the  $\chi^2$  to find the radius, we determined the minimal radius that gives a spectrum similar to the observation at 1, 3, and 5- $\sigma$  (when applicable). We obtained at 5- $\sigma$  a radius  $> 1.3 R_{\text{Jup}}$ , a surface gravity of  $\log_{10}(g) = 3.9 \pm 0.9$  dex, and a temperature of  $T_{\text{eff}} = 1200 \pm 200\text{K}$ . Our grid takes into account solar metallicity and high cloud absorption, suggested by the fact that the object is redder than usual on the CMD. We note that the photometry is also in good agreement with a simple blackbody with a temperature range between 1150 and 1350 K, further indicating a very dusty or cloudy atmosphere with few spectral features. Also in the blackbody case, large effective radii of several  $R_{\text{Jup}}$  are needed to fit the absolute flux density, which, again, may be explained by the possible existence of spatially unresolved circumplanetary material contributing to the measured flux. Our atmospheric models are in this respect oversimplified and the possible presence of circumplanetary material would require substantial modifications of the underlying models, which is beyond the scope of this work.

**Table 2.4:** Astrometric calibrations used for the ADI datasets.

Date	Instrument	Filter	True North correction angle [°]	Rotator offset position [°]	Pixel scale [mas/px]
2012-03-31	NICI	I'	0.0 ± 0.1 <sup>(b)</sup>	180.0 ± 0.1 <sup>(f)</sup>	17.95 ± 0.01 <sup>(d)</sup>
2015-05-03	IRDIS	H2	-1.700 ± 0.076 <sup>(a)</sup>	-135.99 ± 0.11	12.255 ± 0.021 <sup>(a)</sup>
2015-05-03	IRDIS	H3	-1.700 ± 0.076 <sup>(a)</sup>	-135.99 ± 0.11	12.250 ± 0.021 <sup>(a)</sup>
2015-05-31	IRDIS	H2	-1.700 ± 0.076 <sup>(a)</sup>	-135.99 ± 0.11	12.255 ± 0.021 <sup>(a)</sup>
2015-05-31	IRDIS	H3	-1.700 ± 0.076 <sup>(a)</sup>	-135.99 ± 0.11	12.250 ± 0.021 <sup>(a)</sup>
2016-05-14	IRDIS	K1	-1.675 ± 0.080 <sup>(a)</sup>	-135.99 ± 0.11	12.243 ± 0.021 <sup>(a)</sup>
2016-05-14	IRDIS	K2	-1.675 ± 0.080 <sup>(a)</sup>	-135.99 ± 0.11	12.238 ± 0.021 <sup>(a)</sup>
2016-06-01	NaCo	I'	0.518 ± 0.120 <sup>(e)</sup>	89.5 ± 0.1 <sup>(c)</sup>	27.195 ± 0.063 <sup>(e)</sup>

**Notes.** <sup>(a)</sup> Maire et al. (2016b) <sup>(b)</sup> assumed value (no astrometric measurement around the NICI epoch available). <sup>(c)</sup> adopted from Chauvin et al. (2012) <sup>(d)</sup> adopted from Hayward et al. (2014) and Wahhaj et al. (2014) <sup>(e)</sup> Launhardt et al. (2020) <sup>(f)</sup> Cassegrain rotator position angle. There is no information on the uncertainty available; we therefore adopt an uncertainty of 0.1°.

**Table 2.5:** Properties of the point-like source, as derived from the sPCA reduction.

Date	Instr.	Filter	$\Delta$ RA [mas]	$\Delta$ DEC [mas]	Sep[mas]	PA[deg]	$\Delta$ mag	mag <sub>app</sub>	S/N
2012-03-31	NICI	L'	58.7±10.7	-182.7±22.2	191.9±21.4	162.2±3.7	6.59±0.42	14.50±0.42	5.6
2015-05-03	IRDIS	H2	83.1±3.9	-173.5±4.3	192.3±4.2	154.5±1.2	9.35±0.18	18.17±0.18	6.3
2015-05-03	IRDIS	H3	83.9±3.6	-178.5±4.0	197.2±4.0	154.9±1.1	9.24±0.17	18.06±0.17	8.1
2015-05-31	IRDIS	H2	89.4±6.0	-178.3±7.1	199.5±6.9	153.4±1.8	9.12±0.24	17.94±0.24	11.4
2015-05-31	IRDIS	H3	86.9±6.2	-174.0±6.4	194.5±6.3	153.5±1.8	9.13±0.16	17.95±0.17	6.8
2016-05-14	IRDIS	K1	90.2±7.3	-170.8±8.6	193.2±8.3	152.2±2.3	7.81±0.31	16.35±0.31	5.5
2016-05-14	IRDIS	K2	95.2±4.8	-175.0±7.7	199.2±7.1	151.5±1.6	7.67±0.24	16.21±0.24	3.6
2016-06-01	NaCo	L'	94.5±22.0	-164.4±27.6	189.6±26.3	150.6±7.1	6.84±0.62	14.75±0.62	2.7

**Notes.** Astrometry and photometry of the point-like source derived from the sPCA reduction. From left to right: observing epoch, instrument, filter band, offset in right ascension with respect to the star, offset in declination with respect to the star, separation, position angle, magnitude contrast, apparent magnitude, and S/N of the detection.

## 2.7 Summary and conclusions

PDS 70 is a young T-Tauri star hosting a known transition disk with a large gap. Transition disks are thought to host gap-carving planets, and are therefore prime targets to search for forming planets and to characterize their parental disks.

In this work, we have presented VLT/SPHERE optical and NIR observations in polarimetric differential and angular differential imaging mode, carried out with the SPHERE instrument. These observations were complemented with data taken with VLT/NaCo and archival data taken with Gemini/NICI in the  $L'$ -band using angular differential imaging. This Section summarizes the results obtained with the presented data, comprising eight different epochs spanning a time range of five years.

- The disk is clearly detected in all data sets presented in this work and is resolved in scattered light with high angular resolution, confirming the previously reported gap with a size of  $\sim 54$  au.
- For the first time, we detect scattered light from the inner disk. By comparison with a radiative transfer model, we derived that the position angle of the inner disk is approximately the same as the outer disk. We also inferred that the inner disk is not seen pole-on and has a maximum outer radius of  $< 17$  au.
- The disk's far side is brighter than the near side in PDI (VBB-band, J-band), whereas the disk's near side is brighter in ADI (H-band, K-band,  $L'$ -band). This is suggestive for being due to the flared geometry of the disk in connection with Rayleigh scattering from small, sub-micron-sized grains.
- The data revealed a point source at approximately 195 mas separation and a position angle of  $155^\circ$ . The detection is recovered at five different epochs, including the SPHERE/IRDIS, Gemini/NICI and VLT/NaCo instruments in the H, K and  $L'$ -band filter.
- The astrometry of the point source implies that the confusion with a reddened background object is unlikely, and that the object is bound to the star. Due to the astrometric coverage of 4 years, this provides first hints of orbital motion.
- The photometry of the companion shows evidence of very red colours. Comparison with evolutionary models suggests that the photometry is most compatible with a young planetary-mass body with a dusty or cloudy atmosphere, referred to as PDS 70 b.

In this Chapter, we showcased the first unambiguous detection of a young planet in the gap of a transition disk. PDS 70 b is a benchmark object for a so far unexplored population of young planets still embedded in their natal disks, and thus provides an excellent laboratory to test various models related to the formation and early evolution of planetary systems.

## 2.8 Follow-up studies

Following the discovery of PDS 70 b, several follow-up observations have been performed under the leadership of other teams with the aim to confirm the detection and characterize the properties of the planet. This Section provides a summary of the most recent findings that have been reported within the literature as they will be relevant for the subsequent Chapters of this Thesis. Among the below discussed papers, I have contributed as a co-author to Müller et al. (2018), Wagner et al. (2018) and Mesa et al. (2019).

### 2.8.1 Confirmation and first orbital and atmospheric characterization of PDS 70 b

The SPHERE consortium obtained a new epoch with SPHERE/IRDIS in K1K2 dual-band imaging mode within the GTO time on February 24, 2018. The observations were carried out under excellent weather conditions and lead to a clear confirmation of PDS 70 b. These data were published simultaneously with the discovery paper (Keppler et al., 2018) in a follow-up study by Müller et al. (2018). In addition to the confirmation of PDS 70 b, the now extended time baseline of 6 years allowed to explore possible orbital solutions for the planet. This analysis showed to favour a circular,  $\sim 22$  au wide orbit coplanar with the outer disk. This work also presented the first SPHERE/IFS spectrum of PDS 70 b, allowing to establish the SED of the planet from 0.96 to 3.8  $\mu\text{m}$ . Comparison to atmospheric models revealed that the atmosphere is likely cloudy or dusty. The models inferred a temperature range between 1000 and 1600 K, as well as a mass range of 2 to 17  $M_{\text{Jup}}$ , compatible with the mass range derived in Sect. 2.6. The reader is referred to Müller et al. (2018) for further details of this study.

### 2.8.2 A young multiplanetary system at the stage of formation

With the confirmed detection of a young planetary-mass companion, the final proof of PDS 70 b still being *in formation* yet needs to be provided, i.e., by searching for signatures of the accretion process itself. According to theoretical models, the shock-heated infalling accretion flow onto the protoplanet and its circumplanetary disk can reach temperatures

of  $10^4$  K, releasing radiation at the H I recombination lines, such as H $\alpha$  at 656.28 nm (e.g., Szulágyi & Mordasini, 2017; Marleau et al., 2017; Aoyama et al., 2018). Such an emission can be searched for using high-contrast imaging instruments operating in the visible domain (e.g., Close et al., 2014; Cugno et al., 2019; Musso Barucci et al., 2019).

Follow-up observations of PDS 70 with the Magellan Adaptive Optics (MagAO; Close et al., 2012; Morzinski et al., 2016) instrument have revealed a marginal detection of H $\alpha$  emission at the location of PDS70 b (Wagner et al., 2018). Interpreting the signal as being due to the accretion of gas, it infers an accretion rate of  $10^{-8\pm 1} M_{\text{Jup}}/\text{yr}$ . These observations provided first evidence that PDS 70 b is accreting and therefore still at the stage of formation.

At about the same time, PDS 70 was observed with the medium-resolution integral field spectrograph MUSE (Multi Unit Spectroscopic Explorer; Bacon et al., 2010) at the VLT. These observations confirmed strong H $\alpha$  emission from PDS 70 b, and detected yet another H $\alpha$  source, at a larger separation of  $\sim 236$  mas and a position angle of  $\sim 277^\circ$  (Haffert et al., 2019), very close in projection to the bright forward-scattering ring of the outer disk. These results inferred the presence of a second companion in the system, named PDS 70 c hereafter. The respectively estimated orbital radii, 20.6 au and 34.5 au, suspect that the planets are in or near 2:1 mean motion resonance. With the ability of MUSE to spectrally resolve the H $\alpha$  line emission from the planets, Haffert et al. (2019) estimated accretion rates of  $2 \times 10^{-8\pm 0.4} M_{\text{Jup}}/\text{yr}$  and  $1 \times 10^{-8\pm 0.4} M_{\text{Jup}}/\text{yr}$  for PDS 70 b and c, respectively, by using an empirical relation between the H $\alpha$  10% line width and the mass accretion rate established for low-mass T Tauri stars and brown dwarfs (Natta et al., 2004; Rigliaco et al., 2012). Considering radiation hydrodynamic models by Aoyama et al. (2018) and Aoyama & Ikoma (2019), Hashimoto et al. (2020) used the flux ratio of the H $\beta$  and H $\alpha$  lines derived from the data presented by Haffert et al. (2019) to estimate the extinction of PDS 70 b. The authors concluded the optical extinction to be larger than 2.0 mag, setting a lower limit on the mass accretion rate of  $\gtrsim 5 \times 10^{-7} M_{\text{Jup}}/\text{yr}$ . These results imply that detailed modeling is an important ingredient for the correct interpretation of planetary H $\alpha$  signals.

The second planet in the system discovered by Haffert et al. (2019), PDS 70 c, is co-located with the structure in some of the PCA and TLOCI images described in Sect. 2.6. However, this signal appeared less robust and less significant in our data than for PDS 70 b (see Fig. 2.12), in particular at longer wavelengths. Due to its close location to the outer ring we thus had attributed the signal to a disk feature. The H $\alpha$  observations by Haffert et al. (2019) however provide unambiguous evidence for the planetary nature of the source. Follow-up observations of the system with SPHERE, and careful re-analysis of the previous SPHERE data with respect to possible contamination from the outer disk allowed to confirm the presence of PDS 70 c in several epochs from J- to K-band (Mesa et al., 2019). Comparison to atmospheric models indicated a mass for PDS 70 c of less than  $5 M_{\text{Jup}}$  and

an effective temperature around 900 K. This work also revealed the presence of a third feature ('point-like feature'), at very close separations to the star ( $\sim 0.12''$ ). Its rather blue spectrum however is suggestive for reflected stellar light, and suspects the source to be part of the inner disk (Mesa et al., 2019). Most recently, PDS 70 was re-observed with Keck/NIRC2 in the L'-band filter (Wang et al., 2020), recovering both planets.



# 3

## A highly structured disk around the planet host PDS 70 revealed by high-angular resolution observations with ALMA

---

The content of this Chapter is based on [Keppler et al. \(2019\)](#), published in *Astronomy & Astrophysics (A&A)*, 625, 118.

**Details of authorship:** I am the first author of this paper and led this team effort involving 21 co-authors under the supervision of Prof. Thomas Henning, and in close collaboration with Roy van Boekel and Myriam Benisty. The text was written by me, with contributions from Richard Teague to Sect. 3.3.2 and Jaehan Bae to Sect. 3.4.1. I was the PI of the ALMA program of which the data are presented in this Chapter. The data were reduced by myself, with help from Edwige Chapillon and Richard Teague. The fitting of the radial brightness distribution of the dust ring in Sect. 3.3.1 was performed by Paola Pinilla. The hydrodynamical and radiative transfer modeling presented in Sect. 3.4.1 was carried out by Jaehan Bae. Figures 3.1, 3.7, 3.8, 3.3, 3.11, 3.12, and 3.13 were generated using tools by Richard Teague, and Fig. 3.16 was contributed by Jaehan Bae. All co-authors provided comments to the paper manuscript.

### 3.1 Motivation

The previous Chapter has revealed a planetary-mass companion in the transition disk around PDS 70. Being the first robust detection of its kind, PDS 70 thus represents a unique laboratory for characterizing the properties of young planetary systems at the stage of their formation. One important aspect of planet formation is the interaction of embedded planets with their natal environment, the protoplanetary disk. These processes are of peculiar interest because the reshaping and redistribution of matter in the disk through the interactions with giant planets is thought to play an important role for the final planetary system architectures. Their understanding is therefore crucial to understand the outcome of planet formation.

As explained in Sect. 1.4, one of the most promising methods to detect the interaction of

### 3 *A highly structured disk around the planet host PDS 70 revealed by high-angular resolution observations with ALMA*

a young planet with its environment is to trace the spatial distribution of pebble-sized dust and the perturbations induced on the gas velocity field of the disk. While PDS 70 c was still to be discovered at the time this project was carried out, we obtained new ALMA Band 7 observations in dust continuum and  $^{12}\text{CO}$  (3-2) observations of PDS 70 in Cycle 5 with the aim to trace direct and indirect imprints of PDS 70 b on the gas and dust emission of the circumstellar disk. The data were combined with archival observations presented by Long et al. (2018b), thereby obtaining an unprecedented angular resolution of  $\sim 0.07''$  ( $\sim 8$  au).

This Chapter provides a deep analysis of these data. The disk morphology is characterized in both, dust and gas, with the finding that the disk is highly structured in both components. The dust continuum is used to search for circumplanetary material at the location of PDS 70 b. While no significant signal was detected, we present an upper limit on the mass or radius of the CPD, depending on if the optical thin or thick limit is assumed. Following the approach by Teague et al. (2018a), we further derive the gas rotational velocities as a function of radius and find a deviation from Keplerian rotation out to  $\sim 0.8''$  (91 au). These far-out kinematic perturbations imply a pressure gradient that can account for the location of the dust ring well beyond the location of PDS 70 b. The observations are compared to hydrodynamical simulations that include a planet with different masses that cover the estimated mass range that was derived in Chapter 2. We find that even a planet with a mass of  $10 M_{\text{Jup}}$  may not be sufficient to explain the extent of the wide gap, hinting toward the possible existence of an additional companion beyond the orbit of PDS 70 b.

The observing setup and data reduction is described in Sect. 3.2. Section 3.3 presents our results, which are discussed and compared to hydrodynamical simulations in Sect. 3.4. The results are summarized and concluded in Sect. 3.5. Finally, Sect. 3.6 highlights recent findings reported in the literature following the publication of the work presented in this Chapter.

## 3.2 Observations and data reduction

We obtained ALMA Cycle 5 director discretionary time (DDT) observations (Project ID: 2017.A.00006.S, PI: M. Keppler) of PDS 70 in Band 7 on 2, 3 and 6 December 2017 under very good weather conditions (mean precipitable water vapor, pwv,  $\leq 0.9$  mm). For three of the four spectral windows, the correlator was tuned to a center frequency of 357.2, 355.3, and 344.3 GHz for continuum observations in dual-polarization mode with a bandwidth of 2.0 GHz. The fourth spectral window was centered around the  $^{12}\text{CO}$ (3-2) transition at 345.8 GHz with a bandwidth of 0.938 GHz. The quasars J1427-4206, J1337-1257, and J1517-2422 were used as bandpass, phase, and flux calibrators. The calibration was performed

using the Common Astronomy Software Package (CASA), version 5.1.1. The total on-source integration time was 1.9 hours.

In addition to the  $^{12}\text{CO J=3-2}$  line, we detected emission from the HCN (J=4-3; 354.505 GHz),  $\text{HCO}^+$  (J=4-3; 356.734 GHz), and  $\text{H}^{13}\text{CN}$  (J=4-3; 345.340 GHz) lines. In this Chapter, we focus on the dust continuum and  $^{12}\text{CO}$  emission, however.

Because the extended antenna configuration filters out the largest spatial scales in the disk, we made use of the archival Cycle 3 data taken in a similar spectral setup and presented by Long et al. (2018b) to recover the short baselines. Details regarding the observing strategy and setup are described in Long et al. (2018b). We transferred both Cycle 3 and Cycle 5 data to CASA v.5.3.0 and subtracted the continuum emission from the line data using the task UVCNTSUB. We corrected the phase center of the Cycle 3 data for the shift due to the proper motion of the star ((-29.7, -23.8) mas/yr, Gaia Collaboration et al., 2016, 2018) with respect to the Cycle 5 data set. We then combined the two data sets and shifted the phase center by an amount of (0.509'', 0.490''), which was found to be the center of the disk by fitting a two-dimensional Gaussian to the continuum Cycle 5 emission using the UVMODELFIT tool. We finally used the task TCLEAN for imaging, applying Briggs weighting with a robust parameter of 0.5. Because self-calibration of both continuum and CO data did not significantly improve the images, we will base our analysis on the non-self-calibrated data. The resulting beam size for the dust continuum at a mean frequency of 350.6 GHz (855  $\mu\text{m}$ ) is  $74 \times 57$  mas ( $8.4 \times 6.5$  au) with a  $PA$  of  $63^\circ$ . We measured a root mean square (rms) noise level of  $0.026$  mJy beam $^{-1}$  from emission-free regions. For the CO, we obtained a beam size of  $76 \times 61$  mas ( $8.6 \times 6.9$  au) with a  $PA$  of  $60^\circ$  and a channel width of 425 m/s. The noise level per channel is determined to be  $1.26$  mJy beam $^{-1}$ .

## 3.3 Results

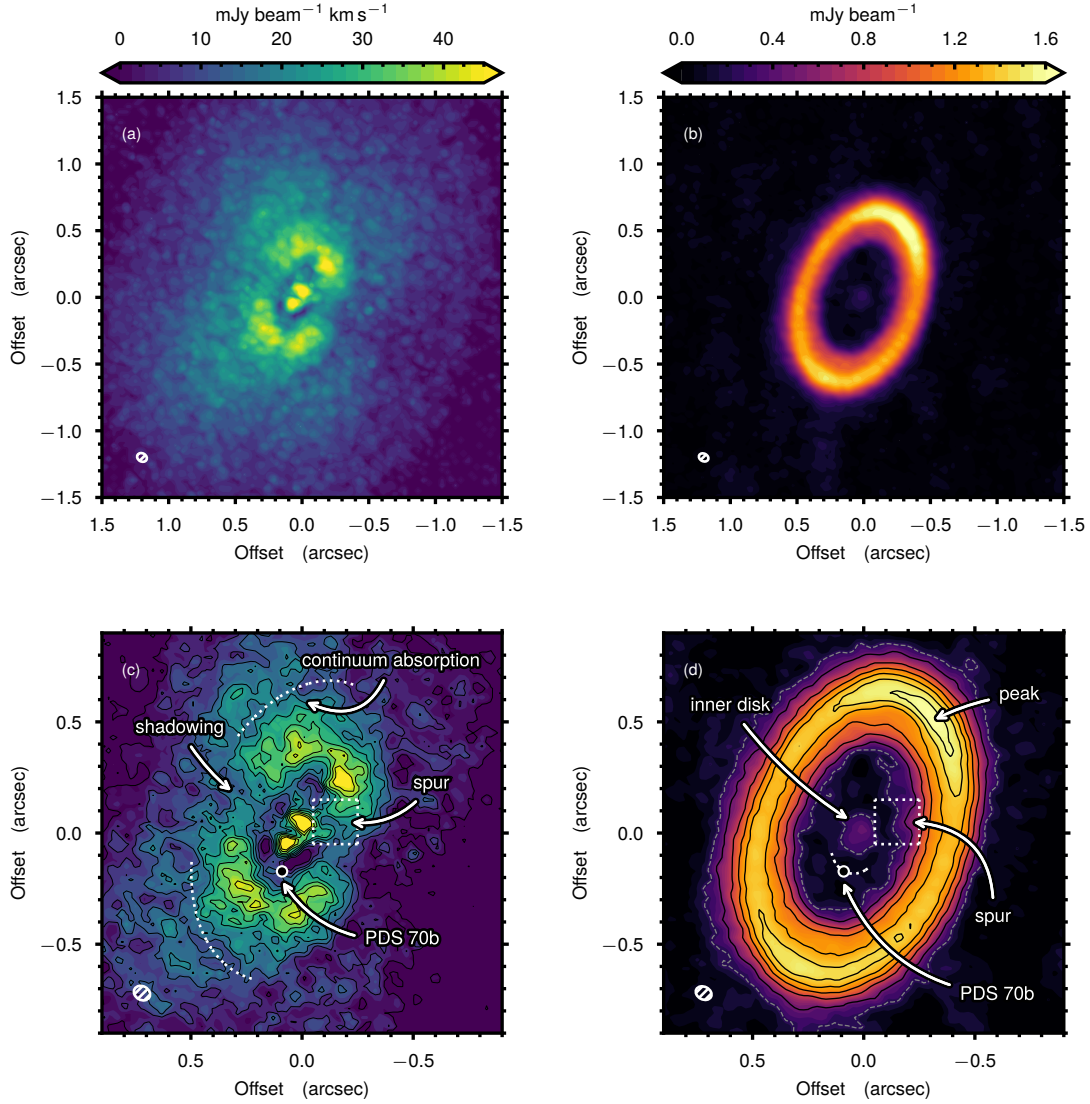
### 3.3.1 855 $\mu\text{m}$ dust continuum

Figure 3.1 (right column) shows the continuum image at 350.6 GHz (855  $\mu\text{m}$ ). The disk is detected at a high signal-to-noise ratio (S/N;  $\sim 65$  at the peak). The integrated flux density of the disk inside  $1.3''$  after applying  $2\sigma$  clipping is  $230 \pm 23$  mJy, where the error bar is dominated by the  $\sim 10\%$  uncertainty of the absolute amplitude calibration of ALMA in Band 7<sup>10</sup>. This is consistent with the value found by Long et al. (2018b). The dust continuum shows evidence of a large cavity, a dust ring with a brightness distribution

---

<sup>10</sup>see <https://almascience.nrao.edu/documents-and-tools/cycle6/alma-proposers-guide>

### 3 A highly structured disk around the planet host PDS 70 revealed by high-angular resolution observations with ALMA



**Figure 3.1:** Observations of the  $^{12}\text{CO}$  (left column) and the 350.6 GHz continuum (right column). The bottom row provides a closer view of the observations including annotations where the color scaling has been stretched to bring out detail. The contours for the  $^{12}\text{CO}$  are starting at 20% of the peak value to the peak in steps of 10%. For the continuum, the gray dashed contour is  $5\sigma$ , and black contours start at  $10\sigma$  and increase in steps of  $10\sigma$ , where  $\sigma = 26 \mu\text{Jy beam}^{-1}$ . The synthesized beams are shown in the bottom left corner of each panel.

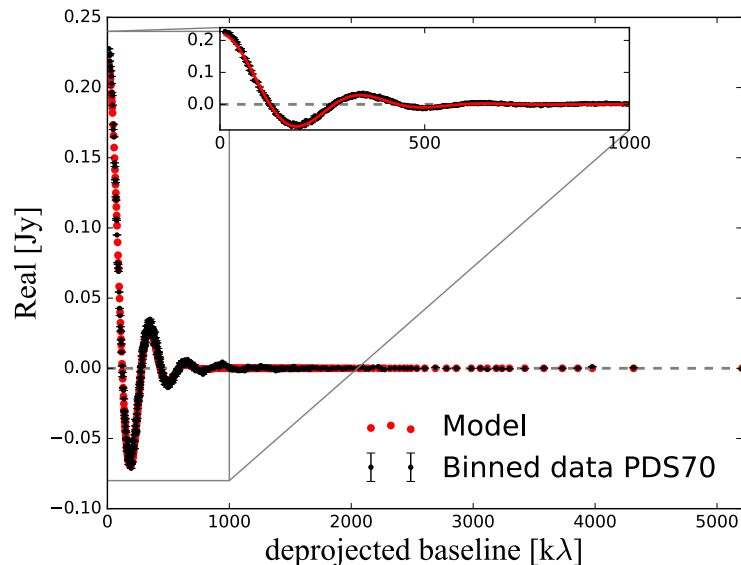


**Figure 3.2:** Results on the MCMC fit of the deprojected and binned visibilities of the dust continuum, following the approach by Pinilla et al. (2018a).

that is slightly asymmetric in both radial and azimuthal direction, an inner disk, as well as a possible bridge feature, all of which we describe in the following paragraphs.

By fitting a two-dimensional Gaussian to the two data sets using the task UVMODELFIT, we find a disk inclination of  $51.7 \pm 0.1^\circ$  and  $52.1 \pm 0.1^\circ$  and a  $PA$  of  $156.7 \pm 0.1^\circ$  and  $159.7 \pm 0.1^\circ$ , for the Cycle 5 and Cycle 3 data sets, respectively. We verified the inclination using only short baselines ( $< 150 \text{ k}\lambda$ , which correspond to the location of the null in the real part of the visibilities, see Fig. 3.2) for the Gaussian fit, which ensured that the cavity is not resolved, as well as by using a disk model. These efforts yielded similarly good fits in all cases; the values for the inclination were consistently within  $3^\circ$ . We note, however, that all these models assume axial symmetry and therefore none of them reproduces the real morphology of the disk. Considering the complexity of the continuum emission that appears to be highly structured, such simple modeling appears limited. We adopt a final value of  $51.7^\circ$  because this corresponds to the model with the fewest assumptions.

### Disk radial and azimuthal morphology

Figure 3.3 (uppermost, gray line) shows the azimuthally averaged and deprojected radial profile of the dust continuum, which clearly reveals a large gap and a ring component. The emission strongly decreases inside the ring, where the flux is reduced by more than 90%.

The radial profile of the ring is asymmetric, which is best seen in the cuts along the major and minor axes (Fig. 3.3, colored lines). The inner edge of the continuum ring reveals a second peak located at a deprojected distance of about  $0.53''$  (60 au). The feature is most

### 3 A highly structured disk around the planet host PDS 70 revealed by high-angular resolution observations with ALMA

pronounced along the major axes, which can be explained by the projection effect as well as by the beam, whose major axis is oriented roughly along the minor axis of the disk. Observations at even higher angular resolution are required to quantify this structure in greater detail.

To quantify the radial brightness distribution of the dust ring, we used the same approach as Pinilla et al. (2018a). We first deprojected the data assuming an inclination of  $51.7^\circ$ , and fit the real part of the deprojected visibilities with a radially asymmetric Gaussian ring using a Markov chain Monte Carlo (MCMC) method using *emcee* (Foreman-Mackey et al., 2013). The best-fit model has a peak radial position of  $73.7 \pm 0.1$  au, and an inner and outer width of  $14.8 \pm 0.1$  au and  $13.4 \pm 0.1$  au. The ring is therefore radially resolved by our observations. The best fit model is overplotted in Fig. 3.3 (black line) and is shown in Fig. 3.2.

We confirm the azimuthal brightness enhancement of the ring that was reported by Long et al. (2018b) on the northwest side of the disk, which peaks at a PA of  $\sim 327^\circ$  and is roughly 13% brighter than the opposite disk side.<sup>11</sup> If the dust is optically thin, the asymmetry could trace the presence of an overdensity. As we argue below, the dust is likely almost optically thick. The brightness enhancement is therefore likely a combination of differences in mass density and temperature. Observations at longer wavelengths are required to break the degeneracies of temperature and density effects and to conclude on the origin of the azimuthal brightness asymmetry.

#### Inner disk

Our image also confirms the detection of a compact signal toward the location of the star, which has been detected and attributed to be a possible inner disk component by Long et al. (2018b) the existence of which is consistent with the NIR excess detected in the SED. Our observations marginally resolve the emission inside the innermost  $\sim 80$  mas (9 au) at a  $5\sigma$  level. Observations at longer wavelengths will enable us to establish the spectral index of this central emission, which is required to exclude the possible contribution from free-free emission.

#### Possible bridge feature

We detect a spur that projects from the dust ring into the gap in the direction of the inner disk at a PA of about  $285^\circ$  (referred to as ‘spur’ in Fig. 3.1 and best seen in panel (d)). This signal is even more clearly detected in the DDT data alone, which have a slightly higher resolution ( $71 \times 56$  mas, see Fig. 3.4). It is possible that the signal forms a bridge feature that

---

<sup>11</sup>Value found by comparing the peak pixel value of the northwest side with the peak pixel value of the southeast side.

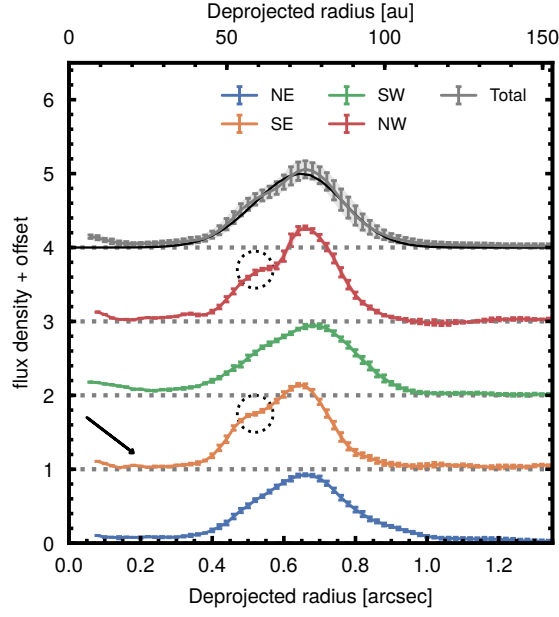


**Figure 3.3:** Radial profiles of the deprojected dust continuum image along the semi-major (red, orange) and the semi-minor (green, blue) axes, as well as averaged over the entire azimuth (gray). The black line in the uppermost plot corresponds to the best-fit model of the radial profile found in Sect. 3.3.1. The deprojection assumes that the continuum is geometrically flat. Radial samples are taken every  $\sim 1/4$  beam (20 mas), and the cuts along the minor and major axes are azimuthally averaged in a cone of  $\pm 10^\circ$  around the corresponding axes. The black arrow highlights a bump in the profile close to the location of PDS 70 b, and the dotted circles mark the location of the second peak.

connects the outer and inner disks. Whereas the spur is detected at high confidence ( $> 5\sigma$ ), the continuous connection to the inner disk in the dust continuum remains to be confirmed with deeper observations. Interestingly, this feature is cospatial with an extended feature found in scattered light (Keppler et al., 2018; Müller et al., 2018, see Fig.3.4). Furthermore, the CO shows evidence of a feature at that same location that seems indeed to connect the outer and inner disk (see Sect. 3.3.2).

### Upper limits on CPD dust mass

Figure 3.3 shows that the radial profile along the southeast semi-major axis presents a marginally (S/N  $\sim 3$ ) enhanced signal at  $\sim 0.2''$ . This roughly corresponds to the expected location of PDS 70 b. We note, however, that flux density variations of similar amplitude are present at several other position angles as well, and the persistence of this signal is therefore to be tested with deeper observations.

Circumplanetary disks (CPD) are expected to have outer radii  $R_{\text{out}}$  of a fraction ( $\sim 30\text{--}70\%$ ) of the Hill radius  $R_{\text{H}}$  (e.g., Quillen & Trilling, 1998; D’Angelo et al., 2003; Ayliffe & Bate, 2009; Szulágyi et al., 2014), where  $R_{\text{H}} = a_{\text{P}} (M_{\text{P}}/3M_{\star})^{1/3}$  and  $a_{\text{P}}$  is distance of the

### 3 A highly structured disk around the planet host PDS 70 revealed by high-angular resolution observations with ALMA

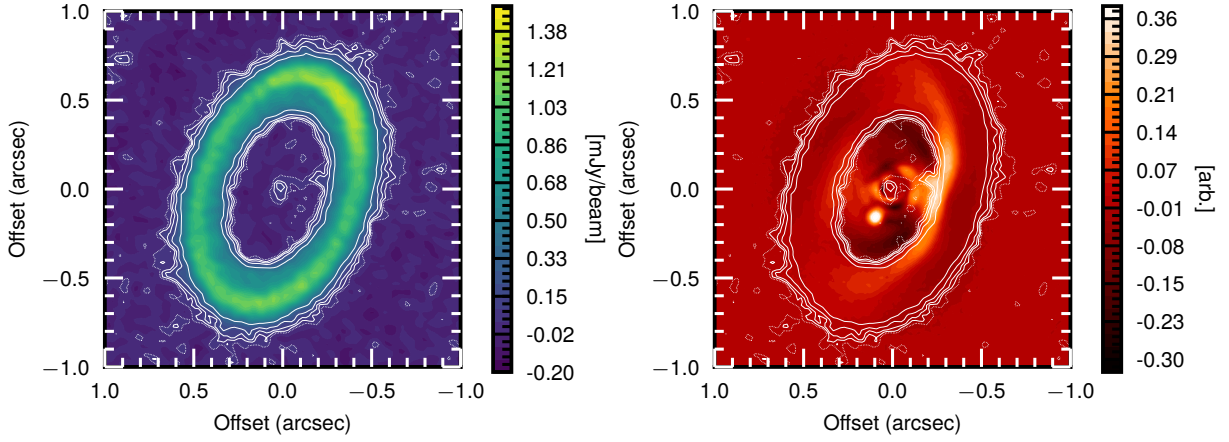


**Figure 3.4:** Cycle 5 dust continuum data (*left*) and SPHERE NIR image (*right*, from Müller et al., 2018), the ALMA Cycle 5 data contours are overlaid in white. The solid contours show levels of 2,3,5, and 10  $\sigma$ , and the dotted line corresponds to 1  $\sigma$ .

planet to the star. For a 5  $M_{\text{Jup}}$  companion at 22 au, this corresponds to  $\sim 0.8\text{-}1.9$  au, and the disk is therefore expected to be unresolved. Our measured noise level of 0.026 mJy  $\text{beam}^{-1}$  translates into a  $5\sigma$  upper limit on the flux density of an unresolved CPD around PDS 70 b of 0.130 mJy  $\text{beam}^{-1}$ .

We compared this value to the theoretically expected emission from a CPD in order to derive an upper limit on the dust mass. For this aim, we followed the approach presented by Isella et al. (2014), where the dust temperature  $T_d$  in the CPD at a given radius  $r$  from the planet is described as

$$T_d^4(r) = T_{irr,\star}^4(a_p) + T_{irr,p}^4(r) + T_{acc}^4(r), \quad (3.1)$$

where  $T_{irr,\star}$  is the temperature of the surrounding circumstellar disk heated by the central star at the distance of the planet to the star,  $T_{irr,p}$  is the temperature due to the heating by the planet itself, and  $T_{acc}$  denotes the contribution from viscous accretion within the CPD.

For  $T_{irr,\star}$  we adopted a value of 19 K at a distance of 22 au from the star, which is estimated from our radiative transfer models in Chapter 2. The irradiation by the planet,  $T_{irr,p}$ , can be estimated (assuming a CPD aspect ratio of 0.1; Zhu et al., 2018) as

$$T_{irr,p}(r) = \left( \frac{L_p}{\sigma_{SB} 40\pi r^2} \right)^{1/4}, \quad (3.2)$$

where we used  $L_p \sim 1.5 \times 10^{-4} L_{\odot}$  as the luminosity of PDS 70 b (Müller et al., 2018). Fi-

nally, the heating due to accreting material is given by

$$T_{acc}^4(r) = \frac{3GM_p\dot{M}_{acc}}{8\pi\sigma_{SB}r^3} \left[ 1 - \left( \frac{r_p}{r} \right)^{1/2} \right], \quad (3.3)$$

where  $\dot{M}_{acc}$  is the mass accretion rate onto the planet and  $r_p$  is the planetary radius. Following [Wagner et al. \(2018\)](#), we assumed  $\dot{M}_{acc} \sim 10^{-8} M_{Jup} \text{yr}^{-1}$  and  $r_p \sim 3 R_{Jup}$  ([Müller et al., 2018](#)).

As in [Isella et al. \(2014\)](#), we assumed a power-law surface density  $\Sigma(r) = C \times r^{-3/4}$ , where  $C$  is the normalization constant for the total CPD dust mass  $M_d = \int_{r_{in}}^{r_{out}} \Sigma(r) 2\pi r dr$ . We therefore computed the expected millimeter flux  $F_d$  for a given  $M_d$  by integrating the flux density contribution from each radius over the entire CPD:

$$F_d = \frac{2\pi \cos i}{d^2} \int_{r_{in}}^{r_{out}} \left( 1 - \exp \left[ -\frac{\Sigma(r)\kappa}{\cos i} \right] \right) \times B_\nu(T_d(r)) r dr. \quad (3.4)$$

Here,  $\kappa$  denotes the dust opacity, which we assumed to be  $3.5 \text{ cm}^2 \text{g}^{-1}$  at  $855 \mu\text{m}$ , linearly scaled from [Andrews et al. \(2012\)](#),  $B_\nu$  is the Planck function evaluated at  $T_d$ , and  $i$  is the CPD inclination, which we assumed to be equal to the inclination of the circumstellar disk ( $51.7^\circ$ ).

We computed the expected flux densities for different CPD dust masses considering outer CPD radii of  $0.3\text{-}0.7 r_H$  and assuming that the CPD touches the planetary surface (e.g.,  $r_{in} = r_p$ , but note that regions in which the temperature exceeds the sublimation temperature of silicates ( $\sim 1500 \text{ K}$ ) were taken out of the integral). The result was compared to our noise level of  $0.026 \text{ mJy beam}^{-1}$  and is shown in [Fig. 3.5](#). With the given choice of parameters, we find a  $5\sigma$  upper dust mass limit of  $\sim 0.01 M_\oplus$  ( $\sim 0.8$  lunar masses). This value is roughly independent of the outer CPD radius, which means that the emission is likely optically thin. As will be shown in the next Section, this detection limit holds for the entire estimated mass range of PDS 70 b.

### Dependency of CPD detection limits on planetary mass and accretion rate

We explore the dependency of the CPD detection limit on the planetary mass and accretion rate. In our approach, the CPD temperature profile results from three contributions: heating from irradiation by the central star, from irradiation by the planet, and from viscous accretion (see [Equ. 3.1](#)). The irradiation by the planet depends on its luminosity, and therefore on its temperature and radius ( $T_p \sim 1200 \text{ K}$ ,  $r_p \sim 3 R_{Jup}$  for PDS 70 b; [Müller et al., 2018](#)), and the contribution from accretional heating is proportional to the product

### 3 A highly structured disk around the planet host PDS 70 revealed by high-angular resolution observations with ALMA

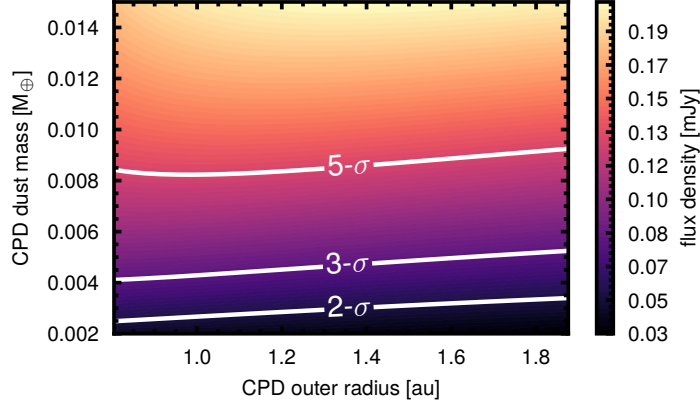


**Figure 3.5:** Theoretically expected flux densities from a CPD around a  $5 M_{\text{Jup}}$  planet at the location of PDS 70 b with different dust masses and outer disk radii, following the prescription from Isella et al. (2014). The contours mark the 2, 3, and  $5\sigma$  detection limits from the observations.

of planet mass and accretion rate (see Equ. 3.2 and 3.3). Their relative contribution can be expressed as

$$\frac{T_{\text{acc}}^4}{T_{\text{irr},p}^4}(r) = \frac{30G}{8\pi\sigma_{\text{SB}}T_p^4 r_p^2} \frac{M_p \dot{M}_{\text{acc}}}{r} \left[ 1 - \left( \frac{r_p}{r} \right)^{1/2} \right] \quad (3.5)$$

This expression has a maximum at about  $2.25 \times r_p$ , and we can therefore write

$$\begin{aligned} \frac{T_{\text{acc}}^4}{T_{\text{irr},p}^4} &\leq \frac{5GM_p \dot{M}_{\text{acc}}}{18\pi\sigma_{\text{SB}}T_p^4 r_p^3} \\ &\approx 0.03 \left( \frac{1200\text{K}}{T_P} \right)^4 \times \left( \frac{3 R_{\text{Jup}}}{R_P} \right)^3 \times \left( \frac{M_P}{5 M_{\text{Jup}}} \right) \times \left( \frac{\dot{M}_{\text{acc}}}{10^{-8} M_{\text{Jup}}/\text{yr}} \right) \end{aligned} \quad (3.6)$$

For the given parameter choice, accretional heating is therefore negligible.

For a planetary mass of  $5 M_{\text{Jup}}$  and radius of  $3 R_{\text{Jup}}$ , Wagner et al. (2018) calculated an accretion rate for PDS 70 b of  $3 \times 10^{-9}$  to  $9 \times 10^{-8} M_{\text{Jup}}/\text{yr}$ , depending on the assumed extinction. Thus, even in case of high extinction and therefore high accretion rate, the term  $T_{\text{acc}}^4/T_{\text{irr},p}^4$  is lower than 0.3, and the contribution from accretional heating is still marginal. We note that the planetary mass cannot be varied independently of the accretion rate because the product  $M_P \dot{M}_{\text{acc}}$  is to be conserved. We therefore conclude that the temperature structure in our calculation is insensitive to the choice of the planet mass within the estimated range for a CPD of a given size.

The outer outer radius does depend on the planet mass, however. The lower the planet

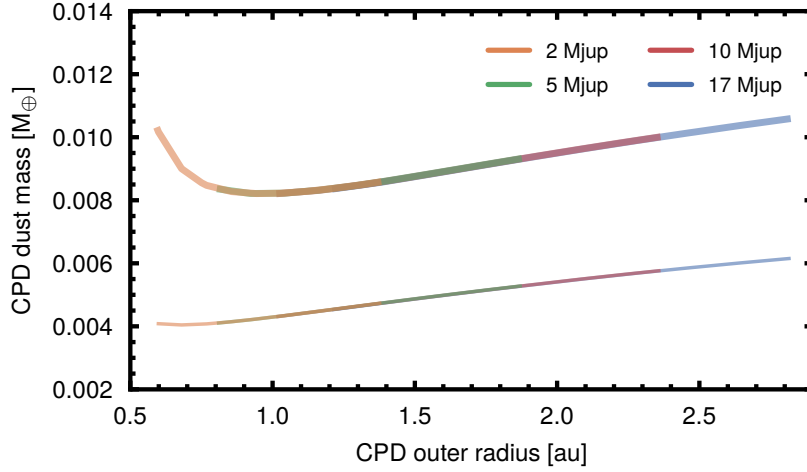


**Figure 3.6:** CPD  $5\sigma$  (thick line) and  $3\sigma$  (thin line) detection limits for different planet masses covering the mass range for PDS 70 b estimated by [Keppler et al. \(2018\)](#) and [Müller et al. \(2018\)](#).

mass, the smaller the disk it will be able to retain. This is illustrated in Fig. 3.6, which shows the  $5\sigma$  and  $3\sigma$  detection limits for the estimated mass ranges based on the comparison of NIR photometry with evolutionary models and atmospheric modeling ([Keppler et al., 2018](#); [Müller et al., 2018](#)). The figure illustrates that 1) at a given CPD size, the CPD flux is independent of the planetary mass, 2) the  $5\sigma$  detection limits (thick lines) are rather constant for all disk sizes, mostly below  $\sim 0.01 M_{\oplus}$ , indicating optically thin emission (except for the case of  $2 M_{\text{Jup}}$ , where emission is in transition to optically thick), and 3) CPDs around planets with different masses cover different ranges of disk sizes.

### 3.3.2 $^{12}\text{CO } J = 3 - 2$

Figures 3.1 (a) and (c) show the  $^{12}\text{CO } J = 3 - 2$  integrated intensity (zeroth-moment) map; panel (c) includes annotations of the main features. The asymmetry with respect to the disk major axis is clear. This is due to the significantly elevated  $\tau \sim 1$  surface of the  $^{12}\text{CO}$ , which is typically assumed to trace disk layers where  $z/r \sim 0.25$  ([Rosenfeld et al., 2013](#)). In addition, several other features are visible, including two gaps (a prominent gap at  $\sim 0.2''$  and a faint gap at  $\sim 0.6''$ ), a bridge-like feature similar to the one observed in the continuum, and apparent shadowing along the major and minor axes that has previously been reported by [Long et al. \(2018b\)](#).

Toward the center of the image, the inner disk component is clearly detected, extending out to approximately 15 au, which is consistent with the estimates from scattered light presented in Chapter 2. For disks shaped by planets, a bright gaseous inner disk (implying

### 3 A highly structured disk around the planet host PDS 70 revealed by high-angular resolution observations with ALMA

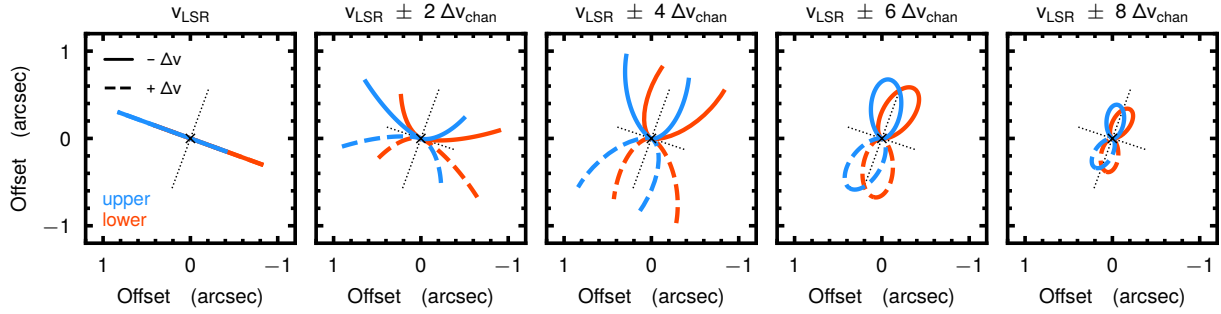


**Figure 3.7:** Iso-velocity contours for the upper (blue) and lower (red) sides of the disk at different velocities with a flared emission surface. Along the major and minor axes, shown by the black dotted lines, the iso-velocity contours overlap, as in the leftmost and rightmost panels, and thus only emission from the upper side of the disk is visible. Conversely, in inter-axis regions, the iso-velocity contours are spatially separated, as in the central panels, so that emission from both sides of the disk reaches the observer. Based on Fig. 4 from Rosenfeld et al. (2013).

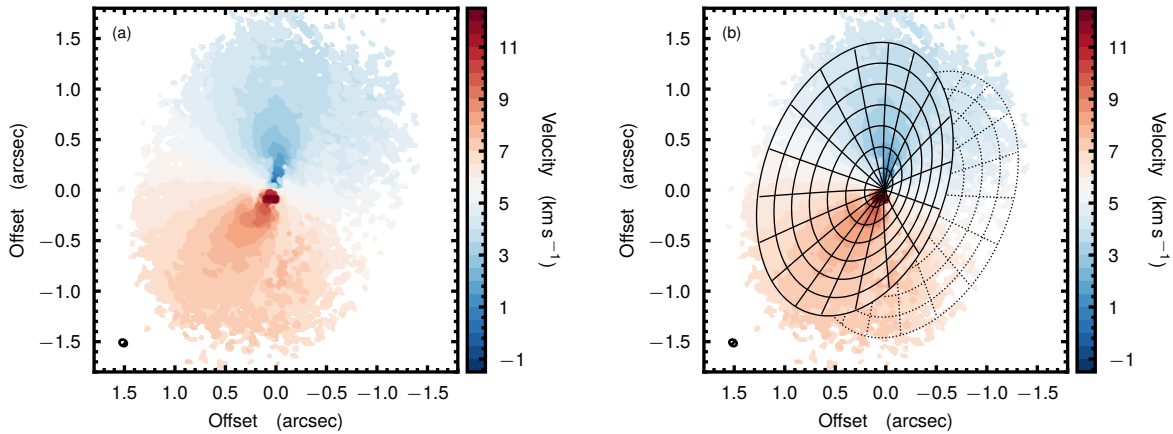


**Figure 3.8:** Rotation map of the  $^{12}\text{CO}$  emission, *left*, using the method presented in Teague & Foreman-Mackey (2018), with the best-fit surface overlaid, *right*. The solid lines show the top surface, and the dotted lines show the far surface.

a gas gap rather than a cavity) is in agreement with the predictions from hydrodynamical models, even for the cases where the planet mass is as high as  $10 M_{\text{Jup}}$  (Facchini et al., 2018).

At about the same location as the spur found in the continuum, the zeroth-moment map shows evidence of an extended signal that connects the inner disk and the outer ring in the northwest region. This signal may be connected to the extended feature detected in the NIR (Keppler et al., 2018; Müller et al., 2018, and Fig. 3.4, right panel, of this Chapter), and might also be related to the features seen in CO and  $\text{HCO}^+$  by Long et al. (2018b) at similar locations. If this feature indeed connects the outer and inner disks, it may be tracing gas flow through the gap from the outer to the inner disk (e.g., Tang et al., 2017;

Casassus et al., 2015; Price et al., 2018). This hypothesis could be confirmed through the detection of localised velocity changes in the given region, which we do not detect with our spectral resolution, however. The nature of this feature therefore needs to be tested with observations at higher spectral and angular resolution.

The inner gap at  $\sim 0.2''$  is likely due to a gap opened by PDS 70 b and is discussed further in Section 3.4.1. The outer gap at  $\sim 0.6''$  can be explained by continuum absorption of the bottom side of the disk: as shown in Fig. 3.7, the contours of equal projected velocity at the top and bottom sides of the disk in regions between the disk major and minor axes are spatially offset. While emission from the bottom side travels through the midplane toward the observer, it is absorbed by the dust, which reduces the integrated flux at that location (e.g., Isella et al., 2018). As emission from the bottom side of the disk is almost entirely absorbed, we conclude that the dust ring is likely optically thick at  $\nu = 345$  GHz, a result which has found at millimeter wavelengths for other disks as well (e.g., Pinilla et al., 2017a).

Along the disk major and minor axes, on the other hand, the iso-velocity contours do overlap. Because the  $^{12}\text{CO}$  is optically thick, emission from the bottom side of the disk is self-absorbed and only the top side is visible. This causes the apparent shadowing along the major and minor axes of the disk (and the shadowing observed in the  $\text{HCO}^+$  data presented by Long et al., 2018b). A more elevated emission layer results in a larger azimuthal variance, because the two sides become more spatially resolved. The difference between the value along an inter-axis region and along an axis will peak at roughly a factor of two, a feature that is commonly seen in the integrated intensity maps of high spatial resolution observations of  $^{12}\text{CO}$  (e.g., Rosenfeld et al., 2013).

### Deriving a $^{12}\text{CO}$ emission surface

Because the  $^{12}\text{CO}$  emission comes from an elevated layer above the midplane, we needed to deproject the data in order to precisely analyze the emission and velocity structure as a function of the radius. For this aim, we wished to derive constraints on the emission height of the  $^{12}\text{CO}$ . Following Teague et al. (2018b), we generated a map of the rotation velocity using the method presented in Teague & Foreman-Mackey (2018)<sup>12</sup>, which is robust against confusion from the near and far sides of the disk<sup>13</sup>. We then fit a Keplerian rotation pattern to the data, including a flared emission surface parameterized as  $z(r) = z_0 \times (r/1'')^\varphi$ , and fixed the inclination at  $i = 51.7^\circ$  to break the degeneracy with the stellar mass. We note that our modeling of the surface height is limited to a generic model of a flared surface because the resolution of our data is limited. To perform more detailed modeling of the

<sup>12</sup>using `bettermoments` (Teague & Foreman-Mackey, 2018)

<sup>13</sup>Carrying out this modeling approach on an intensity-weighted average velocity map (first-moment map), we find a much flatter disk due to the averaging of the upper and lower sides of the disk.

### 3 A highly structured disk around the planet host PDS 70 revealed by high-angular resolution observations with ALMA

emission surface under consideration of spatial variations of the underlying gas density structure, a higher resolution is required. Our modeling results in a tight constraint on the emission surface of

$$z(r) ["] = (0.33 \pm 0.01) \times \left( \frac{r}{1"} \right)^{0.76 \pm 0.01}, \quad (3.7)$$

with the additional parameters of  $M_{\star} = 0.875 \pm 0.03 M_{\odot}$ ,  $\text{PA} = 160.4^{\circ} \pm 0.1^{\circ}$ , and  $v_{\text{LSR}} = 5505 \pm 2 \text{ m s}^{-1}$ . These uncertainties describe the 16th to 84th percentile range of the posterior distributions for each parameter which are symmetric about the median. We note that these uncertainties correspond to the statistical uncertainties and do not take into account the systematic uncertainties that may be significantly larger. Figure 3.8 shows the best-fit emission surface overlaid on the rotation map.

Using this emission surface, the data were deprojected into bins of constant radius and were azimuthally averaged with the resulting integrated intensity profiles shown in Fig. 3.9. The radial profile of the integrated flux density in the top panel shows a clear gap at  $0.2''$  ( $\sim 23 \text{ au}$ ), consistent with the orbit of PDS 70b (Keppler et al., 2018; Müller et al., 2018) and a gap width of  $\sim 0.1''$ . Because of the very high optical depth of  $^{12}\text{CO}$ , any visible gap feature requires a significant depletion of gas or considerable change in gas temperature (e.g., Facchini et al., 2018).

Using the brightness temperature,  $T_{\text{B}}$ , presented in Fig. 3.9 (lower panel) as a proxy of the gas temperature, we infer a drop in the local gas temperature across the gap. This is consistent with a surface density depletion of the gas, which would move the  $\tau = 1$  surface of the  $^{12}\text{CO}$  deeper within the disk, closer to the cooler midplane, therefore dropping the temperature. One possibility to clearly distinguish the effects of temperature and density on the brightness temperature is to use the CO line width as a tracer for temperature variations (Teague et al., 2018a), for which higher spectral resolution is required than given by our data, however.

From the integrated flux density profile, we find that the gap extends from about  $0.1$  to  $0.3''$  ( $\sim 11$  to  $34 \text{ au}$ ). It is spatially resolved, and does not seem to extend out to the location of the dust continuum ring, although it is not possible to measure the  $^{12}\text{CO}$  depletion accurately because of its large optical depth. This preferential depletion of grains compared to gas within a cavity is a common feature for transition disks (van der Marel et al., 2015, 2016).

#### $^{12}\text{CO}$ rotation curve

Radial gas pressure gradients perturb the gas rotation velocity and are used as tracers for planet-induced perturbations (Pérez et al., 2015; Pinte et al., 2018b; Teague et al., 2018a).

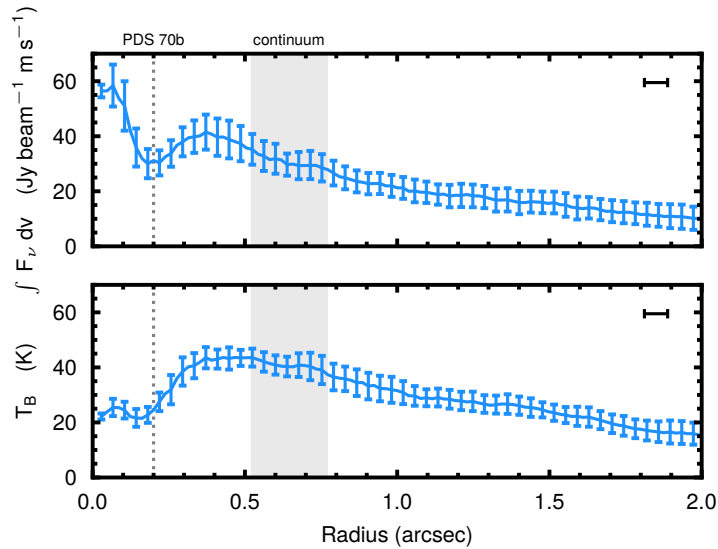


**Figure 3.9:** Radial profiles of the  $^{12}\text{CO}$  integrated intensity, *top*, and brightness temperature, *bottom*. Radial samples are taken every  $1/4$  beam and the error bar shows the standard deviation in the azimuthal bin. The vertical dotted line shows the orbit of PDS 70b, while the gray shaded region shows the extent of the continuum ring. The beam size is shown in the top right corner of each panel.

Velocity distortions by the planet at the close-in location of 22 au are small, such that their detection in single-channel maps as described by [Pinte et al. \(2018b\)](#) is hampered by our limited angular and spectral resolution (see also Sect. 3.4.1), and further by the relatively low S/N of the CO emission at the location of the planet (well within the CO-integrated flux density gap). To improve the S/N of potential kinematic perturbations we therefore used of an azimuthally averaged rotation curve of the  $^{12}\text{CO}$  data to probe the underlying gas density structure ([Teague et al., 2018a](#)). This is even possible in cases when the line emission is optically thick. Whereas a negative pressure gradient induces sub-Keplerian rotation, a positive pressure gradient would cause super-Keplerian rotation.

Following the method described in [Teague et al. \(2018b\)](#), we inferred the rotation profile by determining the rotation velocity for each radius which allows for all spectra in an annulus to be shifted back to the same systemic velocity<sup>14</sup>. We ran ten different realizations of this, randomizing the pixels taken from each annulus (making sure they are separated by at least one FWHM of the beam), and randomizing the radial locations of the annuli while maintaining a radial bin width of a quarter beam width. The resulting rotation curve and the residual relative to the best-fit Keplerian profile are plotted in Fig. 3.10.

The absolute scale of the deviation from Keplerian rotation depends on the reference Keplerian velocity and therefore on the assumed stellar mass. The systematic uncertain-

<sup>14</sup>A Python implementation of this method, *eddy* (see [Teague, 2019](#)), is publicly available at <https://github.com/richteague/eddy>.

3 A highly structured disk around the planet host PDS 70 revealed by high-angular resolution observations with ALMA

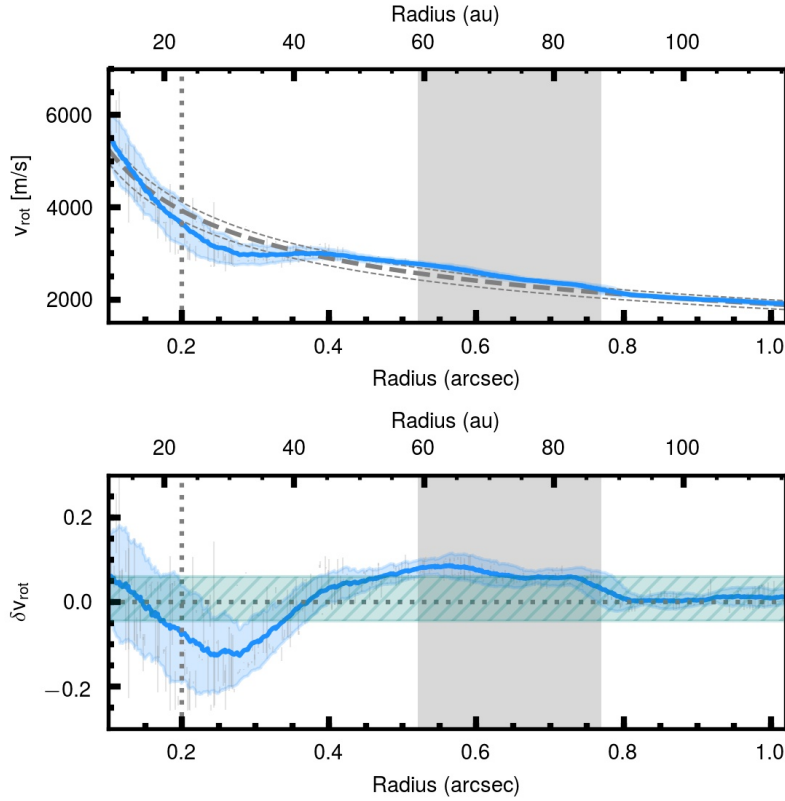


**Figure 3.10:** *Top:* Measured rotation curve with  $1\sigma$  uncertainties. The blue line and blue shadowed area show the running mean and its standard deviation. The dashed gray lines show the Keplerian rotation curve assuming the best-fit stellar mass ( $0.88 M_{\odot}$ , thick) and including the  $3\sigma$  uncertainties on the stellar mass (corresponding to  $0.79$  and  $0.97 M_{\odot}$  respectively, thin) derived from the rotation map fitting. The uncertainties of the stellar mass correspond to the statistical uncertainties and do not include the systematics. *Bottom:* Relative residuals (blue solid) and uncertainties (blue shaded area) between a smooth Keplerian curve and the inferred rotation curve. The green hatched area highlights the uncertainty of the absolute scaling of  $\delta v_{\text{rot}}$  inferred by the  $3\sigma$  statistical uncertainties on the stellar mass. In both panels, the gray shaded region shows the extent of the continuum ring. The vertical dotted line shows the orbit of PDS 70 b and the shaded vertical gray region traces the location of the continuum emission.

ties on the dynamical determination of the stellar mass as well as the parameterization of the surface together with the fact that our fiducial model for the rotation velocity does not take into account the overall pressure gradient in the disk may cause the uncertainty of the absolute scaling to be as large as 10%. Figure 3.10 (bottom panel) shows the residuals of the rotation curve (blue), where the green hatched area marks the uncertainty of the zero-point of  $\delta v_{\text{rot}}$  inferred by the  $3\sigma$  statistical uncertainties of the stellar mass. Within these uncertainties, the peak of the continuum ring ( $\sim 0.65''$ ) lies close to the location where  $\delta v_{\text{rot}}$  recovers Keplerian rotation and therefore where pressure reaches its maximum.

A significant deviation of up to  $\sim 12\%$  at  $\sim 0.2''$  is observed, which is suggestive of significant changes in the gas pressure at this location, consistent with the structure observed in the rotation map in Fig. 3.8. The rotation curve clearly demonstrates a positive pressure gradient between  $\sim 0.4$  and  $0.8''$ , reaching a maximum at about  $0.55''$ . This implies that the gas density is likely depleted beyond  $\sim 0.4''$ , and therefore suggests that the gap is in reality larger than what is observed in integrated emission: if the gap were only as wide as the gap in the  $^{12}\text{CO}$  integrated emission, then we would expect the peak residual of the rotation curve to fall at the edge of the gap at  $\sim 0.3''$  (see Fig. 1 in Teague et al., 2018a, for example), but the peak is found closer to  $0.55''$ . The shape of the residual curve in the inner disk,  $r < 0.3''$ , is dominated by the steep gradients in the intensity profile that are due to both the inner disk and the gap; this makes a direct analysis challenging. For a beam of a given size, the spectrum, and thus the velocity of the gas traced, observed at each pixel corresponds to the average of all spectra within the beam centered on that pixel, weighted by their line intensities and the beam shape. If the intensity gradient across the beam is steep, this will cause the sampled velocity to be strongly biased toward the region of highest intensity, rather than the beam center.

This effect is illustrated in Fig. 3.11 (left). For a smooth radial disk intensity profile, the figure shows for each distance the sampled radius, that is, the radius within the beam at which the velocity receives the highest weighting and which therefore corresponds to the effective radius at which the velocity is observed. This is shown for different power-law exponents of the radial intensity profile of the disk. We note that the steeper the intensity profile, the greater the bias of the sampled radius toward smaller radii, and the greater the overestimate of the measured velocity.

This is even more complex when the intensity profile deviates from a simple power law, as in the presence of a gap structure. The additional steep gradients at the gap edges cause regions closer to the inner gap edge to become even more biased toward smaller distances and therefore higher velocities, whereas regions close to the outer gap edge are biased toward larger distances and lower velocities. Figure 3.11 (bottom right) shows the deviation from Keplerian rotation, assuming an intensity profile with a gap structure centered around  $0.2''$  and a beam size of 76 mas (top right). The resulting  $\delta v_{\text{rot}}$  profile is asymmetric

### 3 A highly structured disk around the planet host PDS 70 revealed by high-angular resolution observations with ALMA

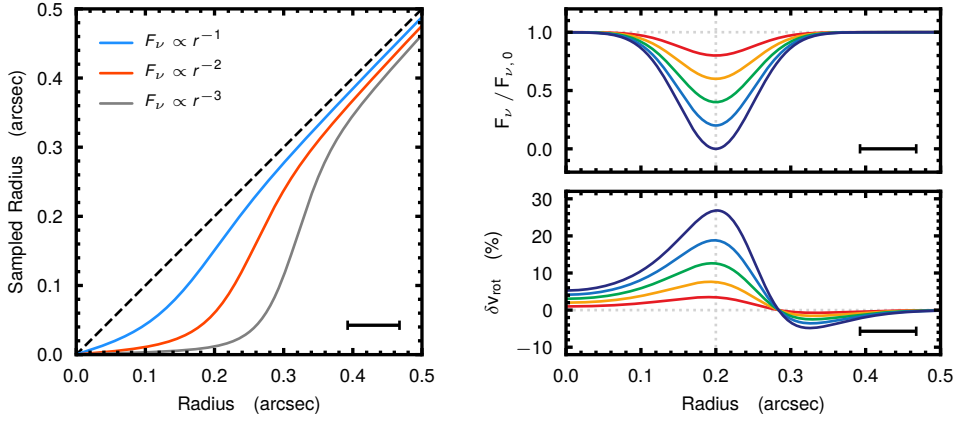


**Figure 3.11:** Effect of beam convolution in the presence of intensity gradients on the radial sampling of the rotation velocity. The left panel illustrates the deviation of the sampled radius (i.e. the radius within the beam at which the intensity and therefore the weighting of the velocity is highest due to the convolution with the beam) from the real radius in the presence of smooth intensity profiles with different power-law indices. The effect is stronger for steeper intensity profiles. The right panels shows the effect of beam convolution in the presence of a gap-shaped intensity profile with varying depths (upper right) on the resulting residual rotation curve (bottom right). In both cases, a beam size of 76 mas is assumed, shown by the horizontal black bar.

with respect to the gap center, with super-Keplerian rotation in the inner regions changing into sub-Keplerian rotation beyond  $\sim 0.3''$ , and the strength of the deviation is sensitive to the gap depth. This beam-smearing effect is added to the deviation from Keplerian rotation that is due to the planet-induced pressure gradient.

Figure 3.12 demonstrates the effects of this bias using the radial intensity profile from Fig. 3.9 and compares this effect to the functional form from the pressure gradient (shown in light blue). The resulting profile is the combination of both factors, whose relative amplitudes depend on the gap shape. While this limits interpretation, these effects are fully accounted for with forward modeling, as presented in Section 3.4.1.

#### Potential point source

We tentatively detect a point source in the  $^{12}\text{CO}$  emission maps at a projected separation of  $\sim 0.39''$  and a PA of  $\sim 260^\circ$ . This corresponds to a deprojected radius of  $\sim 71$  au, if it comes from the midplane. The peak is detected at a  $\sim 6\sigma$  level and is spatially offset from the Keplerian emission pattern. Figure 3.13 shows the spectrum extracted at the location of the source, and three channel maps showing the offset nature of the emission. The signal appears at a velocity of around  $6.45 \text{ km s}^{-1}$ , corresponding to a redshift of roughly 1 km/s with respect to the line center of the Keplerian profile. The spectrum also shows a blueshifted peak, whose emission may be biased from the bottom side of the disk, how-

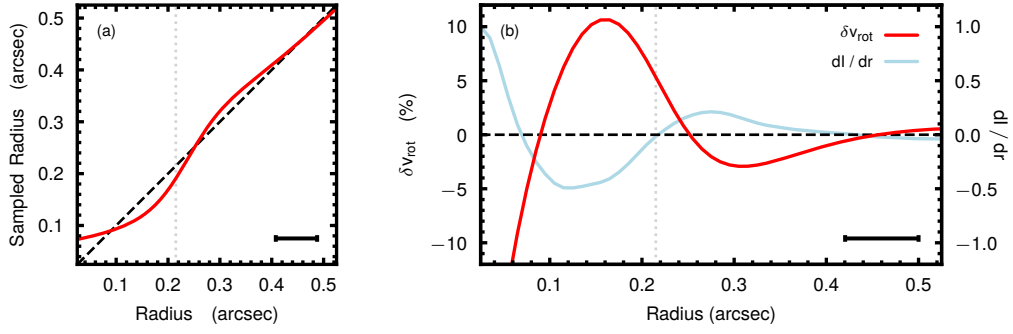


**Figure 3.12:** Similar to Fig. 3.11, but using the observed intensity profile from Fig. 3.9. The left panel shows the bias in the sampled radius caused by the gap at  $0.2''$ , shown by the vertical dashed line. The right panel shows the resulting deviation in velocity expected by this bias in red. For contrast, the blue line shows the deviations expected from a pressure gradient, here using the normalized radial gradient of the intensity as a proxy. The recovered  $\delta v_{\text{rot}}$  therefore is a combination of these two effects.

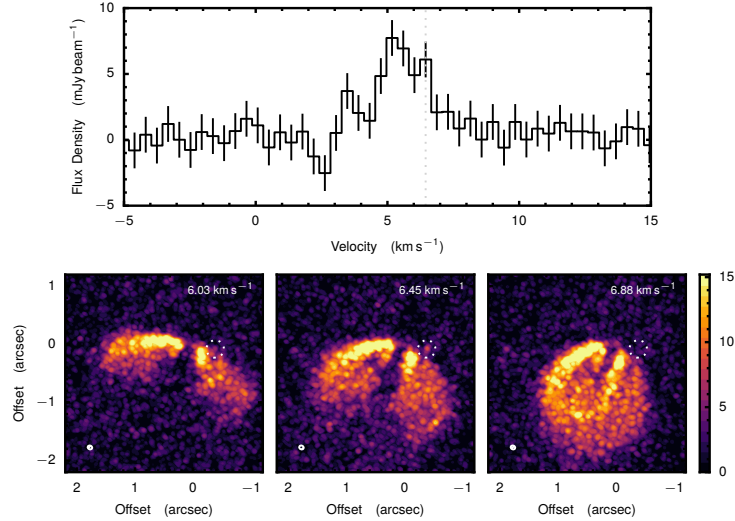


**Figure 3.13:** Top panel: CO line profile extracted at the location of the point source. Bottom panel: CO channel maps around  $6.45 \text{ km/s}$ . The white circle indicates the location of the point source.

ever. Interestingly, if it were located in the midplane, the source would be located well within the dust continuum ring, close to the dip between the main and the tentative second peak detected in the continuum profiles (see Sect. 3.3.1). Spatially offset emission has been shown to potentially be a signature of a CPD (Pérez et al., 2015), as the additional rotation of the CPD would shift the emission from the Keplerian pattern. If the signal were indeed connected to a forming embedded planet, this might explain the azimuthal gap found in the  $\text{HCO}^+$  emission at a similar location (Long et al., 2018b) because chemical changes due to heating from the planet may locally deplete  $\text{HCO}$  (Cleeves et al., 2015).

Additional observations are required to confirm the potential point source.

## 3.4 Discussion

As shown by theoretical studies, the interaction of a massive body with the disk opens a gap in the gas (e.g., [Lin & Papaloizou, 1986b](#)). The perturbation of the local gas density causes a change in the local pressure gradient, which manifests itself in two ways. First, it generates a pressure bump outside the planetary orbit, trapping large dust particles (while small particles that are well coupled to the gas may still enter the gap). This leads to a spatial segregation of large and small grains (e.g., [Pinilla et al., 2012a](#)). Second, the change in pressure gradient manifests itself in a local deviation from Keplerian rotation the amplitude of which is sensitive to the planet mass ([Teague et al., 2018a](#)).

Our aim is to investigate the impact of PDS 70 b on the observed disk morphology. For this purpose we carried out hydrodynamic and radiative transfer simulations that we present in the next section.

### 3.4.1 Hydrodynamic and radiative transfer models

#### Model setup

To simulate interaction between PDS 70 b and the circumstellar disk of PDS 70, we carried out three-dimensional hydrodynamic calculations using FARGO3D ([Benítez-Llambay & Masset, 2016; Masset, 2000](#)). We adopted the disk density and aspect ratio profiles used in [Chapter 2](#)

$$\Sigma_{\text{gas}}(R) = \Sigma_c \left( \frac{R}{R_c} \right)^{-1} \exp\left(-\frac{R}{R_c}\right) \quad (3.8)$$

and

$$\frac{H}{R} = \left( \frac{H}{R} \right)_p \times \left( \frac{R}{R_p} \right)^f, \quad (3.9)$$

where  $R_c = 40$  au,  $R_p = 22$  au is the distance of PDS 70 b assuming a circular orbit,  $(H/R)_p = 0.089$ , and  $f = 0.25$ .  $\Sigma_c = 2.87 \text{ g cm}^{-2}$  was chosen such that the total gas mass in the disk was  $0.003 M_\odot$ , consistent with the model presented in [Chapter 2](#). The surface density profiles are shown in [Fig. 3.14 \(a\)](#). We assumed a vertically isothermal disk temperature structure and used an isothermal equation of state.

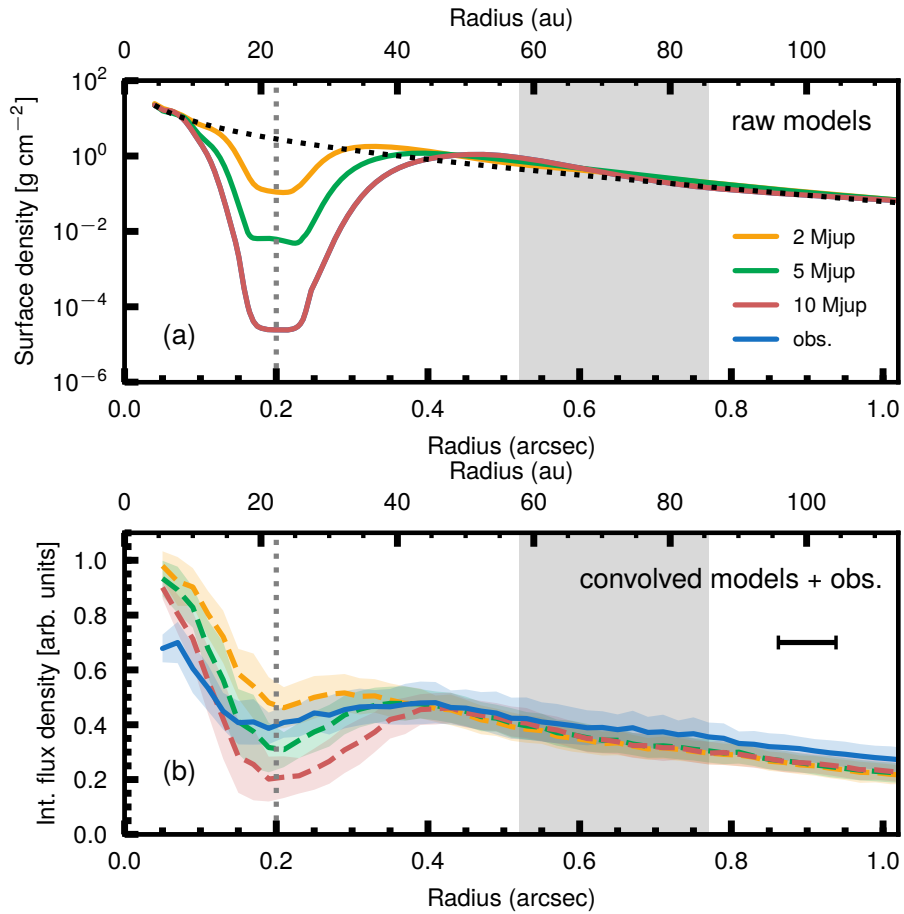


**Figure 3.14:** Comparison of hydrodynamical models including a 2  $M_{\text{Jup}}$  (yellow), 5  $M_{\text{Jup}}$  (green), and 10  $M_{\text{Jup}}$  (red) planet located at 0.2'' with the observations (blue). (a): Azimuthally averaged surface density profiles of hydrodynamical simulations. The dotted line corresponds to the initial unperturbed surface density profile. (b): Integrated azimuthally averaged CO flux density of observations and ALMA-simulated models, after applying  $2\sigma$  clipping. In each panel, the gray shaded area indicates the extension of the continuum ring, and the vertical dotted line corresponds to the approximate location of PDS 70 b. The black bar in the second panel indicates the major axis of the beam (0.076'').

The simulation domain extends from  $r = 0.2 R_p$  to  $9 R_p$  in the radial direction, from  $\pi/2 - 0.4$  to  $\pi/2$  in the meridional direction, and from 0 to  $2\pi$  in the azimuthal direction. We adopted 256 logarithmically spaced grid cells in the radial direction, 48 uniformly spaced grid cells in the meridional direction, and 420 uniformly spaced grid cells in the azimuthal direction. A disk viscosity of  $\alpha = 10^{-3}$  was added to the simulations. This value of turbulence is consistent with the level of turbulence constrained for the protoplanetary disks around TW Hya (Teague et al., 2016, 2018c; Flaherty et al., 2018) and HD 163296 (Flaherty et al., 2015, 2017).

### 3 A highly structured disk around the planet host PDS 70 revealed by high-angular resolution observations with ALMA

We tested three planet masses: 2, 5, and 10  $M_{\text{Jup}}$ , covering the range of potential planet masses proposed in Chapter 2, assuming a 0.85 solar-mass star. The simulations ran for 1000 orbits, after which we find that the gap width and depth reached a quasi-steady state. This is in agreement with other planet-disk interaction simulations from the literature (e.g., Duffell & MacFadyen, 2013; Fung et al., 2014; Kanagawa et al., 2015a). The radial profile of the deviations from Keplerian rotation after 1000 orbits is shown in Fig. 3.15 (b).

We generated  $^{12}\text{CO}$  image cubes using the radiative transfer code RADMC3D version 0.41<sup>15</sup>. We first computed the thermal structure of the disk by running a thermal Monte Carlo calculation. To do so, we placed a 0.85 solar-mass star at the center. This star had an effective temperature of 3972 K and a radius of 1.26  $R_{\odot}$  (Pecaut & Mamajek, 2016; Keppler et al., 2018), emitting  $10^8$  photon packages. As in Keppler et al. (2018), we considered two grain size distributions whose number density followed a power law as a function of the grain size  $a$  with  $n(a) \propto a^{-3.5}$ : small grains ranged from 0.001 to 0.15  $\mu\text{m}$  and large grains ranged from 0.15 to 1000  $\mu\text{m}$ . The relative mass fraction of small to large grains was 1/31, implying that about 3% of the total dust mass was confined within the small grain population. This is consistent with previous radiative transfer models of PDS 70 (Dong et al., 2012; Keppler et al., 2018). We assumed that the grains are composed of 70 % astronomical silicates (Draine, 2003b) and 30 % amorphous carbon grains (Zubko et al., 1996). The grain opacity was computed according to the Mie theory using the BHMIE code (Bohren & Huffman, 1983).

$\text{CO}$  line radiative transfer was done under local thermal equilibrium (LTE) assumptions, assuming a constant  $^{12}\text{CO}$  to  $\text{H}_2$  ratio of  $10^{-4}$  (e.g., Lacy et al., 1994; Williams & Best, 2014). A local spatially unresolved microturbulence was added at a constant level of 30  $\text{m s}^{-1}$ . This choice is equivalent to  $\alpha$  of a few  $\times 10^{-3}$ . We simulated the ALMA observations using the SIMOBSERVE task in CASA version 5.1.2. using the same velocity resolution, synthesized beam, and on-source integration time as were used in the observations. Thermal noise from the atmosphere and from the antenna receivers was added by setting the *thermalnoise* option in the *simobserve* task to *tsys-atm*. Using the same tools as for the observations, we derived the velocity-integrated flux density, as well as the rotation profiles for each simulation (Figures 3.14 and 3.15).

#### Comparison with observations

The disk density distribution from the hydrodynamic model and a simulated  $^{12}\text{CO}$  zeroth-moment map are presented in Fig. 3.16. The 5  $M_{\text{Jup}}$  planet opens a gap around its orbit, which is clearly visible in the simulated zeroth moment map. We find that velocity kinks associated with the planet-driven spiral arms are present in raw simulated channel maps,

---

<sup>15</sup><http://www.ita.uni-heidelberg.de/~dullemond/software/radmc-3d/>

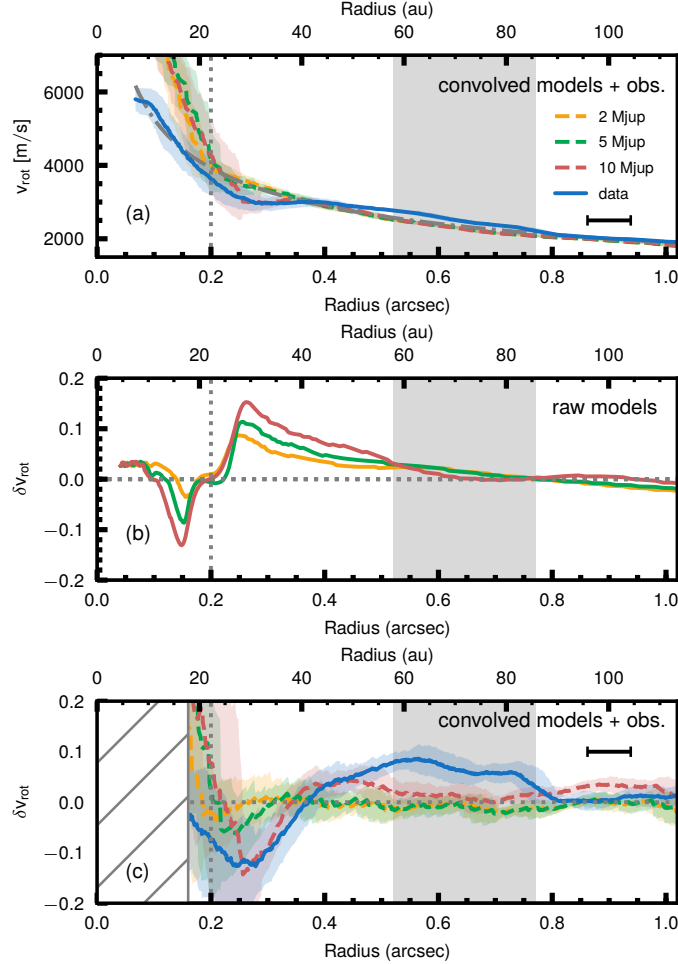


**Figure 3.15:** Comparison of hydrodynamical models including a 2  $M_{\text{Jup}}$  (yellow), 5  $M_{\text{Jup}}$  (green), and 10  $M_{\text{Jup}}$  (red) planet located at  $0.2''$  with the observations (blue). **(a):** Rotation velocity as a function of deprojected distance. The gray dash-dotted line indicates the unperturbed Keplerian profile around a  $0.88 M_{\odot}$  star. **(b):** Deviation from Keplerian rotation of the hydrodynamical simulations at the  $\tau=1$  surface. **(c):** Deviation from Keplerian rotation of ALMA-simulated models and observations. The plot shows the running mean and standard deviations. The inner region up to 160 mas is affected by beam confusion effects and is therefore blocked out. In each panel, the gray shaded area indicates the extension of the continuum ring, and the vertical dotted line corresponds to the approximate location of PDS 70 b. The black bar in the first and third panel indicates the major axis of the beam ( $0.076''$ ).

### 3 A highly structured disk around the planet host PDS 70 revealed by high-angular resolution observations with ALMA

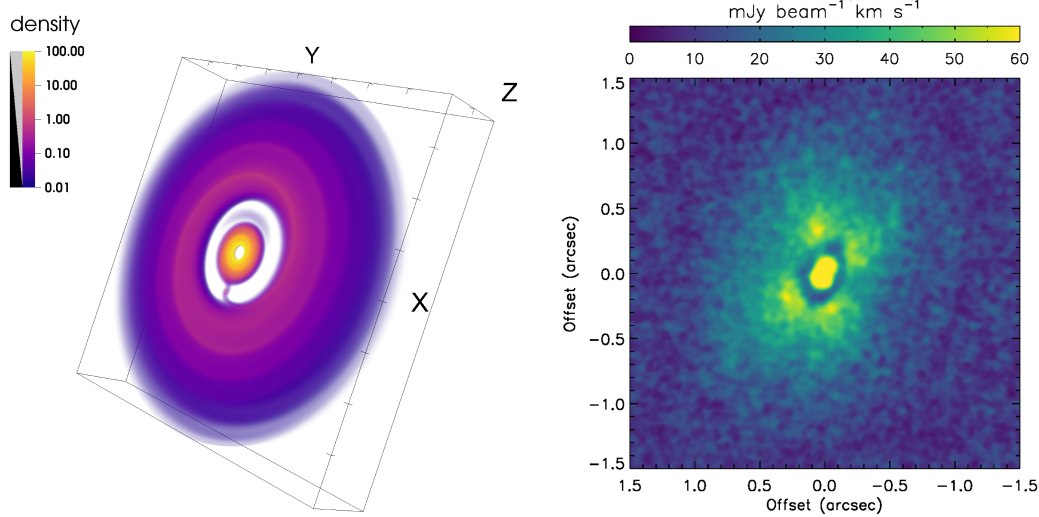


**Figure 3.16:** *Left:* Three-dimensional volume rendering of the gas density (in a normalized unit with logarithmic scaling) after evolution of 1000 orbits in the inner 100 au of the model disk with a  $5 M_{\text{Jup}}$  planet at 22 au. Ticks on the axes mark every 25 au. *Right:* Simulated  $^{12}\text{CO}$  zeroth-moment map based on the hydrodynamic model presented in the left panel.

similar to what is found in HD 163296 (Pinte et al., 2018b). However, the velocity distortions are too small and thus smeared out after convolution with the ALMA beam.

We compare the radial profiles of the simulated and observed integrated flux densities in Figure 3.14 (b). The profiles show evidence of a depletion in integrated flux density at the location of the planet, which is stronger for higher planet masses. The width and depth of the depleted flux density in the observations are reasonably well reproduced by a  $5 M_{\text{Jup}}$  planet. We note that the models appear to overestimate the increase in flux density toward the inner disk. Because CO is optically thick, this is likely caused by a different temperature structure of the inner disk region, the reason for which could be a different density profile than assumed (e.g., overestimation of the actual density in the inner part of the disk, or a different gap shape), but needs further investigation with higher angular resolution that is able to better resolve these inner regions.

Figure 3.15 (panel a) presents the absolute rotation profiles, and the residual  $\delta v_{\text{rot}}$  profiles before and after radiative transfer and ALMA simulations are shown in panels b and c, respectively. We note two points: first, a comparison of the residual model profiles before and after convolution alters the overall shape of the rotation curves. Second, the residual curve of the PDS70 disk follows the general shape of the modeled curves, but it differs with respect to the location of the maximum, as well as the velocity gradient toward the inner disk.

The change in the shape of the rotation curve when simulating the observations is due to beam convolution effects in the presence of strong radial gradients in intensity and velocity. As described in Sect. 3.3.2, sharp edges in the flux density profile induce a dis-

tortion in the measurement of the rotation curve because the velocities measured within one beam are biased toward those at the highest line intensity. This causes the velocity to be overestimated in the inner region of the gap and underestimated at the outer edge of the gap.

The resulting rotation curve is of a characteristic shape that is asymmetric with respect to the gap center (see Fig. 3.11). It shows evidence of strong super-Keplerian rotation in the inner gap region, and a weaker region of sub-Keplerian rotation at the outer gap edge. This effect is now superimposed on the effect of the planet-induced pressure gradient on the rotation profile (sub-/super-Keplerian rotation inside/outside the planetary orbit). This effect can be fully accounted for when performing forward modeling. As Fig. 3.15 (c) shows, all convolved model profiles show this characteristic shape, and the amplitudes of their minima and maxima depend on the planetary mass.

The observed rotation curve of PDS 70 shows the same characteristic transition from sub-Keplerian to super-Keplerian transition as the models. While we found that the width and depth of the integrated flux density profiles seem consistent with the effect of a  $5 M_{\text{Jup}}$  planet, we find that the radial location and the amplitude of the minimum  $\delta v_{\text{rot}}$  of the rotation curve of the PDS 70 disk is best matched by the perturbations created by a  $10 M_{\text{Jup}}$  planet. We note, however, that our hydrodynamic models consider a vertically isothermal temperature structure, whereas in a more realistic approach (introducing a more physical prescription for the vertical temperature structure), the deviation from Keplerian rotation may be higher in the disk surface than in the midplane, implying that the  $\delta v_{\text{rot}}$  in the current models may be underestimated (Bae et al in prep.; see also Fig. 3 of Teague et al., 2018a). Relaxing the isothermal assumption and introducing a more physical prescription of the vertical temperature structure may be able to solve this discrepancy, but is beyond the scope of this study.

Toward the inner region the observed rotation curve is flatter, which may again be due to a slightly different gap shape (i.e., a flatter inner edge). The most conspicuous difference to the models is the region of super-Keplerian rotation beyond the planet, which extend farther out than in the models. As shown in Sect. 3.3.2, within the uncertainties, the observed rotation curve returns to Keplerian rotation close to the location of maximum emission in the continuum ring ( $\sim 0.65''$  or 74 au) (see Fig. 3.10). This is consistent with the interpretation of large grains being trapped in the region of maximum pressure (e.g., Pinilla et al., 2012a). While we have shown that the observed integrated flux density profile can be reproduced well by one planet of  $5 M_{\text{Jup}}$ , the large extension of super-Keplerian rotation and the concomitant far-out location of the continuum ring imply that the gap is wider in reality than predicted by all the models. It therefore appears within our model assumptions that only one planet located at the orbit of PDS 70 b may not be sufficient to generate a kinematic signature in the disk with the inferred width or maintain a contin-

### 3 A highly structured disk around the planet host PDS 70 revealed by high-angular resolution observations with ALMA

uum ring at  $\sim 74$  au. This scenario needs to be probed by future observations at higher spectral resolution.

This is consistent with gap width considerations in the literature. As an example, hydrodynamical and dust simulations suggest that the accumulation of large dust grains is expected to be found at roughly  $10 r_{\text{H}}$  outward of the planetary orbit (Pinilla et al., 2012a; Rosotti et al., 2016). For a  $10 M_{\text{Jup}}$  planet at the location of the PDS 70 b orbit, the dust ring would therefore be expected at about 46-56 au, assuming a stellar mass of  $0.88 M_{\odot}$ .

This suggests that an additional low-mass planet located beyond PDS 70 or the combination with other physical mechanisms such as photoevaporation or dead zones may be needed to explain the outward-shifted location of the pressure bump. Models indeed predict that large gaps in transitional disks can be reproduced by introducing multiple planets (Dodson-Robinson & Salyk, 2011; Zhu et al., 2011; Duffell & Dong, 2015). Detailed modeling of the system by introducing multiple planets as well as deep observations are required to constrain the planetary architecture that is responsible for the observed features; this is beyond the scope of this study.

An alternative scenario to explain the distant location of the ring compared to the position of PDS 70 b is to consider that the ring traces a secondary pressure bump. Single planets can indeed open multiple gaps in a disk with low viscosity, or alternatively, vortices generated at the edge of a gap can lead to a secondary ring (Lobo Gomes et al., 2015). In this latter scenario, the primary ring, located at  $\sim 50$  au (corresponding to  $\sim 10 r_{\text{H}}$  from a  $5 M_{\text{Jup}}$  planet at 22 au), would be depleted. The secondary ring would be located at  $\sim 1.5 \times$  the location of the primary ring (Lobo Gomes et al., 2015), corresponding to  $\sim 75$  au, which is where the dust ring is found in the PDS 70 system. Furthermore, secondary vortices may be generated at the edge of the secondary ring. If this is the case, this may also explain the azimuthal asymmetry observed in the dust continuum. A detailed exploration of this scenario will be the subject of a follow-up study.

#### 3.4.2 Upper limit on CPD dust mass

The detection of  $\text{H}\alpha$  emission at the location PDS 70 implies that PDS 70 b is actively accreting (Wagner et al., 2018) and therefore likely possesses an accretion disk. Still, we can only derive upper limits on the circumplanetary disk with our data. Models of planet formation predict circumplanetary dust around young planets, implying that CPDs should be frequent. However, searches for circumplanetary material in the submillimeter/millimeter continuum around other young substellar companions have been unsuccessful, although active accretion through the  $\text{H}\alpha$  and/or  $\text{Pa}\beta$  lines was detected in some of these cases (e.g., Isella et al., 2014; Bowler et al., 2015; MacGregor et al., 2017; Wolff et al., 2017; Ricci et al., 2017; Pineda et al., 2019). Our upper limit on the CPD dust content of  $\sim 0.01$

$M_{\oplus}$  is similar to that derived for other systems (Pineda et al., 2019).

The detection of CPDs in the (sub-)millimeter regime may be challenging for several reasons. First, CPDs are expected to be very small, which substantially reduces the emitting area and therefore the expected signal. Second, because the large grains are substantially trapped in the outer dust ring, the replenishment of large grains within the gap is expected to be inefficient. Even if small grains pass the gap and replenish the CPD, the radial drift is expected to be extremely efficient when they grow. The radial drift will deplete the large grains very fast (Pinilla et al., 2013; Zhu et al., 2018). A search for the CPD using gas kinematics as a tracer or NIR observations might therefore be more promising.

### 3.5 Summary and conclusions

The young planet PDS 70 b is the most robust case of a directly imaged forming planet in the gap of a transition disk. We obtained ALMA Band 7 DDT observations in Cycle 5 and combined them with previous Cycle 3 data (Long et al., 2018b) to study the natal environment of the planet at high angular resolution ( $\sim 0.07''$ ) in dust continuum and at the  $^{12}\text{CO}$  J=3-2 transition. Our conclusions are listed below.

- We detected the emission from the dust continuum as a highly structured ring. Its radial distribution peaks at  $\sim 74$  au. The inner edge of the ring shows evidence of a marginally resolved second ring component that peaks at around 60 au. We also detected a spur that projects into the gap at a PA of about  $285^\circ$  and confirmed an azimuthal brightness asymmetry with a brightness enhancement of about 13% in the northwest part of the ring.
- We derived upper limits on the circumplanetary disk. Based on the noise level of the image we infer a  $5\sigma$  upper dust limit lower than  $\sim 0.01 M_{\oplus}$ .
- The CO-integrated intensity shows evidence of two radial intensity depressions; the inner depression of the flux density lies at  $\sim 0.2''$  (corresponding to the location of PDS 70 b) and a second gap at about  $0.6''$ . The inner gap is most likely carved by PDS 70 b. Comparison of the flux density profile to hydrodynamical simulations showed that the gap width and depth is best reproduced by a  $5 M_{\text{Jup}}$  body. The outer gap can be explained by the dust being optically thick. Furthermore, we found evidence for an azimuthal intensity modulation that is due to self-absorption by optically thick CO. We also detected a bridge-like feature in the CO at the location of the spur seen in the continuum as well as the inner disk, which extended out to  $\sim 15$  au. Finally, we reported the tentative detection of a possible point source in the

### 3 A highly structured disk around the planet host PDS 70 revealed by high-angular resolution observations with ALMA

$^{12}\text{CO}$  emission maps, the existence of which needs to be confirmed with additional observations.

- We detected significant deviation from Keplerian rotation inside  $\sim 0.8''$ . The width of the  $\delta v_{\text{rot}}$  feature is consistent with the far-out location of the dust ring. Comparison to hydrodynamical simulations implies that the depth of the kinematic signature is best matched by a  $\sim 10 M_{\text{Jup}}$  object (within our model assumption of an isothermal disk), but the width of the feature suggests that one planet alone located at the orbit of PDS 70 b may not be sufficient to generate a gap with the inferred extension. An additional physical mechanisms or a second low-mass body may be required to explain the disk morphology. Future observations at higher angular and spectral resolution will allow us to place tighter constraints on the planetary system architecture that can account for all of the observed features in the PDS 70 disk morphology.

These observations presented in this Chapter demonstrate the potential of PDS 70 to test planet-disk interactions by the comparison of sub-millimeter interferometric data with hydrodynamical simulations. The observations show that PDS 70 b is carving a deep gap in both, dust and gas as predicted by theoretical models, and that the continuum ring is consistent with the trapping of pebble-sized particles at the outer edge of the gap. As pointed out in Sect. 2.8, a second planet in the system, PDS 70 c, was discovered by [Haffert et al. \(2019\)](#) after the publication of the work presented in this Chapter.

## 3.6 Follow-up studies

This Section summarizes recent findings reported in the literature which followed the publication of the data presented in this Chapter, and which are relevant for the subsequent Chapter. Among the below discussed papers, I have contributed as a co-author to [Isella et al. \(2019\)](#) and [Bae et al. \(2019\)](#).

### 3.6.1 Discovery of continuum emission associated with the PDS 70 protoplanets

Following the publication of the work presented in this Chapter, the data processing was revisited by [Andrea Isella](#), revealing two inaccuracies in the presented data calibration ([Isella et al., 2019](#)). First, the pipeline calibration of the observations acquired in 2016 by [Long et al. \(2018b\)](#) had applied an incorrect calibrator flux. As a result, the flux density of the disk presented in this Chapter, which included the data from [Long et al. \(2018b\)](#), was overestimated by about 25%. Moreover, in contrast to our self-calibration attempts

leading to no significant improvement of the data quality, [Isella et al. \(2019\)](#) found an improvement of the peak S/N by about 40% by applying self-calibration. The reason why the self-calibration of the data reduction presented in Sect. 3.2 failed is due to an incorrect setting of the `spwmap` parameter in the CASA task `applycal`. This parameter defines the calibration table solutions obtained from which spectral window are applied to which window. Only if this parameter is set correctly, the self-calibration is properly applied, which was not the case for the reduction presented in this Chapter. It should be noted that this did not affect the morphology of the outer disk (which was our major subject in this Chapter), but lead to a not optimized noise level.

The improved self-calibration by [Isella et al. \(2019\)](#) allowed to push the noise level in the continuum down to  $\sim 19 \mu\text{Jy beam}^{-1}$ . The final image revealed a spatially unresolved source in the dust continuum at the location of PDS 70 c at a S/N of  $\sim 5.6$ . This source is coincidental with the ‘spur’ reported in this Chapter, which, however, did not appear detached from the outer ring in our data reduction. The spatially unresolved detection of continuum emission by [Isella et al. \(2019\)](#) being co-spatial with an accreting planet is highly suggestive for the presence of circumplanetary dust thermally emitting at sub-millimeter wavelengths. The measured peak intensity of  $106 \pm 19 \mu\text{Jy beam}^{-1}$  by [Isella et al. \(2019\)](#) suggests a circumplanetary disk with a dust mass between  $2 \times 10^{-3} M_{\oplus}$  and  $4.3 \times 10^{-3} M_{\oplus}$ . This results means a benchmark detection of the first CPD with ALMA.

Another compact continuum source was detected by [Isella et al. \(2019\)](#) close to the location of PDS 70 b. However, because of a spatial offset of  $\sim 74$  mas from the NIR counterpart of PDS 70 b, its nature remained inconclusive and needs to be confirmed through follow-up observations.

The presence of circumplanetary dust around both planets has also been inferred from NIR observations. As pointed out in Chapter 2 and in [Müller et al. \(2018\)](#), the very red photometric colors, the featureless spectrum and larger than expected radii derived for PDS 70 b may be explained by a contribution of spatially unresolved circumplanetary material to the measured flux. Indeed, [Christiaens et al. \(2019\)](#) found in their spectrum of PDS 70 b taken with VLT/SINFONI excess emission beyond  $\sim 2 \mu\text{m}$ , which they could most plausibly model with a combination of planetary atmospheric and CPD emission. Similarly, the very red colors found for PDS 70 c ([Mesa et al., 2019](#); [Wang et al., 2020](#)) are indicative for the presence of dust.

### 3.6.2 Planet-disk interactions in the presence of two planets

Knowing of the existence of PDS 70 c, [Bae et al. \(2019\)](#) run hydrodynamical simulations of planet-disk interaction including both planets, PDS 70 b and c. These simulations showed that the observed features, such as the radial location of the wide continuum

*3 A highly structured disk around the planet host PDS 70 revealed by high-angular resolution observations with ALMA*

ring, trapping pebble-sized dust grains at large distances, is well in agreement with the simulations. The simulations also suggested that the planets settled into 2:1 mean motion resonance early in their evolution, and could remain dynamically stable over timescales of several million years.

# 4

## An in-depth view of PDS 70 with ALMA at high spectral resolution

---

The content of this Chapter is based on a paper in preparation by Keppler et al., *in prep.*

### 4.1 Motivation

High-angular resolution observations across a range of wavelengths from the optical to the (sub-)millimeter regime during the last years have revealed a stunning variety of substructures within protoplanetary disks (e.g., Andrews et al., 2018; Long et al., 2018a; Avenhaus et al., 2018). Many of the detected gaps, rings, and spirals are thought to be signposts of ongoing planet formation. Great advancements in theory have been put forward to understand the details of planet-disk interactions (e.g., Papaloizou et al., 2007; Kley & Nelson, 2012; Baruteau et al., 2014; Bae et al., 2018, and references therein), and to establish how the observed disk structures can be related to the properties of the putative planets driving them (e.g., de Juan Ovelar et al., 2013; Dong et al., 2015b; Kanagawa et al., 2015a; Rosotti et al., 2016; Dong & Fung, 2017; Zhang et al., 2018; Lodato et al., 2019).

Into particular focus has recently come the potential of molecular line observations with ALMA as a tool to trace the presence of embedded planets within disks. As explained in Sect. 1.4, the interaction of a forming giant planet with the surrounding gas is thought to imprint in the disk as a kinematic signature, which can be revealed by e.g., deviations of the azimuthally averaged rotation curve from a smooth, Keplerian profile (Teague et al., 2018a), by spatial distortions of the disk emission in individual channel maps (Pinte et al., 2018b), by residuals in the rotation (i.e., first moment) maps after subtraction of the disk rotation curve (Pérez et al., 2018), or by a local broadening of the spectral line shape, due to the vertical motion of the gas within planet-induced gaps (Dong et al., 2019) or by the rotation of the CPD itself (Perez et al., 2015).

Several planet candidates have been inferred through their kinematic signatures (Teague et al., 2018a; Pinte et al., 2018b, 2019, 2020; Casassus & Pérez, 2019; Pérez et al., 2020). So far, they have eluded confirmation from direct imaging, at least for the cases

where such observations are available (Ginski et al., 2016; Guidi et al., 2018; Rich et al., 2019), which suggests that their masses are lower than the current detection limits provided by high-contrast imaging, or that they are highly extinguished by the circumstellar material.

With two directly imaged planets embedded within a circumstellar disk, PDS 70 is thus a unique testbed to probe the effects of planet-disk interactions on the gas kinematics. While in the previous Chapter we introduced and analyzed ALMA data of PDS 70 at high spatial resolution, we present in this Chapter a new dataset at similar angular resolution, but four times higher spectral resolution, since a sufficiently high spectral resolution is key to unravel the kinematic structure of the disk. The main aim of these observations is to search for direct and indirect imprints of the planets in the gas structure of the disk, traced by  $^{12}\text{CO}$  and  $^{13}\text{CO}$ . Section 4.2 summarizes the observations and data reduction strategy. We present our results in Sect. 4.3 which are discussed in Sect. 4.4. Section 4.5 provides a summary of the chapter.

## 4.2 Observations and data reduction

PDS 70 was observed by ALMA in Band 7 with five executions on 2019 August 13, 16, 19 and 21 as part of project 2018.1.01774.S (PI: M. Keppler). Two executions were carried out during the same night (August 19). The total time on source was about 4.2 hours. The array included 46 antennas, configured to cover baseline lengths from 41 m to 3.6 km. The precipitable water vapor (PWV) levels reached minimum and maximum values of  $\sim 0.4$  mm (August 13) and  $\sim 1.0$  mm (August 19). The correlator processed five spectral windows centered at 330.6, 333.1, 343.5, 345.3 and 345.8 GHz with bandwidths of 234, 1875, 1875, 117, and 117 MHz, respectively. This set up ensured to include the  $^{12}\text{CO}$  J=3-2 transition at 345.8 GHz,  $^{13}\text{CO}$  J=3-2 at 330.6 GHz, and  $\text{H}^{13}\text{CN}$  J=4-3 at 345.3 GHz. Quasar J1427-4206 was used for amplitude and bandpass calibration. Phase calibration was performed using J1407-4302.

Because after completion the resulting beam was found to be slightly larger than what was requested in the proposal, the observations formally failed the quality assurance process by ALMA. Additional observations are being scheduled for the next period as soon as the proper configuration is offered again in order to reach the requested beam size. Because the configuration schedule did not allow to obtain these additional observations within a time of three months, we requested the delivery of the intermediate data according to the stale data policy<sup>16</sup>. These intermediate data are the subject of this Chapter, and

---

<sup>16</sup>see p.13 of ALMA User's Policies, <https://almascience.eso.org/documents-and-tools/cycle4/alma-user-policies>

will be complemented as soon as the additional observations are carried out.

The data were calibrated by the pipeline in CASA v5.6. before moving to CASA v5.4. for imaging and self-calibration. As a first step, the data were time-averaged by  $\sim 6$  seconds in order to reduce the size of the data. In order to properly center the data, we fitted an ellipse to the outer continuum ring in the image plane. The center of the fitted ellipse, J2000 14h08m10.1026s -41d23m53.0269s, was subsequently applied for the centering process using the `fixvis` task. As a cross-check, we repeated the ellipse fitting on our previous continuum data at comparable angular resolution presented in Chapter 3, which were observed in December 2017. We find a shift of the ellipse center between December 2017 and August 2019 of  $\sim 41$  mas, which is slightly less than the expected proper motion of the star during that time interval of  $\sim 65$  mas (Gaia Collaboration et al., 2016, 2018). We then shifted the coordinate system using the `fixplanets` task to J2000 14h08m10.107s -041.23.52.996, in order to be compatible with the coordinates from Isella et al. (2019). This is a crucial step in order to be able to properly combine datasets taken at different observation epochs. In order to account for small variations in the absolute flux scale between the different executions, the individual executions was rescaled to match the absolute flux of the first execution, which shows evidence of the highest S/N and lowest PWV value.

#### 4.2.1 Continuum self-calibration and imaging

To generate the continuum, all channels with line emission, as well as those showing unphysical emission at the edges of the spectral windows were flagged. Then, the channels were averaged with a channel bandwidth of 125 MHz to further decrease the size of the data. We then performed four rounds of phase self-calibration on the continuum. In the first round phase gains were calculated on a time interval corresponding to the scan length, independently for each spectral window in order to correct of any phase offset between the spectral bands. In a second iteration, phase gains were computed for each polarization independently. In the third and fourth round, we averaged on polarizations and spectral windows, using solution intervals of 300 and 60 seconds, respectively. We discarded a final round of amplitude self-calibration since it lead to worse results. As can be seen in Fig. 4.1, the self-calibration did improve the overall noise structure, which appears quite uniform after the self-calibration process. We produced the final image using briggs weighting with five different values for the robust ( $r$ ) parameter ( $r = -0.3, r = 0.0, r = 0.3, r = 0.5, r = 2.0$ ). The resulting beam size, disk integrated flux density, image rms and peak S/N are reported in Table 4.1. Using  $r = 0.0$  we obtain an angular resolution similar to the continuum image presented in Chapter 3, while achieving a slightly lower image rms ( $22.7 \mu\text{Jy beam}^{-1}$  for our new data versus  $26 \mu\text{Jy beam}^{-1}$  of that presented in Chapter 3). The final continuum image has a frequency of 338.2 GHz

(887  $\mu\text{m}$ ).

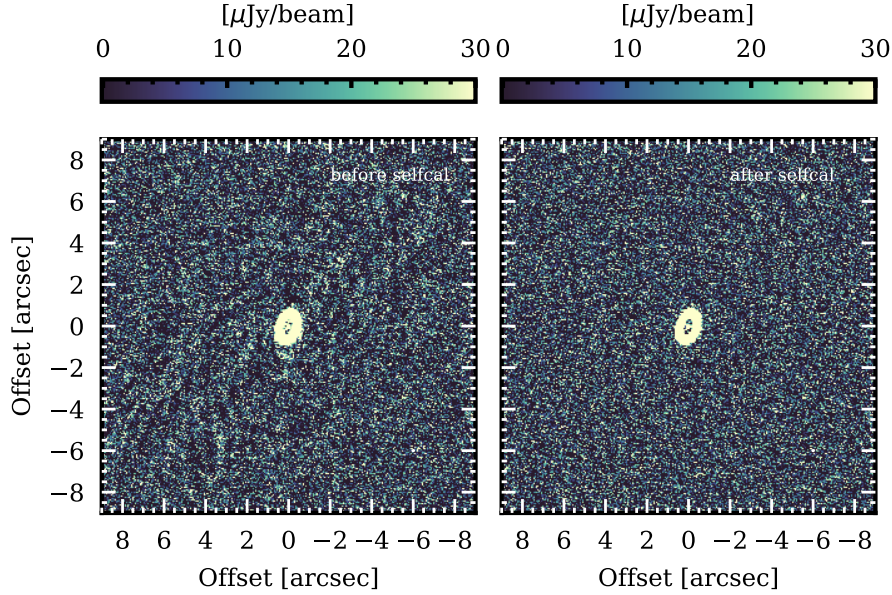


**Figure 4.1:** Zoom out of continuum (‘LB2’) image before (*left*) and after (*right*) self-calibration imaged with briggs weighting using robust  $r = 0.5$ . The color stretch is chosen such to optimize the display of the noise structure.

## 4.2.2 CO imaging

We applied the solutions from the continuum self-calibration to the  $^{12}\text{CO}$  and  $^{13}\text{CO}$  data, before subtracting the continuum using the `uvcontsub` task. Imaging was then performed applying a Keplerian mask, assuming the stellar and disk parameters as derived in Chapter 3. We generated cubes with channel widths of 110 m/s for  $^{12}\text{CO}$  and of 120 m/s for  $^{13}\text{CO}$  using robust parameters of  $r = 0.0, 0.3, 0.5, 2.0$ .

## 4.2.3 Combination with previous data

In addition to the new data presented in this Chapter, PDS 70 has been observed with ALMA in Band 7 within two other programs at a lower spectral resolution, as presented in Long et al. (2018b) and Keppler et al. (2019) (see Chapter 3). Although the focus in this Chapter is set on the spectral analysis of the PDS 70 disk, requiring the highest spectral resolution possible, we prepared a complementary dataset combining the visibilities of all these three datasets in order to maximise the sensitivity, however, at the cost of spectral resolution. In order to avoid confusion, we will in the following refer to the data obtained by Long et al. (2018b) including mostly short baselines, as ‘SB1’, while the data including longer baselines presented in Keppler et al. (2019) (Chapter 3) will be denoted as ‘LB3’,

	$r = -0.3$	$r = 0.0$	$r = 0.3$	$r = 0.5$	$r = 2.0$
<b>continuum ('LB2')</b>					
beam size	$0.071'' \times 0.052''$	$0.075'' \times 0.055''$	$0.081'' \times 0.061''$	$0.087'' \times 0.065''$	$0.110'' \times 0.084''$
disk total flux [mJy]	199.6	197.9	198.1	197.6	199.0
rms [ $\mu$ Jy beam <sup>-1</sup> ]	29.6	22.7	18.8	17.3	16.4
peak S/N	53.9	78.2	111.3	138.0	216.0
<b>continuum combined ('SB1+LB2+LB3')</b>					
beam size	$0.054'' \times 0.038''$	$0.060'' \times 0.045''$	$0.068'' \times 0.054''$	$0.076'' \times 0.060''$	$0.103'' \times 0.085''$
disk total flux [mJy]	161.7	161.7	161.8	161.9	165.6
rms [ $\mu$ Jy beam <sup>-1</sup> ]	21.6	16.3	13.1	12.1	15.0
peak S/N	37.0	61.8	102.3	135.3	192.4
<sup>12</sup> CO ('LB2')					
beam size	-	$0.073'' \times 0.059''$	$0.079'' \times 0.063''$	$0.085'' \times 0.066''$	$0.110'' \times 0.082''$
rms [mJy beam <sup>-1</sup> ]	-	2.6	2.2	2.1	1.8
<sup>12</sup> CO combined ('SB1+LB2+LB3')					
beam size	-	$0.071'' \times 0.055''$	$0.078'' \times 0.061''$	$0.083'' \times 0.067''$	$0.105'' \times 0.087''$
rms [mJy beam <sup>-1</sup> ]	-	1.2	1.0	0.9	0.8
<sup>13</sup> CO ('LB2')					
beam size	-	$0.077'' \times 0.061''$	$0.084'' \times 0.065''$	$0.090'' \times 0.068''$	$0.112'' \times 0.084''$
rms [mJy beam <sup>-1</sup> ]	-	3.1	2.8	2.5	2.2

**Table 4.1:** Imaging results for our new ('LB2') and combined ('SB1+LB2+LB3') datasets.

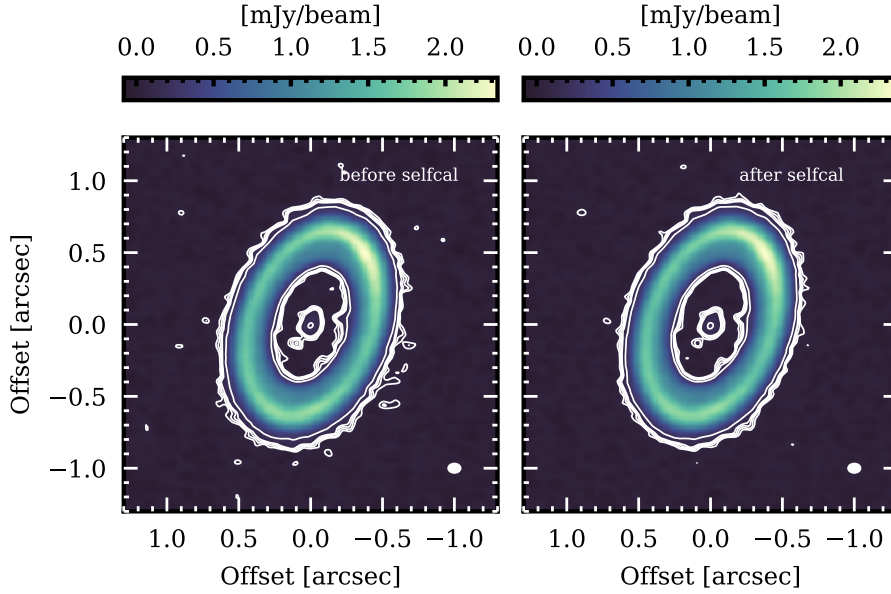


**Figure 4.2:** Zoom out of continuum (‘LB2’) image before (*left*) and after (*right*) self-calibration imaged with briggs weighting using robust  $r = 0.5$ . White contours are drawn at  $3, 4, 5, 6, 12 \times \sigma$ . The beam is shown on the lower right corner.

whereas those introduced in this Chapter will be named ‘LB2’. The combined dataset will therefore be referred to as ‘SB1+LB2+LB3’.

In order to perform the combination, we first fitted ellipses on the continuum ring of each dataset, and re-centered each of them on the resulting ellipse center. We rescaled the absolute flux of each dataset, taking the flux scale of the ‘LB3’ observations as a reference. We then combined the data using the `concat` task and performed five rounds of phase self-calibration on the continuum, going down to a solution interval of 30 seconds.

We also used the combined dataset to image the  $^{12}\text{CO}$  cubes, using a channel width of 425 m/s. Note that no self-calibration was applied to the combined  $^{12}\text{CO}$  data; this step will be part of future work. The  $^{13}\text{CO}$  line was not included in the previous datasets, so no combined datacubes could be produced. The resulting image properties for both continuum and  $^{12}\text{CO}$  are listed in Table 4.1.

## 4.3 Results

### 4.3.1 Continuum

This section presents an analysis of the morphology observed in the dust continuum. Our goal is to provide an analysis which is as independent from previous data as possible. We will therefore focus mostly on the new dataset (‘LB2’). Only in context of the potential CPD

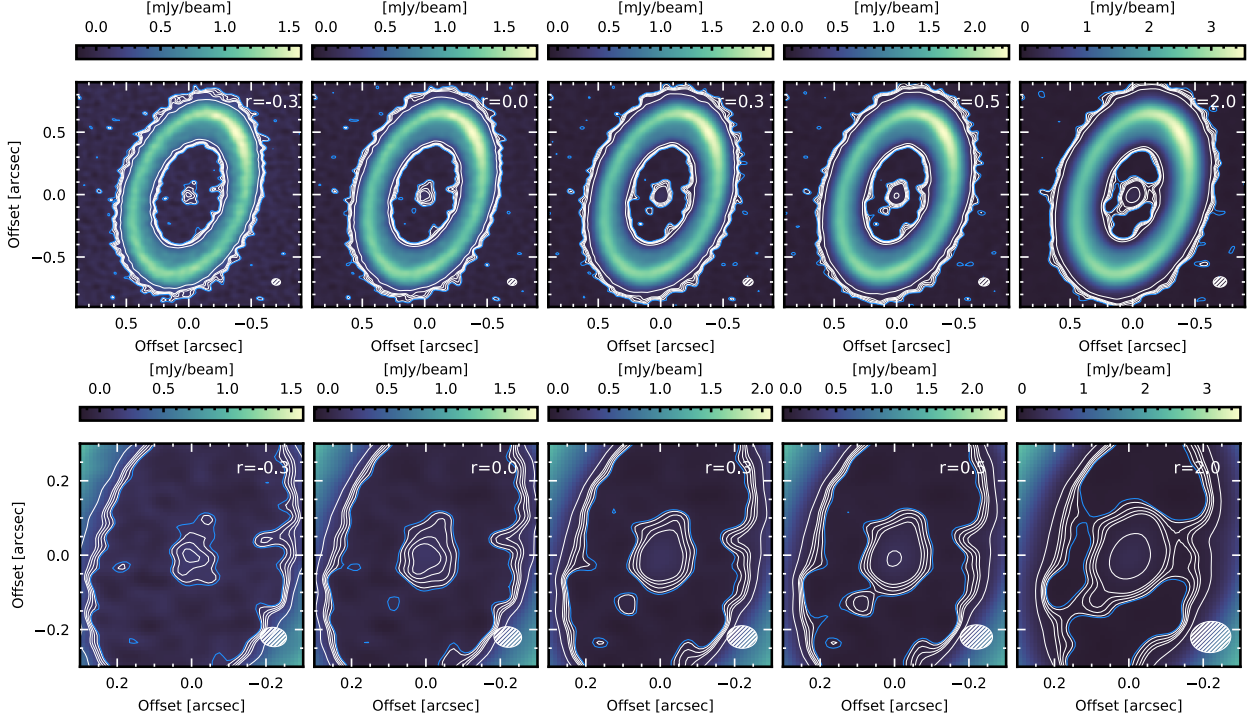


**Figure 4.3:** Continuum images of our new dataset (‘LB2’) after self-calibration imaged with different robust parameters ( $r = -0.3, 0.0, 0.3, 0.5, 2.0$ ; from left to right). White contours are drawn at  $3, 4, 5, 6, 12 \sigma$ . The blue contour corresponds to  $2.5 \sigma$ . The beam is shown on the lower right corner. The bottom row corresponds to a zoom-in view of the top row. North is up and East is to the left.

signals (Sect. 4.3.1), we will also take into account the combined dataset (‘SB1+LB2+LB3’).

### Outer disk

The final continuum images reconstructed with different robust parameters are shown in Fig. 4.3. Similar to our previous observations in Chapter 3, the disk appears as a large, ring-like structure with a faint inner disk component in the center.

The total flux density of the disk integrated over an elliptical mask with a semi-major axis of  $1.5''$  and a semi-minor axis of  $0.975''$  is  $\sim 199$  mJy, as reported in Table 4.1. We note that this result is in contrast with the value of 177 mJy reported by Isella et al. (2019). However, there is a slight difference in wavelength: while the data referred to in Isella et al. (2019) have a wavelength of  $850 \mu\text{m}$ , our new data presented in this Chapter were observed at a wavelength of  $887 \mu\text{m}$ . Typically, the spectral energy distribution of TDs at sub-millimeter wavelengths falls off with a slope  $\alpha_{\text{mm}}$  (also denoted as millimetre spectral index) of  $\sim 2-3.5$  (Pinilla et al., 2014). Assuming a spectral index of  $\alpha_{\text{mm}} = 2.5$ , we would expect the integrated flux density of the new data to be  $\sim 9\%$  lower with respect to the previous data, while it is actually  $\sim 12\%$  higher. The uncertainty on the absolute flux

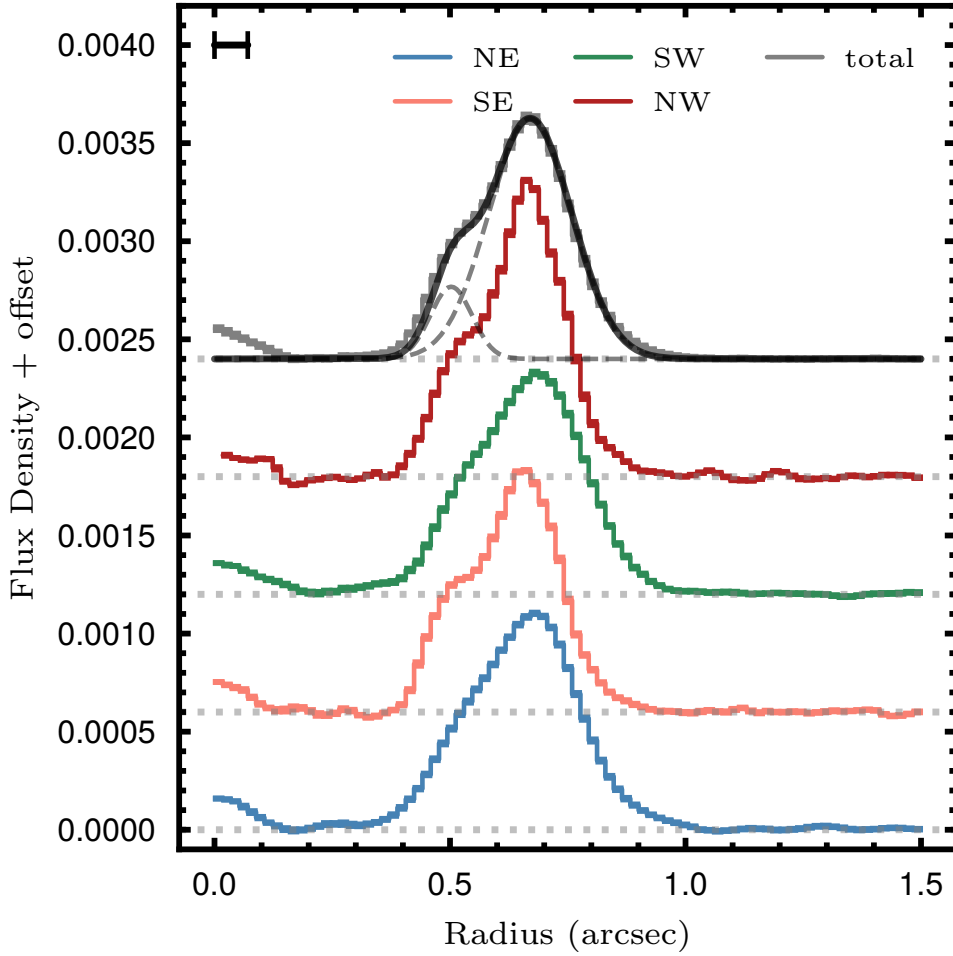


**Figure 4.4:** Radial profiles of the  $r = -0.3$  continuum image of the new dataset (‘LB2’) along the major axis (red, yellow), as well as along the minor axis (blue, green), and averaged over the entire azimuth (grey). The black solid line traces the best-fit radial profile resulting from a composition of two Gaussians, drawn with gray dashed lines. The beam major axis of the image is indicated on the upper left corner.

calibration with ALMA is on the order of  $\sim 10\%$ <sup>17</sup>, thus, it could marginally account for these differences. Still, the origin of the flux differences needs to be investigated in detail in order to exclude any possible issue during the calibration process. For this reason, the absolute flux scales reported in this Chapter need to be taken with some caution and are considered to be preliminary.

Figure 4.4 shows the radial profiles of the continuum image (using  $r = -0.3$ ) along the disk major and minor axes, as well as averaged over the entire azimuth. We clearly see a ripple at the inner edge of radial profile along the major axis, as well as of the azimuthally averaged profile. The feature was already pointed out in Chapter 3, although it appeared

<sup>17</sup>see ALMA technical handbook: <https://almascience.eso.org/documents-and-tools/latest/documents-and-tools/cycle8/alma-technical-handbook>

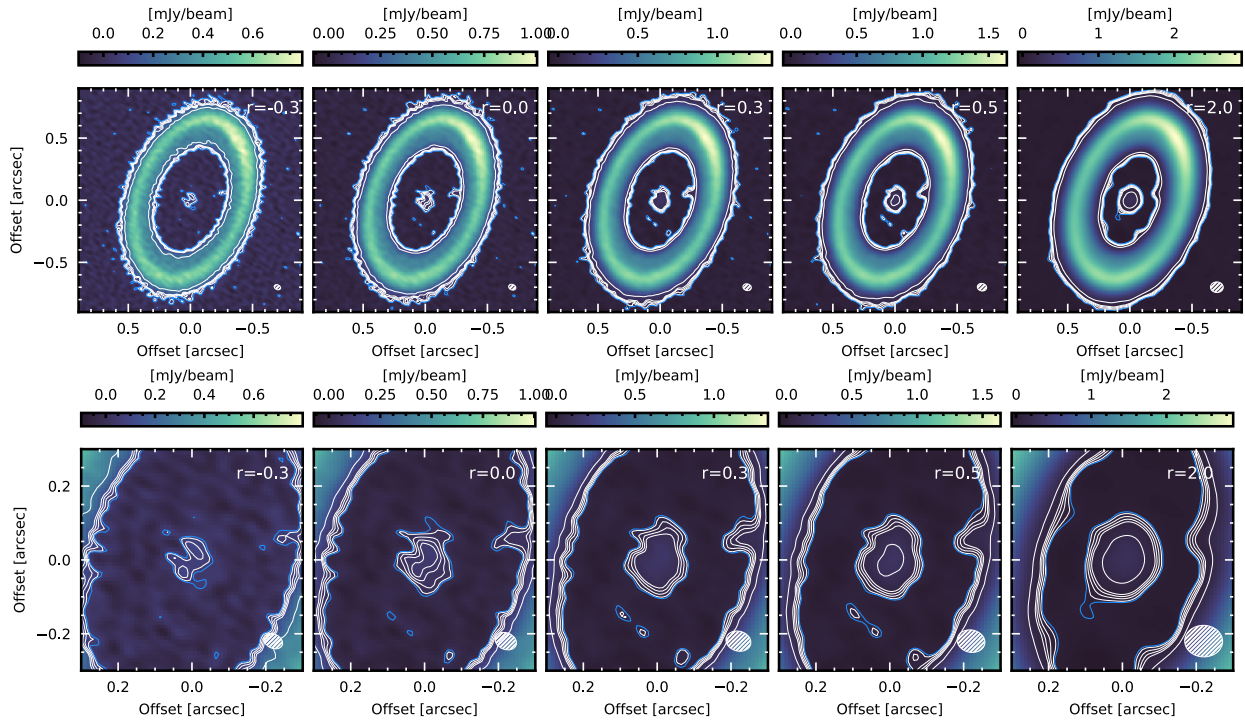


**Figure 4.5:** Same as Fig. 4.3 but for the combined ('SB1+LB2+LB3') dataset.

less prominently in the previous data, and is suggestive that the outer ring is actually composed of a double-ring. In Chapter 3, we parametrized the azimuthally averaged profile of the outer ring with a Gaussian function with different widths along the inner and outer edges of the profile. MCMC fitting of the deprojected visibilities resulted in a peak location at 73.7 au, and with an inner and outer width of 14.8 and 13.4 au, respectively. Because we are now better resolving the structure of the inner edge, we followed here a different approach, and parametrized the radial profile as the sum of two symmetric Gaussians with different amplitudes centered at different radial distances. We visually find a best match using a Gaussian function peaking at 76 au with a standard deviation of 10 au, plus another Gaussian peaking at 57 au with a standard deviation of 5 au. The amplitude of the inner Gaussian is reduced to 30% of the amplitude of the outer Gaussian. The two Gaussians and their sum are overplotted on the azimuthally averaged profile of Fig. 4.4 (uppermost line). A more detailed analysis of the outer ring structure, including new data at  $\sim 30$  mas resolution will be dedicated in a forthcoming project (Benisty et al. in prep.).

### Planetary signals within cavity

As can be seen from Fig. 4.3, the inner cavity is not completely empty. In addition to the inner disk component, we detect a spur at the Western inner edge of the disk, as well as a

robust value	peak intensity
$r=-0.3$ [ $\mu$ Jy beam $^{-1}$ ]	–
$r=0.0$ [ $\mu$ Jy beam $^{-1}$ ]	68
$r=0.3$ [ $\mu$ Jy beam $^{-1}$ ]	75
$r=0.5$ [ $\mu$ Jy beam $^{-1}$ ]	82
$r=2.0$ [ $\mu$ Jy beam $^{-1}$ ]	95
Isella et al. (2019) [ $\mu$ Jy beam $^{-1}$ ]	73-100

**Table 4.2:** Peak intensity of the compact continuum signal close to PDS 70 b measured in the new data (‘LB2’) for different robust values, in comparison with that reported in Isella et al. (2019).

compact emission to the South-East of the inner disk.

The spur at the Western edge is consistent with the feature detected in Chapter 3, which was later identified as a point-like source co-located with the NIR emission of PDS 70 c (Isella et al., 2019), separated by about 65 mas from the inner edge of the outer continuum ring. In most of the images of Fig. 4.3, the source is not separated from the outer ring, due to the moderate angular resolution (beam major axis of 75-110 mas for robust values between 0.0 and 2.0). Only when imaging our data with  $r = -0.3$  (beam major axis 71 mas), we obtain an angular resolution that starts to separate the source and the outer ring (see left panel of Fig. 4.3). Due to the limited angular resolution we are thus not able to derive meaningful values for the flux density of the source.

We note a second compact emission source located at  $\sim 90$  mas to the South-East of the star, close to but not exactly at the location of the continuum source found by Isella et al. (2019) and denoted as PDS 70 b<sub>smm</sub>. The source appears in the  $r = 0.0, 0.3,$  and  $0.5$  images at  $\sim 2.5-4\sigma$ . In the  $r = 2.0$  image, it is not visible as a source separated from the inner disk any more, due to dilution by the relative large beam size (110 mas). It is further not detected in the  $r = -0.3$  image, due to the elevated noise level. We measured the peak intensity of that source for the  $r = 0.0, 0.3, 0.5$  images and list them in Tab. 4.2. It appears to increase with larger robust values (i.e., increasing beam size). If the source was a point source, its peak intensity would not change with the beam size, as long as it remains unresolved. In the current case, the increasing peak intensity with increasing beam size could be explained by the fact that with a lower angular resolution, more and more diffuse emission is smeared into the beam. Such a behaviour, however, would also be consistent with the case where the source was not a point source, but somewhat spatially extended. In any case, the peak intensities are roughly consistent with those presented by Isella et al. (2019) for PDS 70 b<sub>smm</sub> by Isella et al. (2019) (see Tab. 4.2). However, we remind the reader that a possible flux calibration issue remains to be solved, and no conclusion on the absolute peak intensity can be drawn.

Figure 4.5 presents the continuum images resulting from the combination of the new

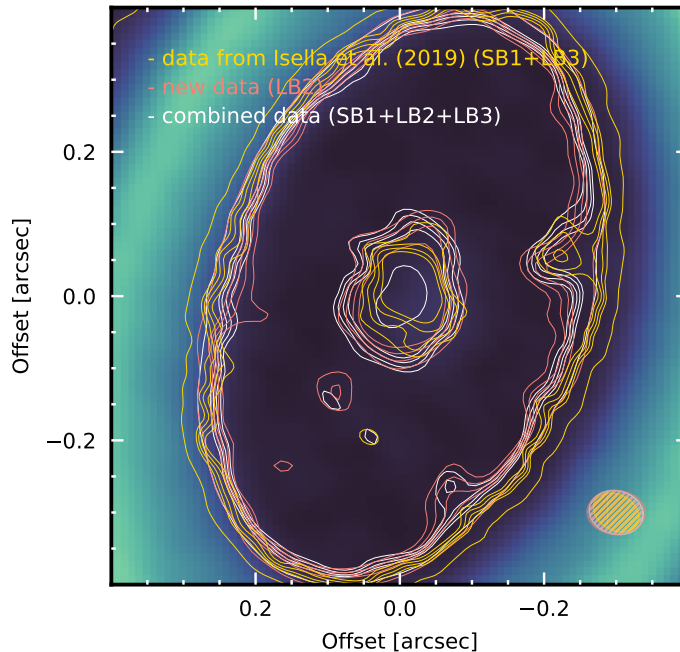


**Figure 4.6:** Combined  $r = 0.5$  image from Fig.4.5 overlaid by its own contours (white). In addition, the contours of the  $r=0.3$  image published in Isella et al. (2019) (yellow), and the  $r=0.5$  image of our new (LB2) data (red contours) are overplotted. In each case, contours are plotted at 3, 4, 5, 6, and 12  $\sigma$ .

and previous datasets ('SB1+LB2+LB3'). Interestingly, the compact emission discussed here decomposes in the  $r = 0.0, 0.3,$  and  $0.5$  images now into two separate sources at relatively low S/N ( $2.5-3\sigma$ ). These two sources likely correspond to a combination of both, the source detected in Isella et al. (2019) (lower right compact emission), and in our new data (upper left compact emission). Those appear now on the same image as we have combined the visibilities from both datasets. This is clearly illustrated in Fig. 4.6 where we overlaid the contours of the new ('LB2') image (red) and the one from Isella et al. (2019) (yellow), to that of the combined dataset (white), all three at comparable angular resolution.

### 4.3.2 Analysis of $^{12}\text{CO}$ and $^{13}\text{CO}$

#### Peak brightness temperature and integrated intensity

From our three-dimensional cubes, we generated maps of peak brightness temperature and zeroth moment using bettermoments (Teague & Foreman-Mackey, 2018).

**Outer disk.** Figure 4.7 presents the peak brightness temperature and zeroth moment maps of the  $^{12}\text{CO}$  emission generated for different robust parameters of our new ('LB2') data. For completeness, those for the combined dataset ('SB1+LB2+LB3') are presented in Fig. A.3, which show a very similar morphology as the maps generated for the 'LB2' data. Here, we will only discuss the morphology of the outer disk, the gap and the inner disk regions will be discussed below. The morphology of the peak brightness temperature of the outer disk is asymmetric with respect to the disk major axis. This is due to the projection effect of an inclined disk with a flaring geometry. Because the  $^{12}\text{CO}$  emission is optically thick, its peak brightness temperature traces the gas temperature at the layer where  $^{12}\text{CO}$  becomes optically thick. Due to the projection, along the near (West) side of the disk, we are looking into the midplane of the disk, which exhibits much lower temperatures, and which appears therefore dark on the peak brightness temperature map. We further note the presence of a potential gap-like substructure at the South-East edge of the disk, highlighted on the right panel of Fig. 4.7. This is even better visible on the high-passed filtered images presented in Fig. 4.8. The robustness and nature of this structure will be investigated in future work.

The zeroth moment maps of the outer disk in Fig. 4.7 show azimuthal intensity depletions along the disk major and minor axes. This is related to self absorption of the optically thick  $^{12}\text{CO}$  and was already described in Chapter 3. Similarly, we note a ring-like structure (marked by an arrow), which is due to absorption by the optically thick continuum.

Peak brightness map and zeroth moment maps of  $^{13}\text{CO}$  are shown in Fig. 4.9. It can be seen that the emission is of much less S/N and shows a smaller radial extension, due to the lower abundance of  $^{13}\text{CO}$  with respect to  $^{12}\text{CO}$ . Also here, the peak brightness temperature maps appear asymmetric across the major axis for the same reason as for  $^{12}\text{CO}$  explained above.

**Inner disk region.** Figure 4.10 presents a zoom-in of the peak brightness temperature and moment zero maps generated for the  $^{12}\text{CO}$  imaged with different robust parameters. The peak brightness temperature maps show a significant drop inside the inner edge of the continuum ring.

Also the zeroth moment maps show evidence of a deep gap inside the inner edge of the continuum. Within the gap, we note two main features. First, we detect the inner disk component. It appears to be composed of two main lobes, separated by the disk minor axis. This is likely related to a low S/N of the inner disk emission in channels at high velocity offset from the systemic velocity, which would contribute to the innermost disk regions close to the star. Due to the high spectral resolution, the S/N of the emission in these channels is below the threshold of  $3\sigma$  at which we have clipped the data prior to generate the zeroth moment map. This hypothesis is supported by the fact that this effect

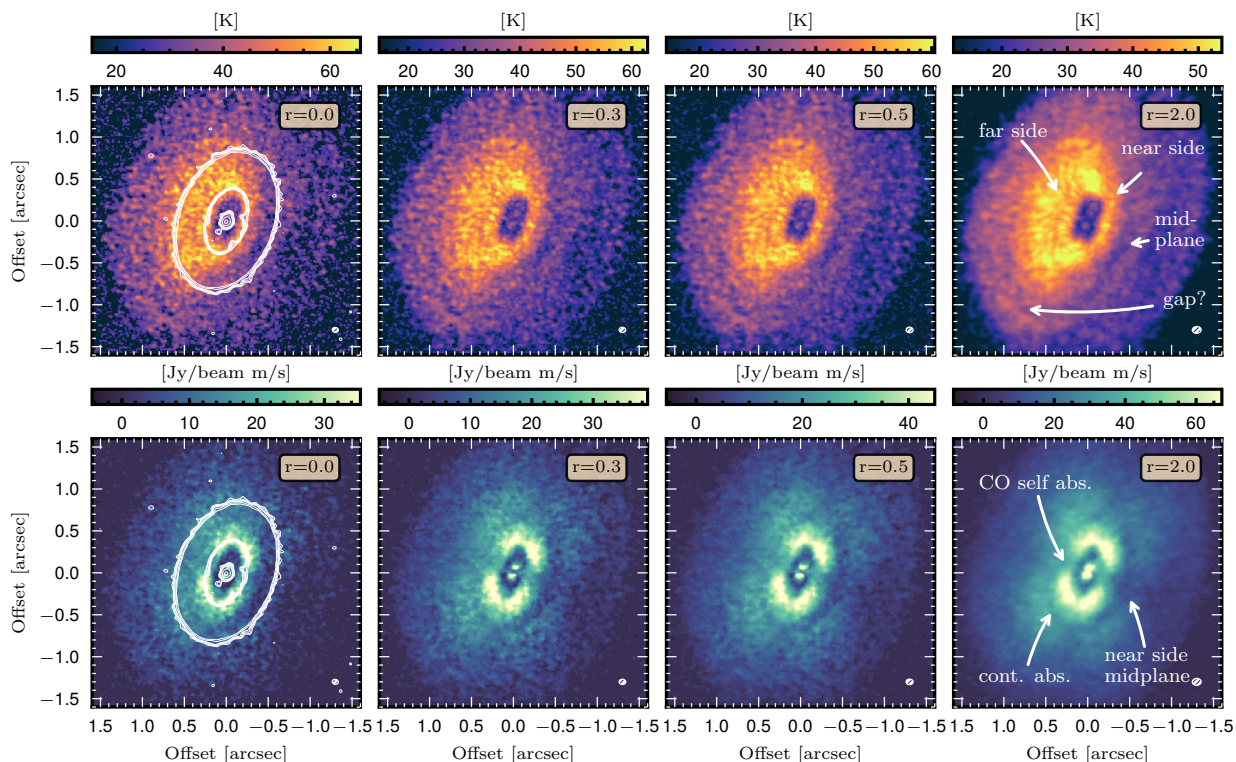


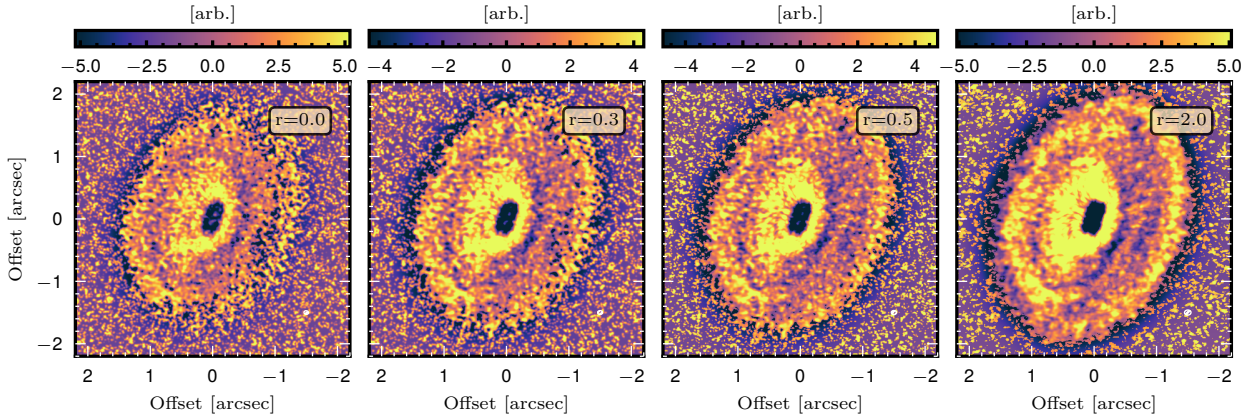
**Figure 4.7:** Zoom out of peak brightness temperature (top row) and zeroth moment maps (bottom row) calculated by adopting an intensity threshold of  $3\sigma$ , and spectrally smoothing over three channels. The maps are generated for robust parameters 0.0, 0.3, 0.5, 2.0 (from left to right). Contours from the continuum  $r = 0.5$  image ( $3, 4, 5, 6, 9, 12 \times \sigma$ ) are overplotted in white on the most left panel.

appears less strong for higher robust values, which have a higher point source sensitivity. Second, as already noted in Chapter 3, there is a bridge-like feature on the Western side ( $PA \sim 270 - 280$ ) that seems to connect the outer and the inner disk. This is best seen on the  $r = 0.3$  and  $r = 0.5$  zeroth moment maps. In the  $r = 2.0$  map, the large beam starts to smear emission from the outer disk into the gap, such that this bridge-like feature is not well visible any more.

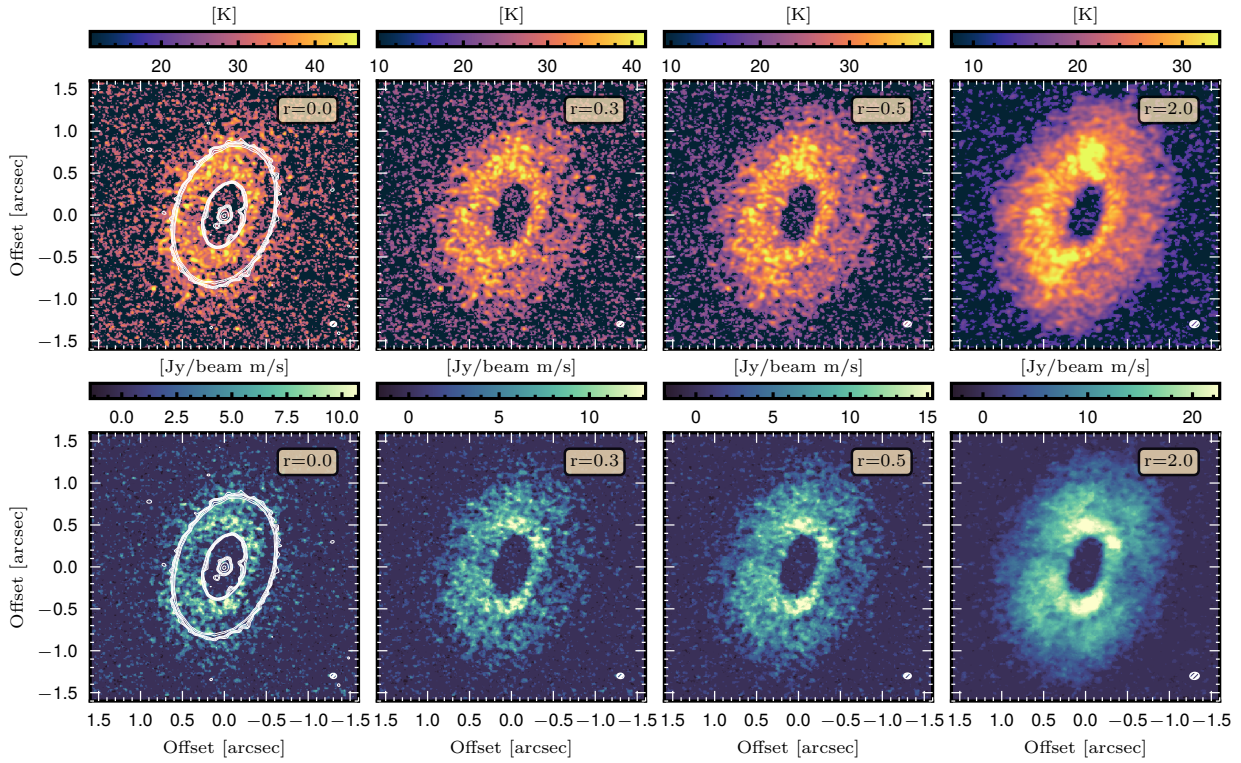
Figure 4.11 shows the same zoom-in of peak brightness temperature and zeroth moment maps but for  $^{13}\text{CO}$ . We can see that the signal in the inner region of the peak brightness temperature is of very low level, and large parts are clipped away during the  $3\sigma$ -clipping process. The same is true for the zeroth moment. In contrast to  $^{12}\text{CO}$ , we do not detect emission from the inner disk in  $^{13}\text{CO}$ .

Figure 4.12 shows radial profiles of the  $^{12}\text{CO}$  and  $^{13}\text{CO}$  azimuthally averaged, deprojected integrated intensity and peak brightness temperature. In order to deproject the data, we used the emission surfaces derived in Sect. 4.3.2. The gap is well visible in the integrated intensity with both,  $^{12}\text{CO}$  and  $^{13}\text{CO}$ . It is co-located with PDS 70 b and c, the

#### 4 An in-depth view of PDS 70 with ALMA at high spectral resolution



**Figure 4.8:** High-pass filtered  $^{12}\text{CO}$  peak brightness maps for different robust values to make the substructures better visible.



**Figure 4.9:** Same as Fig. 4.7 but for  $^{13}\text{CO}$ .

position of which is indicated by the gray dotted lines.

#### Analysis of channel maps

In a given channel map, the emission is concentrated around the isovelocity contours (e.g., Rosenfeld et al., 2013). These are regions where the projected velocity of the gas equals the velocity of the channel. Thanks to the high spatial resolution of our data, we are able to

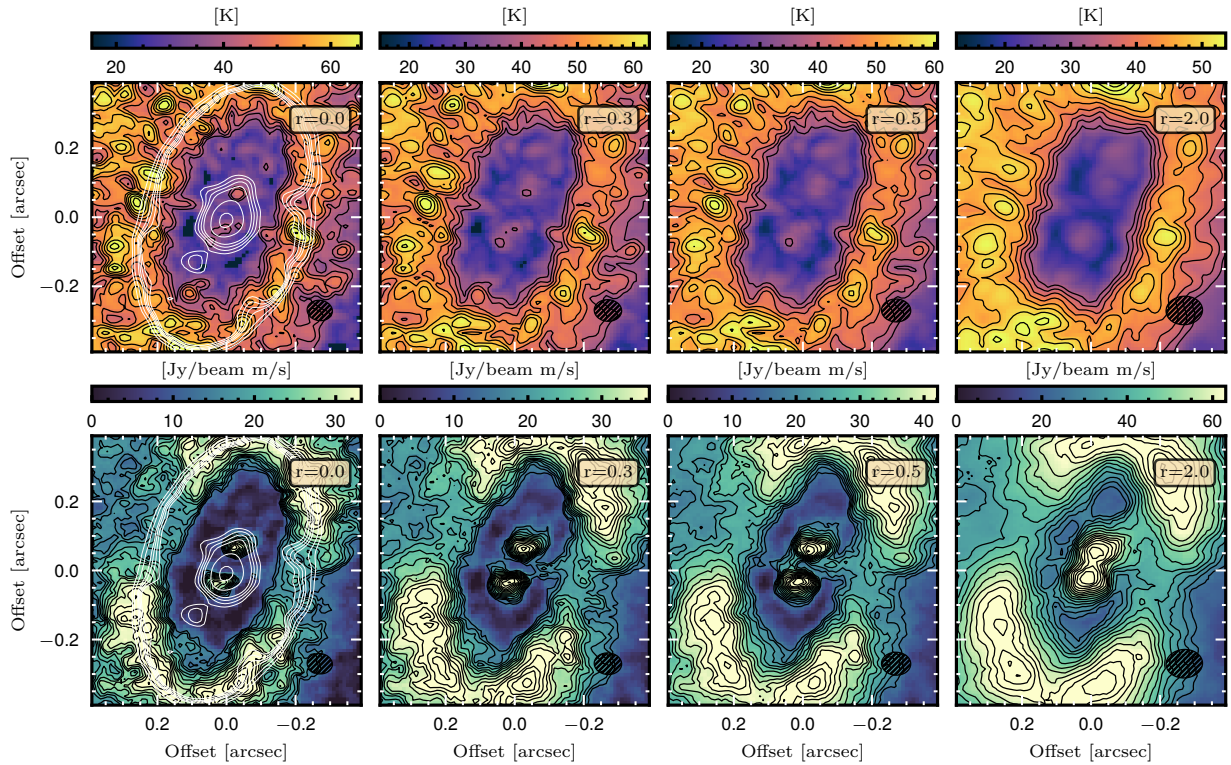


**Figure 4.10:** Zoom in of peak brightness (top row) and zeroth moment maps (bottom row) calculated by adopting an intensity threshold of three times the noise level, and spectrally smoothing over three channels. The maps are generated from four different cubes imaged with robust parameters 0.0, 0.3, 0.5, 2.0 (from left to right). The beam size is shown on the lower right corner. Black contours mark levels of 0.4, 0.5, 0.6, ..., 0.9  $\times$  peak value (top row), and 0.3, 0.4, 0.5, ... 0.9  $\times$  peak value (bottom row). Contours from the continuum  $r=0.5$  image (3, 4, 5, 6, 9, 12  $\times$   $\sigma$ ) are overplotted in white.

separate the emission originating from isovelocity regions of the top and bottom surface, as well as from the near and far side of the disk. This is illustrated on the  $^{12}\text{CO}$  channel maps presented in Fig. 4.13, where arrows indicate the emission from the corresponding disk regions. Because the emission from the bottom side is observed through the dusty disk, some channel maps show evidence of reduced emission along the bottom side isovelocity contours due to absorption of  $^{12}\text{CO}$  by the optically thick continuum ring (marked by arrow).

Figure 4.14 presents channel maps of  $^{13}\text{CO}$ . Comparing the morphology of the isovelocity regions to that of the  $^{12}\text{CO}$  channel maps we note that at a given velocity, the top and bottom surfaces of  $^{13}\text{CO}$  are geometrically much closer to each other than for  $^{12}\text{CO}$  on Fig. 4.13 (note that the two cubes are imaged at slightly different velocity spacings of 110 m/s and 120 m/s, respectively). This is due to the fact that the  $^{13}\text{CO}$  emission surface is located at lower altitudes because of its lower optical depth. The emission surfaces of  $^{12}\text{CO}$  and  $^{13}\text{CO}$  are discussed in more detail in Sect. 4.3.2.

#### 4 An in-depth view of PDS 70 with ALMA at high spectral resolution

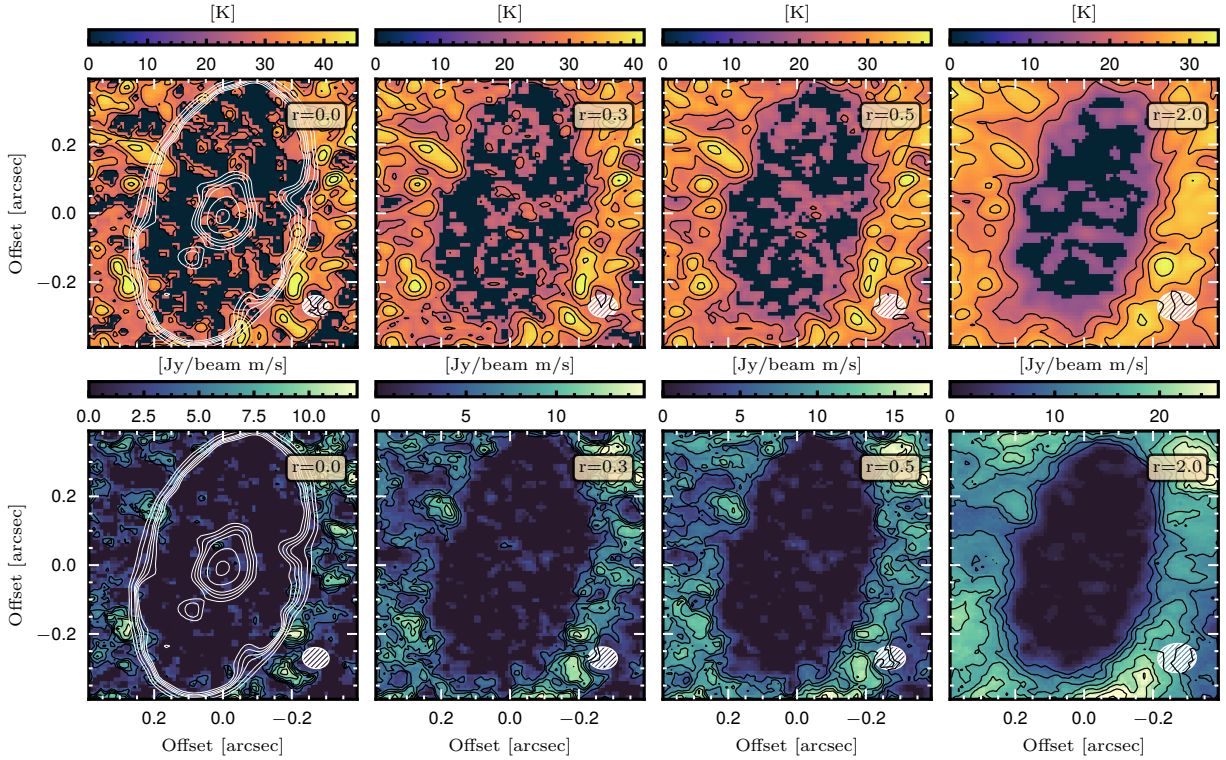
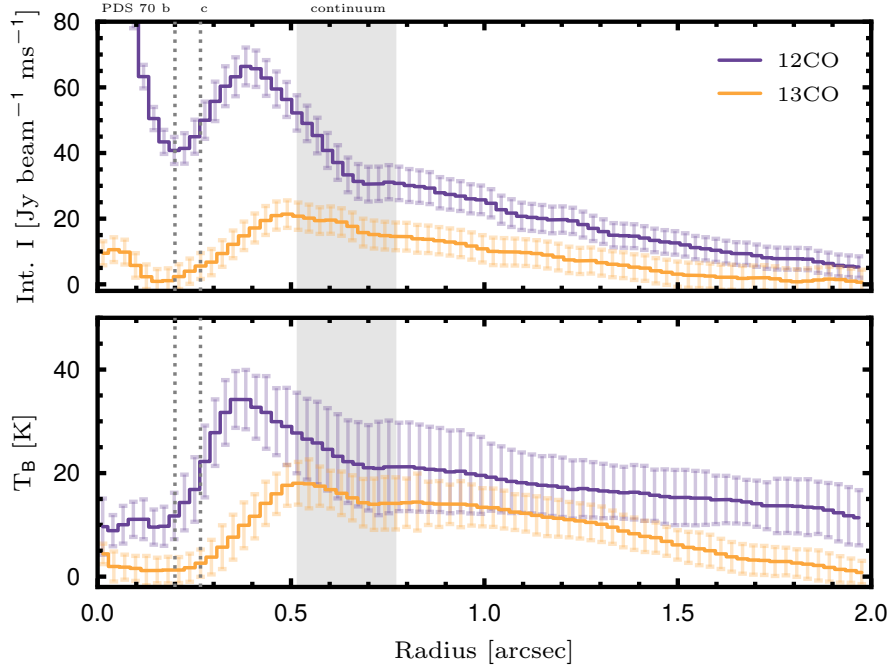


Figure 4.11: Same as Fig. 4.10 but with  $^{13}\text{CO}$ .

The perturbation of the disk kinematics by a giant planet is expected to cause a localized distortion of the isovelocity contours in channels where the emission sweeps across the location of the planet (Perez et al., 2015; Pinte et al., 2018b). In order to search for such localized features, we generate zoom-in views of the channel maps. Figure 4.15 shows channel maps where the emission of the disk is close in projection to the location of PDS 70 c. We overplot the expected isovelocity contours for the given channels. Those were evaluated assuming an emission surface as derived in Sect. 4.3.2, and a stellar mass of  $0.9 M_{\odot}$ . We plot the contours for the top surface (red) and bottom surface (blue) separately. Overall, the peak emission appears to follow the expected contours. However, in the channel map corresponding to a velocity of 4.55 km/s (and marginally also to 4.66 km/s), a slight distortion of the peak emission along the contour of the top near side of the disk, as marked by the white arrow, is visible. To test the robustness of the feature, we plot the channel map corresponding to 4.55 km/s extracted from the cubes imaged with different robust parameters in Fig. 4.17. The distortion is visible in all four maps imaged with different robust parameters, and is most clearly seen in the  $r = 0.0$  cube, which provides the highest angular resolution. This may indicate that the feature may be real, and not solely an artifact from the imaging process. In order to verify if the feature is spatially localized or related to an azimuthally extended disk structure, we plot in the bottom right panel of Fig. 4.15 the channel map corresponding to a velocity of 6.42 km/s. This velocity has a similar absolute



**Figure 4.12:** Radial profiles of integrated intensity (top) and brightness temperature (bottom) for  $^{12}\text{CO}$  and  $^{13}\text{CO}$  ( $r=2.0$ ).

offset from the systemic velocity (5.5 km/s) as the one from the channel with the velocity distortion discussed above (4.55 km/s), but corresponds to the red-shifted, instead of to the blue-shifted part of the disk<sup>18</sup>. If the disk structure (more precisely, the  $^{12}\text{CO}$  emission structure) was azimuthally symmetric, the morphology of the emission in channels with identical absolute offsets from the systemic velocity should be the same, apart from being mirrored across the disk minor axis. If the feature on the 4.55 km/s channel map was e.g., due to the pressure gradient at the outer edge of the gap, we should thus see it as well in the 6.42 km/s channel map. Comparing now the channel maps corresponding to 4.55 and 6.42 km/s on Fig. 4.15, however, we do not note a similar distortion of the emission along the top and near disk side isovelocity contour on the 6.42 km/s channel. This suggests that the feature is spatially localized.

We note that we do not clearly detect a corresponding asymmetry in the  $^{13}\text{CO}$  channel maps (see Fig. 4.16). Here, the emission along the isovelocity contours is fainter and more diffuse, related to its lower abundance and thus lower optical depth compared to  $^{12}\text{CO}$ .

We also searched for velocity distortions in other regions of the disk, in particular close

<sup>18</sup>Unfortunately, the given channel spacing of the cube prevents us from showing a channel which is centered on a velocity which corresponds *exactly* to the same absolute velocity offset.

#### 4 An in-depth view of PDS 70 with ALMA at high spectral resolution

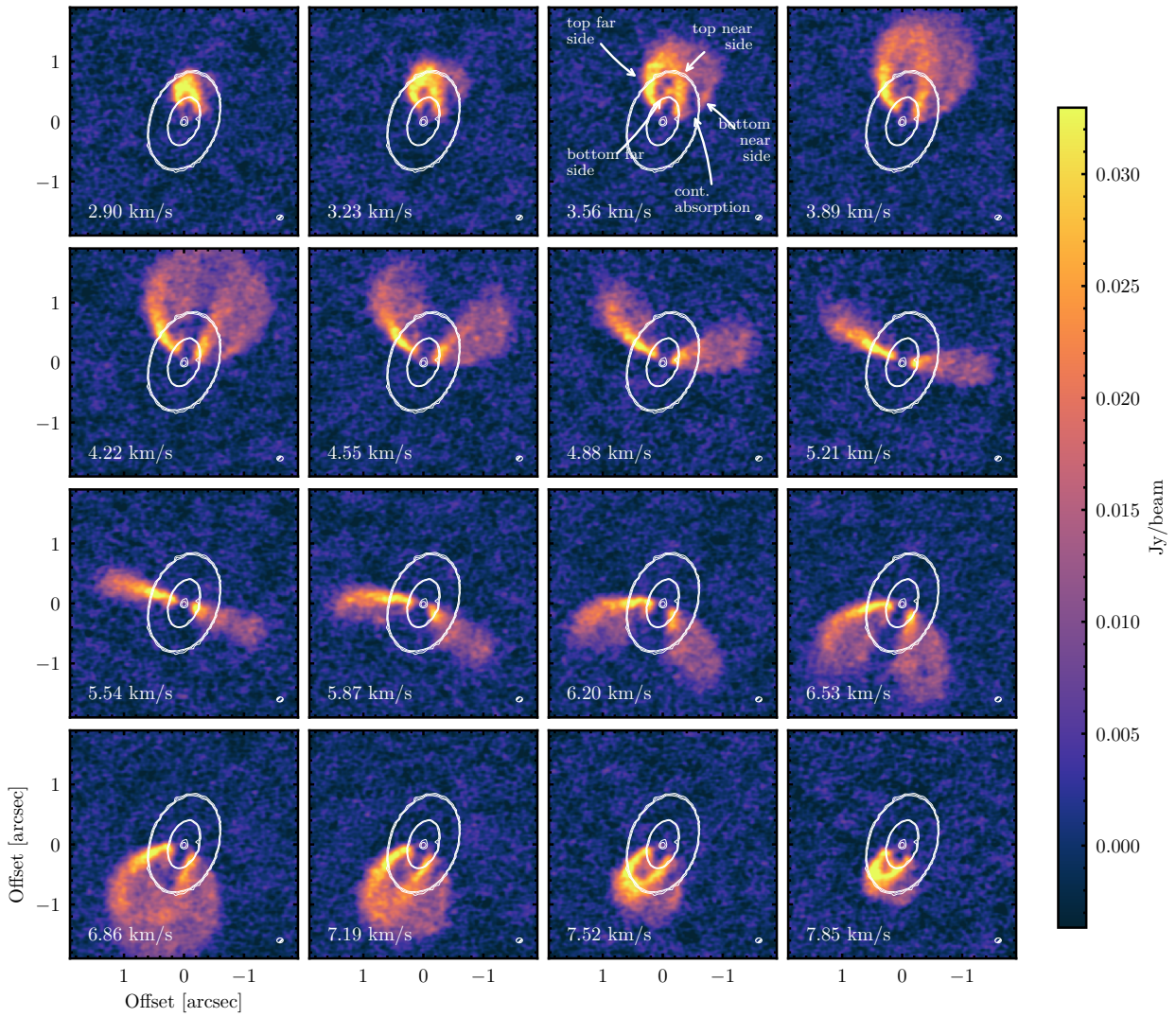


**Figure 4.13:** Channel maps of  $^{12}\text{CO}$ , imaged with  $r=2.0$ . The plot shows every third channel of the cube. The beam is shown on the lower right of each panel. Contours of the  $r=0.3$  continuum image are overplotted in white at 6, 9, 12  $\sigma$ . Arrows on the third panel in the first row indicate emission regions of top and bottom near/far sides, as well as of where  $^{12}\text{CO}$  is absorbed by the continuum ring.

to PDS 70 b. This is challenged, however, by the fact that PDS 70 b is located within the deeply depleted cavity, and even closer to the star. As a consequence, the emission of  $^{12}\text{CO}$  in the individual channel maps close to PDS 70 b is extremely faint, in the  $r=0.5$  cube only at a  $\sim 3\sigma$  level. We show the corresponding channel maps in Fig. A.2 but defer a corresponding analysis of the emission morphology in the individual channel maps to future work. Degrading the spectral resolution to achieve a higher sensitivity per channel map may help to facilitate this issue.

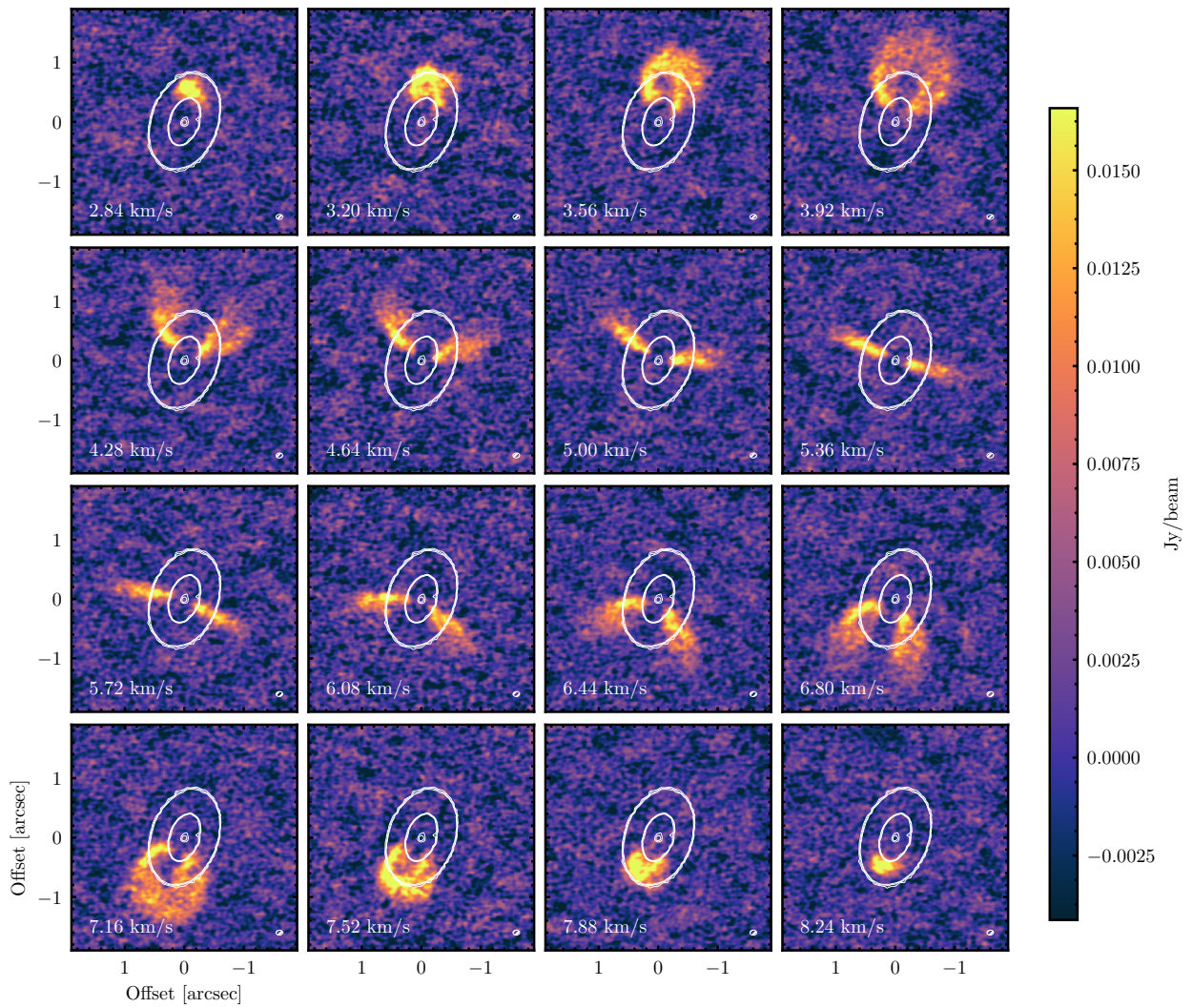


**Figure 4.14:** Same as Fig. 4.13 but for  $^{13}\text{CO}$ .

## Spectral analysis

Another potential diagnostic for localized perturbations in the disk kinematics is the spectral line shape. For example, hydrodynamical simulations by [Perez et al. \(2015\)](#) suggested that the rotation of the CPD may be detectable through a local broadening of the CO line.

For a general analysis of the line shapes in the PDS 70 disk we plot in Fig. 4.18 (top panel) spectra extracted within a cone of  $14^\circ$  around the disk far-side minor axis for different radial bins between  $0.15''$  and  $1.0''$ . Inside  $\sim 0.3''$ , the line profiles are very broad and of very low amplitude. The low amplitude is likely a combined effect of high depletion and low temperatures of  $^{12}\text{CO}$  within the cavity. The broad width can be explained by the strong Keplerian shear across the beam. Due to the finite size of the beam ( $0.085''$ ), more and more emission from the inner disk, rotating at high velocities is smeared into the beam when sampling regions between  $\sim 0.1''$ - $0.3''$ , resulting in a particularly broad line profile.

#### 4 An in-depth view of PDS 70 with ALMA at high spectral resolution

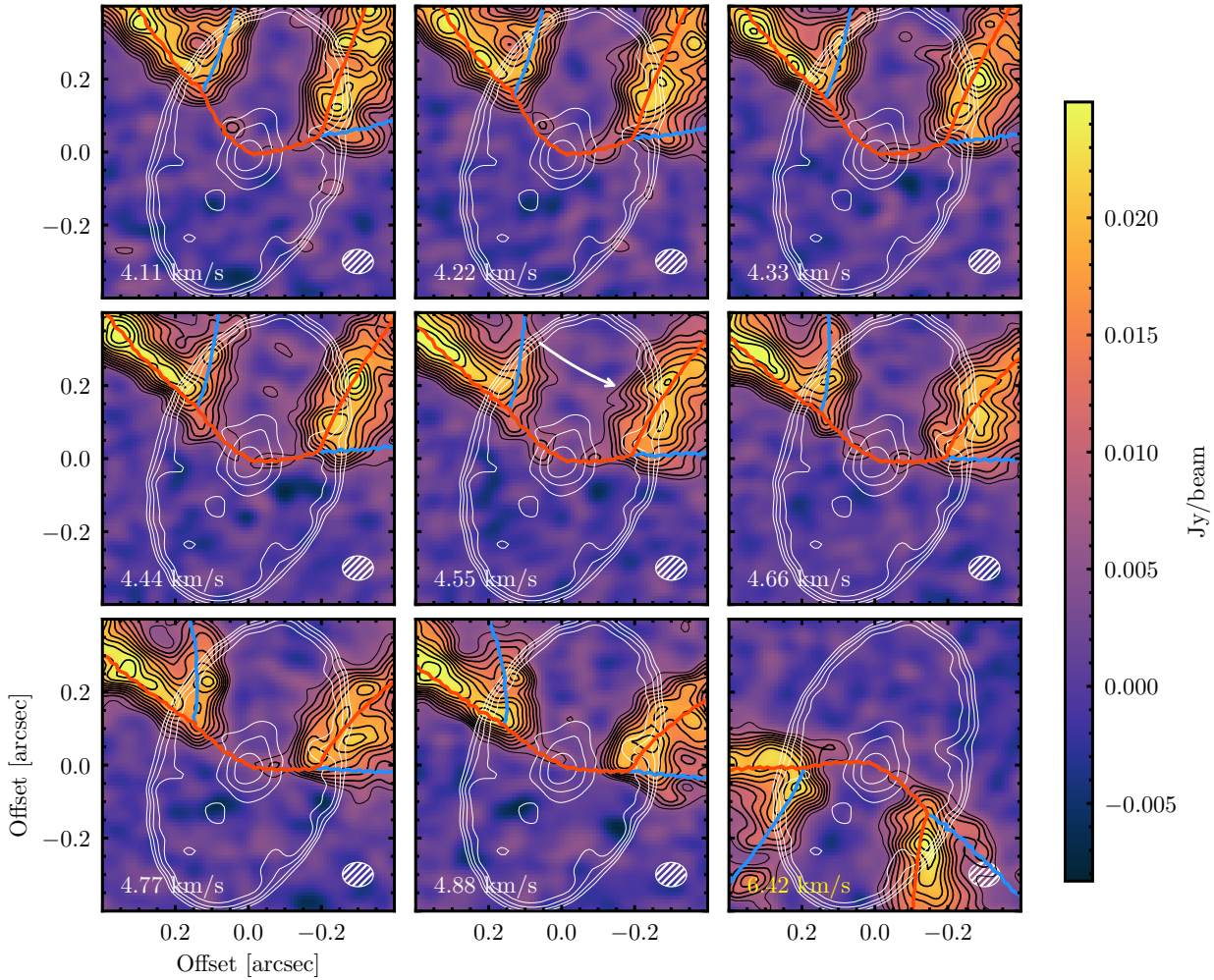


**Figure 4.15:** Zoom-in of channel maps of  $^{12}\text{CO}$ . The white arrow indicates the location of the local distortion described in the text. The beam is shown on the lower right of each panel. The lower right panel shows the channel with opposite velocity offset with respect to the systemic velocity as the 4.55 km/s channel.

In order to estimate the line width we fitted the spectral lines for each radial bin with a Gaussian function. We note that in the presence of a very optically line, the core of the line may saturate and thus not be well represented by a Gaussian any more. Regarding the spectra presented here, however, we find that a Gaussian sufficiently well fits the spectral line shapes for our purpose of a more qualitative analysis. The best-fit solutions are overplotted with solid lines on the spectra of the panel of Fig. 4.18, and the resulting line FWHM as a function of radius are plotted on the bottom panel of Fig. 4.18. The line width drops from  $\sim 2.7$  km/s at  $0.15''$  (17 au) to  $\sim 0.5$  km/s at  $1.0''$  (113 au).

The width of the spectral lines is, at least for the outer disk, likely dominated by thermal broadening. The contribution from turbulent motions within the gas is expected to be low, typically one order of magnitude smaller than thermal broadening (Teague et al.,

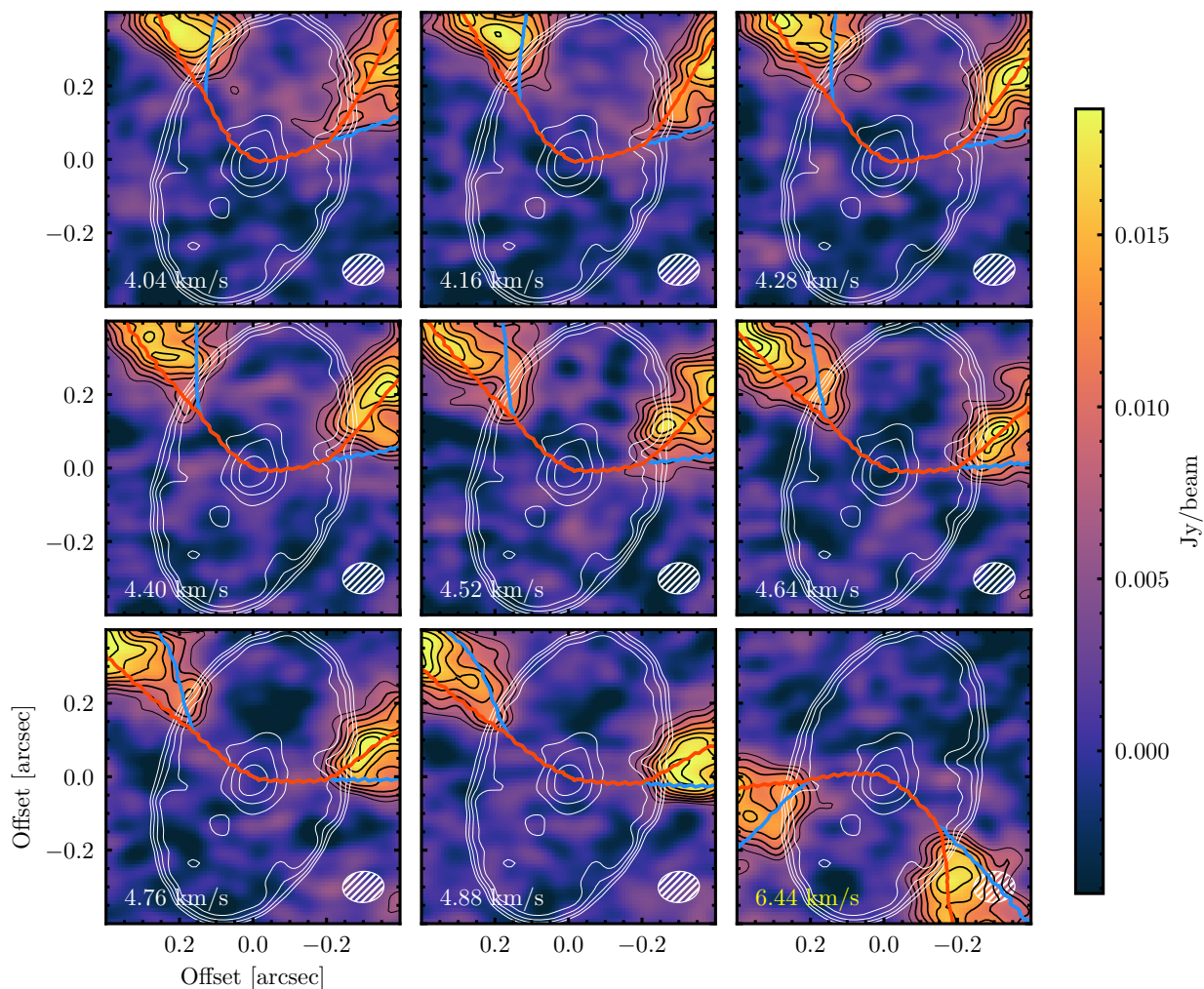


**Figure 4.16:** Zoom of channel maps of  $^{13}\text{CO}$ , using the  $r = 2.0$  cube. The beam is shown on the lower right of each panel.

2016). Because we extracted the spectra along the minor axis, the bulk gas is expected to move in perpendicular direction with respect to the line of sight. Therefore, line broadening through the gas motion should be minimized at this location. However, as explained above, the line width in the inner regions are significantly affected by the Keplerian shear across the beam due to the limited angular resolution. Correcting for the Keplerian shear, and constraining the individual contributions of thermal broadening, turbulent broadening and Keplerian shear as presented by Teague et al. (2016), if possible, is devoted to future work.

We can test the spectral line shape not only as a function of radius, but also as a function of azimuth for a given radius. As explained in Sect. 4.3.2, for an axisymmetric disk, we expect the emission in channel maps with identical absolute velocity offset from the systemic velocity to be symmetric across the disk minor axis. Similarly, we expect spectra

#### 4 An in-depth view of PDS 70 with ALMA at high spectral resolution

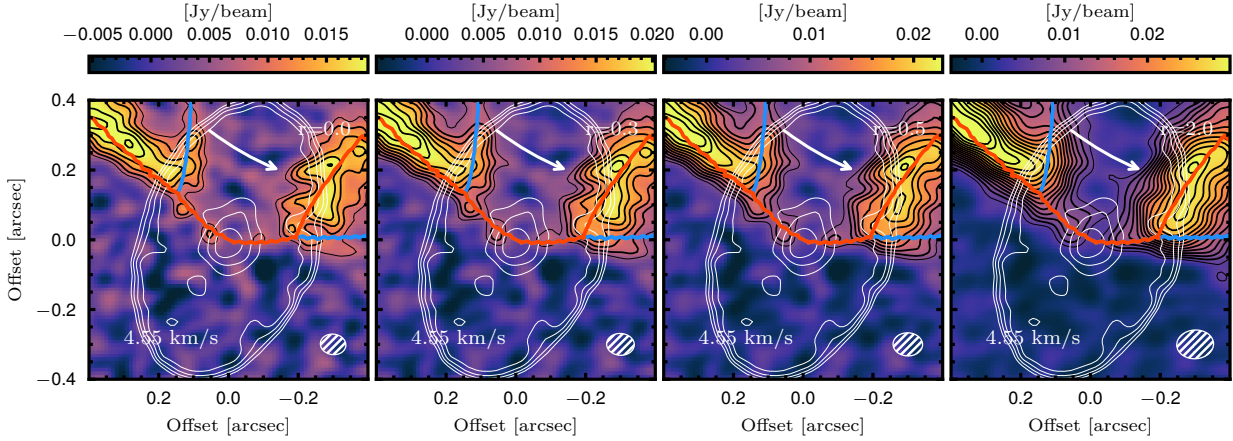


**Figure 4.17:** Zoom-in of channel maps at 4.55 km/s for different robust parameters ( $r=0.0, 0.3, 0.5, 2.0$ , from left to right). The channel width is 110 ms. Black contours are drawn at 4, 5, 6, 7, 8, ...  $\sigma$ . The faint black contour corresponds to  $3\sigma$ . Contours from the continuum imaged with  $r=0.3$  at 3, 6, 9, 12 $\sigma$  are overplotted in white. Isovelocity contours from the top and bottom surface of the disk are overplotted in red and blue, respectively.

extracted from locations symmetric across the disk minor axis (i.e., from locations with the same polar angle offset with respect to the disk minor axis) to be symmetric across the systemic velocity. We can use this fact in order to search for any spectral line asymmetries that could be related to local perturbations in the disk kinematics.

Figure 4.19 presents the spectra extracted in a given annulus between  $0.6''$  and  $0.65''$  at different azimuthal bins covering an azimuth of  $15^\circ$  each. Note that the polar angle  $\theta$  quoted here is defined as the angle with respect to the red-shifted (i.e. Southern) semi-major axis of the disk (in contrast to the position angle which is measured East of North direction). Negative polar angles correspond to the far (North-East) side, while positive polar angles refer to the near (South-West) side. The two spectra extracted at symmetric locations across the minor axis (i.e. at polar angles that are symmetric with respect to the disk minor axis) along the far side (left panel) and near side (right panel) are plotted on the same line. Thus, the spectral line shapes of these pairs should be compared with respect to each other.

As expected, each pair of spectra is very symmetric with respect to the systemic velocity. Depending on polar angle, the lines show evidence of an asymmetric, non-Gaussian shape, due to the resolved contributions from the bottom side of the disk (see Fig. 10 of Teague et al., 2018b). This can best be seen at position angles away from the major and minor axis (e.g., at polar angles of  $-45^\circ$  and  $-135^\circ$ ). Along the disk major and minor axes the isovelocity contours of the top and bottom side overlap, and as a result the contribution from the bottom side is (at least partially) hidden due to the high optical depth of  $^{12}\text{CO}$  (as illustrated on Fig. 3.7 in Chapter 3).

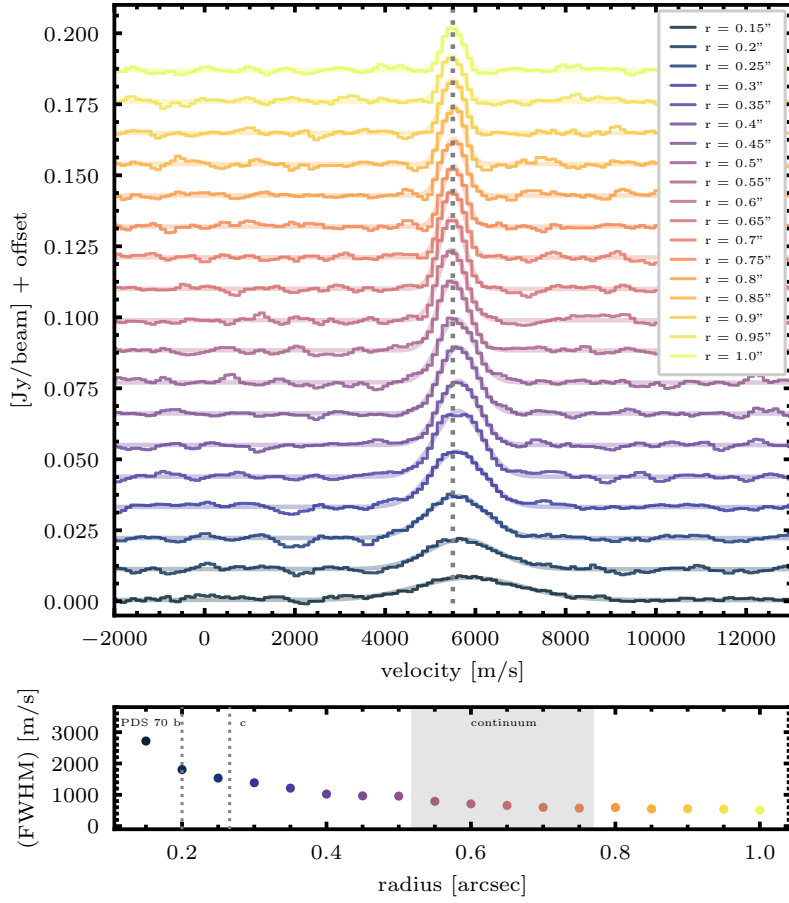


**Figure 4.18:** *Top panel:*  $^{12}\text{CO}$  spectra extracted from the  $r=0.5$  cube at different radial (50 mas spacing) bins extracted from the far-side semi-minor axis. For each spectrum, we overplot the best-fit line profile in solid lines. *Bottom panel:* FWHM as obtained from the spectral line fitting. The gray shaded area marks the location of the continuum ring, and the dotted lines indicate the deprojected distances of PDS 70 b and c.

The spectra extracted from the near side are generally of lower S/N. This is due to a projection effect. Because the  $^{12}\text{CO}$  emission results from a three dimensional geometry with finite thickness, there are less spatial pixels contributing to a given radial annulus (defined in the disk midplane) at the near side than compared to the far side. We note a slight peak in the spectrum extracted at a polar angle of  $120^\circ$  at a velocity of about 2.5 km/s (highlighted by the black arrow on Fig. 4.19). Further, in order to search for potential spectral peculiarities at the location of PDS 70 c, we extracted the spectra in a radial range between  $\sim 0.24''$  and  $0.29''$ , which includes the orbital (deprojected) separation of PDS 70 c ( $0.27''$ ; Mesa et al., 2019). The spectra are shown in Fig. A.6. As expected from the analysis

#### 4 An in-depth view of PDS 70 with ALMA at high spectral resolution

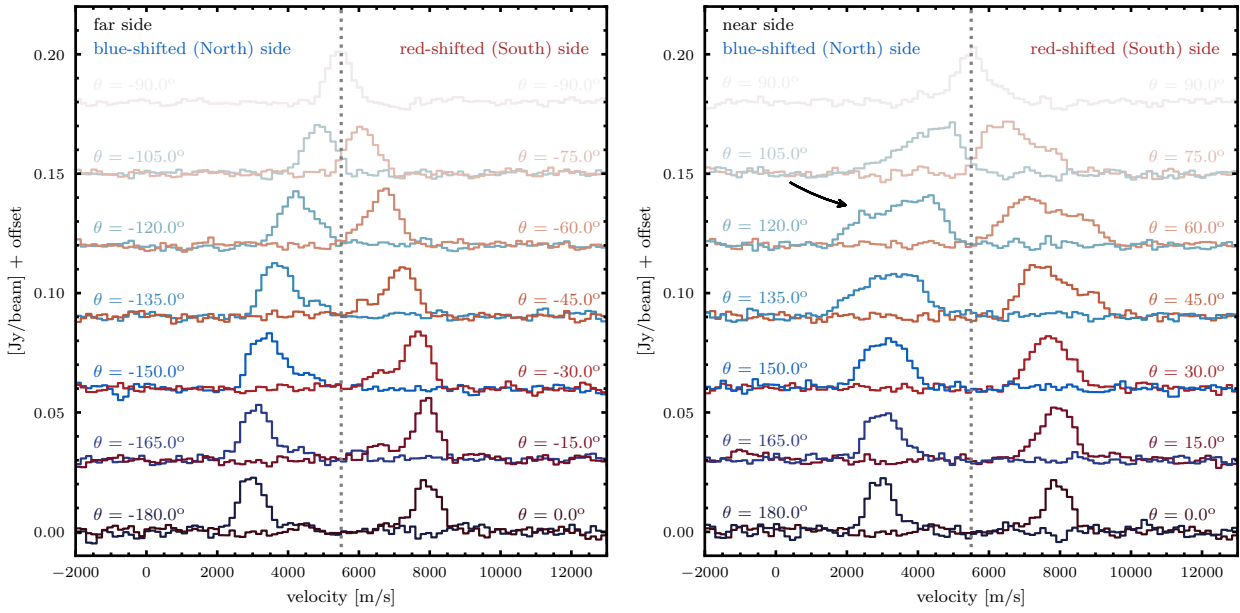


**Figure 4.19:** Symmetrically extracted spectra from the ‘LB2’  $r = 0.5$  cube between  $0.6''$  and  $0.65''$  for different azimuthal bins. Spectral resolution was downgraded to  $150 \text{ m/s}$  to improve the S/N.

of Fig. 4.18 the emission at these close distances is of very low amplitude, and thus of low S/N, challenging a robust study of the line profiles. It should be noted that the spectra extracted from the near side between polar angles of  $\sim 150^\circ$ - $120^\circ$  may potentially show evidence of some additional, blueshifted emission around  $2000 \text{ m/s}$  (as indicated by the black arrow). Interestingly, these regions of the disk are close to the location of PDS 70 c. However, the low S/N does not allow a definitive conclusion at this point. More tests need to be done to conclude on the robustness of the features reported here (e.g., testing cubes imaged with different robust parameters, and different channel widths), which is deferred to future work. We note that the spectra at radii similar to the (deprojected) distance of PDS 70 b ( $\sim 0.20''$ ; Mesa et al., 2019) are of even lower S/N and are therefore not presented in this work. Observations at higher angular resolution (thus, reducing the beam smearing effect) would help to expand the here proposed analysis to the inner disk regions.

#### Surface fitting

Recently, Pinte et al. (2018a) presented a method to empirically locate the CO emission surface of protoplanetary disks from high spectral and spatial resolution ALMA observations. If the angular resolution of observations is sufficiently high, the emission along the isovelocity contours of the near and far side of the disk surface is spatially separated in the channel maps. For channel maps with velocities not too close and not too far from the systemic velocity, these isovelocity contours of the upper surface consist of two arms

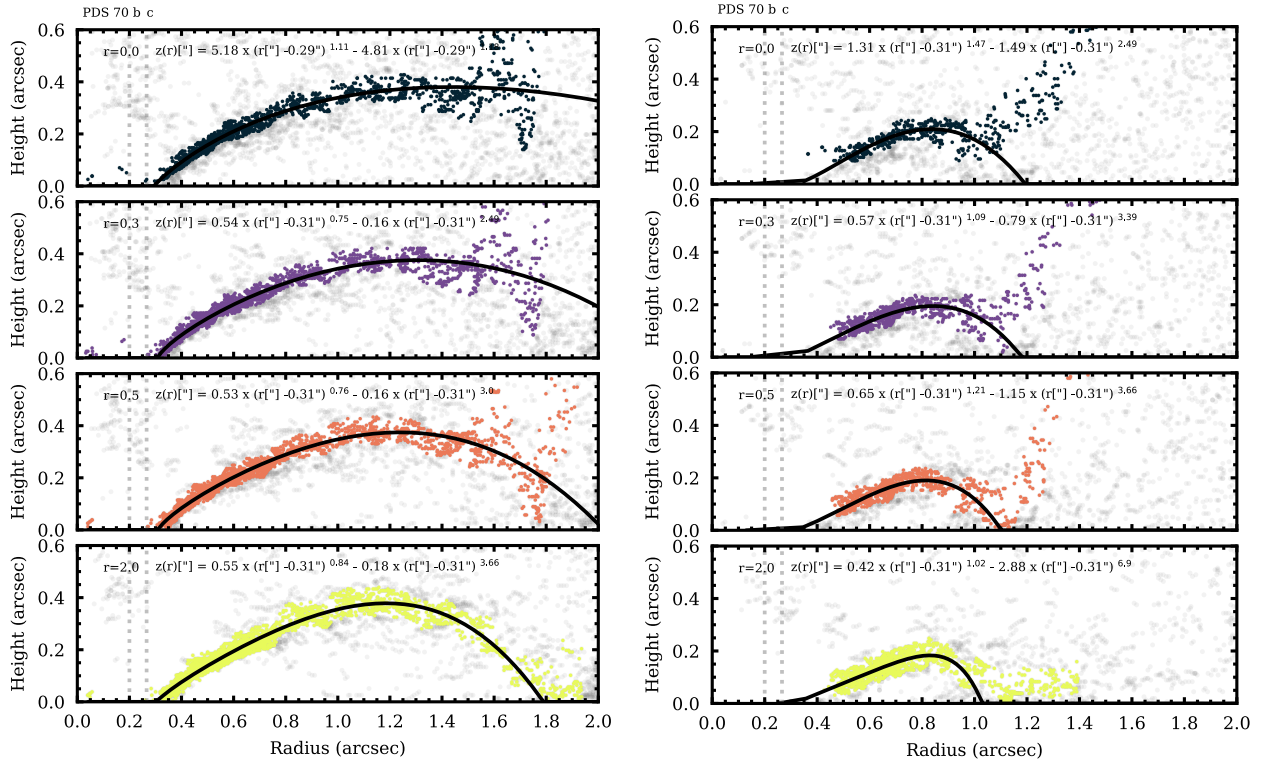


**Figure 4.20:** Emission surfaces recovered for  $^{12}\text{CO}$  (left) and  $^{13}\text{CO}$  (right) for cubes generated with different robust parameters ( $r = 0.0, 0.3, 0.5, 2.0$ , from top to bottom). Best-fit surface parametrizations are overlotted in black. The gray dots correspond to low S/N points that were excluded from the analysis.

(one from the near and one from the far side, respectively) which connect with each other at larger distances, similar to a tea-cup handle form (see Fig. 4.13). For a given channel map and a given distance from the center along disk midplane major axis, it is possible to localize the two corresponding points on the isovelocity curve of the near and far side, respectively. The offset of their midpoint from the disk major axis is given by the altitude of the disk at that radius. Measuring the emission peaks along the isovelocity contours of the near and far side for different radial samplings, and repeating this procedure on multiple channel maps thus allows to robustly recover the emission height as a function of radius.

We applied this procedure on our  $^{12}\text{CO}$  and  $^{13}\text{CO}$  data<sup>19</sup> in order to recover the emission height of the  $^{12}\text{CO}$  disk. We repeated this for four cubes imaged with  $r = 0.0, 0.3, 0.5$ , and  $2.0$ . The results are shown in Fig. 4.20 for  $^{12}\text{CO}$  and  $^{13}\text{CO}$ , respectively, where we masked points corresponding to low S/N (gray points). Comparing all  $^{12}\text{CO}$  cubes, the points define a well defined emission height between  $\sim 0.3''$ - $1.25''$ , and those of  $^{13}\text{CO}$  between  $\sim 0.5''$ - $1.0''$ .

<sup>19</sup>Using an implementation by R. Teague

We fitted a two-component power law function to these points of the form:

$$z(r) = z_0 (r - r_{min})^\psi - z_1 (r - r_{min})^\phi. \quad (4.1)$$

The solutions are shown with black lines in Fig. 4.20. For both,  $^{12}\text{CO}$  and  $^{13}\text{CO}$ , we note that the drop-off at larger distances is better defined for higher robust values, while for the lowest robust values the measurements are very noisy. This is due to the fact the higher robust cubes have a higher point-source sensitivity, and are thus more sensitive in the outer regions. We therefore adopt the solution found for the  $r = 2.0$  as solution for our emission surface parametrization<sup>20</sup>.

We then find for the  $^{12}\text{CO}$  the following emission surface:

$$z(r) [m] = 0.55 \left( \frac{(r - 0.31'')}{1''} \right)^{0.84} - 0.18 \left( \frac{(r - 0.31'')}{1''} \right)^{3.66}, \quad (4.2)$$

and for the  $^{13}\text{CO}$ :

$$z(r) [m] = 0.42 \left( \frac{(r - 0.31'')}{1''} \right)^{1.02} - 2.88 \left( \frac{(r - 0.31'')}{1''} \right)^{6.90}, \quad (4.3)$$

where the midplane radius  $r$  is measured in units of arcseconds.

## 4.4 Discussion

### 4.4.1 Continuum signal of PDS 70 b

Figure 4.21 shows the SPHERE and MUSE images published by Müller et al. (2018) and Haffert et al. (2019), with the contours of the dust continuum ( $r = 0.5$ ) overplotted. The continuum dip on the Western inner edge of the outer disk well coincides with the NIR and  $\text{H}\alpha$  emission of PDS 70 c. The compact continuum emission to the South-West of the inner disk described above is close, but slightly offset toward the North with respect to the NIR and  $\text{H}\alpha$  source. While Isella et al. (2019) also found an offset of the continuum source PDS 70 b<sub>smm</sub> with respect to the NIR location of PDS 70 b, the offset was directed in opposite, South-West direction, compared to what we find in the new data. This all means that either we see two different sources in our new ('LB2') and in the previous

<sup>20</sup>We note that for the  $^{13}\text{CO}$  surfaces we fixed  $r_{min} = 0.31''$ , because inside  $\sim 0.5''$   $^{13}\text{CO}$  emission is so weak that we cannot obtain measurements for the emission surface

(‘LB3’) data, or we see the same source which has moved with respect to the star between the two epochs.

The spatial separation of the compact emissions in Fig. 4.5 is about 76 mas. The observations from Kepler et al. (2019) and Isella et al. (2019) were taken in December 2017, while the new data presented in this chapter were observed in August 2019. If we assume that the two continuum signals are related to circumplanetary dust around PDS 70 b, we can compare this spatial displacement with the expected proper motion of PDS 70 b. We find that within the given time interval, PDS 70 b should have moved by about 14 mas<sup>21</sup>. Therefore, the measured offset of the two compact continuum sources in the different datasets are inconsistent with orbital motion of PDS 70 b.

We note that at the same time as when the observations of our new data were taken (August 2019), PDS 70 was observed with ALMA at high,  $\sim 30$  mas resolution (progID: 2018.A.00030.S, PI: M. Benisty). These data will be key to confirm whether PDS 70 b<sub>smm</sub> is a real source, depending on if those data yield an independent detection or not. If so, they will provide a  $\sim 3$  times more accurate astrometry<sup>22</sup>, and thus shed light into the puzzling astrometry of PDS 70 b<sub>smm</sub> (Benisty et al. in prep.).

#### 4.4.2 Potential $^{12}\text{CO}$ kink feature close to PDS 70 c?

The perturbation of the Keplerian velocity field through the generation of spiral arms by a giant planet has been predicted to produce a local deformation in the molecular emission around the location of the planet, namely, where the spiral wakes are being launched (Perez et al., 2015). Recently, Pinte et al. (2018b) observed a spatially and spectrally localized distortion of the isovelocity contours in the disk around HD 163296. The authors showed using hydrodynamical simulations that this feature could be reproduced by the perturbation induced by a  $2 M_{\text{Jup}}$  planet. Moreover, a similar velocity feature was detected in co-location with a gap in the continuum emission in the disk around HD 97048, as well as in several of the disks observed within the DSHARP program (Pinte et al., 2019, 2020). The interpretation of being a planet-induced feature is appealing here because most alternative mechanisms proposed to create perturbations in the pressure structure of the disk and thus leading to similar velocity signatures would result in azimuthally symmetric features, in contrast to the spatially localized velocity deviation as found by Pinte et al. (2018b).

Taking into account the  $^{12}\text{CO}$  geometry of the emission surface derived in Sect. 4.3.2, the velocity distortion is located at a polar angle of about  $120^\circ$  and at a deprojected mid-

---

<sup>21</sup>The expected spatial displacement was estimated using the web-based tool <https://www.wheretheplanet.com/>

<sup>22</sup>The astrometric accuracy of ALMA is on the order of 10% of the synthesized beam size, see <https://science.nrao.edu/facilities/vla/docs/manuals/oss/performance/positional-accuracy>.

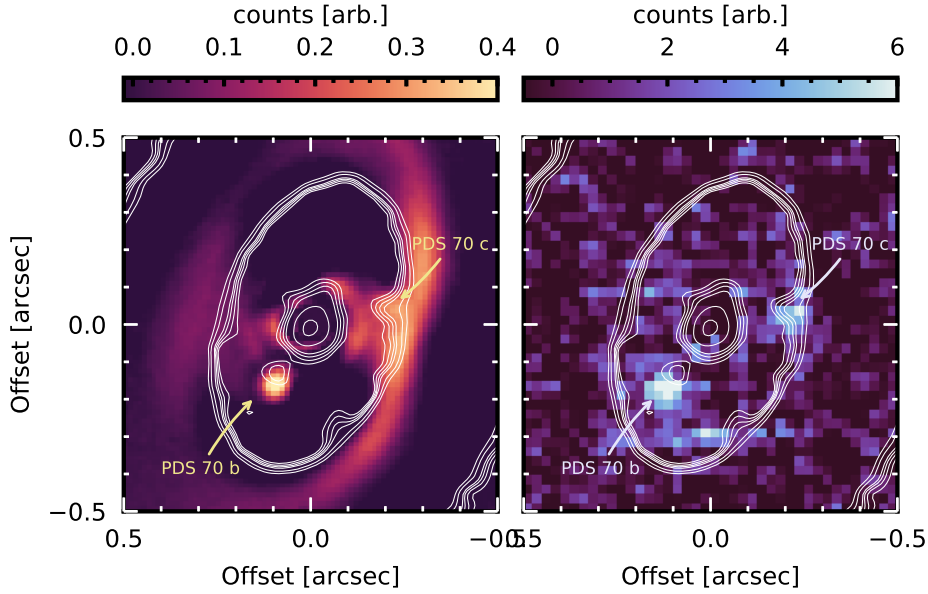


**Figure 4.21:** SPHERE (left; Müller et al., 2018) and MUSE (right; Haffert et al., 2019) images with ALMA contours ( $r=0.5$ ) overplotted. The contours are drawn at 3, 4, 5, 6, 9,  $12 \times$  rms. The NIR and  $H\alpha$  positions of PDS 70 b and c are indicated by arrows. It can be clearly seen that the continuum source is slightly shifted toward the North with respect to the NIR and  $H\alpha$  sources of PDS 70 b.

plane radius between about  $0.3''$ - $0.6''$ . The feature is visible mainly in the channel map at  $4.55$  km/s, and potentially as well at  $4.66$  km/s (Fig. 4.15). The feature is therefore found at a spatially and spectrally limited extent. If we assumed the feature being caused by PDS 70 c, we would expect its velocity signature to be co-located at a similar polar angle and deprojected midplane radius as the planet. The spur associated with the continuum signal of PDS 70 c described in Sect. 4.3.1 is located at a polar angle of about  $110^\circ$ , and at a deprojected midplane radius of about  $0.3''$ , thus at a similar polar angle, but slightly inward of the velocity signature.

We note that detailed hydrodynamical simulations are required in order to compare the expected velocity signature of PDS 70 c, including the involved projection effects, with the observations, in order to draw conclusions on the nature of the detected feature. Recently, using  $^{12}\text{CO}$  data at more coarse velocity resolution, we have derived the azimuthally averaged rotation velocity of the PDS 70 disk as a function of radius, finding a deviation from Keplerian rotation of about 10% at  $0.3''$  (see Chapter 3). It remains to be tested with simulations if a localized perturbation such as the one discussed here, if confirmed to be real, could (at least partly) account for the velocity deviation found when averaging over the entire azimuth of the disk.

Finally, we note that the feature could also be the result of the imaging reconstruction process. In particular with data at low S/N, the emission can become of patchy struc-

ture, potentially mimicking the presence of a velocity kink. While we note, however, that even in the  $r=0.0$  cube, having the lowest S/N, contours at  $> 6\sigma$  are distorted at the given location, we have to test the robustness of the feature with data a higher sensitivity and angular resolution to draw a final conclusion about the detected feature. The completion of the here presented ALMA project within the next observing period with an additional execution, to fully fulfill our requested constraints, could help in that prospect.

### 4.4.3 Emission surfaces

In Sect. 4.3.2 we have obtained an empirical fit of the emission surfaces of the  $^{12}\text{CO}$  and  $^{13}\text{CO}$  isotopologue emission. In both cases, the emission surface height is increasing with radius and dropping down at large radii. The radial profile of the emission height follows a power law with an index of  $\sim 0.84$  ( $\sim 1.02$ ) out to a radius of about  $1.25''$  or 140 au ( $1.0''$  or 113 au) for  $^{12}\text{CO}$  ( $^{13}\text{CO}$ ). The  $^{12}\text{CO}$  power law index is similar to the power law index of 0.76 which was found in Chapter 3 by fitting a parametric Keplerian model assuming a conical emission surface to the rotation map.

Comparing the emission surfaces of  $^{12}\text{CO}$  and  $^{13}\text{CO}$ , we find that the  $^{13}\text{CO}$  surface is found at lower altitudes. At a distance of 100 au ( $0.88''$ ), the  $^{12}\text{CO}$  surface is found at a height of 36 au, while that of  $^{13}\text{CO}$  is located at a height of 20 au, implying a ratio of  $\sim 1.8$ . Similar ratios of the  $^{12}\text{CO}/^{13}\text{CO}$  emission heights on the order of 1.5-2.5 were also found for other disk (Pinte et al., 2018a; Teague et al., 2020). The  $^{13}\text{CO}$  emission surface is found at lower altitudes with respect to  $^{12}\text{CO}$  due to its respectively lower abundance, causing it to become optically thick at lower heights.

Probing different vertical layers in protoplanetary disks is important in order to establish the vertical temperature structure. Theoretical considerations have established that protoplanetary disks have a vertical temperature gradient, where the surface layers, intercepting the stellar irradiation, are warmer than the midplane, which is shielded from direct illumination (e.g., D'Alessio et al., 1998). This picture is consistent with the fact that the brightness temperature traced for  $^{13}\text{CO}$  is consistently lower than that of  $^{12}\text{CO}$  (see Fig. 4.12), assuming that the emission of both isotopologues are optically thick, and that their brightness temperatures can therefore be used as a proxy for the local gas temperature. Recently, Dullemond et al. (2020) have developed a method to trace the gas temperature even deeper in the disk, within the midplane, of moderately inclined disk. This method relies on observations with sufficient angular resolution to spatially separate the top and bottom sides of the disk in individual channel maps of a very optically thick line emission. Such an approach will be tested with our observations in the near future.

Interestingly, the  $^{12}\text{CO}$  emission surface is shaped such that it approaches a negligible vertical extension inside of  $\sim 0.3''$ . This is another indication that the cavity is strongly de-

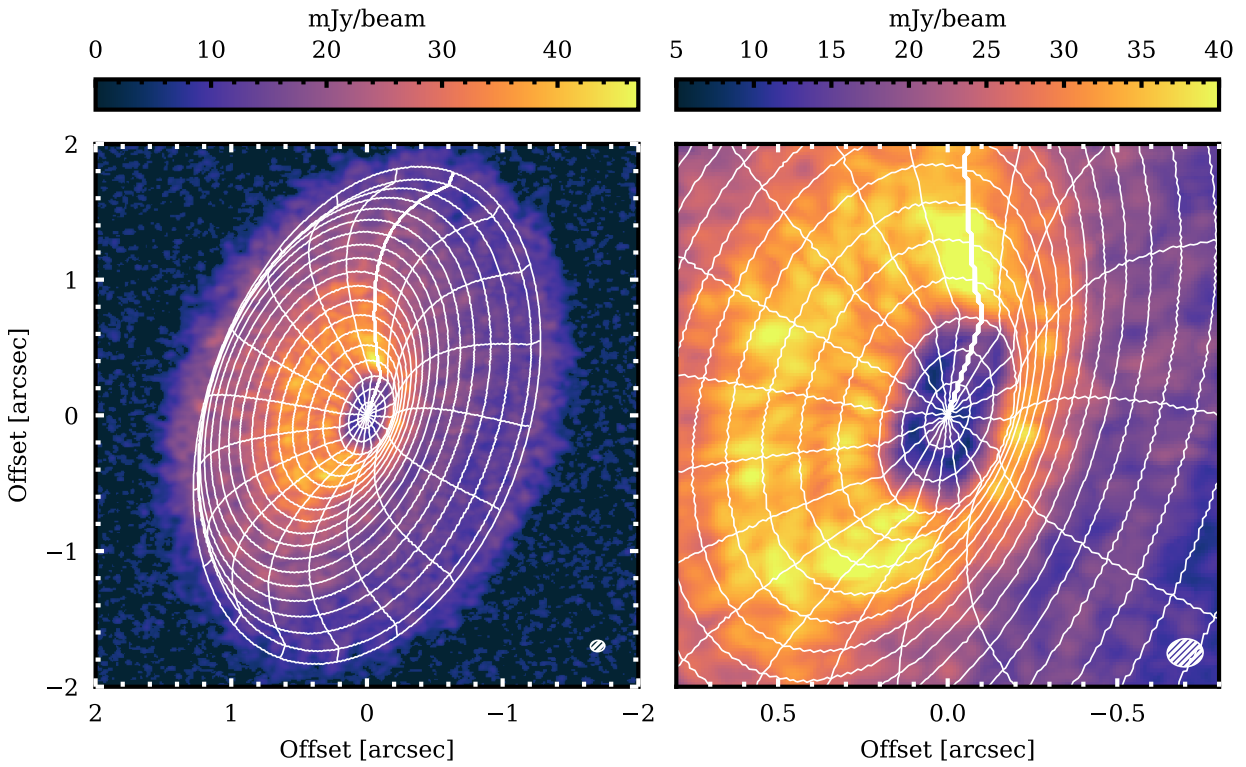


**Figure 4.22:** 3D surface representation of best-fit  $^{12}\text{CO}$  emission surface overplotted on peak intensity map. The right panel is a zoom-in view of the left panel.

pleted: the steep decrease of surface density within the continuum ring, likely as a result of planet-disk interactions, lead to a drop in emission surface and temperature. Regarding  $^{13}\text{CO}$  the emission inside  $\sim 0.5''$  is too low such that we cannot constrain its emission surface inside that radius.

Figure 4.22 illustrates the  $^{12}\text{CO}$  3D surface contours overplotted on the peak brightness temperature map.

## 4.5 Summary and conclusions

In this Chapter, ALMA Band 7 observations of the dust continuum, and of the  $^{12}\text{CO}$  and  $^{13}\text{CO}$  emission lines at high-angular resolution ( $\sim 0.9''$ ) and unprecedented spectral resolution ( $\sim 0.11 \text{ km/s}$ ) were presented. The main goal of these observations is to search for kinematic imprints of PDS 70 b and c within the disk. Our main findings can be summarized as follows:

- We confirm the detection of an asymmetric radial profile of the dust continuum. The azimuthally averaged profile can be described by the superposition of two Gaussian components, centered at 57 and 76 au, respectively.

- We confirm the continuum detection of PDS 70 c<sub>smm</sub>, previously detected as a ‘spur’ in Chapter 3, and identified as a compact emission source co-located with PDS 70 c by Isella et al. (2019). Due to the limited angular resolution, however, we are not able to detect the source as emission separated from the outer dust ring.
- We detect another compact continuum source to the South-East of the inner disk. It is close to, but not exactly co-located with neither the NIR emission of PDS 70 b nor the sub-millimeter source PDS 70 b<sub>smm</sub> identified by Isella et al. (2019). If the source identified by Isella et al. (2019) was identical to that detected in our new data, its proper motion would be inconsistent with that of PDS 70 b. Observations at higher angular resolution are required to solve this puzzling finding.
- Peak brightness temperature and integrated intensity of both <sup>12</sup>CO and <sup>13</sup>CO show evidence of a steep drop within the continuum gap, consistent with the cavity being strongly depleted of gas.
- The <sup>12</sup>CO peak brightness temperature map shows potentially evidence of a gap-like substructure, the robustness and nature of which still has to be confirmed.
- We detect a potential distortion of the <sup>12</sup>CO velocity field in a particular channel map close to the location of PDS 70 c. The robustness of the feature and its potential connection with PDS 70 c remains to be confirmed.
- The spectral lines of <sup>12</sup>CO and <sup>13</sup>CO within the cavity are of very low amplitude and significantly broadened by the Keplerian shear, challenging the search for imprints of PDS 70 b and c in the local spectral line shapes. Future work will be devoted to a detailed analysis in this prospect, in order to confirm potential spectral features reported in this Chapter.
- Finally, we derive the emission surface of <sup>12</sup>CO and <sup>13</sup>CO. <sup>12</sup>CO is found at about twice the altitude as <sup>13</sup>CO, consistent with measurements from other disks. The emission surface within the cavity is found to be of very low vertical extension. This is another indication that the cavity is strongly depleted, consistent with the presence of planets carving a deep gap in the disk.

The dataset presented in this Chapter is extremely rich in information, and has a high potential for more details and aspects to be extracted from in future work. Next steps of the analysis will not only include a profound investigation of the potential features reported in this Chapter. These new data will also allow to perform a detailed analysis of the disk kinematics by establishing the rotation profile, similar to that presented in Chapter 3, but at considerably higher spectral resolution. Further, detailed hydrodynamical simulations

#### *4 An in-depth view of PDS 70 with ALMA at high spectral resolution*

will be useful for the interpretation of any detected features. We note however that the location of PDS 70 b and c within the strongly depleted cavity at very close separations with respect to the star and the inner disk challenges the search for faint structures related to the planets. Observations at higher angular resolution, in addition to the given spectral resolution, would be highly beneficial to that goal.

# 5

## SPHERE observations of binary-disk interactions in GG Tau A

---

The content of this Chapter is based on [Keppler et al. \(2020\)](#), published in *Astronomy & Astrophysics (A&A)*, 639, 62.

**Details of authorship:** I am the first author of this paper and led this team effort involving 33 co-authors under the supervision of Prof. Thomas Henning, and in close collaboration with Roy van Boekel and Myriam Benisty. The text was written by me, with contributions to Sects. 5.6 and A.3.2 by Anna Penzlin, and to Sect. 5.3 by Antonio Garufi. I performed the analysis of the polarimetric data, as well as the radiative transfer post-processing of the hydrodynamical simulations. The polarimetric data was reduced by Rob van Holstein. The hydrodynamical simulations were performed by Anna Penzlin. The schematic illustration of Fig. 5.2 was generated by Thomas Müller, and Figs. 5.10 and A.8 were contributed by Anna Penzlin. All co-authors provided comments to the paper manuscript.

### 5.1 Motivation

Almost half of all main-sequence solar-type stars are found in binary or higher-order multiple systems (e.g., [Raghavan et al., 2010](#); [Duchêne & Kraus, 2013](#)), and it is thought that the fraction of multiple systems is even higher among pre-main sequence stars (e.g., [Duchêne, 1999](#); [Kraus et al., 2011](#)). More than 4000 detections of extrasolar planets around single stars to date show that the assembly of planetary bodies is a common byproduct of star formation. The high abundance of multiple stars on the one hand and planetary companions on the other hand thus raises the question about the possible formation pathways and prevalence of planets in multiple systems. Understanding the properties and initial conditions in circumbinary protoplanetary disks is therefore an important step in approaching this question.

This Chapter presents new high-resolution ( $\sim 0.04''$ ) NIR polarimetric observations of

the circumbinary disk around GG Tau A obtained with the SPHERE instrument. These observations reveal the circumbinary environment at unprecedented detail. The analysis of the disk morphology confirms previously known disk substructures and reveal new features within the circumbinary disk. The observations are compared to hydrodynamical simulations in order to investigate whether the observed structures can be explained by binary-disk interactions. This Chapter is structured as follows: first, Sect. 5.2 introduces the context of circumbinary disks, while Sect. 5.3 provides a revision of the stellar parameters of GG Tau A, followed by the presentation of the observations in Sects. 5.4 & 5.5. Section 5.6 presents the modeling efforts, which are discussed in context with the observations in Sect. 5.7. Sect. 5.8 provides a summarizes the results of this study.

## 5.2 Context

While our understanding of the building-up of planets within protoplanetary disks around single stars has significantly advanced in the past years, less is known about the conditions of planet formation in multiple systems (e.g., [Thebault & Haghhighipour, 2015](#)). In contrast to the single-star case, the evolution of material in the circumbinary and individual circumstellar disks in multiple systems will (depending on the binary parameters such as mass ratio, orbital separation, and eccentricity) be dominated by the gravitational perturbation of the central binary. As a consequence, the binary-disk interaction has severe implications for the planet formation process. Tidal interactions exerted by the binary are expected to truncate the individual circumstellar disks, reducing their masses, outer radii, and viscous timescales (e.g., [Papaloizou & Pringle, 1977](#); [Artymowicz & Lubow, 1994](#); [Rosotti & Clarke, 2018](#)). In addition, the tidal torques will truncate the circumbinary disk from the inner edge by opening a large inner cavity. Despite the resulting separation of circumbinary and circumstellar material, gas streams through the gap may form, supplying the circumstellar disks with material from the outer circumbinary disk (e.g., [Artymowicz & Lubow, 1996](#); [Muñoz et al., 2020](#)). While observational trends infer binary interaction to be indeed destructive for disks in many cases (e.g., [Bouwman et al., 2006](#); [Duchêne, 2010](#); [Harris et al., 2012](#); [Cox et al., 2017](#); [Akeson et al., 2019](#); [Manara et al., 2019](#)), potentially impeding the formation of planets, several massive disks around binary systems are known and have been observed at high angular resolution (e.g., UY Aur, HD142527, HD 34700 A; [Hioki et al., 2007](#); [Tang et al., 2014](#); [Avenhaus et al., 2017](#); [Monnier et al., 2019](#)).

Despite the potential complications for planet formation induced by the gravitational perturbations from the binary, more than 100 planets in binary systems have already been

discovered (e.g., [Martin, 2018](#); [Bonavita & Desidera, 2020](#))<sup>23</sup>. Most of these planets are found to orbit only one of the binary stars (i.e., ‘S-type’, i.e., circumstellar planets). The reason for this certainly is that the radial velocity and transit photometry methods, which represent the most successful planet detection methods in terms of numbers, are strongly biased toward planets on short orbital periods. Nevertheless, about 20 planets have been discovered on orbits surrounding both binary components (i.e., ‘P-type’, i.e., circumbinary planets) (e.g., [Doyle et al., 2011](#); [Orosz et al., 2019](#)). The statistical analysis of the first direct-imaging survey dedicated to finding planets orbiting two stars suggests that the distributions of planets and brown dwarfs are indistinguishable between single and binary stars within the error bars ([Bonavita et al., 2016](#); [Asensio-Torres et al., 2018](#)). This implies that planet formation in multiple systems, and in particular, in circumbinary disks indeed occurs.

Most of the circumbinary planets were detected with the Kepler space telescope on close ( $\lesssim 1$  au) orbits around eclipsing binary systems. Interestingly, they seem to orbit their host systems close to the stability limit, implying that migration processes and planet-disk interactions may have played a crucial role during their early evolution (e.g., [Kley & Haghighipour, 2014](#)). It is therefore clear that the observation and characterization of circumbinary disks provide the unique opportunity of testing the conditions and setup for possible planet formation in multiple systems.

One of these cases is GG Tau. Located at a distance of 150 pc (see Sect. 5.3; [Gaia Collaboration et al., 2016, 2018](#)), GG Tau is a young ( $\sim 1$ -4 Myr; [White et al., 1999](#); [Hartigan & Kenyon, 2003](#); [Kraus & Hillenbrand, 2009](#)) hierarchical quintuple system composed of two main components, GG Tau Aa/b and GG Tau Ba/b, at a projected separation of about  $\sim 10''$  ( $\sim 1500$  au) ([Leinert et al., 1991, 1993](#)). The northern and more massive binary, GG Tau Aa/b (projected separation  $\sim 0.25''$ , corresponding to  $\sim 38$  au) is surrounded by a bright and well-studied circumbinary disk. Recent interferometric observations suggest that the secondary component, GG Tau Ab, is a binary itself (GG Tau Ab1/2) at a projected separation of about 31.7 mas ( $\sim 4.8$  au) ([Di Folco et al., 2014](#)).

The circumbinary disk around GG Tau A is observed as a large and massive disk with a cleared cavity. While the gaseous disk extends out to more than  $\sim 850$  au and reveals a reduced amount of gas in the inner region (e.g., [Guilloteau et al., 1999](#); [Dutrey et al., 2014](#); [Phuong et al., 2020a](#)), the population of large dust grains observed at (sub-)millimeter wavelengths is confined within a narrow ring surrounding a deeply depleted dust cavity, spanning a full width of  $\sim 60$ -80 au centered at a radial distance of about 250 au with respect to the system barycenter (e.g., [Andrews et al., 2014](#); [Dutrey et al., 2014](#); [Tang et al., 2016](#)). Scattered-light observations in the optical, near- and thermal infrared regime in-

---

<sup>23</sup>see also <http://www.univie.ac.at/adg/schwarz/multiple.html> ([Schwarz et al., 2016](#))

fer that the inner edge of the outer disk of the small-grain population is located at about  $\sim 190$ - $200$  au (e.g., [Krist et al., 2002](#); [Duchêne et al., 2004](#); [Itoh et al., 2014](#); [Yang et al., 2017](#)). Such a radial concentration of dust is indicative of particles being trapped within a pressure maximum at the edge of the cavity, as expected for binary-disk interactions (e.g., [de Juan Ovelar et al., 2013](#); [Cazzoletti et al., 2017](#)).

To what extent the tidal interactions of GG Tau Aa/b are responsible for the observed gap size has remained controversial, however. Because the radial location of the gas pressure maximum depends on the binary semimajor axis and eccentricity (e.g., [Artymowicz & Lubow, 1994](#)), the knowledge of the binary orbit is required in order to compare the observed gap size with theoretical predictions. Based on almost two decades of orbital monitoring, a best-fit orbit with a semimajor axis of 36 au and an eccentricity of 0.28 has been established ([Köhler, 2011](#)). However, this orbital solution assumes that the orbit is coplanar with the circumbinary ring; when this assumption is relaxed, the orbital solution is less well constrained and allows for larger orbit sizes. Several theoretical studies have concluded that in order to explain the observed gap size of  $\sim 190$  au, the binary orbit should have a semimajor axis of about  $\sim 65$  au, that is, about one-third of the gap size. To still remain consistent with the astrometric constraints, such a large binary orbit would have to be misaligned with respect to the circumbinary disk (e.g., [Beust & Dutrey, 2005](#); [Cazzoletti et al., 2017](#); [Aly et al., 2018](#)). It is clear that the respective geometry and orientation of binary orbit and circumstellar and circumbinary disk will have a severe effect on the potential of planet formation. Therefore, a detailed knowledge of these parameters is required.

### 5.3 Stellar properties

Although several authors have studied the stellar properties of GG Tau A (e.g., [White et al., 1999](#); [Hartigan & Kenyon, 2003](#); [Kraus & Hillenbrand, 2009](#)), the discovery of the binarity of GG Tau Ab by [Di Folco et al. \(2014\)](#) needs to be taken into account. In this work, we re-calculated the stellar masses and ages following this notion and the newly known distance  $d$  to the system. A negative parallax has been reported for GG Tau A ([Gaia Collaboration et al., 2018](#)), probably because of its binarity (see also [Luhman, 2018](#)), with an absolute value of 6.65 mas. GG Tau B, lying about  $10''$  farther south than GG Tau A, has a positive parallax of 6.66 mas. Because the two components are known to be bound, we used a parallax of 6.66 mas (150 pc) as a proxy for the distance of GG Tau A. We note, however, that the parallax measured for GG Tau B is likely affected by its own binarity as well, such that the distance of the system remains somewhat uncertain.

We assumed spectral types of M0, M2, and M3 for GG Tau Aa, Ab1, and Ab2 and an extinction of 0.3 mag for Aa and 0.45 mag for Ab1/2, as determined by [Hartigan & Kenyon \(2003\)](#) and [Di Folco et al. \(2014\)](#). The corresponding stellar effective temperatures were obtained using the temperature scale of [Rajpurohit et al. \(2013\)](#) calibrated by their NTT spectra. We further assumed stellar luminosities derived by [Hartigan & Kenyon \(2003\)](#), rescaled to 150 pc, considering that their luminosity measured for Ab represents the sum of the luminosities of Ab1 and Ab2 with a respective luminosity ratio of  $\sim 2:1$  (see [Di Folco et al., 2014](#); [Brauer et al., 2019](#)). We derived stellar masses and ages by comparing the locations of the GG Tau A components on a Hertzsprung-Russell diagram with those predicted by a set of five pre-main-sequence tracks ([Siess, PARSEC, MIST, Baraffe, Dartmouth; Siess et al., 2000](#); [Bressan et al., 2012](#); [Dotter, 2016](#); [Choi et al., 2016](#); [Baraffe et al., 2015](#); [Dotter et al., 2008](#)). This yielded the following possible ranges for stellar masses and ages: 0.6-0.7  $M_{\odot}$  and 2.4-3.1 Myr for Aa, 0.3-0.5  $M_{\odot}$  and 2.2-5.6 Myr for Ab1, and 0.2-0.4  $M_{\odot}$  and 2.7-10.0 Myr for Ab2. We adopted the median of these values as our final stellar masses and ages: 0.65  $M_{\odot}$  and 2.8 Myr for Aa, 0.3  $M_{\odot}$  and 2.8 Myr for Ab1, and 0.2  $M_{\odot}$  and 3.1 Myr for Ab2.

Our inferred ages are well within the range of ages derived in previous studies ( $\sim 1$ -4 Myr; [White et al., 1999](#); [Hartigan & Kenyon, 2003](#); [Kraus & Hillenbrand, 2009](#)). Stars in multiple systems are generally assumed to form simultaneously and thus to be coeval. While Aa and Ab1 appear to be coeval according to our analysis, the age derived for Ab2 appears slightly older. However, increasing the luminosity of Ab2 by only 7% reconciles the ages of all three stars. This has almost no effect on the derived mass of Ab2 because the evolutionary tracks run almost vertically in the Hertzsprung-Russell diagram at these young ages.

While the median values of our inferred stellar masses add up to 1.15  $M_{\odot}$ , which is slightly lower than the dynamical mass of the system derived through the CO observations of  $1.37 \pm 0.08 M_{\odot}$  ([Guilloteau et al., 1999](#), scaled to 150 pc), the range of possible stellar masses constrained by our models does not exclude a total mass of 1.37  $M_{\odot}$ . We note, however, that the determination of spectral types, effective temperatures, and luminosities, as well as the evolutionary models (e.g., by not taking the effect of magnetic fields into account; [Simon et al., 2019](#); [Asensio-Torres et al., 2019](#)) is hampered by some uncertainty, which might explain any discrepancy between our inferred values and those derived from the CO observations. Furthermore, our inferred total stellar mass might be underestimated if any of the components has an additional as yet undiscovered close-in stellar companion.

The circumbinary disk is observed at an inclination of  $37^{\circ}$  and at a position angle of  $277^{\circ}$  ([Guilloteau et al., 1999](#)). The system parameters are summarized in Table 5.1.

**Table 5.1:** Properties of the GG Tau A system assumed in this study.

<b>Stellar parameters</b>	Aa	Ab1	Ab2	ref.
Spectral type	M0	M2	M3	a,b
L [ $L_{\odot}$ ]	0.44	0.153	0.077	a,b,c
Teff [K]	3900	3400	3200	d
Mass [ $M_{\odot}$ ]	0.65	0.30	0.20	e
Age [Myr]	2.8	2.8	3.1	e
<b>Disk properties</b>				
inclination		$37 \pm 1^{\circ}$		f
position angle		$277 \pm 1^{\circ}$		f

**Notes.** References: a) Hartigan & Kenyon (2003), b) Di Folco et al. (2014), c) Brauer et al. (2019), d) Rajpurohit et al. (2013), e) this work, f) Guilloteau et al. (1999).

## 5.4 Observations and data reduction

GG Tau A was observed with SPHERE (Beuzit et al., 2019) as part of the guaranteed-time observations (GTO) during the night of 2016 November 18. The IRDIS instrument (Dohlen et al., 2008) was used in the dual-beam polarimetric imaging (DPI) mode (Langlois et al., 2014; de Boer et al., 2020; van Holstein et al., 2020), applying the H-band filter ( $1.625 \mu\text{m}$ ; pixel scale  $12.25 \text{ mas/px}$ ), and the telescope operated in field-tracking mode. One polarimetric cycle consisted of tuning the half-wave plate position at four different angles ( $0^{\circ}$ ,  $45^{\circ}$ ,  $22.5^{\circ}$ , and  $67.5^{\circ}$ , respectively). At each of these positions, we took 15 frames with an exposure time of 4 s each. A total of 11 polarimetric cycles was carried out, resulting in a total integration time on the science target of about 44 minutes. No coronagraph was used during the observations, inducing a slight saturation at the location of both Aa and Ab. Weather conditions were relatively stable during the observations (seeing at  $500 \text{ nm} \sim 0.6''\text{-}0.9''$ , coherence time  $\sim 3 \text{ ms}$ , and wind speed  $\sim 10 \text{ m/s}$ ). We measured a point spread function (PSF) full width at half-maximum (FWHM) of about  $43 \text{ mas}$  by fitting a Moffat pattern to the unsaturated images obtained with a neutral density filter.

The data were reduced using the IRDAP pipeline<sup>24</sup> (van Holstein et al., 2020). In short, after basic steps of data reduction (dark subtraction, flat fielding, bad-pixel correction, and centering), the pipeline obtains the clean Stokes  $Q$  and  $U$  frames using the double-difference method. The data are then corrected for instrumental polarization and cross-talk effects by applying a detailed Mueller matrix model that takes the complete optical path of the light beam into account. After correcting for instrumental effects, the pipeline determines, and if desired, also subtracts, any remaining stellar polarization. This is measured by quantifying the flux in the  $Q$  and  $U$  images from regions without polarized disk

<sup>24</sup><https://irdap.readthedocs.io>

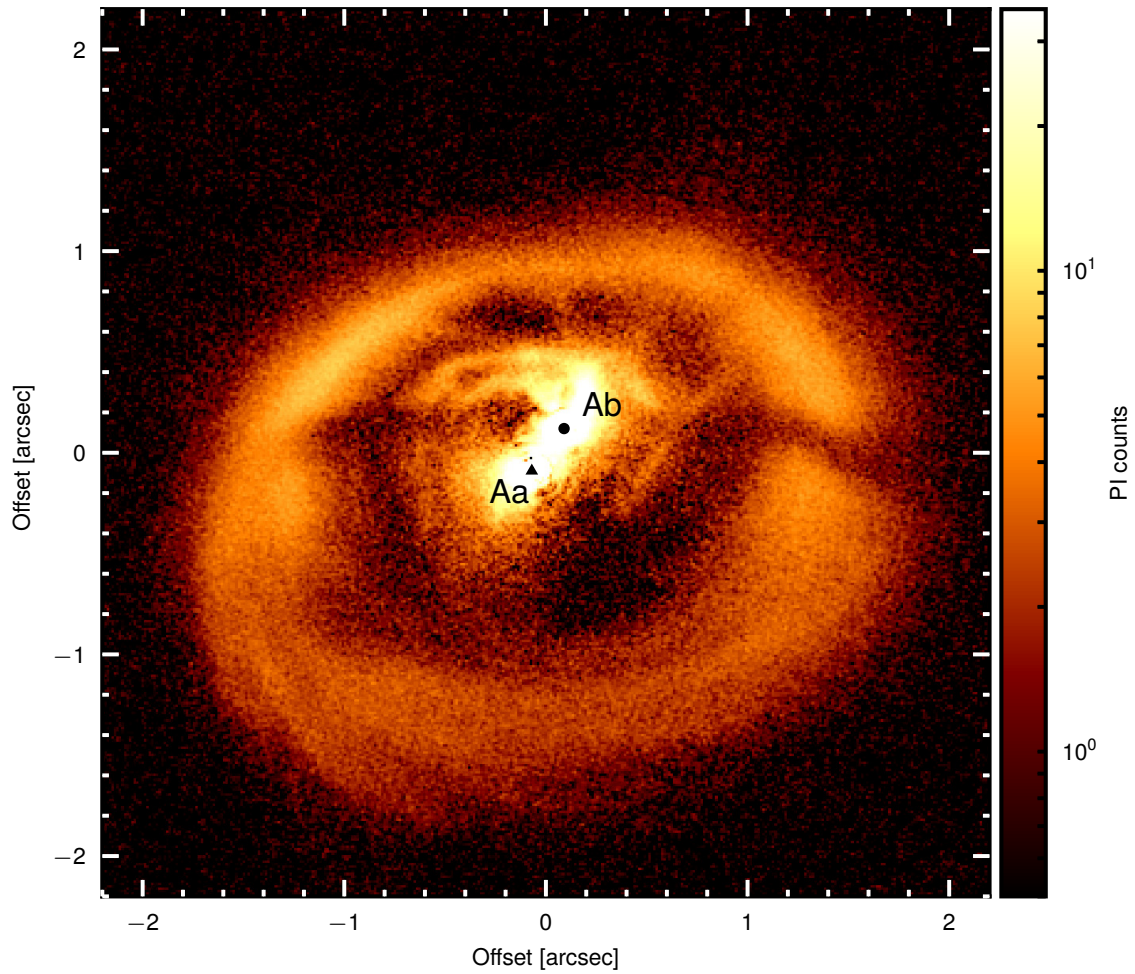


**Figure 5.1:** SPHERE polarized intensity ( $PI$ ) image of GG Tau A. The image is centered on the expected location of the system’s center of mass. The locations of GG Tau Aa and Ab are marked by a black triangle and circle, respectively. North is up and east is to the left.

emission. From the final  $Q$  and  $U$  images, a linear polarized intensity ( $PI$ ) image is then obtained, following  $PI = \sqrt{Q^2 + U^2}$ . This final image is corrected for true north (Maire et al., 2016a). For details regarding the pipeline, we refer to van Holstein et al. (2020). Finally, the images were recentered on the expected location of the center of mass, assuming a mass ratio between GG Tau Aa and GG Tau Ab1/2 of 0.77 (see Sect. 5.3).

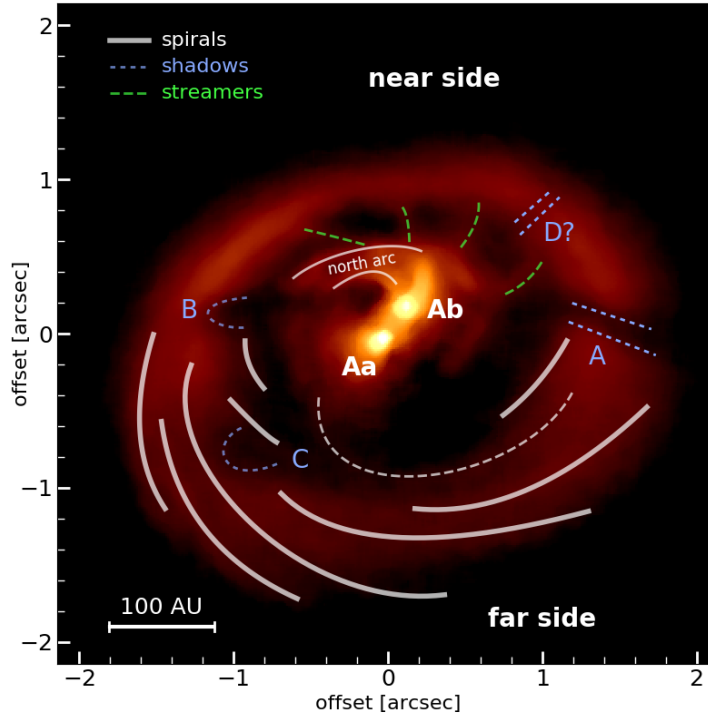


**Figure 5.2:** Schematic overview of the features in the outer circumbinary ring detected in our SPHERE *PI* image. The image is centered on the location of GG Tau Aa and was smoothed for illustration purposes.

## 5.5 Results

The final *PI* image is shown in Fig. 5.1. In our image, the binarity of GG Tau Ab1/2 is not resolved, therefore we refer to this component in the following as Ab. The image shows bright emission close to Aa and Ab, followed by a gap that is surrounded by the bright circumbinary ring. The circumbinary ring is highly structured, with several shadowed regions, as well as several fine filament structures connecting the northern side of the ring with the close environment of the binary, and spiral structures in the southern disk region. Figure 5.2 presents a schematic overview of the detected features in the outer disk region. The following sections are dedicated to a detailed characterization of the different disk regions and categories of substructures.

### 5.5.1 Inner region

Our final image, after correction for the instrumental polarization effects, reveals a residual unresolved polarized intensity signal at the locations of both Aa and Ab. We measure a linear polarization degree and angle of 0.33% and  $37.1^\circ$  at the location of Aa, and 1.12% and  $8.7^\circ$  at the location of Ab. A non-negligible amount of residual polarization can be

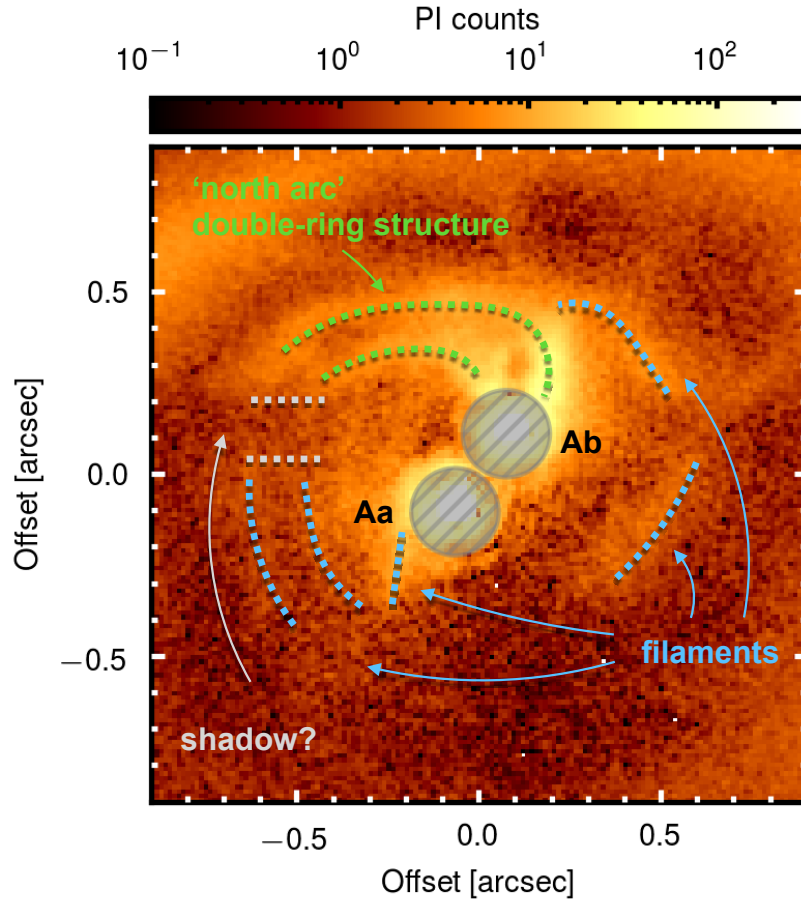


**Figure 5.3:** Zoom on the inner region after subtraction of the stellar polarization on Aa. The dotted lines highlight the detected features: the 'north arc', revealing a double-arc structure (green), several filaments (light blue) and a possible shadow lane (gray dashed). See Sect. 5.5.1 for details. The immediate stellar environments ( $< 120$  mas) are masked out. North is up and east is to the left.

interpreted as signal from unresolved circumstellar material such as a disk observed at nonzero inclination (e.g., van Holstein et al., 2020; Keppler et al., 2018; Garufi et al., 2020). The circumstellar material around both components is confirmed by the measurement of non-negligible extinction ( $A_V = 0.3$  mag and 0.45 mag toward Aa and Ab, respectively; Hartigan & Kenyon, 2003), as well as accretion signatures from hydrogen-recombination lines and  $10 \mu\text{m}$  silicate features found at the location of both components (White et al., 1999; Hartigan & Kenyon, 2003; Skemer et al., 2011). While we cannot make a statement about the inclinations of the disks from our measurements (except for excluding the case where the disks would be seen face-on and are circular symmetric: in this case, the polarized signal would cancel out), the measured angles of linear polarization indicate that the disks are oriented at position angles of  $\sim 127^\circ$  and  $\sim 99^\circ$  (i.e., perpendicular to the direction of linear polarization), respectively. We note that close to the stars, the radiation

field is dominated by their individual illumination, and the contribution to the measured residual  $PI$  from the respective other star can be neglected (see Sect. A.3.1). Observations at higher angular resolution and/or detailed modeling are required to better constrain the orientation of the circumstellar disks.

Any unresolved circumstellar material may create a halo of polarization signal around the star. Because this unresolved polarized signal can affect the analysis of the immediate circumstellar environments, we subtracted these polarized signals (i.e., the total intensity halo multiplied by the degree of polarization) individually for Aa and Ab. While subtracting the polarization signal of Aa slightly increases the contrast of the fine structures in the immediate stellar environment, subtracting the polarization signal of Ab instead blurs these structures. This can be explained by the fact that the measured polarization degree of Ab is somewhat higher than that of Aa. Therefore, subtracting the polarization signal of Ab adds an artificial polarization halo around Aa, which weakens the fine structures in its environment. Subtracting the (less strongly) polarized signal of Aa, however, does not noticeably affect the environment of Ab. Figure 5.3 shows the resulting image after subtraction of the polarization signal of Aa with annotations of the detected features. The immediate stellar environments that are affected by the diffraction pattern are masked out. In all the images, the inner region appears highly structured, as highlighted in Fig. 5.3 by the dotted lines. Most prominently, the ‘north arc’, an extended structure to the northeast of Ab observed in previous scattered light images (e.g., Krist et al., 2002, 2005; Itoh et al., 2014; Yang et al., 2017), is clearly detected and appears in our SPHERE image to be composed of a double-arc structure at projected separations of  $\sim 0.38''$  and  $\sim 0.48''$ . This double-arc structure may extend along the entire eastern side to the south, interrupted by a dark lane extending from Ab toward the east (see the dotted gray lines in Fig. 5.3). This dark lane seems to be connected to the shadow observed in the outer disk at a similar position angle (see Sect. 5.5.4). We furthermore detect two additional filament structures northwest and southwest of Ab. It is unclear, however, whether they are related to the double-arc system on the eastern side. Finally, another filament is detected immediately southeast of Aa, pointing toward the south.

Figure 5.4 (left panel) shows the angles of linear polarization overplotted on the inner disk region. The polarization angles  $\theta$  were calculated according to  $\theta = 0.5 \times \arctan(U/Q)$ , within bins of 3 pixels. Within the entire inner region, the polarization vectors appear to be generally aligned in azimuthal direction, as expected for light that is scattered off dust particles illuminated by a central source. Deviations from azimuthal polarization, as in the southwest from Aa, for example, may be due to the complex illumination pattern by the binary, or they might indicate multiple scattering events (e.g., Canovas et al., 2015). We note that the disk substructures we detected and highlight in Fig. 5.3 cannot be explained by a potential interference of polarization vectors in the presence of two

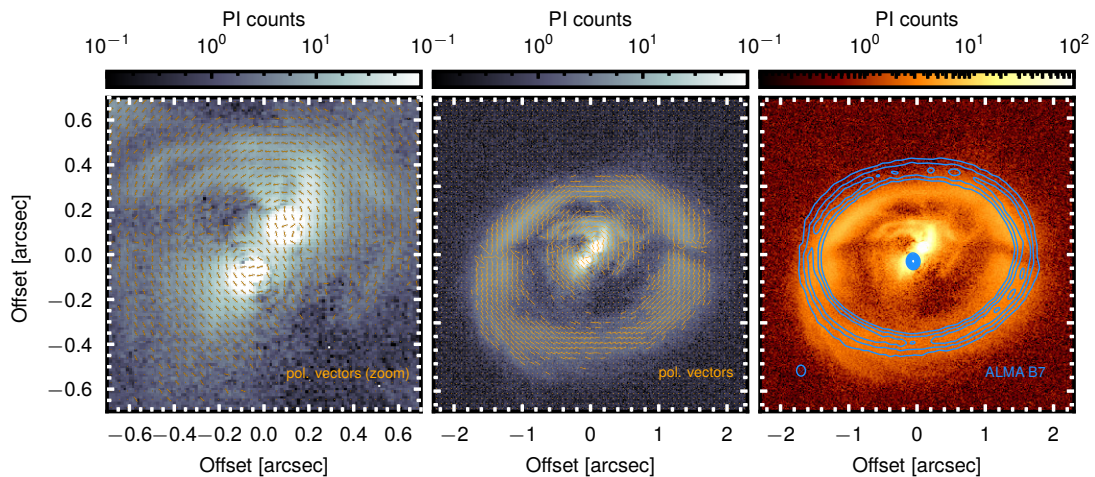


**Figure 5.4:** *Left and center:* SPHERE *PI* image with lines indicating the angle of linear polarization overplotted, showing two different fields of view ( $0.7'' \times 0.7''$ ,  $2.3'' \times 2.3''$ ). The lines have an arbitrary length. For the computation of the polarization angles, we ignored bins at which the binned polarized intensity values  $\leq 1.9$ . *Right:* polarized intensity image with ALMA Band 7 (0.9 mm) continuum contours overplotted (blue). The ALMA observations were published in [Phuong et al. \(2020a\)](#). The ALMA image was registered such that the inner continuum emission, attributed to a circumstellar disk around Aa, coincides with the NIR position of Aa. Contours are shown at 20, 30,..., 80, 90% of the peak intensity. The beam size is indicated in the lower left corner.

illumination sources, which might in principle lead to cancelling *PI* out if the polarization vectors included an angle of  $90^\circ$  (see Sect. A.3.1). This illustrates that small grains scatter light from the central illumination sources within a large region around the binary.

## 5.5.2 Outer disk geometry

As in previous observations, the outer circumbinary disk appears as a large elliptical ring. The polarization angles in the center panel of Fig. 5.4 (here calculated within bins of 6 pixels) show that also in the outer disk, the detected signal is overall well polarized in the azimuthal direction. Only emission within two shadowed regions (shadows A and B, see Sect. 5.5.4) appears to be less consistently aligned, owing to the lower signal-to-noise ratio. We note that while the circumbinary ring appears bright in (sub-)millimeter continuum observations (e.g., [Guilloteau et al., 1999](#); [Dutrey et al., 2014](#); [Tang et al., 2016](#); [Phuong et al., 2020a](#)), the region inside the ring reveals little to no signal at these wavelengths, except for an unresolved source at the location of Aa. This is illustrated by an overlay of the SPHERE image with the contours of the ALMA dust continuum at 0.9 mm ([Phuong et al., 2020a](#)) in

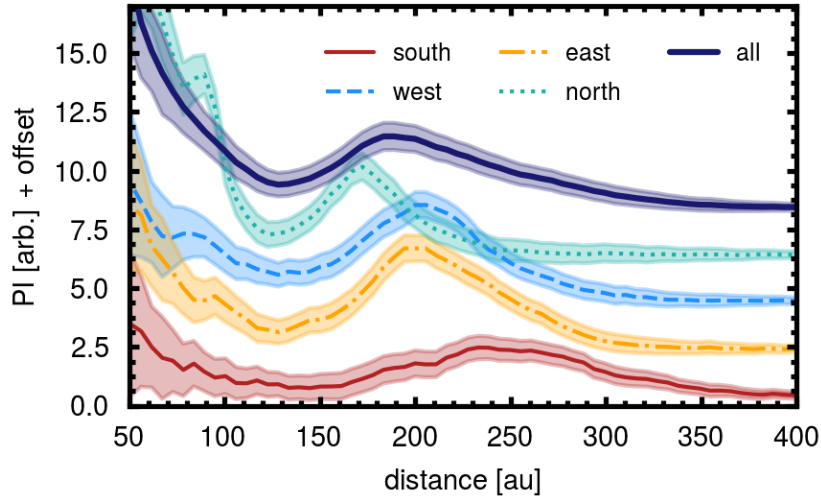


**Figure 5.5:** Radial disk profiles, taking into account the disk inclination of  $37^\circ$ . The profiles are drawn along the major (east, west) and minor (north, south) axes within an azimuthal cone of  $\pm 20^\circ$  around the corresponding axes, as well as averaged over all azimuths. The radial bin size is 3 pixels.

Fig. 5.4 (right). This may imply that dust grains are mostly of small size inside the cavity, consistent with large grains being trapped in the outer circumbinary ring, while small grains, well coupled to the gas, can still enter the cavity (e.g., Pinilla et al., 2012b; de Juan Ovelar et al., 2013; Cazzoletti et al., 2017). The comparison of the SPHERE and ALMA images also shows an obvious shift of the ring roughly along the disk minor axis, which is due to a projection effect related to the fact that the ALMA dust continuum traces the disk midplane, while the near-infrared SPHERE observations image the scattering surface of the disk. This is explained in detail in the following.

Figure 5.5 shows the radial deprojected profiles of the linear polarized intensity averaged along the major and minor axes, as well as averaged over the complete range of azimuthal angles. The polarized intensity along the major axis peaks around 200 au. Although the derivation of the profiles takes the projection by the disk inclination into account, the profiles along the near (north) and far (south) side of the minor axis appear very different: while the profile along the near side is quite peaked and peaks farther in than the major axis ( $\sim 175$  au), the profile of the far side is much broader and peaks at a much larger distance ( $\sim 250$  au). The different peak locations along the minor axis reflect a shifted geometric center of the ring because the ring is not geometrically flat, but has a non-negligible thickness. Similarly, the different profile shapes (broad versus peaked) are also connected to the geometrical thickness because the inclination of the disk allows us to see the inner rim of the southern (far) side, while for the north (front) side, the inner wall is hidden and only the upper surface is visible (e.g., Silber et al., 2000; Krist et al., 2005).

To quantify the outer ring geometry, we extracted radial profiles within azimuthal bins of  $20^\circ$  width. For each azimuthal bin, we determined the location of maximum brightness by fitting a polynomial function to the radial profile and then fitting an ellipse to the radial peak locations at all position angle bins. We find that the ring can be fit with an ellipse of eccentricity 0.64, a semimajor axis of 216 au, and a position angle of  $288^\circ$ . The geometric center of the ellipse is offset by 32 au toward the south from the assumed center of mass. These results compare well with the values found in previous scattered-light studies at similar wavelengths (e.g., McCabe et al., 2002). If the disk were geometrically flat and intrinsically circular, an eccentricity of 0.64 would imply an inclination of  $39.7^\circ$ . This value is slightly higher than the inclination of  $37^\circ \pm 1^\circ$  derived from (sub-)millimeter continuum observations (Guilloteau et al., 1999; Andrews et al., 2014) because the geometric thickness of the disk affects the scattered-light observations (e.g., Guilloteau et al., 1999; McCabe et al., 2002; Krist et al., 2002). The measured offset  $\Delta s$  of the geometric center of the ellipse from the assumed system barycenter can be used to constrain the scattering surface height  $H_{\tau=1}$  along the ellipse according to  $H_{\tau=1}(r) = \Delta s(r)/\sin(i)$  (e.g., de Boer et al., 2016). Our measured offset  $\Delta s$  of 32 au therefore corresponds to a scattering height of  $\sim 53$  au at the inner edge of the ring ( $\sim 200$  au). Because the scattering surface height typically traces layers at about 2-3 times the pressure scale height  $H_p$ , this would imply an aspect ratio of  $H_p/R \sim 0.09-0.13$ , which compares well with constraints from other disks (e.g., Villenave et al., 2019). We stress that this should only be considered as a rough estimate because azimuthal variations of the surface brightness, due to the azimuthal dependence of phase function and polarization degree, as well as the abundance of disk substructures such as shadows and spirals, may complicate a precise determination of the isophotes to which our ellipse was fit.

Finally, a precise knowledge of the vertical thickness of the ring is required in order to determine the disk eccentricity from the scattered-light data. However, optically thin millimeter observations indicate that the intrinsic eccentricity of the ring is rather low because the continuum, which traces the emission from the disk midplane and whose shape is therefore less biased by geometrical effects, can be well fit by an intrinsically circular model ring at the given angular resolution (beam major axes of  $0.45''$  and  $0.67''$ ; Piétu et al., 2011; Andrews et al., 2014).

### 5.5.3 Streamers

We detect four filament-like structures connecting the inner edge of the outer disk and the outer edge of the northern arc, as indicated in green in Fig. 5.2. Some of these structures have previously been described as ‘bridges’ by Itoh et al. (2014) and Yang et al. (2017).

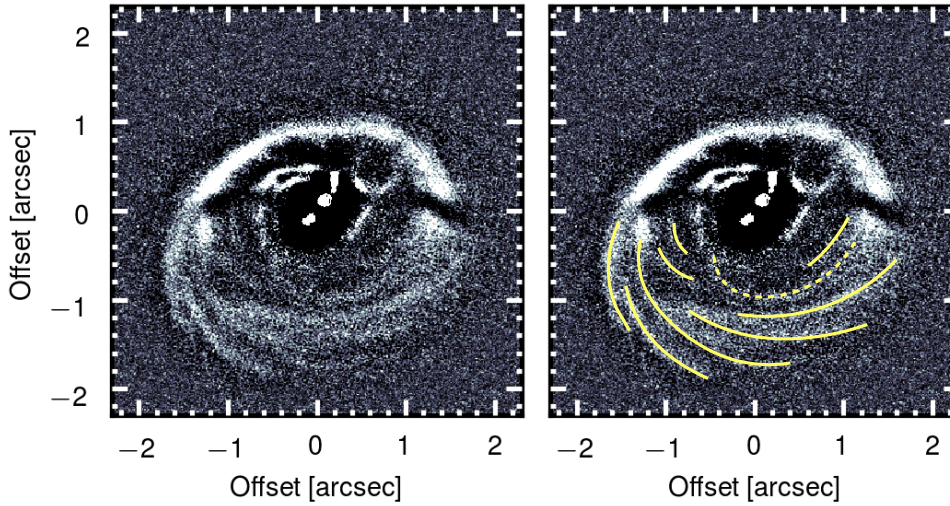


**Figure 5.6:** High-pass filtered PI image of GG Tau A (*left*) with highlighted spiral structures (*right*). The dashed line highlights the possible connection of the outer disk to Aa.

In order to measure the position angles of these structures, we deprojected the image, assuming  $i = 37^\circ$  and  $PA = 277^\circ$ . The connecting points of the filaments at the inner edge of the outer disk are found at approximately  $PA \sim 296^\circ, 331^\circ, 0^\circ$ , and  $36^\circ$  (from west to east). The filaments are not aligned with the radius vector pointing toward the center of mass, but are tilted by increasing angles from west to east of  $\sim 13^\circ$  to  $26^\circ$  with respect to the radial direction. The measured  $PA$ s imply that the azimuthal spacing of the filaments is about  $29^\circ, 35^\circ$ , and  $36^\circ$ . When we adopt an arbitrary uncertainty on the  $PA$  measurement of  $5^\circ$ , this translates into a mean spacing of  $33.3 \pm 2.9^\circ$ . When we assume that the outer disk is in Keplerian rotation around a center of mass with  $1.15 M_\odot$ , the azimuthal spacing of the filaments may imply that the filaments are launched by periodic perturbations occurring at the inner edge of the disk ( $180 \pm 20$  au) every  $208 \pm 29$  years.

The binary best-fit semimajor axis of 36.4 au constrained by Köhler (2011) (scaled here to 150 pc) translates into an orbital period of about 205 years, assuming a central binary mass of  $1.15 M_\odot$ . The azimuthal spacing of the filaments would therefore be compatible with being triggered by a periodic perturbation occurring once every binary orbit, when the secondary passes at apocenter and comes closest to the disk edge. Interestingly, when we assume that the binary orbit is coplanar with the disk, the binary has just passed apastron (McCabe et al., 2002).

We interpret the filaments as accretion streams. Accretion streams close to the north arc have previously been suggested by continuum observations at 1.1 mm (Piétu et al., 2011), as well as by the CO J = 6-5 emission line, which show deviation from Keplerian rotation that may be compatible with infall motion (Dutrey et al., 2014). Furthermore, the  $^{12}\text{CO}$  gas distribution within the cavity shows a highly inhomogeneous structure consisting of

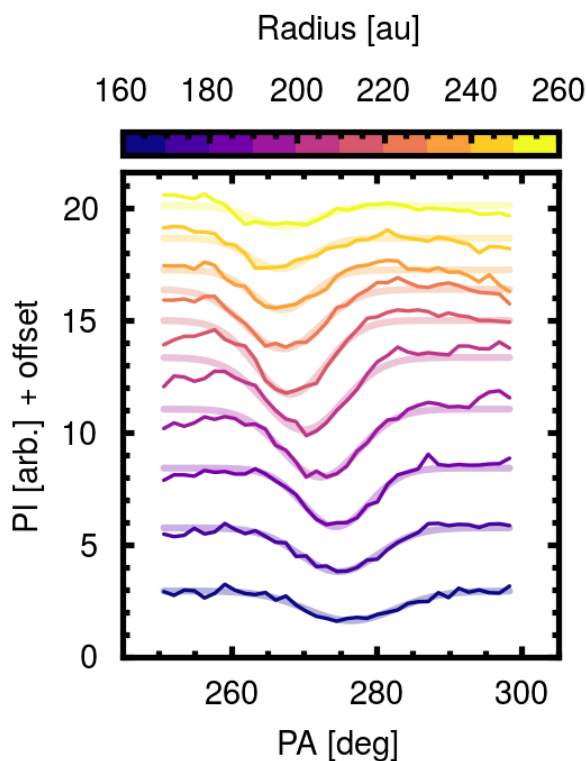


**Figure 5.7:** Azimuthal profiles of the western shadow at different (deprojected) radial bins between 160 and 260 au. The smooth, shadowed lines correspond to the best-fit Gaussian profiles, respectively.

several fragments (Dutrey et al., 2014). One of these CO fragments coincides with the location of the northern arc. As noted by Yang et al. (2017), the entire northern arc may thus itself be part of a large accretion stream.

### 5.5.4 Shadows

We detect three shadowed regions, known from previous scattered-light observations (e.g., Silber et al., 2000; Itoh et al., 2014; Yang et al., 2017), at  $PA \sim 275^\circ$ ,  $\sim 86^\circ$ , and  $\sim 132^\circ$ , and labeled A, B, and C in Fig. 5.2. In addition, we detect a tentative fourth shadow, labeled 'D', at a  $PA$  of about  $320^\circ$  and possibly related to a less prominent gap detected at a similar location ( $PA \sim 310^\circ$ ) by Krist et al. (2005).

The most prominent shadow is a dark lane close to the western major axis of the disk (shadow 'A'). To measure the shadow location, we deprojected the disk assuming an inclination of  $37^\circ$ , transformed the image into polar coordinates, and traced the azimuthal profile of the shadow in different radial bins. We then fit a Gaussian profile with negative amplitude to these profiles. At the inner and outer edge of the ring ( $\sim 175$  au and

$\sim 245$  au), we find the shadow center to be located at  $PA$  of  $274.8^\circ$  and  $266.7^\circ$ , respectively. The tilt of the shadow is therefore about  $8^\circ$ . We furthermore measured the contrast of the surface brightness in polarized intensity within the shadow lane with respect to the disk just north of it, resulting in a contrast of about 2.6.

Using the Subaru datasets taken in 2001 January and 2011 September, Itoh et al. (2014) measured an anticlockwise rotation of the shadow of  $5.9^\circ$  and  $4.9^\circ$  between both epochs for the inner and outer disk edges, respectively. If the movement were linear in time, we would expect a further displacement by  $\sim 2.5\text{--}3^\circ$  between 2011 and our SPHERE dataset taken in 2016 November. In order to verify the movement, we repeated our procedure of determining the shadow location on the total intensity frame of the 2011 Subaru dataset. We measure a shadow  $PA$  of  $274.4^\circ$  and  $268.1^\circ$  at the inner and outer edge of the disk as defined above. Compared to the values we measured on our SPHERE dataset above ( $274.8^\circ$  and  $266.7^\circ$ ), we therefore cannot confirm a linear movement of the shadow between 2011 and 2016. The shadow positions instead appear to be stable.

It has been suspected that this western shadow may be cast by circumstellar material (e.g., Itoh et al., 2014), such as by an inclined disk around one of the binary components, as in the case of HD 142527 (Marino et al., 2015). Shadow ‘B’ (and the dark lane to the east of Ab detected in the inner region, see Sect. 5.5.1) may be just the east side of this same shadow (see also Brauer et al., 2019). We can estimate the expected brightness contrast of the shadow lane with respect to the adjacent nonshadowed disk region under the hypothesis that one or two of the illumination sources are blocked by an optically thick inclined disk. A disk region that does not lie in any shadow is illuminated by all three stars, and it will therefore receive a total flux of  $F_{\text{tot}} = (1/4\pi) \times (L_{\text{Aa}}/d_{\text{Aa}}^2 + L_{\text{Ab1}}/d_{\text{Ab1}}^2 + L_{\text{Ab2}}/d_{\text{Ab2}}^2)$ , where  $d_x$  is the distance of component  $x$  to the shadowed disk region. When one of the stellar components is surrounded by an inclined optically thick disk, this will cast a shadow on the outer disk, which will therefore only be illuminated by the two remaining sources. Using the stellar luminosities as defined in Table 5.1, and estimating a distance of Aa and Ab to shadow ‘A’ of  $\sim 181$  au and  $\sim 156$  au, respectively (as measured on the deprojected image), we would expect a contrast of  $\sim 2.4$  for a disk around Aa, a contrast of  $\sim 1.7$  for a disk around Ab (i.e., a circumbinary disk around Ab1/2), and a contrast of  $\sim 1.4$  and  $\sim 1.2$  for a disk around Ab1 and Ab2, respectively. The measured contrast of 2.6 from our SPHERE data would therefore favor the shadow to be cast by an inclined disk around Aa or Ab, rather than around Ab1 or Ab2.

Min et al. (2017) have developed an analytical description with which the orientation of an inner shadow-casting disk can be derived from measuring the orientation of the shadows cast on the outer disk. We repeated the same procedure for GG Tau A, assuming that the shadow is cast by a disk around either Aa or Ab. For this purpose, we measured the position angle of the line connecting the two shadows of about  $90^\circ$ , and the vertical

(projected) offset of this line of 21.2 au and -9.7 au from Aa and Ab, respectively. Inserting these values into equations 7 and 10 of [Min et al. \(2017\)](#), we obtain a disk position angle of about  $90^\circ$  for the shadow-casting disk for both cases. Assuming an outer disk aspect ratio of 0.1-0.15, and assuming that the scattering surface is found at about 2-3 times the pressure scale height, we furthermore find an inclination of  $\sim 72^\circ$ - $81^\circ$  if the disk were found around Aa, and an inclination of  $\sim 96^\circ$ - $100^\circ$  if it were found around Ab. Considering the outer disk inclination of  $37^\circ$ , the misalignment of a disk around Aa and Ab would then be  $\sim 35^\circ$ - $44^\circ$  and  $\sim 59^\circ$ - $63^\circ$ , respectively.

Recently, [Brauer et al. \(2019\)](#) have investigated the effect of circumstellar disks around the binary components on the brightness distribution within the circumbinary ring using radiative transfer modeling. In one of their setups, they simulated an inclined circumstellar disk around Ab2 (while keeping a coplanar disk around Aa). In this case, their simulations were able to reproduce a sharp shadowed lane at the location of shadow 'A', as well as a symmetric eastern shadow (corresponding to shadow 'B'), although they found it to be shallower in brightness contrast than in the observations. We suggest here that an inclined disk around Ab (i.e., a circumbinary disk around both Ab1 and Ab2) or around Aa would be more compatible with the measured contrast.

### 5.5.5 Spirals

We detect multiple spiral structures in the southern part of the disk. For an improved identification, we processed the image by a high-pass filter, that is, we convolved the image with a Gaussian filter ( $\sigma = 9$  px) and subtracted it from the original image. The spiral structures are clearly seen in this image (Fig. 5.6). Interestingly, one spiral arm is tentatively found to cross the gap, and if confirmed, connects the southwestern circumbinary ring to the immediate circumstellar environment of Aa (see the dashed yellow line in Fig 5.6, right). Thin filaments in the southeast disk have previously been suggested from the observations by [Krist et al. \(2005\)](#), who interpreted these structures as possible signs of binary-disk interactions. Furthermore, [Tang et al. \(2016\)](#) and [Phuong et al. \(2020b\)](#) found at an angular resolution of  $\sim 0.3$ - $0.4''$ , that the radial distribution of CO brightness in the outer disk exhibits several spiral structures.

## 5.6 Modeling

We performed hydrodynamical simulations in order to model the system and its evolution. The main goal was to verify whether the binary might be qualitatively responsible for the observed gap size and features within the circumbinary ring.

### 5.6.1 Hydrodynamical model setup

We carried out hydrodynamical simulations of the gas disk using the GPU version of PLUTO (Mignone et al., 2007) by Thun & Kley (2018). The simulations were 2D and isothermal. We used a polar radially logarithmic grid ranging from one binary semimajor axis ( $a_{\text{bin}}$ , 35 au) to  $40 a_{\text{bin}}$  (1400 au) with 684 cells in radial and 584 cells in azimuthal direction. Because the separation of Ab1 and Ab2 ( $\sim 5$  au; Di Folco et al., 2014) is smaller than the inner edge of the circumbinary ring ( $\sim 200$  au), we considered Ab1 and Ab2 together as a single component, Ab, and the entire system was treated as a binary. The binary components Aa and Ab were assumed to have masses of  $0.75 M_{\odot}$  and  $0.67 M_{\odot}$ , implying a mass ratio of 0.89, similar to the mass ratio of 0.77 derived in Sect. 5.3. As shown in Thun & Kley (2018), minor changes in the mass ratio of the binary affect the disk dynamics only very slightly. The binary orbit was set to have a semimajor axis of 35 au and an initial eccentricity of 0.28, consistent with the observations (Köhler, 2011). Furthermore, the binary orbit was assumed to be coplanar with the circumbinary disk plane. We ran two different models that differed only in the adopted radial temperature profile. In the first model, we considered a temperature profile constrained by the  $^{13}\text{CO}$  molecule (Guilloteau et al., 1999), tracing the disk surface temperature, and in the second model, we applied a temperature profile constrained by the dust continuum (Dutrey et al., 2014), tracing the midplane temperature,

$$T_{\text{surface}} = 20 K \cdot \frac{300 \text{ au}}{r} \quad (5.1)$$

$$T_{\text{midplane}} = 13.8 K \cdot \frac{200 \text{ au}}{r}. \quad (5.2)$$

By considering these two different temperature profiles, which are sensitive to the warm disk surface and to the cool midplane, respectively, we covered the two limiting cases. The aspect ratio  $h = H/r$  of the disk was determined by the sound speed  $c_s$  and Keplerian orbital frequency  $\Omega_k$ , and therefore results from the assumed temperature profile as follows:

$$h = \frac{c_s}{\Omega_k r} = \sqrt{\frac{k_B}{GM_{\text{bin}}\mu m_p}} \cdot \sqrt{Tr}, \quad (5.3)$$

with  $M_{\text{bin}}$  the binary mass,  $\mu=2.3$  the mean molecular weight,  $m_P$  the proton mass, and  $R$  the radial distance from the system barycenter in the disk plane. With our chosen temperature profile, we obtain a constant aspect ratio corresponding to the following values:

$$h_{\text{surface}} \approx 0.15 \quad (5.4)$$

$$h_{\text{midplane}} \approx 0.11. \quad (5.5)$$

The initial surface density follows a power law  $\propto r^{-1.5}$  normalized in such a way that the total disk mass amounts to 10% of the binary mass ( $0.14 M_{\odot}$ ). As the inner  $3 a_{\text{bin}}$  of the disk are unstable, the initial density profile inside of  $2.5 a_{\text{bin}}$  exponentially decays to  $e^{-1}$  of the smooth profile within  $0.1 a_{\text{bin}}$ . The boundary conditions of the simulations were defined as in [Thun & Kley \(2018\)](#). We simulated the gas content of the disk assuming an  $\alpha$  viscosity with a constant Shakura-Sunyaev parameter of  $10^{-3}$  throughout the disk.

The computational time needed to reach the actual disk structure from the initial power-law profile can be long ([Kley et al., 2019](#)). To ensure a feasible time step for the grid code, we did not include the stars themselves in the simulation domain, but the inner grid boundary was set to a radius of  $1 a_{\text{bin}}$  (35 au) and we added the binary as n-bodies inside the domain to create the potential, using a gravitational softening parameter of 0.6 (see [Kley et al., 2019](#)). As discussed in [Kley et al. \(2019\)](#), such an inner boundary does not change the dynamics of the circumbinary disk or gap width. The outer disk edge is an open boundary that assumes a continuation of the power-law disk. We note that the simulations do not take GG Tau B into account, which is observed at a projected separation of about 1400 au from GG Tau A. Because this outer companion may accrete from and/or truncate the outer parts of the disk (see, e.g., [Beust & Dutrey, 2006](#)), it is therefore possible that the density in the outer parts of the disk is overestimated in the simulation. We ran both models for 28 000 binary orbits ( $\approx 4.9$  Myr).

### 5.6.2 Postprocessing of hydrodynamical simulations

To investigate the appearance of our simulated disks in scattered light, we generated images in polarized intensity using the radiative transfer code RADMC-3D ([Dullemond et al., 2012](#)). We included a radiation field from two stellar components with luminosities of  $0.44 L_{\odot}$  and  $0.20 L_{\odot}$  and temperatures of 3900 K and 3400 K, respectively. In order to generate a 3D view from the simulated disk, we expanded the 2D surface density distribution

resulting from the hydrodynamical simulations along the vertical axis, assuming a Gaussian density distribution with constant aspect ratios of 0.15 and 0.11, consistent with the assumed temperature laws in the simulations (see Sect. 5.6.1). We assumed the dust to be well mixed with the gas. This is a valid assumption because at  $1.67 \mu\text{m}$ , the scattered light is dominated by micron-sized dust grains, which are well coupled to the gas. We thus assumed the dust density distribution to be identical to that of the gas, scaled by a factor of 0.01, which corresponds to a typically assumed dust-to-gas ratio of 1 to 100 in protoplanetary disks.

We assumed the dust number density  $n$  as a function of grain size  $a$  to follow a power law of the form  $n(a) \propto a^{-3.5}$ . The grains were considered to be distributed between sizes of  $0.005 \mu\text{m}$  and  $0.5 \mu\text{m}$ , as assumed in the modeling efforts by Brauer et al. (2019). We assumed that 5% of the total dust mass is contained within this population of small grains, corresponding to a fraction of  $5 \times 10^{-4}$  of the total disk gas mass. Our dust mixture was composed of 70% astronomical silicates (Draine, 2003b) and 30% amorphous carbon grains (Zubko et al., 1996). We computed the Stokes Q and U frames at  $1.67 \mu\text{m}$ , taking the observed inclination and position angle of the disk into account. The simulations were run using  $10^8$  photon packages in order to obtain images with high signal-to-noise ratios. Finally, we convolved our images with a Gaussian kernel with an FWHM of 43 mas.

### 5.6.3 Modeling results and comparison to observations

Both models ran for 28 000 binary orbits ( $\approx 4.9$  Myr), during which the system reached a converging configuration of a stable sized, eccentric, precessing cavity around the binary and a stable circumbinary disk after about 10 000 binary orbits ( $\approx 1.7$  Myr). In the simulations, mass is constantly accreted onto the stars through accretion streams. Therefore the disk loses a fraction of about  $5.2 \cdot 10^{-6}$  of its mass per binary orbit (or  $3.0 \cdot 10^{-8}$  per year). As a result, the initial disk mass of  $0.14 M_{\odot}$  has decreased at the end of the simulation to 86% of its initial value ( $0.12 M_{\odot}$ ). This is in excellent agreement with the disk mass constraints from observations ( $\sim 0.12 M_{\odot}$ , Guilloteau et al., 1999). We did not take the accretion onto the stars into account as it is not resolved in the domain.

The final gas density distributions for both simulations are displayed in Fig. 5.8 (left and center left columns). They show evidence of large cleared inner regions. The gap in the gas is found to have a semimajor axis (defined as the location where the gas density has decreased to 10% of its peak value) of  $4.77 a_{\text{bin}}$  (167 au) and an eccentricity of 0.34 in the case of the midplane temperature ( $h = 0.11$ ), and a semimajor axis of  $3.85 a_{\text{bin}}$  (135 au) and an eccentricity of 0.25 in the case of the (higher) surface temperature ( $h = 0.15$ ).

The surface density shows an azimuthal asymmetry, with the density peaking in direction of the disk apocenter. The reason is that the gas velocity is slowest at these locations,

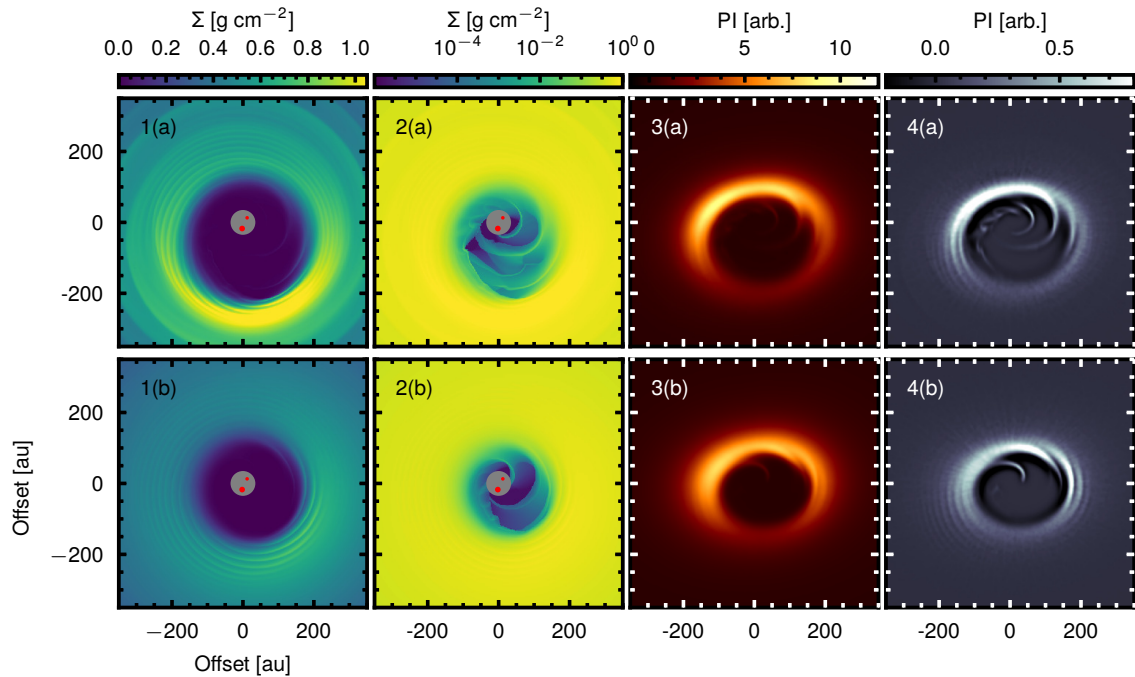


**Figure 5.8:** Surface density output of our simulations in linear (left column; 1 (a) and (b)) and logarithmic (center left column; 2 (a) and (b)) color stretch. The center right column (3 (a) and (b)) shows the simulated polarized intensity images evaluated at  $1.67 \mu\text{m}$ . This image was calculated after inclining and orienting the disk as in the observations. The right column (4 (a) and (b)) shows the polarized intensity image of the center right column, processed with a high-pass filter. In each column, the panel in the first row (a) corresponds to the model with  $h = 0.11$ , the panel in the second row (b) to  $h = 0.15$ .

leading to an enhancement of material in these regions. Fig. 5.8 (left column) shows that the circumbinary ring is structured by numerous tightly wound fine spirals. Furthermore, the logarithmic color stretch for the surface density (Fig. 5.8, center left column) reveals the structure of material flow through the cavity. Spiral streams occur in the simulation, periodically driven by the circumbinary rotation, accelerating the close-by infalling material. Our simulations show regularly stripped-off material streams from the outer disk, similar to the observations, while the exact morphology and orientation of the filaments is not reproduced. These differences may be related to the fact that we do not know the exact initial conditions of the system, with some parameters such as its mass related to some uncertainty. Another possible caveat in the simulations is the fact that we did not simulate the direct circumstellar material, but the simulation domain was cut inside of about 35 au. The presence of material in that region (such as the ‘northern arc’) may affect the flow dynamics and dust morphology within the cavity. Furthermore, it may affect the morphology of the material flow that Ab itself is a binary.

The postprocessed polarized intensity images are shown in the center right column of

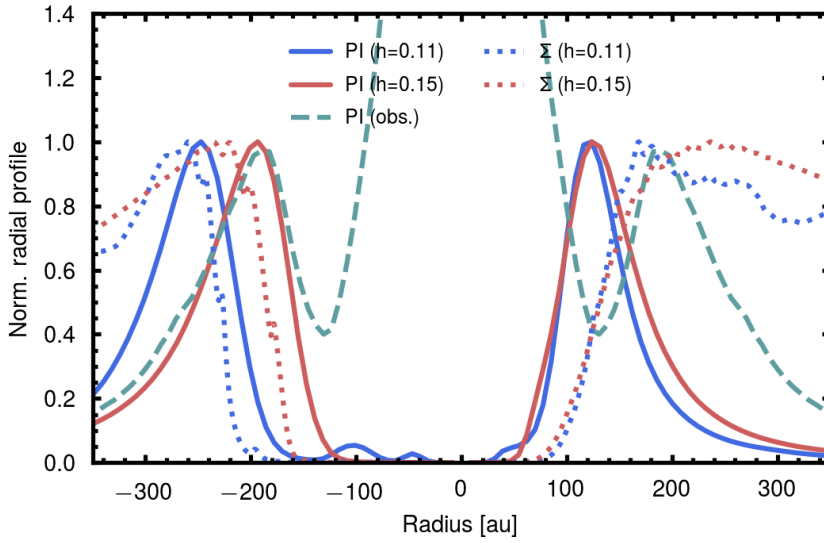


**Figure 5.9:** Radial profiles along the disk major axes (within a cone of  $\pm 30^\circ$ ) of the two models drawn from the gas surface densities (dotted) and the deprojected, simulated polarized intensity images (solid lines). As a comparison, the radial profile of the observed, deprojected disk averaged over all azimuths is plotted (dashed).

Fig. 5.8. The intensity also shows clear azimuthal variations here. Because the disk is optically thick in the near-infrared regime, the azimuthal dependence of the large-scale surface brightness is not sensitive to the surface density, but to the dust phase function and polarization degree. As expected, the near side is significantly brighter than the far side. The simulated polarized intensity images also show substructures within the circumbinary ring. While the contrast of the spirals in the circumbinary ring appears faint, they become very well visible when the images are treated with a high-pass filter, similarly to the observations (Fig. 5.8, right column). We note, however, that the simulated view of the disk in scattered light may be biased by our simplified treatment of the vertical structure of the disk.

Figure 5.9 shows the radial profiles of the simulated gas surface densities (dotted blue and red lines) along the disk major axes. We find a disk semimajor axis (defined as the distance where the profile peaks) of about 215-230 au. Assuming that the large dust particles traced by millimeter observations are being trapped at the location of maximum gas density, these findings are well comparable with the observations: using the optically thin continuum emission between 1.3 mm to 7.3 mm, Andrews et al. (2014) observed the continuum to peak at about 250 au. Figure 5.9 also shows the radial profiles of the simulated deprojected polarized intensity images along the disk major axes (solid blue and red lines). In each of the cases, the polarized intensity profile peaks slightly ahead of the gas density. This can be explained by the fact that the peak of the scattered light profile traces the location of the inner wall of the ring, where illumination is strongest, and not directly

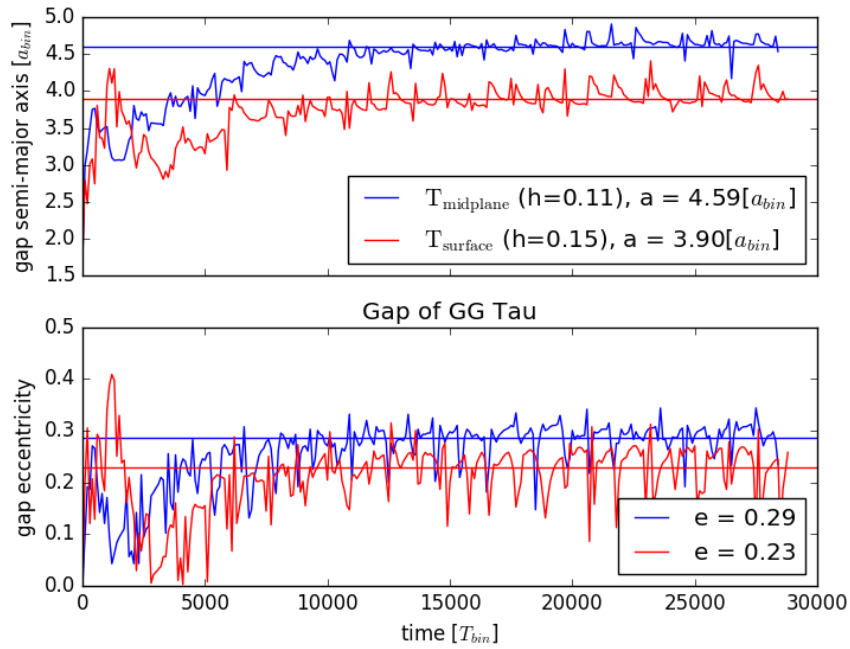


**Figure 5.10:** Size and eccentricity evolution of the cavity around GG Tau A created by the PLUTO simulations for the midplane temperature and surface temperature of the disk.  $a_{bin}$  is 35 au and the initial disk mass is 0.1 binary masses.

the dust density distribution. The semimajor axes of the disk in the polarized intensity images are measured to be 180 au and 160 au, respectively. This is slightly shorter than the location of the peak of the mean (i.e., averaged over all azimuths) deprojected radial profile of the observed *PI* image ( $\sim 190$  au). One reason might be that the slope of the inner edge of the gas disk may in reality be somewhat sharper than in the simulations, which might be connected to the exact value of the binary eccentricity (e.g., [Miranda et al., 2017](#)), or to other disk properties such as the assumed temperature profile, density, distribution, and viscosity. Furthermore, the rim location inferred from the scattered light observations may be overestimated because of possible shadowing from one (or several) circumstellar disks around the three individual components ([Brauer et al., 2019](#)).

Finally, the simulated gap cleared by the binary becomes eccentric, with mean eccentricity values of  $\sim 0.2-0.3$ . As noted in Sect. 5.5.2, it is difficult to extract reliable information about the disk eccentricity from the scattered-light observations, but the (sub-)millimeter observations indicate that the eccentricity of the disk is probably rather low ([Guilloteau et al., 1999](#); [Andrews et al., 2014](#)). This might indicate a lower disk viscosity than assumed in our simulations, as discussed in Sect. 5.7.3.

## 5.7 Discussion

### 5.7.1 Accretion streams within the circumbinary gap

We interpret the filaments detected in our observations that we described in Sect. 5.5.3 as accretion streams. According to theoretical models, circumbinary accretion is thought to proceed onto the stars from the outer circumbinary disk through accretion streams, which are repeatedly torn off at the inner edge of the disk near the apocenter of the binary orbit. This is consistent with what is seen in our simulations. Such a phase-dependent pulsed accretion process has been seen in numerous theoretical studies (e.g., Günther & Kley, 2002; Dunhill et al., 2015; Duffell et al., 2019). Time-variable spectroscopic signatures of accretion activity (e.g., through hydrogen recombination lines) correlated with the binary orbital phase have been observed in some tight (spectroscopic) binary systems (e.g., Mathieu et al., 1997; Kóspál et al., 2018). While the detection of pulsed accretion is usually restricted to very tight systems (because of the restricted time base), the detection of periodic streamers in GG Tau A, if confirmed, would be the first indication of such processes in a wider system.

The hypothesis that the filaments in GG Tau A indeed trace accretion streams fits the overall picture well. With large grains being trapped in the outer circumbinary disk, the detected streamers refill the immediate environment of Ab predominantly with gas and small grains, which is compatible with the strong silicate feature observed at the location of GG Tau Ab (Skemer et al., 2011). The formation of large, massive circumstellar disk(s) around Ab1/2, however, may be inhibited by its binary nature despite continuous replenishment of material, which could explain the nondetection of millimeter flux at the location of Ab (Dutrey et al., 2014).

### 5.7.2 Spiral structures as imprints of binary-disk interaction

Our SPHERE observations show several spiral structures in the southern disk region. Our simulations show that this is an expected outcome of binary-disk interactions and is also consistent with other modeling efforts, which do show that the generation of spiral density waves is a common result of binary-disk interaction, in particular, for cases where the binary orbit has nonzero eccentricity (e.g., Miranda et al., 2017; Price et al., 2018). Observations of circumbinary disks have brought observational evidence of such spiral structures in these systems (e.g., Avenhaus et al., 2017; Monnier et al., 2019). In addition, large accretion streams, such as the tentative connection from the southern disk to the primary, Aa, are also expected from simulations (e.g., Mösta et al., 2019). In this respect, the detected spiral features agree well with our expectations from simulations of circumbinary disks,

where the binary orbit has moderate eccentricity. We note that in addition to this, the external binary-disk interactions with GG Tau B (projected separation of  $\sim 1500$  au) might also be able to trigger spiral waves in the GG Tau A disk (e.g., [Dong et al., 2016](#)). This scenario may be addressed by future work.

However, theoretical models have shown that in addition to binary-disk interactions, several different processes can also drive the generation of spirals in disks, such as a low-mass companion on an orbit inside or outside of the disk (e.g., [Dong et al., 2015b](#)), gravitational instability (e.g., [Dong et al., 2015a](#); [Dipierro et al., 2015](#); [Nelson & Marzari, 2016](#); [Meru et al., 2017](#)), or a combination of both (e.g., [Pohl et al., 2015](#)), as well as temperature fluctuations as a result of shadowing by a warped or misaligned inner disk (e.g., [Montesinos et al., 2016](#)). In order to discern between the companion and gravitational instability scenario, observations at comparably high resolution of the dust continuum, probing the midplane of the disk, are required (e.g., [Rosotti et al., 2020](#)). However, we regard the last scenario as rather unlikely because in this case, the spiral arms would be expected to diverge from a location close to where the scattered-light shadows are located. In contrast, several spiral arms seem to rather originate from a point located on the outer ring at a  $PA$  of  $\sim 120^\circ$ . Interestingly, at this  $PA$  (but slightly outward of the near-infrared peak emission, at radial distances of  $\sim 215$ - $270$  au), an asymmetric structure within the CO distribution has been found, showing evidence of a significantly increased temperature ([Dutrey et al., 2014](#); [Tang et al., 2016](#)). This so-called ‘hot spot’ was interpreted as an area with locally enhanced density and temperature, heated by a possible embedded planet at the formation stage ([Phuong et al., 2020b](#)). While we still consider binary-disk interaction as the most obvious driving force for the spirals observed in the scattered light, a possible connection or interference with this hypothetical forming body needs to be investigated with complementary observations.

### 5.7.3 Gap size as a result of binary-disk interactions

Our simulations show that a binary with a semimajor axis of 35 au is able to create a gap in a coplanar disk with a size that is comparable to our observations. Our inferred gap sizes ( $4.8 a_{\text{bin}}$  and  $3.9 a_{\text{bin}}$  for the two temperature regimes) agree with previous studies of other systems, in which cavity sizes ranging from three to six binary separations were found (e.g., [Thun & Kley, 2018](#)).

We note that our gap estimates are significantly larger than those derived by previous studies of the GG Tau A circumbinary ring. As an example, considering the best-fit astrometric solution of the binary under the assumption that the orbit is coplanar with the outer disk ( $a_{\text{bin}} \sim 36$  au), [Beust & Dutrey \(2005\)](#) predicted a gap size of  $2$ - $3.3 a_{\text{bin}}$ , which they noted to be obviously incompatible with the observations. This apparent discrep-

ancy between observed and simulated gap sizes was confirmed by the hydrodynamical simulations of [Cazzoletti et al. \(2017\)](#), who tested the binary-disk coplanar case considering different disk temperature profiles and a range of values for the viscosity. The authors found the simulated gas distribution to peak at radial distances smaller than  $\sim 160$  au, which contrasts with the observed millimeter continuum peak at about 250 au. As a possible solution of this discrepancy, [Beust & Dutrey \(2005\)](#) proposed to drop the assumption that the binary orbit was coplanar with the disk. In this case, the most plausible orbit has a semimajor axis of  $\sim 65$  au, an eccentricity of 0.44, and a disk-orbit misalignment of about  $25^\circ$  ([Köhler, 2011](#)). This latter scenario, a binary on a wide, disk-misaligned orbit was tested with hydrodynamical simulations by [Aly et al. \(2018\)](#). The authors found that they were indeed able to reproduce the observed gap size, assuming a binary separation of  $\sim 60$  au and a binary-disk misalignment of  $\sim 30^\circ$ .

The differences between these earlier estimates and our own gap values are probably mainly due to a difference in timescales. While our simulations were run for 28 000 orbits, previous studies such as those of [Nelson & Marzari \(2016\)](#), [Cazzoletti et al. \(2017\)](#) and [Aly et al. \(2018\)](#) stopped their simulations after about 1000-2000 orbits or fewer, and they therefore studied earlier stages of the disk evolution to define the gap size and eccentricity. Because the disk evolution starts from an azimuthally symmetric density distribution, our simulations show that the disk crosses meta-stable symmetric states between 1100 and 1700 orbits. This is illustrated in Fig. A.8, which shows the evolution of the gap semimajor axis and gap eccentricity over the first 20 000 orbits. However, this meta-stable state is an artifact of the setup and does not correspond to the convergent behavior of a circumbinary disk because the binary will excite the disk to eccentric motion. The disk will eventually evolve to a larger, more eccentric, stable gap, as the full evolution in Fig. 5.10 shows. Although this evolution is slow, it converges well within the lifetime of the disk. Therefore the simulations of [Cazzoletti et al. \(2017\)](#) and our simulations agree well with each other during the earlier stages, but our longer simulation time shows that the gap will widen with progressing evolution. We accordingly conclude that the observed gap size can be explained by the long-term action (10 000 orbits) of a binary with a separation of 35 au that is coplanar with the disk.

We note that our choice for the viscous  $\alpha$ -parameter of  $10^{-3}$  does not affect our conclusion. As the disk starts at more than 10 au with rather low density, a low level of turbulence driven by the magnetorotational instability seems to be a reasonable assumption, and we consider our value a realistic choice. However, the relatively high mass of the disk may lead to an even lower viscosity. We therefore compared our results with a simulation using an even lower  $\alpha$  parameter of  $10^{-4}$ . Our test run shows that lowering  $\alpha$  affects the gap size only slightly, reducing it by less than 10%. The fact that in this case, a lower  $\alpha$  viscosity slightly shrinks the gap size, is related to the relatively high binary eccentricity

of GG Tau A ( $\epsilon \sim 0.3$ ). For eccentricities  $\geq 0.15$ , the eccentricity of the disk is directly affected by the binary eccentricity. Because the transfer of angular momentum is weaker, lowering  $\alpha$  decreases the apocenter distance of the disk, while the pericenter distance remains constant, thus lowering the gap eccentricity and resulting in a slightly smaller net gap size (Penzlin et al. in prep.). Similarly, Cazzoletti et al. (2017) observed no strong dependence of the location of the gas density peak on the assumed value of  $\alpha$ . However, a lower  $\alpha$  value would result in a significantly less eccentric gap. Therefore a low viscosity may even be consistent with the fact that the disk does not appear very eccentric in the continuum observations.

In summary, our simulations suggest that a tight,  $\sim 35$  au binary orbit that is coplanar with the outer disk is sufficient to create a gap in the disk of the observed size. However, we note that some misalignment within the system cannot be excluded, in particular, in view of the shadows on the outer disk, which may imply the presence of misaligned circumstellar material. Final conclusion on the orbital parameters of the binary and the respective disk-orbit orientation requires further astrometric monitoring as the current orbital coverage is still sketchy (Maire et al. in prep.).

#### 5.7.4 Implications for planet formation

The case of GG Tau A shows that in certain configurations, multiple systems are able to sustain massive, gas-rich disks over several million years. The accumulation of dust particles outside the cavity induced by the gravitational perturbation of the binary may enhance the dust-to-gas ratio in the outer ring. Such an accumulation of dust is a necessary condition for planet formation to occur. Using numerical simulations, Holman & Wiegert (1999) developed an empirical relation between the binary orbit (semi-major axis and eccentricity) and the smallest stable orbit of a hypothetical circumbinary planet. Using their relation, considering a binary separation of 36 au and an eccentricity of 0.28, planet orbits outside of  $\sim 3.4 a_{\text{bin}}$  (122 au) are predicted to be stable. While the planet formation process may be quite susceptible to the perturbation by a binary (e.g., Thebault & Haghighipour, 2015), this calculation implies that *if* a planet formed within the circumbinary ring (i.e. outside 120 au), its orbit would be dynamically stable. High-contrast imaging observations (e.g., Asensio-Torres et al., 2018) are needed to constrain the possible planet population in the circumbinary environment.

## 5.8 Summary and conclusions

We have observed the circumbinary environment of GG Tau A in polarized light with SPHERE/IRDIS in H-band at unprecedented angular resolution. We analyzed the disk

morphology and compared our observations to hydrodynamical simulations. The following Section summarizes our findings.

- The inner region appears to be highly structured. Our image suggests that the previously reported northern arc is composed of a double-arc structure. We furthermore detect various filament-like structures in the immediate circumbinary environment. Small dust grains scattering off light from the binary appear to be distributed in a large area around the binary.
- We clearly detect previously suggested filament-like structures connecting the outer ring with the northern arc. The azimuthal spacing of the streamers may be consistent with a periodic perturbation by the binary, tearing off material from the inner edge of the outer disk once during each orbit.
- We confirm detection of three shadowed regions cast on the outer disk, as well as a tentative fourth shadow, suggesting the presence of an inclined circumstellar disk around Aa or Ab. We do not confirm a linear movement of the western shadow lane since 2011 that was suggested by previous observations.
- We ran hydrodynamical simulations including the binary on an eccentric and disk coplanar orbit with a semimajor axis of 35 au. The simulations ran for 28 000 orbits, which covers the estimated age of the system. The final disk configuration shows evidence of spiral structures in the outer ring as well as within the cavity, similar to the observations.
- The resulting disk size is in qualitative agreement with the observations, which implies that a coplanar binary orbit  $\sim 35$  au in size may be sufficient to explain the size of the ring. Astrometric follow-up observations are required to provide a final conclusion on the size and orientation of the binary orbit.

With these observations, we revealed the substructures imprinted by binary-disk interactions at unprecedented detail. The case of GG Tau A shows that in certain configurations, multiple systems are able to sustain massive, gas-rich disks for several million years, providing potentially favourable conditions for planet formation.

# 6

## Summary and Outlook

---

Protoplanetary disks are the birthplaces of planets. Within a few million years, the typical lifetime of a disk, giant planets are thought to form out of these disks through the assembly of a solid core, and subsequent accretion of a gaseous envelope. While many theoretical models addressing the planet formation process exist, various questions are still unanswered, mainly hampered by non-existent constraints from observations. The detection of more than 4300 planets (as of August 2020) show that planet formation is statistically a frequent process, which is observed to result in a diverse variety of exoplanetary properties and system architectures. Understanding the planet formation process and the initial physical conditions under which it takes place, is crucial in order to explain the observed exoplanet population. The observation and characterization of protoplanets, still in formation, and of their natal environment is therefore key to that goal. The advent of high-contrast and high-angular resolution instruments such as SPHERE and ALMA have opened the possibility to quest for these young, forming planetary systems. Still, the detection of young planets embedded in their disks has shown to be challenging; only a handful of candidates have been reported prior to this Thesis, and most of them are still under debate.

This Thesis focused on the observations of young stars still hosting their protoplanetary disks, and of circumbinary disks as the precursors of planetary systems which have been found around multiple stars. The goal of these observations was to characterize the structures of these disks and to search for direct and indirect signposts of forming planets. The next Section summarizes the results.

### 6.1 Summary

Chapter 2 (published in [Keppler et al., 2018](#)), presented near-infrared multi-epoch and multi-band observations PDS 70, taken with the SPHERE instrument in polarimetric and

angular differential imaging observing mode, complemented with data from the NACO and HiCIAO instruments.

A detailed analysis of the scattered light images confirmed the presence of a large,  $\sim 54$  au sized gap within the disk, and revealed for the first time scattered light from the inner disk component. Comparison to radiative transfer simulations allowed to constrain the orientation and radial extension of the inner disk. Further, the scattered light images of the outer disk showed evidence of an azimuthal brightness variation, depending on the filter band. The observed behaviour was suggestive to being caused by Rayleigh scattering from small, sub-micrometer sized dust grains populating the surface layers of the flared disk.

Most importantly, the observations revealed a point source located at a projected separation of  $\sim 195$  mas from the star and at a position angle of  $\sim 155^\circ$ . The detection was confirmed at five different epochs, including different instruments and filter bands. Analysis of the point source astrometry allowed to exclude the nature of a background object and revealed first hints of orbital motion. Extraction of its photometry and comparison to evolutionary models suggested the object to be most compatible with a young planetary-mass companion with a dusty or cloudy atmosphere. The source is referred to as PDS 70 b hereafter.

Follow-up observations by [Wagner et al. \(2018\)](#) and [Haffert et al. \(2019\)](#), after the publication of the work presented in Chapter 2, revealed the detection of  $H\alpha$  emission at the location of PDS 70 b. Because  $H\alpha$  is a commonly used tracer for gas accretion, these observations provided the final proof that the planet is still at the stage of formation. PDS 70 b is therefore the first unambiguously detected giant planet still at stage of formation, and thus an excellent laboratory to test various theoretical models in context with the planet formation process.

In order to study the natal environment of PDS 70 b, and to explore the potential of the disk as a testbed for planet-disk interactions, Chapter 3 (published in [Keppler et al., 2019](#)) presented ALMA observations of PDS 70 at high angular resolution ( $\sim 0.07''$ ) in dust continuum and at the  $^{12}\text{CO}$  J=3-2 transition.

A detailed analysis of the dust continuum revealed a highly structured ring peaking at a radius of  $\sim 74$  au with a marginally resolved second ring component along the inner edge, an azimuthal over-brightness in North-West direction, as well as a spur projecting from the continuum ring into the gap. Finally, an upper limit on circumplanetary dust around PDS 70 b of  $\sim 0.01 M_\oplus$  was derived.

These observations revealed that also the  $^{12}\text{CO}$  emission appeared highly structured. The integrated intensity showed evidence of an inner disk component, as well as a bridge-like feature close to the location of the spur found in the continuum. The most prominent

feature in integrated intensity, however, was a deep gap in the inner region, co-located with PDS 70 b, which suggests that it is being carved by the planet. Comparison to hydrodynamical simulations showed a best match of the integrated intensity radial profile with a  $5 M_{\text{Jup}}$  body.

Perturbations in the surface density profile, such as gaps, come along with a modification of the radial pressure gradient, which affects the rotation velocity of the gas (e.g., [Teague et al., 2018a](#)). Analysis of the kinematic structure of the disk using the  $^{12}\text{CO}$  emission revealed significant deviation from Keplerian rotation inside  $0.8''$ . The width of the kinematic perturbation was found to be comparable to the location of the dust ring, consistent with the picture of large dust grains, traced by the continuum, being trapped at the location of maximum pressure, which is, where gas recovers Keplerian rotation. The comparison of the derived rotation curve to hydrodynamical simulations implied that the depth of the kinematic signature could be best matched with the perturbations caused by a  $\sim 10 M_{\text{Jup}}$  planet at the location of PDS 70 b, but also lead to the conclusion that one planet may not be sufficient to explain its radial extent. This finding suggested that an additional mechanism, such as an additional low-mass companion may be needed to account for the observed disk morphology.

Shortly after the publication of the work presented in Chapter 3, [Haffert et al. \(2019\)](#) reported, along with PDS 70 b, a second compact  $\text{H}\alpha$  source in the system, implying the presence of a another planetary-mass object, PDS 70 c. Furthermore, a subsequent revision of the continuum data presented in Chapter 3 by [Isella et al. \(2019\)](#) identified the above reported spur as a separate point-source co-located with PDS 70 c, suggesting the presence of circumplanetary dust. The authors also recovered another compact continuum source close, but slightly offset from the location of PDS 70 b; its nature still remains to be confirmed.

In order to search for imprints of planet-disk interactions in the PDS 70 disk, Chapter 4 was dedicated to ALMA observations of PDS 70 at high angular ( $\sim 0.09''$ ) as well as spectral ( $\sim 0.11 \text{ km/s}$ ) resolution, including the  $^{12}\text{CO}$  and  $^{13}\text{CO}$  molecular lines, and the dust continuum.

Both lines were shown to trace a deep gap inside the continuum ring, co-located with the planets. At a radius of 100 au,  $^{12}\text{CO}$  emission was found to arise from a layer located at about 1.8 times as high as that of  $^{13}\text{CO}$ , as a result of optical depth effects, similar to observations of other disks ([Pinte et al., 2018a](#); [Teague et al., 2020](#)).

The molecular emission in one of the  $^{12}\text{CO}$  channel maps showed a tentative distortion in its velocity field close to the location of PDS 70 c, reminiscent of the ‘kink’ feature reported by [Pinte et al. \(2018b\)](#). Analysis of the spectral line shapes within the cavity were shown to be highly affected by strong CO depletion and broadening caused by the Keple-

rian shear, challenging the search for local signatures related to PDS 70 b and c. Detailed analysis of potential features will be addressed by future work.

The images of the dust continuum provided an independent confirmation of the spur reported in Chapter 3. The detection of a compact continuum source close to PDS 70 b, but slightly offset from its near-infrared location reported in Chapter 2 as well as from the continuum source detected by Isella et al. (2019) remains puzzling. Observations at higher angular resolution will be helpful to conclude on the nature of the signal.

Finally, Chapter 5 (published in Keppler et al., 2020) was dedicated to a detailed analysis of GG Tau A, one of the largest and most massive circumbinary protoplanetary disks. The analysis was based on new high-resolution observations in polarized light taken with the SPHERE instrument, revealing the disk at unprecedented detail. The disk was found to be highly structured, showing evidence of a large,  $\sim 180$  au wide gap, as well as several filaments, shadows, and spirals. In particular, the observations revealed streamer-like structures connecting the outer ring with the immediate circumbinary environment, suggesting that those are released through the periodic perturbation by the binary, tearing off material from the inner edge of the outer disk once during each orbit.

A large fraction of the detected features was shown to be in qualitative agreement with hydrodynamical simulations modeling the binary-disk interactions. The simulations were adapted to the specific case of GG Tau A, assuming the binary orbit to be coplanar with the outer disk, covering the estimated age of the system. In particular, the observed gap size was well reproduced, suggesting that no binary-disk misalignment was needed to explain the large extent of the gap. This result contrasted with previous simulations reported in the literature, leading to the conclusion that simulations of binary-disk interactions needed to cover a sufficient simulation time to converge to a stable configuration.

The case of GG Tau A illustrated that binary-disk interactions play a major role in reshaping the circumbinary material. The trapping of dust in the circumbinary ring could possibly provide a reservoir with favourable conditions for planet formation to take place.

## 6.2 Outlook

PDS 70 is the first, and so far only robustly detected planetary system caught at the stage of formation. This benchmark system now opens the door to observationally explore a so far uncharted population of young, forming planets and to probe various aspects related to the formation and early evolution of planetary systems. In the frame of this Thesis, first steps toward the exploration of the properties of PDS 70 b and its imprints on the circumstellar disk have been undertaken. Still, many more remain to be taken in the future.

The atmospheric characterisation of PDS 70 b and c will benefit from spectrally resolved observations taken at complementary wavelengths to the IFS spectra presented in Müller et al. (2018) and Mesa et al. (2019). A proposal to observe PDS 70 b in the low-resolution ( $R \sim 50$ ) long-slit spectroscopy mode of IRDIS (PI: M. Keppler) was granted four hours accorded with highest priority. The observations are being queued for execution at the telescope. These data will bridge the so far unsampled spectral range between the H- and K-band, and therefore connect the steep blueward slope revealed by IFS with the relatively flat K- and L-band photometry.

At slightly longer wavelengths, around the K-band, GRAVITY has recently proven to be a powerful instrument for the spectroscopic study of exoplanets (Gravity Collaboration et al., 2019, 2020). The spectral properties of planetary atmospheres in this wavelength range are of particular interest as it covers prominent absorption features by carbon monoxide (CO) and methane (CH<sub>4</sub>). Assuming thermochemical equilibrium, for atmospheres of low-mass objects at higher temperatures, the main carbon-bearing molecule is CO, while at lower temperatures, the main carbon reservoir transitions from CO to CH<sub>4</sub> (e.g., Lodders & Fegley, 2002; Madhusudhan et al., 2016), with important consequences for the spectral appearance. This transition is thought to take place around an equilibrium temperature of  $\sim 1200$  K, but the detailed processes involved at this transition are still a topic of active research (e.g., Vos et al., 2019). With effective temperatures of  $\sim 1000$ - $1200$  K, the PDS 70 planets would thus provide an excellent opportunity to study the atmospheric properties close to this transition boundary.

Further, the C/O ratio in planetary atmospheres has been proposed to be a tracer of formation history. The C/O ratio of gas in protoplanetary disk is predicted to increase with distance, from a stellar composition in the innermost regions to super-stellar values (i.e., to values above the stellar C/O ratio) further out, due to freeze-out effects past the H<sub>2</sub>O, CO<sub>2</sub> and CO ice lines (Öberg et al., 2011). As explained in Sect. 1.2, in the core accretion scenario, a giant planet is formed through the accretion of a gaseous envelope on a solid core. Therefore, the composition of the planetary atmosphere should reflect that of the disk at the location where it formed. Because in the case of PDS 70 we likely know where the planets obtained their bulk envelope, constraining the C/O ratios from a spectroscopic study of the atmospheres of PDS 70 b and c, together with estimating the ice line locations (e.g., Qi et al., 2015) could provide a powerful test to probe this hypothesis (Gravity Collaboration et al., 2020).

Another planetary property imprinted by the formation process is spin. The rotation rate of giant planets is thought to be related to the accretion process during formation, spinning up to values close to the breakup velocity. This velocity corresponds to the maximum rate at which a planet (or star) can rotate in a stable way, because otherwise the equatorial centrifugal force would exceed the gravitational force. The Solar System gas gi-

ants rotate with spin rates well below their break-up velocities, a trend which has also recently been observed for young extrasolar low-mass companions (Bryan et al., 2018; Xuan et al., 2020). These studies suggested that the rotation rates may be regulated during the formation process itself, possibly through magnetic coupling between the planet and the CPD (Takata & Stevenson, 1996; Batygin, 2018). Determining the spins of PDS 70 b and c, e.g., by measuring the broadening of atmospheric absorption lines using high-resolution spectroscopy as done for  $\beta$  Pic b by Snellen et al. (2014), could therefore provide a worthy test for the initial rotation rates of giant planets during the formation process. Such a project could be the goal of next-generation imaging instruments coupled to adaptive optics with high-dispersion spectroscopy such as ELT/METIS (resolving power  $R \sim 10^5$  at L and M-band, Brandl et al., 2012) or ELT/HARMONI ( $R \sim 2 \times 10^4$  at K-band, Thatte et al., 2016).

Further potential to scrutinize the properties of PDS 70 b and c also relies on the long wavelength end. Measurements of the spectral index (i.e., the slope of the spectral energy distribution of disks at long wavelengths) are commonly used to infer on the maximum grain size distribution residing in the disk. The existence of large grains in disks is determined by processes such as radial drift and grain growth, processes which can give insights into the disk properties. For example, Pinilla et al. (2017b) argued that the low spectral indices measured in several brown dwarf disks, indicative for large millimeter-sized dust grains, may hint toward the presence of several pressure bumps that keep these large grains from drifting inward on short timescales. PDS 70 now provides the first opportunity to expand such studies to the planetary-mass regime. ALMA is capable to reach an angular resolution of  $\sim 0.04''$  in Band 6 ( $\sim 1.3$  mm) in the most extended configuration<sup>25</sup>. The combination of observations with ALMA in Band 6 and 7 at comparably high angular resolution could thus allow to establish the spectral index for the CPD around PDS 70 c. Another important step for the characterization of the CPD properties would be to build a bridge between the near-infrared and sub-millimeter part of the combined, planet and CPD SED, using next-generation high-contrast imagers in the mid-infrared such as JWST/MIRI. Further, mid-infrared spectroscopy of the CPD (such as with ELT/METIS in N-band) could be a worthy project for the characterization of circumplanetary dust.

Finally, searching for other planets embedded in the disk, e.g., that could be responsible for the double-ring structure of the outer continuum ring, will be another goal for future observations. Constraints on additional planets will give us insights about the structuration of a multi-planetary system at the stage of formation.

---

<sup>25</sup>see Table A-1 of ALMA proposer's guide:  
<https://almascience.eso.org/proposing/proposers-guide>

It is clear that for a full exploration of planet properties at the stage of formation, the discovery and characterisation of other young, forming planets is essential. As described in Sect. 1.5, the presence of circumstellar dust can significantly challenge the detection of forming planets with Direct Imaging. The discovery of PDS 70 b has highly benefited from being located within a very wide and deep gap, excluding a possible confusion with distorted and asymmetric disk features. A target selection focused toward transition disks with large gaps is therefore a favourable strategy. We proposed for such a project with SPHERE in P104 (PI: M. Keppler); 22.5 hours were granted to search for planetary companions in 8 PDS70-like transition disks with large gaps. The observations have been carried out, and the data are ready to be analyzed. Naturally, the above proposed ideas for further characterization of PDS 70 can be applied to any new protoplanet that will be found in the future.

Most quests for planets have so far focused on single star systems. While binary-disk interactions can heavily truncate or destroy the circumstellar and circumbinary disks, the case of GG Tau A presented in Chapter 5 shows that in certain configurations, binary systems can retain massive circumbinary disks for several million years, with possibly favourable conditions for planet formation. Proposed for SPHERE observations in P105 (PI: Keppler), 12 hours were granted at highest priority to search for forming planets around 6 tight binaries and characterize the circumbinary disks. Being currently in the queue to be observed, this pilot study represents a first step towards the observational exploration of potential planet-forming disks around binary stars.



# A

## Supplementary material

---

### A.1 Supplementary material for Chapter 2

This section presents contrast maps (Fig. A.1), as well as photometry and astrometry of PDS 70 b (Tab. A.1) as retrieved with the sPCA, ANDROMEDA, PCA SpeCal, and TLOCI reductions.

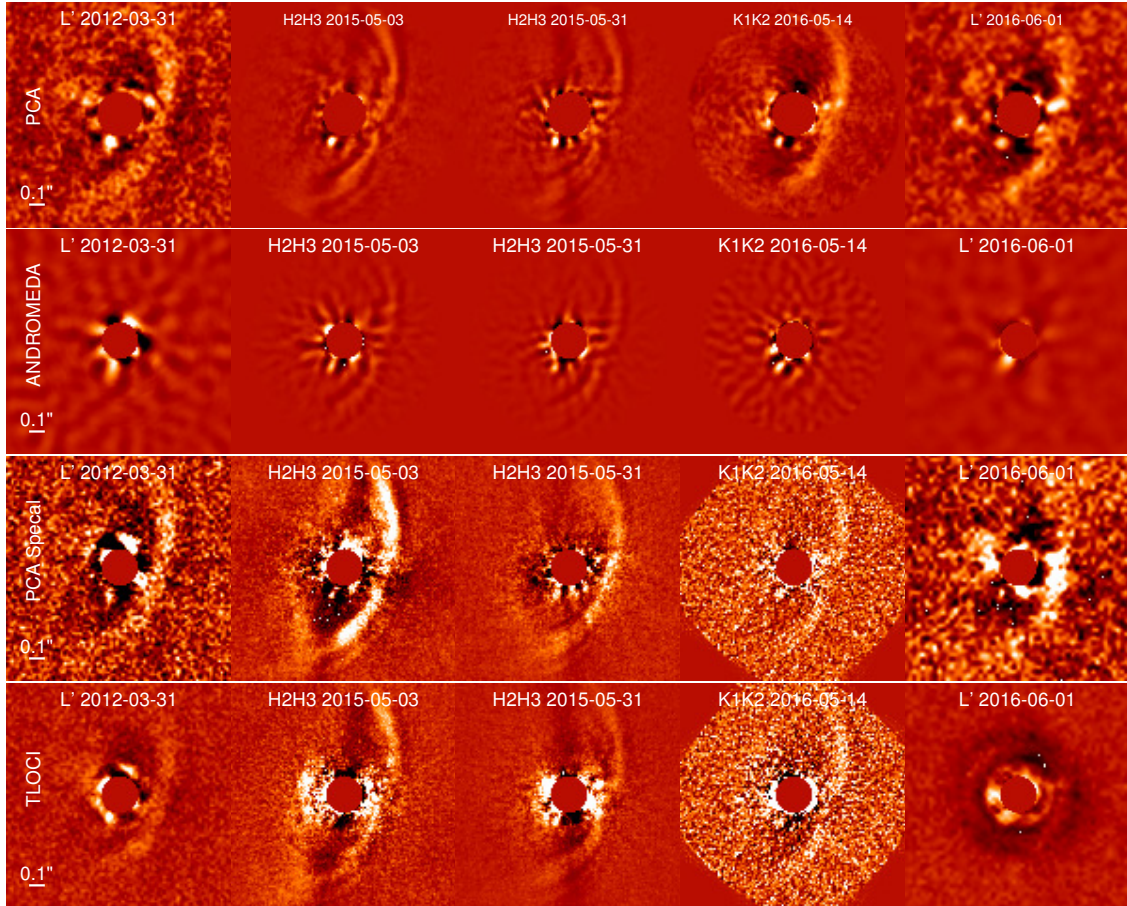


**Figure A.1:** Contrast maps of the point source detection as retrieved with the sPCA reduction (first row), ANDROMEDA (second row), PCA SpeCal (third row), and TLOCI (fourth row). From left to right: NICI L'-band (2012-03-31), IRDIS H2H3-band (2015-05-03), IRDIS H2H3-band (2015-05-31), IRDIS K1K2-band (2016-05-14), NaCo L'-band (2016-06-01). The sPCA images were smoothed with a Gaussian kernel of size  $0.5 \times \text{FWHM}$ . North is up and east is to the left. The brightness levels were adapted individually for visibility purposes.

**Table A.1:** Comparison of photometry and astrometry of the companion candidate, as derived from the ANDROMEDA, PCA-SpeCal and TLOCI reductions.

Date	Instrument	Filter	Sep[mas]	PA[deg]	$\Delta$ mag	S/N
Results from sPCA						
2012-03-31	NICI	L'	191.9±21.4	162.2±3.7	6.59±0.42	5.6
2015-05-03	IRDIS	H2	192.3±4.2	154.5±1.2	9.35±0.18	6.3
2015-05-03	IRDIS	H3	197.2±4.0	154.9±1.1	9.24±0.17	8.1
2015-05-31	IRDIS	H2	199.5±6.9	153.4±1.8	9.12±0.24	11.4
2015-05-31	IRDIS	H3	194.5±6.3	153.5±1.8	9.13±0.16	6.8
2016-05-14	IRDIS	K1	193.2±8.3	152.2±2.3	7.81±0.31	5.5
2016-05-14	IRDIS	K2	199.2±7.1	151.5±1.6	7.67±0.24	3.6
2016-06-01	NaCo	L'	189.6±26.3	150.6±7.1	6.84±0.62	2.7
ANDROMEDA						
2012-03-31	NICI	L'	211.1±3.5	162.7±0.3	6.85±0.32	4.3
2015-05-03	IRDIS	H2	191.7±3.3	154.3±0.2	9.69±0.25	5.5
2015-05-03	IRDIS	H3	189.7±2.6	154.4±0.1	9.47±0.25	5.0
2015-05-31	IRDIS	H2	200.6±2.9	153.1±0.2	9.49±0.20	6.1
2015-05-31	IRDIS	H3	194.3±2.9	153.2±0.2	9.35±0.17	6.9
2016-05-14	IRDIS	K1	190.8±1.6	152.1±0.2	7.81±0.21	6.2
2016-05-14	IRDIS	K2	195.4±2.3	152.0±0.2	7.51±0.25	4.7
2016-06-01	NaCo	L'	148.2±8.4	152.0±0.5	5.60±0.32	3.6
PCA (SpeCal)						
2012-03-31	NICI	L'	190.3±12.3	160.6±3.7	7.0 ±0.1	2.2
2015-05-03	IRDIS	H2	206.5±4.8	156.8±1.3	9.7 ±0.2	5.0
2015-05-03	IRDIS	H3	208.0±4.9	156.7±1.2	9.6 ±0.2	5.1
2015-05-31	IRDIS	H2	196.4±4.4	155.7±1.1	9.1 ±0.1	14.2
2015-05-31	IRDIS	H3	197.0±6.0	155.5±1.6	8.9 ±0.1	14.7
2016-05-14	IRDIS	K1	198.5±3.7	152.5±1.1	8.1 ±0.1	17.1
2016-05-14	IRDIS	K2	200.0±3.0	152.6±0.9	7.5 ±0.1	17.5
2016-06-01	NaCo	L'	181.8±18.8	148.4±5.9	6.9 ±0.5	2.4
TLOCI						
2012-03-31	NICI	L'	187.7±35.9	160.5±10.9	7.1±0.6	1.9
2015-05-03	IRDIS	H2	198.1±26.2	154.1± 7.5	9.4±0.8	1.4
2015-05-03	IRDIS	H3	195.3±20.6	154.9± 6.0	9.2±0.6	1.9
2015-05-31	IRDIS	H2	196.5±14.1	154.9± 4.1	9.6±0.3	3.4
2015-05-31	IRDIS	H3	199.9±15.4	154.8± 4.4	9.5±0.4	2.7
2016-05-14	IRDIS	K1	192.0±24.2	151.0± 7.2	8.1±0.5	2.1
2016-05-14	IRDIS	K2	201.0±27.2	152.2± 7.7	7.9±0.6	1.8
2016-06-01	NaCo	L'	181.7±54.4	147.8±17.2	7.1±1.3	0.9

**Notes.** The current implementation of the astrometric error estimation for our TLOCI reduction is unreliable for the L' datasets. We therefore used a conservative uncertainty of 2 pixels for the angular separation and the position angle for these datasets.

## A.2 Supplementary material for Chapter 4

This Section presents a zoom-in view of the  $^{12}\text{CO}$  channels maps where the disk emission is close to the location of PDS 70 b (Sect. A.2.1), peak brightness, zeroth moment, and channel maps for the combined ('SB1+LB2+LB3') data (Sect. A.2.2, as well as the comparison of spectra from symmetric disk regions for the inner part of the disk (Sect. A.2.3).

### A.2.1 Zoom-in of channels maps for 'LB2' data

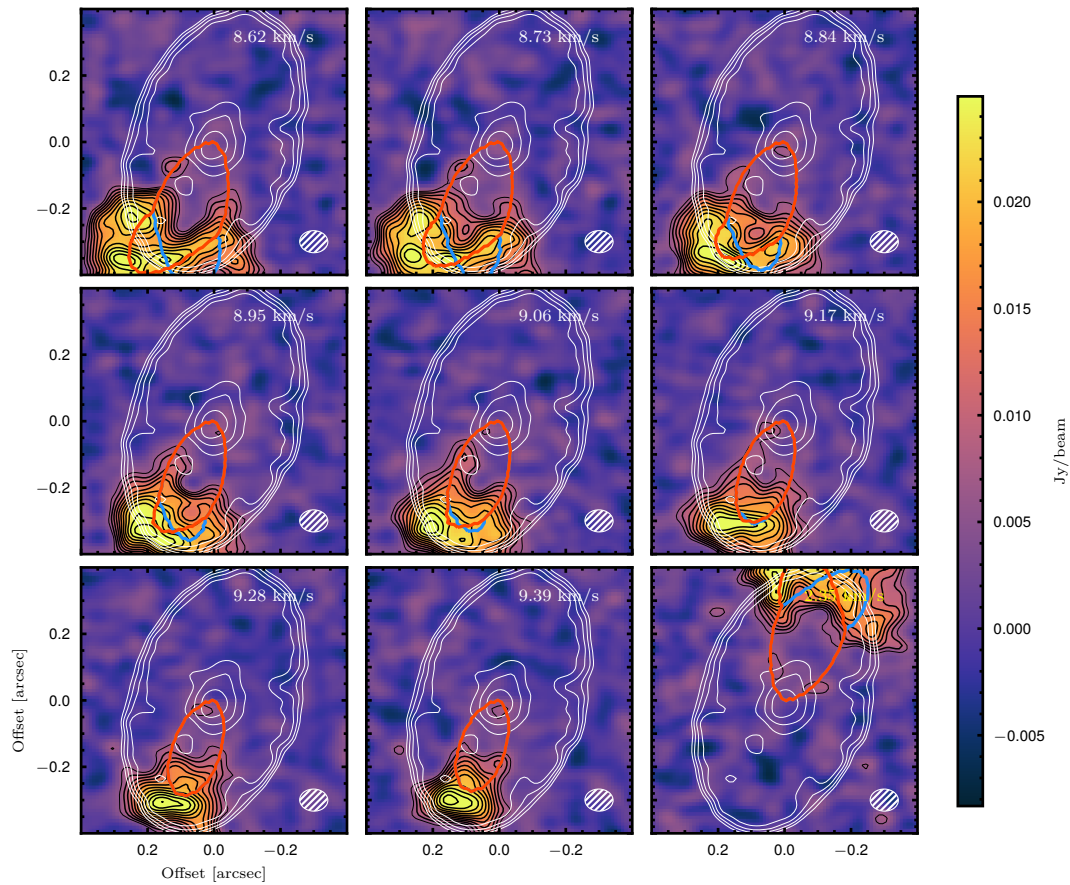


**Figure A.2:** Zoom-in of channel maps of  $^{12}\text{CO}$  ( $r = 0.5$ ) where the disk emission is close to the location of PDS 70 b. Black lines mark contours of 3, 4, 5, ... x channel rms. White contours are drawn from the continuum at 3, 6, 9, 12 x rms.

## A.2.2 Peak brightness, zeroth moment, and channel maps for combined data

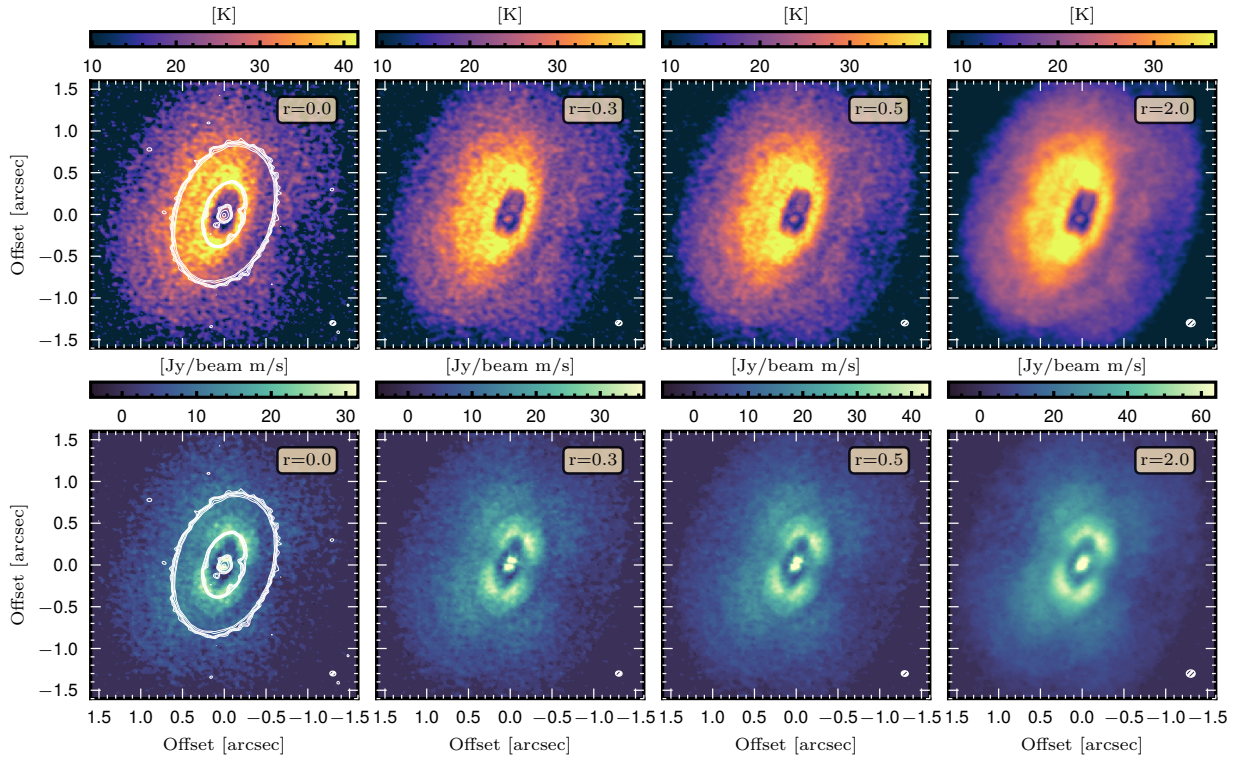


**Figure A.3:** Same as Fig. 4.7, but for the combined (SB1+LB2+LB3) dataset.

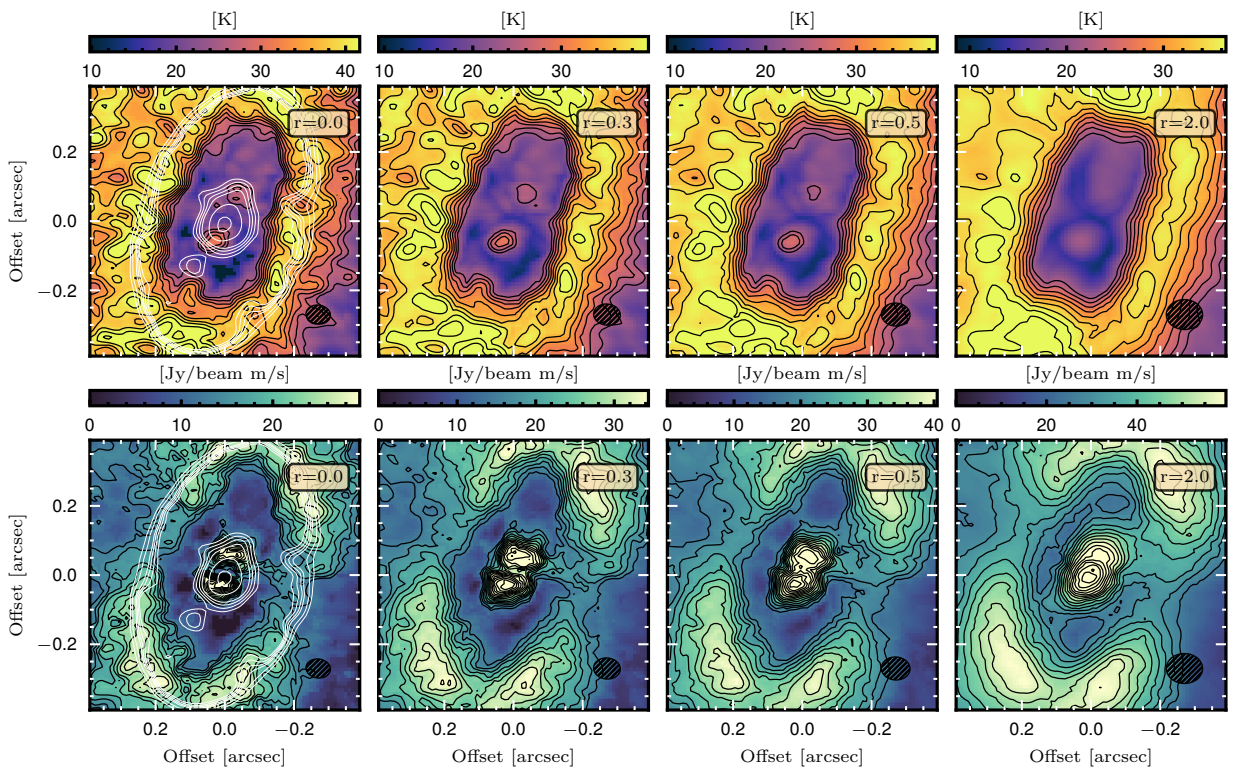


**Figure A.4:** Combined  $^{12}\text{CO}$  zoom-in view of peak brightness temperature and zeroth moment

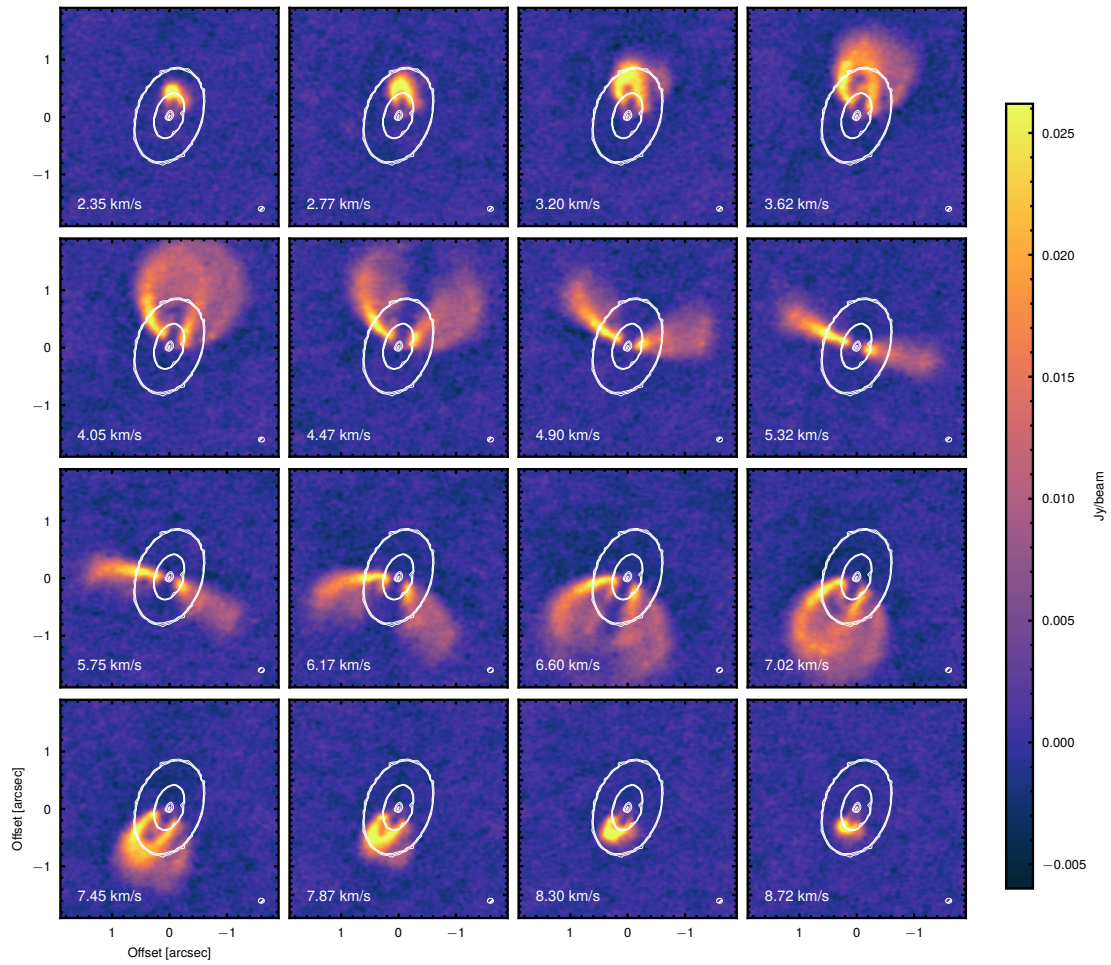


**Figure A.5:** Channel maps of  $^{12}\text{CO}$ . We used here the cube imaged at  $r=2.0$ , and show only every third channel. The beam is shown on the lower right of each panel. The lower right panel shows a channel at 2.35 km/s, which has roughly the same offset from systemic velocity than the channel extracted at 8.73 km/s.

### A.2.3 Opposed spectra for inner disk region

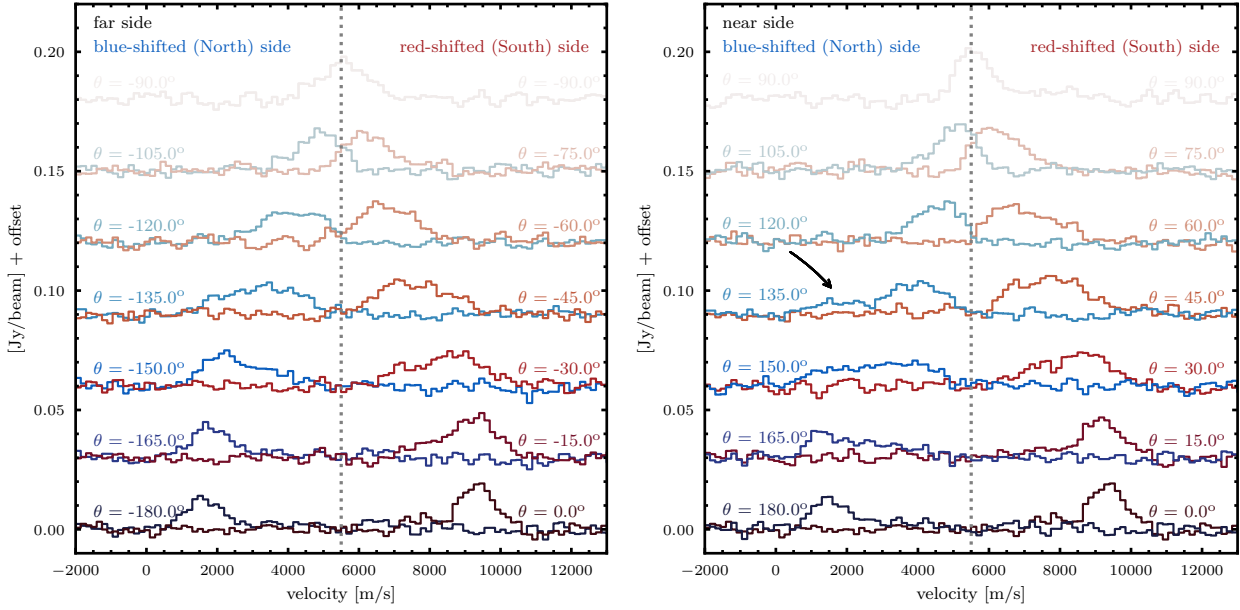


**Figure A.6:** Symmetrically extracted spectra between  $0.24''$  and  $0.29''$  for different azimuthal bins of width  $0.05''$ . The spectral resolution was downgraded to  $150 \text{ m/s}$ . A possible blue-shifted feature along the near side is marked by the black arrow.

## A.3 Supplementary material for Chapter 5

This Section explores the polarized intensity pattern of a disk when illuminated by two sources (Sect. A.3.1) and discusses the early disk evolution phases of the simulations presented in this Chapter compared to those by Cazzoletti et al. (2017) (Sect. A.3.2).

### A.3.1 Polarized intensity pattern in the presence of two illumination sources

In order to investigate how the presence of two illumination sources affects the morphology of *PI*, we generated a toy model of the GG Tau A disk. We considered two illumination sources at a respective separation of  $38 \text{ au}$ , and with luminosities ( $L_a=0.44 L_\odot$ ,  $L_b=0.23 L_\odot$ ) such as is found for GG Tau Aa and Ab. We assumed that the luminosity ratios of Aa and Ab are representative for their H-band flux ratios, which is consistent with the observations by Di Folco et al. (2014), who reported an H-band flux ratio of  $\sim 2.1$ . For each point in the disk plane, we computed the received stellar illumination  $F_{tot} = F_a + F_b \propto L_a/d_a^2 + L_b/d_b^2$ , where  $d_a$  and  $d_b$  is the distance to Aa and Ab, respectively.

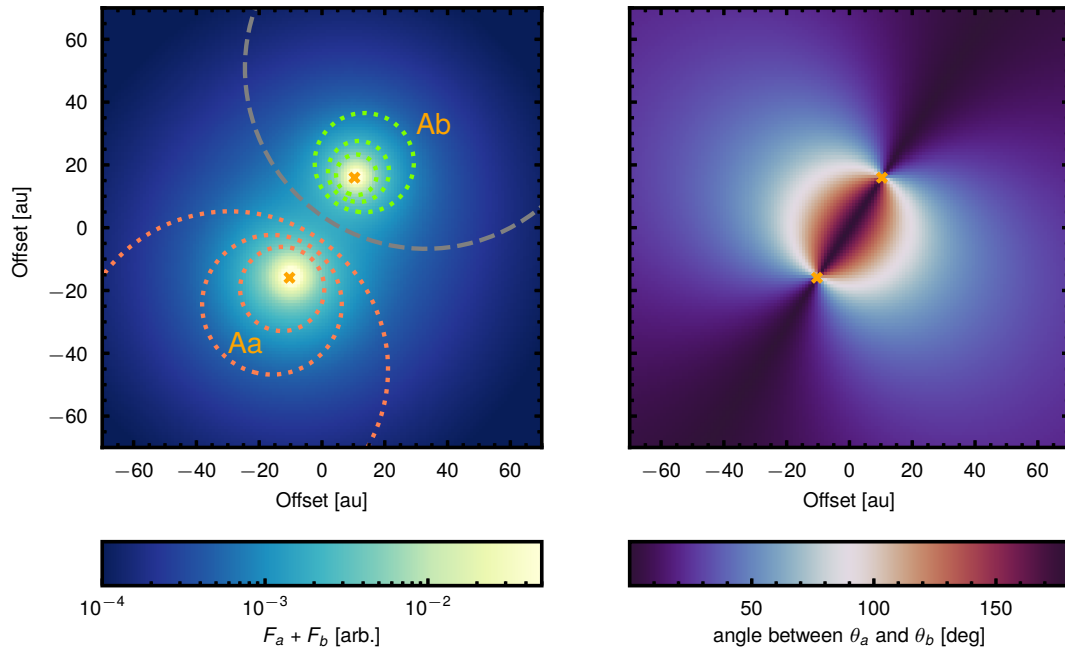
This received stellar flux is proportional to the intensity of scattered linearly polarized light, assuming a homogeneous surface density and degree of linear polarization throughout the disk. We also assumed a flat-disk geometry for simplicity.

Fig. A.7 (left) shows the distribution of  $F_{tot}$  for a face-on view of the disk. The dotted circles trace contours at which the contribution from the respective other star to  $F_{tot}$  is 5, 10 and 20%, that is, where  $F_a/F_{tot} = (0.05, 0.1, 0.2)$  (green) and  $F_b/F_{tot} = (0.05, 0.1, 0.2)$  (red). The 5% contours are found as close as  $\sim 9$  au ( $\sim 5$  au) to the location of Aa (Ab). Because the PSF FWHM of our SPHERE observations is about 40 mas (i.e., 6 au at 150 pc, thus corresponding to a PSF radius of  $\sim 3$  au) the contribution of scattered polarized light from the respective other star to the unresolved polarized signal measured at the locations of GG Tau Aa and Ab is thus expected to be negligible.

We furthermore investigated whether any of our detected disk substructures might be related to the respective orientation of the polarization vectors in the presence of two illumination sources, rather than to a variation in disk surface density or scale height. If, for example, the polarization vectors at a certain point in the disk due to light scattered from Aa and Ab enclosed an angle of about  $90^\circ$ , the polarized signal could cancel out, leading to a locally depressed  $PI$ . Because the orientation of the linear polarization vectors is expected to be orthogonal to the radius vectors connecting a certain point in the disk with the respective illumination sources, it is possible to map the angles enclosed by the two polarization vectors throughout the disk. This map is shown in Fig. A.7 (right). A region with a respective polarization angle difference of  $90^\circ$  indeed lies close to the stars. Farther away, however, from  $\sim a_{bin}$  on, polarization vectors tend to be aligned with respect to each other. This is consistent with our observations, where the polarization vectors are clearly azimuthally orientated throughout the outer disk. While we cannot exclude that some spatial  $PI$  variation close to the binary is caused by the superposition of the polarization vectors, we conclude that this effect cannot be responsible for the generation of any of the disk substructures we detected that are illustrated in Fig. 5.3.

### A.3.2 Early meta-stable simulation phase

Cazzoletti et al. (2017) found a smaller inner cavity after a simulation of about 1000 binary orbits. We can confirm this finding for the early simulation, as shown in Fig. A.8. However, we find that this feature is created by the symmetric initial condition of the gas distribution. After clearing the inner disk from gas in unstable orbits during the first few hundred orbits, the disk reaches a meta-stable configuration. This symmetric configuration will be disturbed by the higher modes of the binary potential and transform into the stable eccentric cavity that is reached after about 10000 binary orbits. The same behavior occurs for less viscous systems a few hundred orbits earlier.



**Figure A.7:** Toy model of the inner disk region of GG Tau A including two illuminating sources. The left panel shows the radiation field generated by the two stars. For each star, the dotted contours mark the regions where the contribution from the other star to the total flux is 5, 10, and 20% (in red, the contribution from GG Tau Ab in the immediate surrounding of GG Tau Aa; in green, vice versa). The grey dashed line traces the contour where  $F_a$  equals  $F_b$ . The right panel maps the angles between the linear polarization vectors resulting from scattering of light from Aa and Ab. In regions in which this angle becomes close to  $90^\circ$ ,  $PI$  could theoretically cancel out.

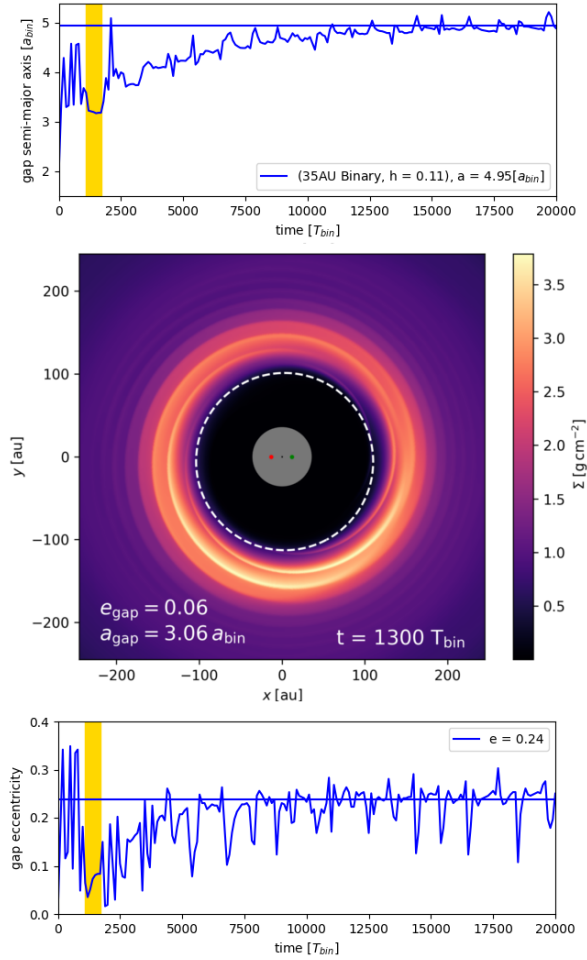


**Figure A.8:** Gap size (top) and eccentricity (bottom) evolution of the cavity around GG Tau A created by our PLUTO simulation for the midplane temperature of the disk. The disk encounters a meta stable symmetric state (highlighted in yellow) with reduced gap size and eccentricity for about 600 orbits. The 2D surface density plot after 1300 orbits is shown in the middle.



# B

### B.1 Acronyms

<b>2D</b>	Two-dimensional.
<b>3D</b>	Three-dimensional.
<b>ADI</b>	Angular differential imaging.
<b>CMD</b>	Color-magnitude diagram.
<b>CPD</b>	Circumplanetary disk.
<b>DI</b>	Direct imaging.
<b>DIT</b>	Digital integration time.
<b>DPI</b>	Dual-beam polarimetric imaging.
<b>ELT</b>	Extremely Large Telescope.
<b>ESO</b>	European Southern Observatory.
<b>FWHM</b>	Full-width at half maximum.
<b>GTO</b>	Guaranteed Time observations.
<b>HWP</b>	Half-wave plate.
<b>IDL</b>	Interactive Data Language.
<b>IFS</b>	Integral Field Spectrograph.
<b>IP</b>	Instrumental polarization.
<b>IRDIS</b>	InfraRed Dual-band Imager and Spectrograph.
<b>ISM</b>	Interstellar medium.
<b>ISPY</b>	Imaging Survey for Planets around Young stars.
<b>JWST</b>	James Webb Space Telescope.
<b>MagAO</b>	Magellan Adaptive Optics.
<b>mas</b>	Milli-arcsecond.
<b>MUSE</b>	Multi Unit Spectroscopic Explorer.
<b>NICI</b>	Near-Infrared Coronagraphic Imager.

<b>NIR</b>	Near-infrared.
<b>NW</b>	North-west.
<b>PA</b>	Position angle.
<b>PCA</b>	Principal component analysis.
<b>PDI</b>	Polarimetric differential imaging.
<b>PMS</b>	Pre-main sequence.
<b>PSF</b>	Point-spread function.
<b>rms</b>	Root mean square.
<b>RT</b>	Radiative transfer.
<b>S/N</b>	Signal-to-noise ratio.
<b>SE</b>	South-east.
<b>SHINE</b>	SpHere INfrared survey for Exoplanets.
<b>SPHERE</b>	Spectro-Polarimetric High-contrast Exoplanet REsearch.
<b>TLOCI</b>	Template Locally Optimized Combination of Images.
<b>VLT</b>	Very Large Telescope.
<b>ZIMPOL</b>	Zurich IMaging POLarimeter.

## B.2 List of Figures

1.1	Evolution of planetary luminosity, radius and effective temperature as a function of time . . . . .	12
1.2	Dust opacities for different grain size distributions . . . . .	14
1.3	Phase functions and polarization degrees . . . . .	15
1.4	Stellar, disk and planetary model SEDs . . . . .	18
1.5	Exemplary $Q, U, Q_\phi, U_\phi$ and $PI$ images . . . . .	22
1.6	Exemplary moment maps . . . . .	27
1.7	Polarimetric images of three transition disks . . . . .	31
2.1	The location of PDS 70 on a HR diagram . . . . .	35
2.2	$Q_\phi$ and $U_\phi$ images of PDS 70 . . . . .	43
2.3	Radial profiles of the VBB and J-band $Q_\phi$ images . . . . .	44
2.4	Azimuthal profiles of the $Q_\phi$ images . . . . .	44
2.5	IRDIS coronagraphic and non-coronagraphic PDI images . . . . .	45
2.6	Disk view of SHINE IRDIS observations obtained with ADI, TLOCI, gradient . . . . .	46
2.7	Disk view of PDS 70 with sPCA, PCA-SpeCal and cADI . . . . .	48
2.8	RT models of PDS 70 . . . . .	50
2.9	Linear polarization degrees and phase functions for different grain sizes . . . . .	51
2.10	Convolved ray-traces $Q_\phi$ -images calculated at $0.7 \mu\text{m}$ . . . . .	52
2.11	Images of the point source detection as retrieved with the sPCA reduction . . . . .	54
2.12	ANDROMEDA S/N maps of the ADI epochs . . . . .	55
2.13	Relative astrometry of PDS 70 b . . . . .	56
2.14	CMDs of PDS 70 b . . . . .	57
2.15	cADI simulations for the $Q_\phi$ images of the J-band observations . . . . .	59
2.16	Photometry of PDS 70 b in comparison with evolutionary models . . . . .	60
3.1	Observations of $^{12}\text{CO}$ and continuum of the PDS 70 disk . . . . .	74
3.2	Results on the MCMC fit of the deprojected and binned visibilities of the dust continuum . . . . .	75
3.3	Radial profiles of the deprojected dust continuum image . . . . .	77
3.4	Cycle 5 dust continuum data compared to the SPHERE NIR image . . . . .	78
3.5	Theoretically expected flux densities from a CPD . . . . .	80
3.6	CPD detection limits for different planet masses . . . . .	81
3.7	Iso-velocity contours of the upper and lower sides of the disk . . . . .	82
3.8	Rotation map of the $^{12}\text{CO}$ emission . . . . .	82
3.9	Radial profiles of the $^{12}\text{CO}$ integrated intensity and brightness temperature . . . . .	85

3.10	Measured rotation curve and relative residuals . . . . .	86
3.11	Effect of beam convolution on the radial sampling of the rotation velocity . . . . .	88
3.12	Effect of beam convolution using the observed intensity profile . . . . .	89
3.13	$^{12}\text{CO}$ line profile and channel maps at the location of the point source . . . . .	89
3.14	Comparison of hydrodynamical models using different planet masses . . . . .	91
3.15	Comparison of hydrodynamical models with observations . . . . .	93
3.16	3D volume rendering of the simulated gas density after 1000 orbits . . . . .	94
4.1	Comparison of continuum before and after self-calibration . . . . .	104
4.2	Zoom-out of continuum before and after self-calibration . . . . .	106
4.3	Continuum imaged with different robust parameters . . . . .	107
4.4	Radial profiles of continuum image . . . . .	108
4.5	Combined continuum image imaged with different robust parameters . . . . .	109
4.6	Contour overlay of continuum image . . . . .	111
4.7	$^{12}\text{CO}$ peak brightness temperature and zeroth moment maps . . . . .	113
4.8	High-pass filtered $^{12}\text{CO}$ peak brightness maps . . . . .	114
4.9	$^{13}\text{CO}$ peak brightness temperature and zeroth moment maps . . . . .	114
4.10	Zoom-in of $^{12}\text{CO}$ peak brightness temperature and zeroth moment maps . . . . .	115
4.11	Zoom-out of $^{12}\text{CO}$ peak brightness temperature and zeroth moment maps . . . . .	116
4.12	$^{12}\text{CO}$ and $^{13}\text{CO}$ radial profiles . . . . .	117
4.13	Channel maps of $^{12}\text{CO}$ . . . . .	118
4.14	$^{13}\text{CO}$ channel maps . . . . .	119
4.15	Zoom-in view of $^{12}\text{CO}$ channel maps . . . . .	120
4.16	Zoom-in view of $^{13}\text{CO}$ channel maps . . . . .	121
4.17	Zoom-in view of $^{12}\text{CO}$ channel maps with different robust parameters . . . . .	122
4.18	$^{12}\text{CO}$ spectra along the far-side disk minor axis . . . . .	123
4.19	Symmetrically extracted spectra between $0.6''$ and $0.65''$ . . . . .	124
4.20	Emission surfaces for $^{12}\text{CO}$ and $^{13}\text{CO}$ . . . . .	125
4.21	Overlay of continuum with SPHERE and MUSE images . . . . .	128
4.22	3D surface of $^{12}\text{CO}$ . . . . .	130
5.1	SPHERE polarized intensity image of GG Tau A . . . . .	139
5.2	Schematic overview of the features in the outer circumbinary ring . . . . .	140
5.3	Zoom on the inner region of the GG Tau A disk . . . . .	141
5.4	SPHERE image with angles of linear polarization, and ALMA overlay . . . . .	143
5.5	Radial disk profiles . . . . .	144
5.6	High-pass filtered $PI$ image of GG Tau A . . . . .	146
5.7	Azimuthal profiles of the western shadow . . . . .	147
5.8	Surface density and images from hydrodynamical simulations . . . . .	153

5.9	Comparison of radial profiles of images from simulations and observations	154
5.10	Size and eccentricity evolution of the cavity created by PLUTO simulations	155
A.1	Contrast maps of the point source	170
A.2	Zoom-in of $^{12}\text{CO}$ channel maps close to PDS70 b	172
A.3	Combined $^{12}\text{CO}$ peak brightness temperature and zeroth moment maps	173
A.4	Combined $^{12}\text{CO}$ zoom-in view of peak brightness temperature and zeroth moment	174
A.5	Combined $^{12}\text{CO}$ channel maps	175
A.6	Symmetrically extracted spectra between 0.24'' and 0.29''	176
A.7	Toy model of the inner disk region including two illuminating sources	178
A.8	Gap size and eccentricity evolution in PLUTO simulations	179

## B.3 List of Tables

2.1	Photometry and stellar parameters of the PDS 70 . . . . .	36
2.2	Observing log of PDS 70 data . . . . .	38
2.3	Parameters for our RT model. . . . .	49
2.4	Astrometric calibrations used for the ADI datasets. . . . .	64
2.5	Properties of the point-like source . . . . .	65
4.1	Imaging results for new and combined datasets . . . . .	105
4.2	Peak intensity of compact source close to PDS 70b . . . . .	110
5.1	Properties of GG Tau A . . . . .	138
A.1	CC Comparison of photometry and astrometry from different reductions . .	171

# C

## List of refereed publications

---

### Publications as first author

- **Kepler, M.**; Benisty, M.; Müller, A.; Henning, Th.; van Boekel, R.; Cantalloube, F.; Ginski, C.; van Holstein, R. G.; Maire, A. -L.; Pohl, A.; Samland, M.; Avenhaus, H.; Baudino, J. -L.; Boccaletti, A.; de Boer, J.; Bonnefoy, M.; Chauvin, G.; Desidera, S.; Langlois, M.; Lazzoni, C.; Marleau, G. -D.; Mordasini, C.; Pawellek, N.; Stolker, T.; Vigan, A.; Zurlo, A.; Birnstiel, T.; Brandner, W.; Feldt, M.; Flock, M.; Girard, J.; Gratton, R.; Hagelberg, J.; Isella, A.; Janson, M.; Juhasz, A.; Kemmer, J.; Kral, Q.; Lagrange, A. -M.; Launhardt, R.; Matter, A.; Ménard, F.; Milli, J.; Mollière, P.; Olofsson, J.; Pérez, L.; Pinilla, P.; Pinte, C.; Quanz, S. P.; Schmidt, T.; Udry, S.; Wahhaj, Z.; Williams, J. P.; Buenzli, E.; Cudel, M.; Dominik, C.; Galicher, R.; Kasper, M.; Lannier, J.; Mesa, D.; Mouillet, D.; Peretti, S.; Perrot, C.; Salter, G.; Sissa, E.; Wildi, F.; Abe, L.; Antichi, J.; Augereau, J. -C.; Baruffolo, A.; Baudoz, P.; Bazzon, A.; Beuzit, J. -L.; Blanchard, P.; Brems, S. S.; Buey, T.; De Caprio, V.; Carillet, M.; Carle, M.; Cascone, E.; Cheetham, A.; Claudi, R.; Costille, A.; Delboulbé, A.; Dohlen, K.; Fantinel, D.; Feautrier, P.; Fusco, T.; Giro, E.; Gluck, L.; Gry, C.; Hubin, N.; Hugot, E.; Jaquet, M.; Le Mignant, D.; Llored, M.; Madec, F.; Magnard, Y.; Martinez, P.; Maurel, D.; Meyer, M.; Möller-Nilsson, O.; Moulin, T.; Mugnier, L.; Origné, A.; Pavlov, A.; Perret, D.; Petit, C.; Pragt, J.; Puget, P.; Rabou, P.; Ramos, J.; Rigal, F.; Rochat, S.; Roelfsema, R.; Rousset, G.; Roux, A.; Salasnich, B.; Sauvage, J. -F.; Sevin, A.; Soenke, C.; Stadler, E.; Suarez, M.; Turatto, M.; Weber, L. (2018), *Discovery of a planetary-mass companion within the gap of the transition disk around PDS 70*, *A&A*, 617, 44 (Chapter 2)
- **Kepler, M.**; Teague, R.; Bae, J.; Benisty, M.; Henning, T.; van Boekel, R.; Chapillon, E.; Pinilla, P.; Williams, J. P.; Bertrang, G. H. -M.; Facchini, S.; Flock, M.; Ginski, Ch.; Juhasz, A.; Klahr, H.; Liu, Y.; Müller, A.; Pérez, L. M.; Pohl, A.; Rosotti, G.; Samland, M.; Semenov, D. (2019), *Highly structured disk around the planet host PDS 70 revealed by high-angular resolution observations with ALMA*, *A&A*, 625, 118 (Chapter 3)

- **Kepler, M.**; Penzlin, A.; Benisty, M.; van Boekel, R.; Henning, T.; van Holstein, R. G.; Kley, W.; Garufi, A.; Ginski, C.; Brandner, W.; Bertrang, G. H. -M.; Boccaletti, A.; de Boer, J.; Bonavita, M.; Brown Sevilla, S.; Chauvin, G.; Dominik, C.; Janson, M.; Langlois, M.; Lodato, G.; Maire, A. -L.; Ménard, F.; Pantin, E.; Pinte, C.; Stolker, T.; Szulágyi, J.; Thebault, P.; Villenave, M.; Zurlo, A.; Rabou, P.; Feautrier, P.; Feldt, M.; Madec, F.; Wildi, F. (2020), *Gap, shadows, spirals, and streamers: SPHERE observations of binary-disk interactions in GG Tauri A*, A&A, 639, 62 (Chapter 5)

## Publications as contributing author cited in this Thesis

- Müller, A.; **Kepler, M.**; Henning, Th.; Samland, M.; Chauvin, G.; Beust, H.; Maire, A. -L.; Molaverdikhani, K.; van Boekel, R.; Benisty, M.; Boccaletti, A.; Bonnefoy, M.; Cantalloube, F.; Charnay, B.; Baudino, J.-L.; Gennaro, M.; Long, Z. C.; Cheetham, A.; Desidera, S.; Feldt, M.; Fusco, T.; Girard, J.; Gratton, R.; Hagelberg, J.; Janson, M.; Lagrange, A.-M.; Langlois, M.; Lazzoni, C.; Ligi, R.; Ménard, F.; Mesa, D.; Meyer, M.; Mollière, P.; Mordasini, C.; Moulin, T.; Pavlov, A.; Pawellek, N.; Quanz, S. P.; Ramos, J.; Rouan, D.; Sissa, E.; Stadler, E.; Vigan, A.; Wahhaj, Z.; Weber, L.; Zurlo, A. (2018), *Orbital and atmospheric characterization of the planet within the gap of the PDS 70 transition disk*, A&A, 617, L2
- Mesa, D.; **Kepler, M.**; Cantalloube, F.; Rodet, L.; Charnay, B.; Gratton, R.; Langlois, M.; Boccaletti, A.; Bonnefoy, M.; Vigan, A.; Flasseur, O.; Bae, J.; Benisty, M.; Chauvin, G.; de Boer, J.; Desidera, S.; Henning, T.; Lagrange, A. -M.; Meyer, M.; Milli, J.; Müller, A.; Pairet, B.; Zurlo, A.; Antonucci, S.; Baudino, J. -L.; Brown Sevilla, S.; Cascone, E.; Cheetham, A.; Claudi, R. U.; Delorme, P.; D’Orazi, V.; Feldt, M.; Hagelberg, J.; Janson, M.; Kral, Q.; Lagadec, E.; Lazzoni, C.; Ligi, R.; Maire, A. -L.; Martinez, P.; Menard, F.; Meunier, N.; Perrot, C.; Petrus, S.; Pinte, C.; Rickman, E. L.; Rochat, S.; Rouan, D.; Samland, M.; Sauvage, J. -F.; Schmidt, T.; Udry, S.; Weber, L.; Wildi, F., (2019), *VLT/SPHERE exploration of the young multiplanetary system PDS70*, A&A, 632, A25
- Isella, Andrea; Benisty, Myriam; Teague, Richard; Bae, Jaehan; **Kepler, Miriam**; Facchini, Stefano; Pérez, Laura (2019), *Detection of Continuum Submillimeter Emission Associated with Candidate Protoplanets*, ApJ, 879, L25
- Wagner, Kevin; Follete, Katherine B.; Close, Laird M.; Apai, Dàniel; Gibbs, Aidan; **Kepler, Miriam**; Müller, André; Henning, Thomas; Kasper, Markus; Wu, Ya-Lin;

Long, Joseph; Males, Jared; Morzinski, Katie; McClure, Melissa (2018), *Magellan Adaptive Optics Imaging of PDS 70: Measuring the Mass Accretion Rate of a Young Giant Planet within a Gapped Disk*, ApJ, 863, L8

- Bae, J.; Zhu, Z.; Baruteau, C.; Benisty, M.; Dullemond, C.P.; Facchini, S.; Isella, A.; **Keppler, M.**; Pérez, L.; Teague, R. (2019), *An Ideal Testbed for Planet-Disk Interaction: Two Giant Protoplanets in Resonance Shaping the PDS 70 Protoplanetary Disk*, ApJ, 884, L41
- Villenave, M.; Benisty, M.; Dent, W. R. F.; Ménard, F.; Garufi, A.; Ginski, C.; Pinilla, P.; Pinte, C.; Williams, J. P.; de Boer, J.; Morino, J. -I.; Fukagawa, M.; Dominik, C.; Flock, M.; Henning, T.; Juhász, A.; **Keppler, M.**; Muro-Arena, G.; Olofsson, J.; Pérez, L. M.; van der Plas, G.; Zurlo, A.; Carle, M.; Feautrier, P.; Pavlov, A.; Pragt, J.; Ramos, J.; Sauvage, J. -F.; Stadler, E.; Weber, L. (2019), *Spatial segregation of dust grains in transition disks. SPHERE observations of 2MASS J16083070-3828268 and RXJ1852.3-3700*, A&A, 624, 7
- Pohl, A.; Benisty, M.; Pinilla, P.; Ginski, C.; de Boer, J.; Avenhaus, H.; Henning, Th.; Zurlo, A.; Boccaletti, A.; Augereau, J. -C.; Birnstiel, T.; Dominik, C.; Facchini, S.; Fedele, D.; Janson, M.; **Keppler, M.**; Kral, Q.; Langlois, M.; Ligi, R.; Maire, A. -L.; Ménard, F.; Meyer, M.; Pinte, C.; Quanz, S. P.; Sauvage, J. -F.; Sezestre, É.; Stolker, T.; Szulágyi, J.; van Boekel, R.; van der Plas, G.; Villenave, M.; Baruffolo, A.; Baudoz, P.; Le Mignant, D.; Maurel, D.; Ramos, J.; Weber, L. (2017), *The Circumstellar Disk HD 169142: Gas, Dust, and Planets Acting in Concert?* ApJ, 850, 52
- Chauvin, G.; Desidera, S.; Lagrange, A. -M.; Vigan, A.; Gratton, R.; Langlois, M.; Bonnefoy, M.; Beuzit, J. -L.; Feldt, M.; Mouillet, D.; Meyer, M.; Cheetham, A.; Biller, B.; Boccaletti, A.; D'Orazi, V.; Galicher, R.; Hagelberg, J.; Maire, A. -L.; Mesa, D.; Olofsson, J.; Samland, M.; Schmidt, T. O. B.; Sissa, E.; Bonavita, M.; Charnay, B.; Cudel, M.; Daemgen, S.; Delorme, P.; Janin-Potiron, P.; Janson, M.; **Keppler, M.**; Le Coroller, H.; Ligi, R.; Marleau, G. D.; Messina, S.; Mollière, P.; Mordasini, C.; Müller, A.; Peretti, S.; Perrot, C.; Rodet, L.; Rouan, D.; Zurlo, A.; Dominik, C.; Henning, T.; Ménard, F.; Schmid, Baruffolo, A.; Baudoz, P.; Baudrand, J.; Blanchard, P.; Bazzon, A.; Buey, T.; Carbillet, M.; Carle, M.; Charton, J.; Cascone, E.; Claudi, R.; Costille, A.; Deboulbe, A.; De Caprio, V.; Dohlen, K.; Fantinel, D.; Feautrier, P.; Fusco, T.; Gigan, P.; Giro, E.; Gisler, D.; Gluck, L.; Hubin, N.; Hugot, E.; Jaquet, M.; Kasper, M.; Madec, F.; Magnard, Y.; Martinez, P.; Maurel, D.; Le Mignant, D.; Möller-Nilsson, O.; Llored, M.; Moulin, T.; Orignère, A.; Pavlov, A.; Perret, D.; Petit, C.; Pragt, J.; Puget, P.; Rabou, P.; Ramos, J.; Rigal, R.; Rochat, S.; Roelfsema, R.; Rousset, G.; Roux, A.; Salasnich, B.; Sauvage, J. -F.; Sevin, A.; Soenke, C.; Stadler, E.; Suarez,

M.; Weber, L.; Wildi, F.; Antonucci, S.; Augereau, J. -C.; Baudino, J. -L.; Brandner, W.; Engler, N.; Girard, J.; Gry, C.; Kral, Q.; Kopytova, T.; Lagadec, E.; Milli, J.; Moutou, C.; Schlieder, J.; SzulÁ;gyi, J.; Thalmann, C.; Wahhaj, Z. (2017), *Discovery of a warm, dusty giant planet around HIP 65426* A&A, 605, L9

- Bonnefoy, M.; Perraut, K.; Lagrange, A. -M.; Delorme, P.; Vigan, A.; Line, M.; Rodet, L.; Ginski, C.; Mourard, D.; Marleau, G. -D.; Samland, M.; Tremblin, P.; Ligi, R.; Cantalloube, F.; Mollière, P.; Charnay, B.; Kuzuhara, M.; Janson, M.; Morley, C.; Homeier, D.; D’Orazi, V.; Klahr, H.; Mordasini, C.; Lavie, B.; Baudino, J. -L.; Beust, H.; Peretti, S.; Musso Bartucci, A.; Mesa, D.; Bézard, B.; Boccaletti, A.; Galicher, R.; Hagelberg, J.; Desidera, S.; Biller, B.; Maire, A. -L.; Allard, F.; Borgniet, S.; Lannier, J.; Meunier, N.; Desort, M.; Alecian, E.; Chauvin, G.; Langlois, M.; Henning, T.; Mugnier, L.; Mouillet, D.; Gratton, R.; Brandt, T.; Mc Elwain, M.; Beuzit, J. -L.; Tamura, M.; Hori, Y.; Brandner, W.; Buenzli, E.; Cheetham, A.; Cudel, M.; Feldt, M.; Kasper, M.; **Keppler, M.**; Kopytova, T.; Meyer, M.; Perrot, C.; Rouan, D.; Salter, G.; Schmidt, T.; Sissa, E.; Zurlo, A.; Wildi, F.; Blanchard, P.; De Caprio, V.; Delboulbé, A.; Maurel, D.; Moulin, T.; Pavlov, A.; Rabou, P.; Ramos, J.; Roelfsema, R.; Rousset, G.; Stadler, E.; Rigal, F.; Weber, L. (2018), *The GJ 504 system revisited. Combining interferometric, radial velocity, and high contrast imaging data* A&A, 618, 63
- Sissa, E.; Gratton, R.; Garufi, A.; Rigliaco, E.; Zurlo, A.; Mesa, D.; Langlois, M.; de Boer, J.; Desidera, S.; Ginski, C.; Lagrange, A. -M.; Maire, A. -L.; Vigan, A.; Dima, M.; Antichi, J.; Baruffolo, A.; Bazzon, A.; Benisty, M.; Beuzit, J. -L.; Biller, B.; Boccaletti, A.; Bonavita, M.; Bonnefoy, M.; Brandner, W.; Bruno, P.; Buenzli, E.; Cascone, E.; Chauvin, G.; Cheetham, A.; Claudi, R. U.; Cudel, M.; De Caprio, V.; Dominik, C.; Fantinel, D.; Farisato, G.; Feldt, M.; Fontanive, C.; Galicher, R.; Giro, E.; Hagelberg, J.; Incorvaia, S.; Janson, M.; Kasper, M.; **Keppler, M.**; Kopytova, T.; Lagadec, E.; Lannier, J.; Lazzoni, C.; LeCoroller, H.; Lessio, L.; Ligi, R.; Marzari, F.; Menard, F.; Meyer, M. R.; Mouillet, D.; Peretti, S.; Perrot, C.; Potiron, P. J.; Rouan, D.; Salasnich, B.; Salter, G.; Samland, M.; Schmidt, T.; Scuderi, S.; Wildi, F. (2018), *High-contrast study of the candidate planets and protoplanetary disk around HD 100546*, A&A, 619, A160

## Publications as contributing author not included in this Thesis

- Lagrange, A. -M.; **Keppler, M.**; Meunier, N.; Lannier, J.; Beust, H.; Milli, J.; Bonnavita, M.; Bonnefoy, M.; Borgniet, S.; Chauvin, G.; Delorme, P.; Galland, F.; Iglesias,

- D.; Kiefer, F.; Messina, S.; Vidal- Madjar, A.; Wilson, P. A. (2018), *Full exploration of the giant planet population around  $\beta$  Pictoris*, *A&A*, 612, 108
- Lagrange, A. -M.; **Kepler, M.**; Beust, H.; Rodet, L.; Meunier, N.; Lillo-Box, J.; Bonnefoy, M.; Galland, F. (2017), *Discovery of a stellar companion to HD 131399A*, *A&A*, 608, 9
  - Grandjean, A.; Lagrange, A. -M.; **Kepler, M.**; Meunier, N.; Mignon, L.; Borgniet, S.; Chauvin, G.; Desidera, S.; Galland, F.; Messina, S.; Sterzik, M.; Pantoja, B.; Rodet, L.; Zicher, N. (2020), *A HARPS RV search for planets around young nearby stars*, *A&A*, 633, 44
  - Lagrange, A. -M.; Meunier, Nadège; Rubini, Pascal; **Kepler, Miriam**; Galland, Franck; Chapellier, Eric; Michel, Eric; Balona, Luis; Beust, Hervé; Guillot, Tristan; Grandjean, Antoine; Borgniet, Simon; Mékarnia, Djamel; Wilson, Paul Anthony; Kiefer, Flavien; Bonnefoy, Mickael; Lillo- Box, Jorge; Pantoja, Blake; Jones, Matias; Iglesias, Daniela Paz; Rodet, Laetitia; Diaz, Matias; Zapata, Abner; Abe, Lyu; Schmider, Francois- Xavier (2019), *Evidence for an additional planet in the  $\beta$  Pictoris system*, *Nature Astronomy*, 3, 1135
  - Wagner, Kevin; Stone, Jordan; Dong, Ruobing; Ertel, Steve; Apai, Daniel; Doelman, David; Bohn, Alexander; Najita, Joan; Brittain, Sean; Kenworthy, Matthew; **Kepler, Miriam**; Webster, Ryan; Mailhot, Emily; Snik, Frans (2020), *First Images of the Protoplanetary Disk around PDS 201*, *AJ*, 159, 252
  - Benisty, M.; Juhász, A.; Facchini, S.; Pinilla, P.; de Boer, J.; Pérez, L. M.; **Kepler, M.**; Muro-Arena, G.; Villenave, M.; Andrews, S.; Dominik, C.; Dullemond, C. P.; Gallenne, A.; Garufi, A.; Ginski, C.; Isella, A. (2018), *Shadows and asymmetries in the T Tauri disk HD 143006: evidence for a misaligned inner disk*, *A&A*, 619, 171
  - Muro-Arena, G. A.; Ginski, C.; Dominik, C.; Benisty, M.; Pinilla, P.; Bohn, A. J.; Moldenhauer, T.; Kley, W.; Harsono, D.; Henning, T.; van Holstein, R. G.; Janson, M.; **Kepler, M.**; Ménard, F.; Pérez, L. M.; Stolker, T.; Tazzari, M.; Villenave, M.; Zurlo, A.; Petit, C.; Rigal, F.; Möller-Nilsson, O.; Llored, M.; Moulin, T.; Rabou, P. (2020), *Spirals inside the millimeter cavity of transition disk SR 21*, *A&A*, 636, 4
  - Muro-Arena, G. A.; Benisty, M.; Ginski, C.; Dominik, C.; Facchini, S.; Villenave, M.; van Boekel, R.; Chauvin, G.; Garufi, A.; Henning, T.; Janson, M.; **Kepler, M.**; Matter, A.; Ménard, F.; Stolker, T.; Zurlo, A.; Blanchard, P.; Maurel, D.; Möller-Nilsson, O.; Petit, C.; Roux, A.; Sevin, A.; Wildi, F. (2020), *Shadowing and multiple rings in the protoplanetary disk of HD 139614*, *A&A*, 635, 121

- Pawellek, Nicole; Moór, Attila; Milli, Julien; Kóspál, Ágnes; Olofsson, Johan; Ábrahám, Péter; **Keppler, Miriam**; Kral, Quentin; Pohl, Adriana; Augereau, Jean-Charles; Boccaletti, Anthony; Chauvin, Gaël; Choquet, Élodie; Engler, Natalia; Henning, Thomas; Langlois, Maud; Lee, Eve J.; Ménard, Francois; Thébault, Philippe; Zurlo, Alice (2019), *A multiwavelength study of the debris disc around 49 Cet*, MNRAS, 488, 3507
- Lagrange, A. -M.; Boccaletti, A.; Langlois, M.; Chauvin, G.; Gratton, R.; Beust, H.; Desidera, S.; Milli, J.; Bonnefoy, M.; Cheetham, A.; Feldt, M.; Meyer, M.; Vigan, A.; Biller, B.; Bonavita, M.; Baudino, J. -L.; Cantalloube, F.; Cudel, M.; Daemgen, S.; Delorme, P.; D’Orazi, V.; Girard, J.; Fontanive, C.; Hagelberg, J.; Janson, M.; **Keppler, M.**; Koypitova, T.; Galicher, R.; Lannier, J.; Le Coroller, H.; Ligi, R.; Maire, A. -L.; Mesa, D.; Messina, S.; MÃ¼eller, A.; Peretti, S.; Perrot, C.; Rouan, D.; Salter, G.; Samland, M.; Schmidt, T.; Sissa, E.; Zurlo, A.; Beuzit, J. -L.; Mouillet, D.; Dominik, C.; Henning, T.; Lagadec, E.; MÃ©nard, F.; Schmid, H. -M.; Turatto, M.; Udry, S.; Bohn, A. J.; Charnay, B.; Gomez Gonzales, C. A.; Gry, C.; Kenworthy, M.; Kral, Q.; Mordasini, C.; Moutou, C.; van der Plas, G.; Schlieder, J. E.; Abe, L.; Antichi, J.; Baruffolo, A.; Baudoz, P.; Baudrand, J.; Blanchard, P.; Bazzon, A.; Buey, T.; Carbillet, M.; Carle, M.; Charton, J.; Cascone, E.; Claudi, R.; Costille, A.; Deboulbe, A.; De Caprio, V.; Dohlen, K.; Fantinel, D.; Feautrier, P.; Fusco, T.; Gigan, P.; Giro, E.; Gisler, D.; Gluck, L.; Hubin, N.; Hugot, E.; Jaquet, M.; Kasper, M.; Madec, F.; Magnard, Y.; Martinez, P.; Maurel, D.; Le Mignant, D.; MÃ¼ller-Nilsson, O.; Llored, M.; Moulin, T.; OrignÃ©, A.; Pavlov, A.; Perret, D.; Petit, C.; Pragt, J.; Szulagyí, J.; Wildi, F. (2019), *Post-conjunction detection of  $\beta$  Pictoris b with VLT/SPHERE*, A&A, 621, 8
- Claudi, R.; Maire, A. -L.; Mesa, D.; Cheetham, A.; Fontanive, C.; Gratton, R.; Zurlo, A.; Avenhaus, H.; Bhowmik, T.; Biller, B.; Boccaletti, A.; Bonavita, M.; Bonnefoy, M.; Cascone, E.; Chauvin, G.; Delboulb , A.; Desidera, S.; D’Orazi, V.; Feautrier, P.; Feldt, M.; Flammini Dotti, F.; Girard, J. H.; Giro, E.; Janson, M.; Hagelberg, J.; **Keppler, M.**; Kopytova, T.; Lacour, S.; Lagrange, A. -M.; Langlois, M.; Lannier, J.; Le Coroller, H.; Menard, F.; Messina, S.; Meyer, M.; Millward, M.; Olofsson, J.; Pavlov, A.; Peretti, S.; Perrot, C.; Pinte, C.; Pragt, J.; Ramos, J.; Rochat, S.; Rodet, L.; Roelfsema, R.; Rouan, D.; Salter, G.; Schmidt, T.; Sissa, E.; Thebault, P.; Udry, S.; Vigan, A. (2019), *SPHERE dynamical and spectroscopic characterization of HD 142527B*, A&A, 622, 96
- Cheetham, A. C.; Samland, M.; Brems, S. S.; Launhardt, R.; Chauvin, G.; S gransan, D.; Henning, T.; Quirrenbach, A.; Avenhaus, H.; Cugno, G.; Girard, J.; Godoy, N.; Kennedy, G. M.; Maire, A. -L.; Metchev, S.; M ller, A.; Musso Barucci, A.; Olofsson, J.; Pepe, F.; Quanz, S. P.; Queloz, D.; Reffert, S.; Rickman, E.; van Boekel, R.; Boc-

- caletti, A.; Bonnefoy, M.; Cantalloube, F.; Charnay, B.; Delorme, P.; Janson, M.; **Kepler, M.**; Lagrange, A. -M.; Langlois, M.; Lazzoni, C.; Menard, F.; Mesa, D.; Meyer, M.; Schmidt, T.; Sissa, E.; Udry, S.; Zurlo, A. (2019), *Spectral and orbital characterisation of the directly imaged giant planet HIP 65426 b*, A&A, 622, 80
- Lazzoni, C.; Zurlo, A.; Desidera, S.; Mesa, D.; Fontanive, C.; Bonavita, M.; Ertel, S.; Rice, K.; Vigan, A.; Boccaletti, A.; Bonnefoy, M.; Chauvin, G.; Delorme, P.; Gratton, R.; Houllé, M.; Maire, A. L.; Meyer, M.; Rickman, E.; Spalding, E. A.; Asensio-Torres, R.; Langlois, M.; Müller, A.; Baudino, J-L.; Beuzit, J. -L.; Biller, B.; Brandner, W.; Buenzli, E.; Cantalloube, F.; Cheetham, A.; Cudel, M.; Feldt, M.; Galicher, R.; Janson, M.; Hagelberg, J.; Henning, T.; Kasper, M.; **Kepler, M.**; Lagrange, A. -M.; Lannier, J.; LeCoroller, H.; Mouillet, D.; Peretti, S.; Perrot, C.; Salter, G.; Samland, M.; Schmidt, T.; Sissa, E.; Wildi, F. (2020), *The search for disks or planetary objects around directly imaged companions: A candidate around DH Tau B*, A&A, in press
  - Chauvin, G.; Gratton, R.; Bonnefoy, M.; Lagrange, A. -M.; de Boer, J.; Vigan, A.; Beust, H.; Lazzoni, C.; Boccaletti, A.; Galicher, R.; Desidera, S.; Delorme, P.; **Kepler, M.**; Lannier, J.; Maire, A. -L.; Mesa, D.; Meunier, N.; Kral, Q.; Henning, T.; Menard, F.; Moor, A.; Avenhaus, H.; Bazzon, A.; Janson, M.; Beuzit, J. -L.; Bhowmik, T.; Bonavita, M.; Borgniet, S.; Brandner, W.; Cheetham, A.; Cudel, M.; Feldt, M.; Fontanive, C.; Ginski, C.; Hagelberg, J.; Janin-Potiron, P.; Lagadec, E.; Langlois, M.; Le Coroller, H.; Messina, S.; Meyer, M.; Mouillet, D.; Peretti, S.; Perrot, C.; Rodet, L.; Samland, M.; Sissa, E.; Olofsson, J.; Salter, G.; Schmidt, T.; Zurlo, A.; Milli, J.; van Boekel, R.; Quanz, S.; Feautrier, P.; Le Mignant, D.; Perret, D.; Ramos, J.; Rochat, S. (2018), *Investigating the young solar system analog HD 95086. A combined HARPS and SPHERE exploration*, A&A, 617, 76
  - Cheetham, A.; Bonnefoy, M.; Desidera, S.; Langlois, M.; Vigan, A.; Schmidt, T.; Olofsson, J.; Chauvin, G.; Klahr, H.; Gratton, R.; D’Orazi, V.; Henning, T.; Janson, M.; Biller, B.; Peretti, S.; Hagelberg, J.; Ségransan, D.; Udry, S.; Mesa, D.; Sissa, E.; Kral, Q.; Schlieder, J.; Maire, A. -L.; Mordasini, C.; Menard, F.; Zurlo, A.; Beuzit, J. -L.; Feldt, M.; Mouillet, D.; Meyer, M.; Lagrange, A. -M.; Boccaletti, A.; **Kepler, M.**; Kopytova, T.; Ligi, R.; Rouan, D.; Le Coroller, H.; Dominik, C.; Lagadec, E.; Turatto, M.; Abe, L.; Antichi, J.; Baruffolo, A.; Baudoz, P.; Blanchard, P.; Buey, T.; Carbillet, M.; Carle, M.; Cascone, E.; Claudi, R.; Costille, A.; Delboulbé, A.; De Caprio, V.; Dohlen, K.; Fantinel, D.; Feautrier, P.; Fusco, T.; Giro, E.; Gluck, L.; Hubin, N.; Hugot, E.; Jaquet, M.; Kasper, M.; Llored, M.; Madec, F.; Magnard, Y.; Martinez, P.; Maurel, D.; Le Mignant, D.; MÅ¶ller-Nilsson, O.; Moulin, T.; OrignÃ©, A.; Pavlov, A.; Perret, D.; Petit, C.; Pragt, J.; Puget, P.; Rabou, P.; Ramos, J.; Rigal, F.; Rochat, S.; Roelfsema, R.;

- Rousset, G.; Roux, A.; Salasnich, B.; Sauvage, J. -F.; Sevin, A.; Soenke, C.; Stadler, E.; Suarez, M.; Weber, L.; Wildi, F. (2018), *Discovery of a brown dwarf companion to the star HIP 64892*, A&A, 615, 160
- Maire, A. -L.; Rodet, L.; Lazzoni, C.; Boccaletti, A.; Brandner, W.; Galicher, R.; Cantalloube, F.; Mesa, D.; Klahr, H.; Beust, H.; Chauvin, G.; Desidera, S.; Janson, **M.**; **Keppler**, M.; Olofsson, J.; Augereau, J. -C.; Daemgen, S.; Henning, T.; Thébault, P.; Bonnefoy, M.; Feldt, M.; Gratton, R.; Lagrange, A.-M.; Langlois, M.; Meyer, M. R.; Vigan, A.; D'Orazi, V.; Hagelberg, J.; Le Coroller, H.; Ligi, R.; Rouan, D.; Samland, M.; Schmidt, T.; Udry, S.; Zurlo, A.; Abe, L.; Carle, M.; DelboulbÃ©, A.; Feautrier, P.; Magnard, Y.; Maurel, D.; Moulin, T.; Pavlov, A.; Perret, D.; Petit, C.; Ramos, J. R.; Rigal, F.; Roux, A.; Weber, L. (2018), *VLT/SPHERE astrometric confirmation and orbital analysis of the brown dwarf companion HR 2562 B*, A&A, 615, 177
  - Gibbs, Aidan; Bixel, Alex; Rackham, Benjamin V.; Apai, Dániel; Schlecker, Martin; Espinoza, Néstor; Mancini, Luigi; Chen, Wen-Ping; Henning, Thomas; Gabor, Paul; Boyle, Richard; Perez Chavez, Jose; Mousseau, Allie; Dietrich, Jeremy; Jay Socia, Quentin; Ip, Wing; Ngeow, Chow-Choong; Tsai, An-Li; Bhandare, Asmita; Marian, Victor; Baehr, Hans; Brown, Samantha; Häberle, Maximilian; **Keppler, Miriam**; Molaverdikhani, Karan; Sarkis, Paula (2020), *EDEN: Sensitivity Analysis and Transiting Planet Detection Limits for Nearby Late Red Dwarfs* AJ, 159, 169

# D

## Bibliography

---

- Absil, O., Milli, J., Mawet, D., et al. 2013, *A&A*, 559, L12 [41](#)
- Akeson, R. L., Jensen, E. L. N., Carpenter, J., et al. 2019, *ApJ*, 872, 158 [134](#)
- Allard, F. 2014, in *IAU Symposium*, Vol. 299, Exploring the Formation and Evolution of Planetary Systems, ed. M. Booth, B. C. Matthews, & J. R. Graham, 271–272 [20](#)
- Allard, F., Hauschildt, P. H., Alexander, D. R., Tamanai, A., & Schweitzer, A. 2001, *ApJ*, 556, 357 [18](#)
- ALMA Partnership, Brogan, C. L., Pérez, L. M., et al. 2015, *ApJ*, 808, L3 [29](#)
- Aly, H., Lodato, G., & Cazzoletti, P. 2018, *MNRAS*, 480, 4738 [136](#), [158](#)
- Amara, A., & Quanz, S. P. 2012, *MNRAS*, 427, 948 [19](#)
- Andrews, S. M. 2020, arXiv e-prints, arXiv:2001.05007 [4](#)
- Andrews, S. M., Rosenfeld, K. A., Wilner, D. J., & Bremer, M. 2011, *ApJ*, 742, L5 [29](#)
- Andrews, S. M., Wilner, D. J., Hughes, A. M., et al. 2012, *ApJ*, 744, 162 [79](#)
- Andrews, S. M., Chandler, C. J., Isella, A., et al. 2014, *ApJ*, 787, 148 [135](#), [145](#), [154](#), [155](#)
- Andrews, S. M., Huang, J., Pérez, L. M., et al. 2018, *ApJ*, 869, L41 [29](#), [101](#)
- Ansdell, M., Williams, J. P., Trapman, L., et al. 2018, *ApJ*, 859, 21 [5](#)
- Aoyama, Y., & Ikoma, M. 2019, *ApJ*, 885, L29 [68](#)
- Aoyama, Y., Ikoma, M., & Tanigawa, T. 2018, *ApJ*, 866, 84 [68](#)
- Appenzeller, I., & Mundt, R. 1989, *A&A Rev.*, 1, 291 [3](#)

- Armitage, P. J. 2011, *ARA&A*, 49, 195 4
- Artymowicz, P., & Lubow, S. H. 1994, *ApJ*, 421, 651 134, 136
- . 1996, *ApJ*, 467, L77 134
- Asensio-Torres, R., Janson, M., Bonavita, M., et al. 2018, *A&A*, 619, A43 135, 159
- Asensio-Torres, R., Currie, T., Janson, M., et al. 2019, *A&A*, 622, A42 137
- Avenhaus, H., Quanz, S. P., Meyer, M. R., et al. 2014a, *ApJ*, 790, 56 44
- Avenhaus, H., Quanz, S. P., Schmid, H. M., et al. 2014b, *ApJ*, 781, 87 40
- . 2017, *AJ*, 154, 33 134, 156
- Avenhaus, H., Quanz, S. P., Garufi, A., et al. 2018, *ApJ*, 863, 44 29, 44, 101
- Ayliffe, B. A., & Bate, M. R. 2009, *MNRAS*, 397, 657 10, 77
- Bacon, R., Accardo, M., Adjali, L., & Anwand, H. 2010, in *Society of Photo-Optical Instrumentation Engineers (SPIE) Conference Series*, Vol. 7735, *Ground-based and Airborne Instrumentation for Astronomy III*, 773508 68
- Bae, J., Pinilla, P., & Birnstiel, T. 2018, *ApJ*, 864, L26 101
- Bae, J., Zhu, Z., Baruteau, C., et al. 2019, *ApJ*, 884, L41 98, 99
- Bailey, V., Meshkat, T., Reiter, M., et al. 2014, *ApJ*, 780, L4 61
- Balbus, S. A., & Hawley, J. F. 1991, *ApJ*, 376, 214 7
- Baraffe, I., Chabrier, G., Barman, T. S., Allard, F., & Hauschildt, P. H. 2003, *A&A*, 402, 701 20, 61, 62
- Baraffe, I., Homeier, D., Allard, F., & Chabrier, G. 2015, *A&A*, 577, A42 20, 137
- Baruteau, C., Crida, A., Paardekooper, S. J., et al. 2014, in *Protostars and Planets VI*, ed. H. Beuther, R. S. Klessen, C. P. Dullemond, & T. Henning, 667 101
- Batygin, K. 2018, *AJ*, 155, 178 166
- Baudino, J.-L., Bézard, B., Boccaletti, A., et al. 2015, *A&A*, 582, A83 63
- Baudino, J.-L., Mollière, P., Venot, O., et al. 2017, *ApJ*, 850, 150 63
- Benisty, M., Juhasz, A., Boccaletti, A., et al. 2015, *A&A*, 578, L6 29, 31

- Benítez-Llambay, P., & Masset, F. S. 2016, *ApJS*, 223, 11 [90](#)
- Bergin, E. A., & Williams, J. P. 2018, arXiv e-prints, arXiv:1807.09631 [4](#)
- Bergin, E. A., Cleeves, L. I., Gorti, U., et al. 2013, *Nature*, 493, 644 [4](#)
- Beust, H., & Dutrey, A. 2005, *A&A*, 439, 585 [136](#), [157](#), [158](#)
- . 2006, *A&A*, 446, 137 [151](#)
- Beuzit, J. L., Vigan, A., Mouillet, D., et al. 2019, *A&A*, 631, A155 [18](#), [138](#)
- Biller, B. A., Males, J., Rodigas, T., et al. 2014, *ApJ*, 792, L22 [29](#)
- Birnstiel, T., & Andrews, S. M. 2014, *ApJ*, 780, 153 [5](#)
- Birnstiel, T., Dullemond, C. P., & Brauer, F. 2010, *A&A*, 513, A79 [6](#)
- Blum, J. 2018, *Space Sci.Rev.*, 214, 52 [4](#), [8](#)
- Bodenheimer, P., & Pollack, J. B. 1986, *Icarus*, 67, 391 [8](#)
- Bohlin, R. C., Savage, B. D., & Drake, J. F. 1978, *ApJ*, 224, 132 [4](#)
- Bohren, C. F., & Huffman, D. R. 1983, *Absorption and scattering of light by small particles* [14](#), [17](#), [50](#), [92](#)
- Boley, A. C., Hayfield, T., Mayer, L., & Durisen, R. H. 2010, *Icarus*, 207, 509 [11](#)
- Bonavita, M., & Desidera, S. 2020, *Galaxies*, 8, 16 [32](#), [135](#)
- Bonavita, M., Desidera, S., Thalmann, C., et al. 2016, *A&A*, 593, A38 [135](#)
- Bonnefoy, M., Marleau, G.-D., Galicher, R., et al. 2014, *A&A*, 567, L9 [62](#)
- Bonnefoy, M., Zurlo, A., Baudino, J. L., et al. 2016, *A&A*, 587, A58 [61](#)
- Bonnefoy, M., Perraut, K., Lagrange, A. M., et al. 2018, *A&A*, 618, A63 [20](#), [57](#), [60](#)
- Boss, A. P. 1997, *Science*, 276, 1836 [8](#), [11](#), [12](#)
- Bouvier, J., Alencar, S. H. P., Harries, T. J., Johns-Krull, C. M., & Romanova, M. M. 2007, in *Protostars and Planets V*, ed. B. Reipurth, D. Jewitt, & K. Keil, 479 [5](#)
- Bouwman, J., Lawson, W. A., Dominik, C., et al. 2006, *ApJ*, 653, L57 [134](#)
- Bowler, B. P., Andrews, S. M., Kraus, A. L., et al. 2015, *ApJ*, 805, L17 [96](#)

- Brandl, B. R., Lenzen, R., Pantin, E., et al. 2012, in Society of Photo-Optical Instrumentation Engineers (SPIE) Conference Series, Vol. 8446, Ground-based and Airborne Instrumentation for Astronomy IV, 84461M 166
- Brauer, R., Pantin, E., Di Folco, E., et al. 2019, *A&A*, 628, A88 137, 138, 148, 149, 152, 155
- Bressan, A., Marigo, P., Girardi, L., et al. 2012, *MNRAS*, 427, 127 137
- Brittain, S. D., Carr, J. S., Najita, J. R., Quanz, S. P., & Meyer, M. R. 2014, *ApJ*, 791, 136 29
- Bryan, M. L., Benneke, B., Knutson, H. A., Batygin, K., & Bowler, B. P. 2018, *Nature Astronomy*, 2, 138 166
- Bryden, G., Różyczka, M., Lin, D. N. C., & Bodenheimer, P. 2000, *ApJ*, 540, 1091 10, 28
- Budde, G., Burkhardt, C., Brennecka, G. A., et al. 2016, *Earth and Planetary Science Letters*, 454, 293 1
- Cameron, A. G. W. 1978, *Moon and Planets*, 18, 5 11
- Canovas, H., Marnard, F., de Boer, J., et al. 2015, *Astronomy and Astrophysics*, 582, L7 40
- Canovas, H., Ménard, F., de Boer, J., et al. 2015, *A&A*, 582, L7 21, 142
- Canovas, H., Rodenhuis, M., Jeffers, S. V., Min, M., & Keller, C. U. 2011, *A&A*, 531, A102 39
- Canovas, H., Montesinos, B., Schreiber, M. R., et al. 2018, *A&A*, 610, A13 39
- Cantalloube, F., Mouillet, D., Mugnier, L. M., et al. 2015, *A&A*, 582, A89 19, 41, 55
- Carbillet, M., Bendjoya, P., Abe, L., et al. 2011, *Experimental Astronomy*, 30, 39 37
- Casassus, S., & Pérez, S. 2019, *ApJ*, 883, L41 30, 101
- Casassus, S., Marino, S., Pérez, S., et al. 2015, *ApJ*, 811, 92 83
- Cazzoletti, P., Ricci, L., Birnstiel, T., & Lodato, G. 2017, *A&A*, 599, A102 136, 144, 158, 159, 176, 177
- Chabrier, G., Baraffe, I., Allard, F., & Hauschildt, P. 2000, *ApJ*, 542, 464 18, 61, 62
- Chauvin, G., Lagrange, A.-M., Dumas, C., et al. 2004, *A&A*, 425, L29 61
- Chauvin, G., Lagrange, A.-M., Beust, H., et al. 2012, *A&A*, 542, A41 64
- Chauvin, G., Desidera, S., Lagrange, A.-M., et al. 2017a, *A&A*, 605, L9 20, 61

- Chauvin, G., Desidera, S., Lagrange, A.-M., et al. 2017b, in SF2A-2017: Proceedings of the Annual meeting of the French Society of Astronomy and Astrophysics, ed. C. Reylé, P. Di Matteo, F. Herpin, E. Lagadec, A. Lançon, Z. Meliani, & F. Royer, 331–335 [40](#)
- Chauvin, G., Gratton, R., Bonnefoy, M., et al. 2018, ArXiv e-prints, arXiv:1801.05850 [57](#), [58](#), [60](#)
- Chiang, E. I., & Goldreich, P. 1997, ApJ, 490, 368 [6](#)
- Choi, J., Dotter, A., Conroy, C., et al. 2016, ApJ, 823, 102 [34](#), [137](#)
- Christiaens, V., Cantalloube, F., Casassus, S., et al. 2019, in AAS/Division for Extreme Solar Systems Abstracts, Vol. 51, AAS/Division for Extreme Solar Systems Abstracts, 101.05 [99](#)
- Claudi, R. U., Turatto, M., Gratton, R. G., et al. 2008a, in Society of Photo-Optical Instrumentation Engineers (SPIE) Conference Series, Vol. 7014, Ground-based and Airborne Instrumentation for Astronomy II, 70143E [37](#)
- Claudi, R. U., Turatto, M., Gratton, R. G., et al. 2008b, in Proceedings of SPIE, Vol. 7014, Ground-based and Airborne Instrumentation for Astronomy II, 70143E [40](#)
- Cleeves, L. I., Bergin, E. A., & Harries, T. J. 2015, ApJ, 807, 2 [89](#)
- Close, L. M., Males, J. R., Kopon, D. A., et al. 2012, in Society of Photo-Optical Instrumentation Engineers (SPIE) Conference Series, Vol. 8447, Adaptive Optics Systems III, 84470X [68](#)
- Close, L. M., Follette, K. B., Males, J. R., et al. 2014, ApJ, 781, L30 [68](#)
- Cox, E. G., Harris, R. J., Looney, L. W., et al. 2017, ApJ, 851, 83 [134](#)
- Cugno, G., Quanz, S. P., Hunziker, S., et al. 2019, A&A, 622, A156 [68](#)
- Currie, T., Brittain, S., Grady, C. A., Kenyon, S. J., & Muto, T. 2017, Research Notes of the American Astronomical Society, 1, 40 [30](#)
- Currie, T., Cloutier, R., Brittain, S., et al. 2015, ApJ, 814, L27 [29](#)
- Currie, T., Marois, C., Cieza, L., et al. 2019, ApJ, 877, L3 [30](#)
- Cutri, R. M., & et al. 2014, VizieR Online Data Catalog, 2328 [36](#)
- Cutri, R. M., Skrutskie, M. F., van Dyk, S., et al. 2003, VizieR Online Data Catalog, 2246 [36](#), [50](#)

D'Alessio, P., Cantö, J., Calvet, N., & Lizano, S. 1998, *ApJ*, 500, 411 [129](#)

D'Angelo, G., Henning, T., & Kley, W. 2003, *ApJ*, 599, 548 [10](#), [77](#)

Dawson, R. I., & Johnson, J. A. 2018, *ARA&A*, 56, 175 [2](#)

de Boer, J., Salter, G., Benisty, M., et al. 2016, *A&A*, 595, A114 [145](#)

de Boer, J., Langlois, M., van Holstein, R. G., et al. 2020, *A&A*, 633, A63 [39](#), [138](#)

de Boer, K., & Seggewiss, W. 2008, *Stars and Stellar Evolution* [3](#)

de Juan Ovelar, M., Min, M., Dominik, C., et al. 2013, *A&A*, 560, A111 [26](#), [36](#), [101](#), [136](#), [144](#)

Delorme, P., Schmidt, T., Bonnefoy, M., et al. 2017, *A&A*, 608, A79 [61](#)

Di Folco, E., Dutrey, A., Le Bouquin, J.-B., et al. 2014, *A&A*, 565, L2 [135](#), [136](#), [137](#), [138](#), [150](#), [176](#)

Dipierro, G., Pinilla, P., Lodato, G., & Testi, L. 2015, *MNRAS*, 451, 974 [29](#), [157](#)

Dobbs, C. L., Krumholz, M. R., Ballesteros-Paredes, J., et al. 2014, in *Protostars and Planets VI*, ed. H. Beuther, R. S. Klessen, C. P. Dullemond, & T. Henning, [3](#) [3](#)

Dodson-Robinson, S. E., & Salyk, C. 2011, *ApJ*, 738, 131 [96](#)

Dodson-Robinson, S. E., Veras, D., Ford, E. B., & Beichman, C. A. 2009, *ApJ*, 707, 79 [12](#)

Dohlen, K., Langlois, M., Saisse, M., et al. 2008, in *Proceedings of SPIE, Vol. 7014, Ground-based and Airborne Instrumentation for Astronomy II*, 70143L [37](#), [138](#)

Dong, R., & Fung, J. 2017, *ApJ*, 835, 146 [10](#), [101](#)

Dong, R., Hall, C., Rice, K., & Chiang, E. 2015a, *ApJ*, 812, L32 [157](#)

Dong, R., Liu, S.-Y., & Fung, J. 2019, *ApJ*, 870, 72 [101](#)

Dong, R., Zhu, Z., Fung, J., et al. 2016, *ApJ*, 816, L12 [157](#)

Dong, R., Zhu, Z., Rafikov, R. R., & Stone, J. M. 2015b, *ApJ*, 809, L5 [101](#), [157](#)

Dong, R., Hashimoto, J., Rafikov, R., et al. 2012, *ApJ*, 760, 111 [35](#), [46](#), [48](#), [92](#)

Dotter, A. 2016, *ApJS*, 222, 8 [34](#), [137](#)

Dotter, A., Chaboyer, B., Jevremović, D., et al. 2008, *ApJS*, 178, 89 [137](#)

Doyle, L. R., Carter, J. A., Fabrycky, D. C., et al. 2011, *Science*, 333, 1602 [135](#)

- Draine, B. T. 2003a, *ARA&A*, 41, 241 [4](#)
- . 2003b, *ApJ*, 598, 1026 [14](#), [15](#), [50](#), [92](#), [152](#)
- Duchêne, G. 1999, *A&A*, 341, 547 [133](#)
- . 2010, *ApJ*, 709, L114 [134](#)
- Duchêne, G., & Kraus, A. 2013, *ARA&A*, 51, 269 [32](#), [133](#)
- Duchêne, G., McCabe, C., Ghez, A. M., & Macintosh, B. A. 2004, *ApJ*, 606, 969 [136](#)
- Duffell, P. C., & Dong, R. 2015, *ApJ*, 802, 42 [96](#)
- Duffell, P. C., D’Orazio, D., Derdzinski, A., et al. 2019, arXiv e-prints, arXiv:1911.05506 [156](#)
- Duffell, P. C., Haiman, Z., MacFadyen, A. I., D’Orazio, D. J., & Farris, B. D. 2014, *ApJ*, 792, L10 [11](#)
- Duffell, P. C., & MacFadyen, A. I. 2013, *ApJ*, 769, 41 [92](#)
- Dullemond, C. P., & Dominik, C. 2004, *A&A*, 421, 1075 [7](#)
- Dullemond, C. P., Isella, A., Andrews, S. M., Skobleva, I., & Dzyurkevich, N. 2020, *A&A*, 633, A137 [129](#)
- Dullemond, C. P., Juhasz, A., Pohl, A., et al. 2012, RADMC-3D: A multi-purpose radiative transfer tool, *Astrophysics Source Code Library*, ascl:1202.015 [16](#), [48](#), [151](#)
- Dullemond, C. P., & Monnier, J. D. 2010, *ARA&A*, 48, 205 [5](#)
- Dunhill, A. C., Cuadra, J., & Dougados, C. 2015, *MNRAS*, 448, 3545 [156](#)
- Dürmann, C., & Kley, W. 2015, *A&A*, 574, A52 [11](#)
- Dutrey, A., di Folco, E., Guilloteau, S., et al. 2014, *Nature*, 514, 600 [135](#), [143](#), [146](#), [147](#), [150](#), [156](#), [157](#)
- Ercolano, B., & Pascucci, I. 2017, *Royal Society Open Science*, 4, 170114 [8](#)
- Espaillet, C., Muzerolle, J., Najita, J., et al. 2014, *Protostars and Planets VI*, 497 [29](#)
- Evans, Neal J., I., Dunham, M. M., Jørgensen, J. K., et al. 2009, *ApJS*, 181, 321 [3](#)
- Facchini, S., Birnstiel, T., Bruderer, S., & van Dishoeck, E. F. 2017, *A&A*, 605, A16 [5](#)

- Facchini, S., Pinilla, P., van Dishoeck, E. F., & de Juan Ovelar, M. 2018, *A&A*, 612, A104 [27](#), [82](#), [84](#)
- Fedele, D., Tazzari, M., Booth, R., et al. 2018, *A&A*, 610, A24 [29](#)
- Fitzgerald, M. P., & Graham, J. R. 2006, *ApJ*, 637, 541 [19](#)
- Flaherty, K., Hughes, A. M., Simon, J. B., et al. 2020, *ApJ*, 895, 109 [8](#)
- Flaherty, K. M., Hughes, A. M., Rosenfeld, K. A., et al. 2015, *ApJ*, 813, 99 [8](#), [91](#)
- Flaherty, K. M., Hughes, A. M., Teague, R., et al. 2018, *ApJ*, 856, 117 [91](#)
- Flaherty, K. M., Hughes, A. M., Rose, S. C., et al. 2017, *ApJ*, 843, 150 [8](#), [91](#)
- Flock, M., Ruge, J. P., Dzyurkevich, N., et al. 2015, *A&A*, 574, A68 [26](#)
- Follette, K. B., Rameau, J., Dong, R., et al. 2017, *AJ*, 153, 264 [30](#)
- Fomalont, E., van Kempen, T., Kneissl, R., et al. 2014, *The Messenger*, 155, 19 [24](#)
- Foreman-Mackey, D., Hogg, D. W., Lang, D., & Goodman, J. 2013, *PASP*, 125, 306 [76](#)
- Fung, J., Shi, J.-M., & Chiang, E. 2014, *ApJ*, 782, 88 [92](#)
- Fusco, T., Sauvage, J. F., Mouillet, D., et al. 2016, in *Society of Photo-Optical Instrumentation Engineers (SPIE) Conference Series*, Vol. 9909, *Adaptive Optics Systems V*, 99090U [37](#)
- Gaia Collaboration, Prusti, T., de Bruijne, J. H. J., et al. 2016, *A&A*, 595, A1 [34](#), [36](#), [56](#), [73](#), [103](#), [135](#)
- Gaia Collaboration, Brown, A. G. A., Vallenari, A., et al. 2018, *A&A*, 616, A1 [34](#), [36](#), [56](#), [73](#), [103](#), [135](#), [136](#)
- Galicher, R., Boccaletti, A., Mesa, D., et al. 2018, *A&A*, 615, A92 [41](#)
- Garufi, A., Avenhaus, H., Pérez, S., et al. 2020, *A&A*, 633, A82 [141](#)
- Ginski, C., Stolker, T., Pinilla, P., et al. 2016, *A&A*, 595, A112 [29](#), [102](#)
- Ginzburg, S., & Chiang, E. 2019, *MNRAS*, 487, 681 [10](#)
- Goebel, S. B., Guyon, O., Hall, D. N. B., et al. 2018, *PASP*, 130, 104502 [19](#)
- Goldreich, P., & Tremaine, S. 1980, *ApJ*, 241, 425 [10](#)

- Gorti, U., Liseau, R., Sándor, Z., & Clarke, C. 2016, *Space Sci.Rev.*, 205, 125 8
- Gratton, R., Ligi, R., Sissa, E., et al. 2019, *A&A*, 623, A140 29
- Gravity Collaboration, Lacour, S., Nowak, M., et al. 2019, *A&A*, 623, L11 165
- Gravity Collaboration, Nowak, M., Lacour, S., et al. 2020, *A&A*, 633, A110 165
- Gregorio-Hetem, J., & Hetem, A. 2002, *Monthly Notices of the Royal Astronomical Society*, 336, 197 34, 35
- Gregorio-Hetem, J., Lepine, J. R. D., Quast, G. R., Torres, C. A. O., & de La Reza, R. 1992, *AJ*, 103, 549 50
- Guidi, G., Ruane, G., Williams, J. P., et al. 2018, *MNRAS*, 479, 1505 102
- Guilloteau, S., Dutrey, A., & Simon, M. 1999, *A&A*, 348, 570 135, 137, 138, 143, 145, 150, 152, 155
- Günther, R., & Kley, W. 2002, *A&A*, 387, 550 156
- Haffert, S. Y., Bohn, A. J., de Boer, J., et al. 2019, *Nature Astronomy*, 3, 749 68, 98, 126, 128, 162, 163
- Haisch, Karl E., J., Lada, E. A., & Lada, C. J. 2001, *ApJ*, 553, L153 7
- Harris, R. J., Andrews, S. M., Wilner, D. J., & Kraus, A. L. 2012, *ApJ*, 751, 115 134
- Hartigan, P., & Kenyon, S. J. 2003, *ApJ*, 583, 334 135, 136, 137, 138, 141
- Hartmann, L., Calvet, N., Gullbring, E., & D'Alessio, P. 1998, *ApJ*, 495, 385 4
- Hashimoto, J., Aoyama, Y., Konishi, M., et al. 2020, *AJ*, 159, 222 68
- Hashimoto, J., Dong, R., Kudo, T., et al. 2012, *ApJ*, 758, L19 35, 36, 38, 40, 42, 43, 45, 46, 50, 54
- Hashimoto, J., Tsukagoshi, T., Brown, J. M., et al. 2015, *ApJ*, 799, 43 35, 36, 57
- Hayward, T. L., Biller, B. A., Liu, M. C., et al. 2014, *PASP*, 126, 1112 64
- Helled, R., Bodenheimer, P., Podolak, M., et al. 2014, in *Protostars and Planets VI*, ed. H. Beuther, R. S. Klessen, C. P. Dullemond, & T. Henning, 643 9
- Henden, A. A., Levine, S., Terrell, D., & Welch, D. L. 2015, in *American Astronomical Society Meeting Abstracts*, Vol. 225, *American Astronomical Society Meeting Abstracts*, 336.16 36

Hendler, N. P., Pinilla, P., Pascucci, I., et al. 2018, *MNRAS*, 475, L62 [36](#)

Herbig, G. H. 1960, *ApJS*, 4, 337 [3](#)

Hinkley, S., Oppenheimer, B. R., Soummer, R., et al. 2007, *ApJ*, 654, 633 [19](#)

Hioki, T., Itoh, Y., Oasa, Y., et al. 2007, *AJ*, 134, 880 [134](#)

Hirschmann, M. M. 2006, *Annual Review of Earth and Planetary Sciences*, 34, 629 [1](#)

Högbom, J. A. 1974, *A&AS*, 15, 417 [25](#)

Holman, M. J., & Wiegert, P. A. 1999, *AJ*, 117, 621 [159](#)

Ikoma, M., & Genda, H. 2006, *ApJ*, 648, 696 [1](#)

Isella, A., Benisty, M., Teague, R., et al. 2019, *ApJ*, 879, L25 [98](#), [99](#), [103](#), [107](#), [110](#), [111](#), [126](#), [127](#), [131](#), [163](#), [164](#)

Isella, A., Carpenter, J. M., & Sargent, A. I. 2009, *ApJ*, 701, 260 [5](#)

Isella, A., Chandler, C. J., Carpenter, J. M., Pérez, L. M., & Ricci, L. 2014, *ApJ*, 788, 129 [78](#), [79](#), [80](#), [96](#)

Isella, A., Testi, L., Natta, A., et al. 2007, *A&A*, 469, 213 [5](#)

Isella, A., Huang, J., Andrews, S. M., et al. 2018, *ApJ*, 869, L49 [83](#)

Itoh, Y., Oasa, Y., Kudo, T., et al. 2014, *Research in Astronomy and Astrophysics*, 14, 1438 [136](#), [142](#), [145](#), [147](#), [148](#)

Izidoro, A., Raymond, S. N., Morbidelli, A. r., Hersant, F., & Pierens, A. 2015, *ApJ*, 800, L22 [2](#)

Johansen, A., & Lambrechts, M. 2017, *Annual Review of Earth and Planetary Sciences*, 45, 359 [12](#)

Kanagawa, K. D., Muto, T., Tanaka, H., et al. 2015a, *ApJ*, 806, L15 [10](#), [26](#), [92](#), [101](#)

Kanagawa, K. D., Tanaka, H., Muto, T., Tanigawa, T., & Takeuchi, T. 2015b, *MNRAS*, 448, 994 [10](#), [28](#)

Kanagawa, K. D., Tanaka, H., & Szuszkiewicz, E. 2018, *ApJ*, 861, 140 [11](#)

Kenyon, S. J., & Hartmann, L. 1987, *ApJ*, 323, 714 [6](#)

Keppler, M., Benisty, M., Müller, A., et al. 2018, *A&A*, 617, A44 [33](#), [67](#), [77](#), [81](#), [82](#), [84](#), [92](#), [141](#), [161](#)

Keppler, M., Teague, R., Bae, J., et al. 2019, *A&A*, 625, A118 [71](#), [104](#), [127](#), [162](#)

Keppler, M., Penzlin, A., Benisty, M., et al. 2020, *A&A*, 639, A62 [133](#), [164](#)

King, H. E., Stimpfl, M., Deymier, P., et al. 2010, *Earth and Planetary Science Letters*, 300, 11 [1](#)

Kley, W. 1999, *MNRAS*, 303, 696 [9](#)

—. 2019, *Saas-Fee Advanced Course*, 45, 151 [12](#)

Kley, W., & Haghighipour, N. 2014, *A&A*, 564, A72 [135](#)

Kley, W., & Nelson, R. P. 2012, *ARA&A*, 50, 211 [10](#), [101](#)

Kley, W., Thun, D., & Penzlin, A. B. T. 2019, *A&A*, 627, A91 [151](#)

Köhler, R. 2011, *A&A*, 530, A126 [136](#), [146](#), [150](#), [158](#)

Kóspál, Á., Ábrahám, P., Zsidi, G., et al. 2018, *ApJ*, 862, 44 [156](#)

Kraus, A. L., & Hillenbrand, L. A. 2009, *ApJ*, 704, 531 [135](#), [136](#), [137](#)

Kraus, A. L., & Ireland, M. J. 2012, *ApJ*, 745, 5 [30](#)

Kraus, A. L., Ireland, M. J., Martinache, F., & Hillenbrand, L. A. 2011, *ApJ*, 731, 8 [133](#)

Krist, J. E., Stapelfeldt, K. R., & Watson, A. M. 2002, *ApJ*, 570, 785 [136](#), [142](#), [145](#)

Krist, J. E., Stapelfeldt, K. R., Golimowski, D. A., et al. 2005, *AJ*, 130, 2778 [142](#), [144](#), [147](#), [149](#)

Kruijer, T. S., Burkhardt, C., Budde, G., & Kleine, T. 2017, *Proceedings of the National Academy of Science*, 114, 6712 [1](#)

Kuhn, J. R., Potter, D., & Parise, B. 2001, *ApJ*, 553, L189 [20](#)

Kuiper, G. P. 1951, *Proceedings of the National Academy of Science*, 37, 1 [11](#)

Lachapelle, F.-R., Lafrenière, D., Gagné, J., et al. 2015, *ApJ*, 802, 61 [61](#)

Lacy, J. H., Knacke, R., Geballe, T. R., & Tokunaga, A. T. 1994, *ApJ*, 428, L69 [92](#)

Lafrenière, D., Jayawardhana, R., & van Kerkwijk, M. H. 2008, *ApJ*, 689, L153 [61](#)

—. 2010, *ApJ*, 719, 497 [61](#)

- Lafrenière, D., Marois, C., Doyon, R., Nadeau, D., & Artigau, É. 2007, *ApJ*, 660, 770 [19](#)
- Lagrange, A. M., Gratadour, D., Chauvin, G., et al. 2009, *A&A*, 493, L21 [19](#)
- Lagrange, A.-M., Bonnefoy, M., Chauvin, G., et al. 2010, *Science*, 329, 57 [55](#)
- Lambrechts, M., & Johansen, A. 2012, *A&A*, 544, A32 [9](#)
- Langlois, M., Dohlen, K., Vigan, A., et al. 2014, in *Proceedings of SPIE*, Vol. 9147, *Ground-based and Airborne Instrumentation for Astronomy V*, 91471R [138](#)
- Launhardt, R., Henning, T., Quirrenbach, A., et al. 2020, *A&A*, 635, A162 [42](#), [64](#)
- Leinert, C., Haas, M., Mundt, R., Richichi, A., & Zinnecker, H. 1991, *A&A*, 250, 407 [135](#)
- Leinert, C., Zinnecker, H., Weitzel, N., et al. 1993, *A&A*, 278, 129 [135](#)
- Ligi, R., Vigan, A., Gratton, R., et al. 2018, *MNRAS*, 473, 1774 [29](#), [58](#)
- Lin, D. N. C., & Papaloizou, J. 1986a, *ApJ*, 307, 395 [10](#)
- . 1986b, *ApJ*, 309, 846 [90](#)
- Lobo Gomes, A., Klahr, H., Uribe, A. L., Pinilla, P., & Surville, C. 2015, *ApJ*, 810, 94 [96](#)
- Lodato, G., Dipierro, G., Ragusa, E., et al. 2019, *MNRAS*, 486, 453 [101](#)
- Lodders, K., & Fegley, B. 2002, *Icarus*, 155, 393 [165](#)
- Long, F., Pinilla, P., Herczeg, G. J., et al. 2018a, *ApJ*, 869, 17 [29](#), [101](#)
- Long, Z. C., Akiyama, E., Sitko, M., et al. 2018b, *ApJ*, 858, 112 [35](#), [46](#), [72](#), [73](#), [76](#), [81](#), [82](#), [83](#), [89](#), [97](#), [98](#), [104](#)
- Lubow, S. H., & D'Angelo, G. 2006, *ApJ*, 641, 526 [10](#)
- Lubow, S. H., Seibert, M., & Artymowicz, P. 1999, *ApJ*, 526, 1001 [9](#)
- Luhman, K. L. 2018, *AJ*, 156, 271 [136](#)
- Lynden-Bell, D., & Pringle, J. E. 1974, *MNRAS*, 168, 603 [4](#)
- Lyra, W., & Umurhan, O. M. 2019, *PASP*, 131, 072001 [7](#)
- MacGregor, M. A., Wilner, D. J., Czekala, I., et al. 2017, *ApJ*, 835, 17 [96](#)
- Machida, M. N., Kokubo, E., Inutsuka, S.-I., & Matsumoto, T. 2010, *MNRAS*, 405, 1227 [9](#)

- Macintosh, B., Graham, J. R., Ingraham, P., et al. 2014, *Proceedings of the National Academy of Science*, 111, 12661 [18](#)
- Madhusudhan, N., Agúndez, M., Moses, J. I., & Hu, Y. 2016, *Space Sci.Rev.*, 205, 285 [165](#)
- Maire, A. L., Bonnefoy, M., Ginski, C., et al. 2016a, *A&A*, 587, A56 [139](#)
- Maire, A.-L., Langlois, M., Dohlen, K., et al. 2016b, in *Proceedings of SPIE*, Vol. 9908, *Ground-based and Airborne Instrumentation for Astronomy VI*, 990834 [39](#), [41](#), [56](#), [64](#)
- Maire, A. L., Rodet, L., Cantalloube, F., et al. 2019, *A&A*, 624, A118 [20](#)
- Manara, C. F., Tazzari, M., Long, F., et al. 2019, *A&A*, 628, A95 [134](#)
- Marino, S., Perez, S., & Casassus, S. 2015, *ApJ*, 798, L44 [148](#)
- Marleau, G. D., & Cumming, A. 2014, *MNRAS*, 437, 1378 [11](#)
- Marleau, G.-D., Klahr, H., Kuiper, R., & Mordasini, C. 2017, *ApJ*, 836, 221 [62](#), [68](#)
- Marleau, G.-D., Mordasini, C., & Kuiper, R. 2019, *ApJ*, 881, 144 [62](#)
- Marley, M. S., Fortney, J. J., Hubickyj, O., Bodenheimer, P., & Lissauer, J. J. 2007, *ApJ*, 655, 541 [11](#), [61](#)
- Marois, C., Correia, C., Galicher, R., et al. 2014, in *Proceedings of SPIE*, Vol. 9148, *Adaptive Optics Systems IV*, 91480U [41](#)
- Marois, C., Lafrenière, D., Doyon, R., Macintosh, B., & Nadeau, D. 2006, *ApJ*, 641, 556 [19](#), [41](#)
- Marois, C., Macintosh, B., Barman, T., et al. 2008, *Science*, 322, 1348 [12](#)
- Marois, C., Zuckerman, B., Konopacky, Q. M., Macintosh, B., & Barman, T. 2010, *Nature*, 468, 1080 [12](#)
- Martin, D. V. 2018, *Populations of Planets in Multiple Star Systems*, 156 [135](#)
- Martinez, P., Dorrer, C., Aller Carpentier, E., et al. 2009, *A&A*, 495, 363 [37](#)
- Masset, F. 2000, *A&AS*, 141, 165 [90](#)
- Masset, F., & Snellgrove, M. 2001, *MNRAS*, 320, L55 [11](#)
- Mathieu, R. D., Stassun, K., Basri, G., et al. 1997, *AJ*, 113, 1841 [156](#)
- Mathis, J. S., Rumpl, W., & Nordsieck, K. H. 1977, *ApJ*, 217, 425 [17](#)

Mayor, M., & Queloz, D. 1995, *Nature*, 378, 355 [2](#)

Mayor, M., Marmier, M., Lovis, C., et al. 2011, arXiv e-prints, arXiv:1109.2497 [2](#)

McCabe, C., Duchêne, G., & Ghez, A. M. 2002, *ApJ*, 575, 974 [145](#), [146](#)

McClure, M. K., Bergin, E. A., Cleeves, L. I., et al. 2016, *ApJ*, 831, 167 [4](#)

McKee, C. F., & Ostriker, E. C. 2007, *ARA&A*, 45, 565 [3](#)

Meech, K., & Raymond, S. N. 2019, arXiv e-prints, arXiv:1912.04361 [1](#), [2](#)

Mendigutía, I., Oudmaijer, R. D., Schneider, P. C., et al. 2018, *A&A*, 618, L9 [30](#)

Meru, F., Juhász, A., Ilee, J. D., et al. 2017, *ApJ*, 839, L24 [157](#)

Mesa, D., Gratton, R., Zurlo, A., et al. 2015, *A&A*, 576, A121 [41](#)

Mesa, D., Keppler, M., Cantalloube, F., et al. 2019, *A&A*, 632, A25 [67](#), [68](#), [69](#), [99](#), [123](#), [124](#), [165](#)

Metchev, S. A., Hillenbrand, L. A., & Meyer, M. R. 2004, *ApJ*, 600, 435 [34](#), [35](#)

Mie, G. 1908, *Annalen der Physik*, 330, 377 [13](#)

Mignone, A., Bodo, G., Massaglia, S., et al. 2007, *ApJS*, 170, 228 [150](#)

Milli, J., Mouillet, D., Lagrange, A.-M., et al. 2012, *A&A*, 545, A111 [20](#), [58](#)

Milli, J., Hibon, P., Christiaens, V., et al. 2017, *A&A*, 597, L2 [61](#)

Min, M., Canovas, H., Mulders, G. D., & Keller, C. U. 2012, *A&A*, 537, A75 [52](#)

Min, M., Dullemond, C. P., Dominik, C., de Koter, A., & Hovenier, J. W. 2009, *A&A*, 497, 155 [16](#)

Min, M., Hovenier, J. W., & de Koter, A. 2005, *A&A*, 432, 909 [13](#)

Min, M., Stolker, T., Dominik, C., & Benisty, M. 2017, *A&A*, 604, L10 [148](#), [149](#)

Miranda, R., Muñoz, D. J., & Lai, D. 2017, *MNRAS*, 466, 1170 [155](#), [156](#)

Monnier, J. D., Harries, T. J., Bae, J., et al. 2019, *ApJ*, 872, 122 [134](#), [156](#)

Montesinos, M., Perez, S., Casassus, S., et al. 2016, *ApJ*, 823, L8 [157](#)

Morbidelli, A., Szulágyi, J., Crida, A., et al. 2014, *Icarus*, 232, 266 [10](#)

- Mordasini, C. 2013, *A&A*, 558, A113 [11](#)
- Mordasini, C., Marleau, G.-D., & Mollière, P. 2017, *A&A*, 608, A72 [11](#), [12](#), [60](#), [61](#), [62](#)
- Morzinski, K. M., Close, L. M., Males, J. R., et al. 2016, in *Society of Photo-Optical Instrumentation Engineers (SPIE) Conference Series*, Vol. 9909, *Adaptive Optics Systems V*, 990901 [68](#)
- Mösta, P., Taam, R. E., & Duffell, P. C. 2019, *ApJ*, 875, L21 [156](#)
- Muñoz, D. J., Lai, D., Kratter, K., & Miranda, R. 2020, *ApJ*, 889, 114 [134](#)
- Müller, A., Keppler, M., Henning, T., et al. 2018, *A&A*, 617, L2 [34](#), [36](#), [47](#), [57](#), [67](#), [77](#), [78](#), [79](#), [81](#), [82](#), [84](#), [99](#), [126](#), [128](#), [165](#)
- Murakawa, K. 2010, *A&A*, 518, A63 [52](#)
- Musso Barucci, A., Cugno, G., Launhardt, R., et al. 2019, *A&A*, 631, A84 [68](#)
- Natta, A., Testi, L., Muzerolle, J., et al. 2004, *A&A*, 424, 603 [68](#)
- Nelson, A. F., & Marzari, F. 2016, *ApJ*, 827, 93 [157](#), [158](#)
- Öberg, K. I., Murray-Clay, R., & Bergin, E. A. 2011, *ApJ*, 743, L16 [165](#)
- Offner, S. S. R., & McKee, C. F. 2011, *ApJ*, 736, 53 [3](#)
- Okuzumi, S., Momose, M., Sirono, S.-i., Kobayashi, H., & Tanaka, H. 2016, *ApJ*, 821, 82 [26](#)
- Olofsson, J., Samland, M., Avenhaus, H., et al. 2016, *A&A*, 591, A108 [55](#)
- Ormel, C. W., & Klahr, H. H. 2010, *A&A*, 520, A43 [9](#)
- Orosz, J. A., Welsh, W. F., Haghhighipour, N., et al. 2019, *AJ*, 157, 174 [32](#), [135](#)
- Papaloizou, J., & Pringle, J. E. 1977, *MNRAS*, 181, 441 [134](#)
- Papaloizou, J. C. B., Nelson, R. P., Kley, W., Masset, F. S., & Artymowicz, P. 2007, in *Protostars and Planets V*, ed. B. Reipurth, D. Jewitt, & K. Keil, 655 [101](#)
- Patat, F., & Romaniello, M. 2006, *PASP*, 118, 146 [21](#)
- Pavlov, A., Möller-Nilsson, O., Feldt, M., et al. 2008, in *Proceedings of SPIE*, Vol. 7019, *Advanced Software and Control for Astronomy II*, 701939 [41](#)
- Paxton, B., Bildsten, L., Dotter, A., et al. 2011, *ApJS*, 192, 3 [34](#)

Paxton, B., Cantiello, M., Arras, P., et al. 2013, *ApJS*, 208, 4 [34](#)

Paxton, B., Marchant, P., Schwab, J., et al. 2015, *ApJS*, 220, 15 [34](#)

Pecaut, M. J., & Mamajek, E. E. 2016, *MNRAS*, 461, 794 [34](#), [36](#), [50](#), [92](#)

Pérez, S., Casassus, S., & Benítez- Llambay, P. 2018, *MNRAS*, 480, L12 [28](#), [101](#)

Perez, S., Dunhill, A., Casassus, S., et al. 2015, *ApJ*, 811, L5 [28](#), [101](#), [116](#), [119](#), [127](#)

Pérez, S., Dunhill, A., Casassus, S., et al. 2015, *ApJ*, 811, L5 [28](#), [84](#), [89](#)

Pérez, S., Casassus, S., Hales, A., et al. 2020, *ApJ*, 889, L24 [30](#), [101](#)

Peslier, A. H., Schönbachler, M., Busemann, H., & Karato, S.-I. 2017, *Space Sci.Rev.*, 212, 743 [1](#)

Phuong, N. T., Dutrey, A., Diep, P. N., et al. 2020a, *A&A*, 635, A12 [135](#), [143](#)

Phuong, N. T., Dutrey, A., Di Folco, E., et al. 2020b, *A&A*, 635, L9 [149](#), [157](#)

Piani, L., Marrocchi, Y., Rigaudier, T., et al. 2020, 369, 1110 [1](#)

Piétu, V., Gueth, F., Hily-Blant, P., Schuster, K.-F., & Pety, J. 2011, *A&A*, 528, A81 [145](#), [146](#)

Pineda, J. E., Szulágyi, J., Quanz, S. P., et al. 2019, *ApJ*, 871, 48 [96](#), [97](#)

Pinilla, P., Benisty, M., & Birnstiel, T. 2012a, *A&A*, 545, A81 [90](#), [95](#), [96](#)

—. 2012b, *A&A*, 545, A81 [144](#)

Pinilla, P., Birnstiel, T., Benisty, M., et al. 2013, *A&A*, 554, A95 [97](#)

Pinilla, P., Birnstiel, T., Ricci, L., et al. 2012c, *A&A*, 538, A114 [10](#)

Pinilla, P., de Juan Ovelar, M., Ataiee, S., et al. 2015a, *A&A*, 573, A9 [36](#)

Pinilla, P., Flock, M., Ovelar, M. d. J., & Birnstiel, T. 2016, *A&A*, 596, A81 [26](#), [36](#)

Pinilla, P., Benisty, M., Birnstiel, T., et al. 2014, *A&A*, 564, A51 [107](#)

Pinilla, P., de Boer, J., Benisty, M., et al. 2015b, *A&A*, 584, L4 [36](#)

Pinilla, P., Pérez, L. M., Andrews, S., et al. 2017a, *ApJ*, 839, 99 [83](#)

Pinilla, P., Quiroga-Nuñez, L. H., Benisty, M., et al. 2017b, *ApJ*, 846, 70 [166](#)

Pinilla, P., Tazzari, M., Pascucci, I., et al. 2018a, *ApJ*, 859, 32 [75](#), [76](#)

Pinilla, P., Benisty, M., de Boer, J., et al. 2018b, *ApJ*, 868, 85 29

Pinte, C., Ménard, F., Duchêne, G., & Bastien, P. 2006, *A&A*, 459, 797 16

Pinte, C., Ménard, F., Duchêne, G., et al. 2018a, *A&A*, 609, A47 28, 124, 129, 163

Pinte, C., Price, D. J., Ménard, F., et al. 2018b, *ApJ*, 860, L13 28, 30, 84, 85, 94, 101, 116, 127, 163

Pinte, C., van der Plas, G., Ménard, F., et al. 2019, *Nature Astronomy*, 3, 1109 28, 30, 101, 127

Pinte, C., Price, D. J., Ménard, F., et al. 2020, *ApJ*, 890, L9 30, 101, 127

Pohl, A., Pinilla, P., Benisty, M., et al. 2015, *MNRAS*, 453, 1768 157

Pohl, A., Sissa, E., Langlois, M., et al. 2017a, *A&A*, 605, A34 39

Pohl, A., Benisty, M., Pinilla, P., et al. 2017b, *ApJ*, 850, 52 29, 31

Pollack, J. B., Hubickyj, O., Bodenheimer, P., et al. 1996, *Icarus*, 124, 62 8, 9

Price, D. J., Cuello, N., Pinte, C., et al. 2018, *MNRAS*, 477, 1270 83, 156

Pringle, J. E. 1981, *ARA&A*, 19, 137 7

Qi, C., Öberg, K. I., Andrews, S. M., et al. 2015, *ApJ*, 813, 128 165

Quanz, S. P., Amara, A., Meyer, M. R., et al. 2015, *ApJ*, 807, 64 29

—. 2013, *ApJ*, 766, L1 29

Quillen, A. C., & Trilling, D. E. 1998, *ApJ*, 508, 707 10, 77

Raghavan, D., McAlister, H. A., Henry, T. J., et al. 2010, *ApJS*, 190, 1 133

Rajpurohit, A. S., Reylé, C., Allard, F., et al. 2013, *A&A*, 556, A15 137, 138

Rameau, J., Follette, K. B., Pueyo, L., et al. 2017, *AJ*, 153, 244 30

Raymond, S. N., & Izidoro, A. 2017, *Icarus*, 297, 134 1

Reggiani, M., Quanz, S. P., Meyer, M. R., et al. 2014, *ApJ*, 792, L23 29

Reggiani, M., Christiaens, V., Absil, O., et al. 2018, *A&A*, 611, A74 30

Riaud, P., Mawet, D., Absil, O., et al. 2006, *A&A*, 458, 317 34, 35

Ribas, Á., Merín, B., Bouy, H., & Maud, L. T. 2014, *A&A*, 561, A54 [7](#)

Ricci, L., Cazzoletti, P., Czekala, I., et al. 2017, *AJ*, 154, 24 [96](#)

Rich, E. A., Wisniewski, J. P., Currie, T., et al. 2019, *ApJ*, 875, 38 [102](#)

Rigliaco, E., Natta, A., Testi, L., et al. 2012, *A&A*, 548, A56 [68](#)

Riols, A., & Lesur, G. 2019, *A&A*, 625, A108 [26](#)

Robin, A. C., Reylé, C., Derrière, S., & Picaud, S. 2003, *A&A*, 409, 523 [56](#)

Rosenfeld, K. A., Andrews, S. M., Hughes, A. M., Wilner, D. J., & Qi, C. 2013, *ApJ*, 774, 16  
[6](#), [81](#), [82](#), [83](#), [114](#)

Rosotti, G. P., & Clarke, C. J. 2018, *MNRAS*, 473, 5630 [134](#)

Rosotti, G. P., Juhasz, A., Booth, R. A., & Clarke, C. J. 2016, *MNRAS*, 459, 2790 [26](#), [96](#), [101](#)

Rosotti, G. P., Benisty, M., Juhász, A., et al. 2020, *MNRAS*, 491, 1335 [157](#)

Ruge, J. P., Flock, M., Wolf, S., et al. 2016, *A&A*, 590, A17 [26](#)

Sallum, S., Follette, K. B., Eisner, J. A., et al. 2015, *Nature*, 527, 342 [30](#)

Samland, M., Mollière, P., Bonnefoy, M., et al. 2017, *A&A*, 603, A57 [20](#), [62](#)

Schmid, H. M., Joos, F., & Tschan, D. 2006, *A&A*, 452, 657 [21](#)

Schmid, H. M., Bazzon, A., Roelfsema, R., et al. 2018, *A&A*, 619, A9 [37](#), [40](#)

Schwarz, R., Funk, B., Zechner, R., & Bazsó, Á. 2016, *MNRAS*, 460, 3598 [135](#)

Shakura, N. I., & Sunyaev, R. A. 1973, *A&A*, 500, 33 [7](#)

Siess, L., Dufour, E., & Forestini, M. 2000, *A&A*, 358, 593 [137](#)

Silber, J., Gledhill, T., Duchêne, G., & Ménard, F. 2000, *ApJ*, 536, L89 [144](#), [147](#)

Simon, M., Guilloteau, S., Beck, T. L., et al. 2019, *ApJ*, 884, 42 [137](#)

Sissa, E., Gratton, R., Garufi, A., et al. 2018, *A&A*, 619, A160 [30](#)

Skemer, A. J., Close, L. M., Greene, T. P., et al. 2011, *ApJ*, 740, 43 [141](#), [156](#)

Snellen, I. A. G., Brandl, B. R., de Kok, R. J., et al. 2014, *Nature*, 509, 63 [166](#)

Soummer, R., Pueyo, L., & Larkin, J. 2012, *ApJ*, 755, L28 [19](#), [41](#)

Spiegel, D. S., & Burrows, A. 2012, *ApJ*, 745, 174 [62](#)

Steinacker, J., Baes, M., & Gordon, K. D. 2013, *ARA&A*, 51, 63 [14](#), [16](#)

Stokes, G. G. 1851, *Transactions of the Cambridge Philosophical Society*, 9, 399 [16](#)

Stolker, T., Sitko, M., Lazareff, B., et al. 2017, *ApJ*, 849, 143 [29](#)

Strom, K. M., Strom, S. E., Edwards, S., Cabrit, S., & Skrutskie, M. F. 1989, *AJ*, 97, 1451 [29](#)

Suriano, S. S., Li, Z.-Y., Krasnopolsky, R., & Shang, H. 2018, *MNRAS*, 477, 1239 [26](#)

Szulágyi, J., Morbidelli, A., Crida, A., & Masset, F. 2014, *ApJ*, 782, 65 [9](#), [10](#), [77](#)

Szulágyi, J., & Mordasini, C. 2017, *MNRAS*, 465, L64 [9](#), [68](#)

Szulágyi, J., Plas, G. v. d., Meyer, M. R., et al. 2018, *MNRAS*, 473, 3573 [26](#)

Takata, T., & Stevenson, D. J. 1996, *Icarus*, 123, 404 [166](#)

Tang, Y.-W., Dutrey, A., Guilloteau, S., et al. 2014, *ApJ*, 793, 10 [134](#)

Tang, Y.-w., Dutrey, A., Guilloteau, S., et al. 2016, *The Astrophysical Journal*, 820, 19 [135](#), [143](#), [149](#), [157](#)

Tang, Y.-W., Guilloteau, S., Dutrey, A., et al. 2017, *ApJ*, 840, 32 [29](#), [82](#)

Tanigawa, T., Ohtsuki, K., & Machida, M. N. 2012, *ApJ*, 747, 47 [9](#)

Tanigawa, T., & Tanaka, H. 2016, *ApJ*, 823, 48 [10](#)

Tazzari, M., Testi, L., Natta, A., et al. 2017, *A&A*, 606, A88 [5](#)

Teague, R. 2019, *The Journal of Open Source Software*, 4, 1220 [28](#), [85](#)

Teague, R., Bae, J., Bergin, E. A., Birnstiel, T., & Foreman-Mackey, D. 2018a, *ApJ*, 860, L12 [28](#), [30](#), [72](#), [84](#), [85](#), [87](#), [90](#), [95](#), [101](#), [163](#)

Teague, R., Bae, J., Birnstiel, T., & Bergin, E. A. 2018b, *ApJ*, 868, 113 [28](#), [83](#), [85](#), [122](#)

Teague, R., & Foreman-Mackey, D. 2018, *Research Notes of the American Astronomical Society*, 2, 173 [82](#), [83](#)

Teague, R., & Foreman-Mackey, D. 2018, *bettermoments: A robust method to measure line centroids*, doi:10.5281/zenodo.1419754 [83](#), [111](#)

- Teague, R., Jankovic, M. R., Haworth, T. J., Qi, C., & Ilee, J. D. 2020, *MNRAS*, 495, 451 [129](#), [163](#)
- Teague, R., Guilloteau, S., Semenov, D., et al. 2016, *A&A*, 592, A49 [8](#), [91](#), [120](#), [121](#)
- Teague, R., Henning, T., Guilloteau, S., et al. 2018c, *ApJ*, 864, 133 [8](#), [91](#)
- Testi, L., Birnstiel, T., Ricci, L., et al. 2014, in *Protostars and Planets VI*, ed. H. Beuther, R. S. Klessen, C. P. Dullemond, & T. Henning, 339 [6](#)
- Thalmann, C., Schmid, H. M., Boccaletti, A., et al. 2008, in *Proceedings of SPIE*, Vol. 7014, *Ground-based and Airborne Instrumentation for Astronomy II*, 70143F [40](#)
- Thalmann, C., Grady, C. A., Goto, M., et al. 2010, *ApJ*, 718, L87 [29](#)
- Thalmann, C., Janson, M., Garufi, A., et al. 2016, *ApJ*, 828, L17 [30](#), [31](#)
- Thatte, N. A., Clarke, F., Bryson, I., et al. 2016, in *Society of Photo-Optical Instrumentation Engineers (SPIE) Conference Series*, Vol. 9908, *Ground-based and Airborne Instrumentation for Astronomy VI*, 99081X [166](#)
- Thebault, P., & Haghhighipour, N. 2015, *Planet Formation in Binaries*, 309–340 [134](#), [159](#)
- Thompson, A. R., Moran, J. M., & Swenson, George W., J. 2017, *Interferometry and Synthesis in Radio Astronomy*, 3rd Edition, doi:10.1007/978-3-319-44431-4 [23](#), [25](#)
- Thun, D., & Kley, W. 2018, *A&A*, 616, A47 [150](#), [151](#), [157](#)
- Tognelli, E., Prada Moroni, P. G., & Degl’Innocenti, S. 2011, *A&A*, 533, A109 [34](#), [35](#)
- Tripathi, A., Andrews, S. M., Birnstiel, T., & Wilner, D. J. 2017, *ApJ*, 845, 44 [5](#)
- Tsukamoto, Y., Machida, M. N., & Inutsuka, S.-i. 2013, *MNRAS*, 436, 1667 [12](#)
- Turner, N. J., Fromang, S., Gammie, C., et al. 2014, in *Protostars and Planets VI*, ed. H. Beuther, R. S. Klessen, C. P. Dullemond, & T. Henning, 411 [8](#)
- van Boekel, R., Benneke, B., Heng, K., et al. 2012, in *Society of Photo-Optical Instrumentation Engineers (SPIE) Conference Series*, Vol. 8442, *Space Telescopes and Instrumentation 2012: Optical, Infrared, and Millimeter Wave*, 84421F [18](#)
- van Boekel, R., Henning, T., Menu, J., et al. 2017, *ApJ*, 837, 132 [29](#)
- van der Marel, N., van Dishoeck, E. F., Bruderer, S., et al. 2016, *A&A*, 585, A58 [84](#)

- van der Marel, N., van Dishoeck, E. F., Bruderer, S., Pérez, L., & Isella, A. 2015, *A&A*, 579, A106 [84](#)
- van der Marel, N., van Dishoeck, E. F., Bruderer, S., et al. 2013, *Science*, 340, 1199 [29](#)
- van Dishoeck, E. F., Bergin, E. A., Lis, D. C., & Lunine, J. I. 2014, in *Protostars and Planets VI*, ed. H. Beuther, R. S. Klessen, C. P. Dullemond, & T. Henning, 835 [1](#)
- van Holstein, R. G., Snik, F., Girard, J. H., et al. 2017, in *Society of Photo-Optical Instrumentation Engineers (SPIE) Conference Series*, Vol. 10400, Society of Photo-Optical Instrumentation Engineers (SPIE) Conference Series, 1040015 [39](#)
- van Holstein, R. G., Girard, J. H., de Boer, J., et al. 2020, *A&A*, 633, A64 [21](#), [39](#), [40](#), [138](#), [139](#), [141](#)
- Vigan, A., Gry, C., Salter, G., et al. 2015, *MNRAS*, 454, 129 [41](#)
- Vigan, A., Moutou, C., Langlois, M., et al. 2010, *MNRAS*, 407, 71 [40](#)
- Villenave, M., Benisty, M., Dent, W. R. F., et al. 2019, *A&A*, 624, A7 [145](#)
- Villenave, M., Menard, F., Dent, W. R. F., et al. 2020, arXiv e-prints, arXiv:2008.06518 [7](#)
- Vos, J. M., Allers, K., Apai, D., et al. 2019, arXiv e-prints, arXiv:1903.06691 [165](#)
- Wagner, K., Stone, J. M., Spalding, E., et al. 2019, *ApJ*, 882, 20 [30](#)
- Wagner, K., Follete, K. B., Close, L. M., et al. 2018, *ApJ*, 863, L8 [67](#), [68](#), [79](#), [80](#), [96](#), [162](#)
- Wahhaj, Z., Liu, M. C., Biller, B. A., et al. 2011, *ApJ*, 729, 139 [61](#)
- . 2014, *A&A*, 567, A34 [64](#)
- Wang, J. J., Ginzburg, S., Ren, B., et al. 2020, *AJ*, 159, 263 [69](#), [99](#)
- Warren, P. H. 2011, *Earth and Planetary Science Letters*, 311, 93 [1](#)
- Waters, L. B. F. M., & Waelkens, C. 1998, *ARA&A*, 36, 233 [3](#)
- Weidenschilling, S. J. 1977, *MNRAS*, 180, 57 [7](#)
- White, R. J., Ghez, A. M., Reid, I. N., & Schultz, G. 1999, *ApJ*, 520, 811 [135](#), [136](#), [137](#), [141](#)
- Williams, J. P., & Best, W. M. J. 2014, *ApJ*, 788, 59 [4](#), [92](#)
- Williams, J. P., & Cieza, L. A. 2011, *ARA&A*, 49, 67 [4](#)

Winn, J. N., & Fabrycky, D. C. 2015, *ARA&A*, 53, 409 2

Wolf, S., Henning, T., & Stecklum, B. 1999, *A&A*, 349, 839 16

Wolff, S. G., Ménard, F., Caceres, C., et al. 2017, *AJ*, 154, 26 96

Xuan, J. W., Bryan, M. L., Knutson, H. A., et al. 2020, *AJ*, 159, 97 166

Yang, Y., Hashimoto, J., Hayashi, S. S., et al. 2017, *AJ*, 153, 7 136, 142, 145, 147

Youdin, A. N., & Goodman, J. 2005, *ApJ*, 620, 459 9

Zhang, K., Blake, G. A., & Bergin, E. A. 2015, *ApJ*, 806, L7 26

Zhang, S., Zhu, Z., Huang, J., et al. 2018, *ApJ*, 869, L47 26, 29, 101

Zhu, Z., Andrews, S. M., & Isella, A. 2018, *MNRAS*, 479, 1850 26, 78, 97

Zhu, Z., Hartmann, L., Nelson, R. P., & Gammie, C. F. 2012, *ApJ*, 746, 110 12

Zhu, Z., Nelson, R. P., Hartmann, L., Espaillat, C., & Calvet, N. 2011, *ApJ*, 729, 47 96

Zubko, V. G., Mennella, V., Colangeli, L., & Bussoletti, E. 1996, *MNRAS*, 282, 1321 14, 15, 50, 92, 152



## Acknowledgements

Looking back at the past four years, I feel fulfilled by an exciting adventure, in both, a scientific and personal context. I am most grateful that I was allowed to meet all these wonderful people along the way – this has been an extremely enriching experience to me.

First and foremost, I would like to thank my advisors Thomas Henning, Roy van Boekel and Myriam Benisty.

To Thomas, I am deeply grateful to you for giving me the opportunity to work on these exciting projects, and guiding me throughout this PhD. Working on PDS 70 has been an wonderful journey, thank you for your confidence, full support and encouragement! I could always count on your invaluable advice and comments. Thank you!

To Roy, thank you for the many exciting and inspiring discussions we had. You had always an open door for me, and took all your time for answering my detailed questions. It was really fun working with you, and I learned so much!

To Myriam, I am very grateful for our great collaboration, without which this Thesis wouldn't have been possible as such. Despite the 12000 km between our offices, you were always there for me, and supported me in all aspects. Thank you for countless virtual discussions – I will miss those! Your enthusiasm to go beyond is truly inspiring.

I would like to thank my Thesis committee members, Thomas, Roy and Kees Dullemond for their helpful advice and stimulating discussions. Thanks to Thomas and Kees for agreeing to referee this Thesis, and to Eva Grebel and Norbert Frank for being part of the examination committee.

A big thank you to Myriam, Roy, Faustine, Martin and Paula for reading various parts of this Thesis and providing comments. This greatly helped to improve the manuscript – thank you!

I also appreciate all the help and contributions from my collaborators. In particular I would like to mention André Müller who was essential to the discovery of PDS 70 b. I am also grateful to Richard Teague, Jaehan Bae, Stefano Facchini, Andrea Isella and Myriam Benisty for working together on the ALMA projects. Thanks for innumerable telecons

and slack discussion. Working with you was a wonderful experience!

Thanks to all the people at MPIA and students from IMPRS who have made this time invaluable. To Paula, Martin and Gabriele for unforgettable adventures, hopefully there are more to follow! Thank you Paula for being there for me, in particular while writing this thesis – your salad is the best in the world! This thesis may not have happened without Gesa: thank you for motivating me on a cloudy observing night in La Silla to apply to IMPRS! A big thank you to Faustine for all your support, cheering me up in tough moments, and providing me with ‘real’ French cheese! I also want to thank the amazing colleagues from extended office 225 for a great office spirit and working environment.

Martin, danke dass du mich einfach immer zum Lachen bringst, und so schon viele dunkle Wolken vertrieben hast. Ich bin glücklich und dankbar dass ich diesen Abschnitt zusammen mit dir gehen darf. Danke dass du immer geduldig, unterstützend und ermutigend für mich da bist, in Zeiten von aufregenden Abenteuern, wie auch in Zeiten von Unruhe und schwierigen Entscheidungen!

An meine Familie: Mama, Papa, Jeannette, Christian, Elias - danke dass ihr mich auf diesem Weg begleitet habt! Ohne euch wäre dies nicht möglich gewesen. Danke für eure bedingungslose Unterstützung, Zuneigung, Ermutigung und euer immer offenes Ohr. Ich kann immer auf euch zählen, dafür bin ich euch unglaublich dankbar!